

HIGH PERFORMANCE MEMS GYROSCOPES

A THESIS SUBMITTED TO  
THE GRADUATE SCHOOL OF NATURAL AND APPLIED SCIENCES  
OF  
MIDDLE EAST TECHNICAL UNIVERSITY

BY

KIVANÇ AZGIN

IN PARTIAL FULFILLMENT OF THE REQUIREMENTS  
FOR  
THE DEGREE OF MASTER OF SCIENCE  
IN  
ELECTRICAL AND ELECTRONICS ENGINEERING

FEBRUARY 2007

Approval of the Graduate School of Natural and Applied Sciences

---

Prof. Dr. Canan ÖZGEN  
Director

I certify that this thesis satisfies all the requirements as a thesis for the degree of Master of Science.

---

Prof. Dr. İsmet ERKMEN  
Head of Department

This is to certify that we have read this thesis and that in our opinion it is fully adequate, in scope and quality, as a thesis for the degree of Master of Science.

---

Prof. Dr. Tayfun AKIN  
Supervisor

**Examining Committee Members**

Prof. Dr. Cengiz BEŞİKÇİ (METU, EEE) \_\_\_\_\_

Prof. Dr. Tayfun AKIN (METU, EEE) \_\_\_\_\_

Prof. Dr. Aydan M. ERKMEN (METU, EEE) \_\_\_\_\_

Asst. Prof. Dr. Haluk KÜLAH (METU, EEE) \_\_\_\_\_

Prof. Dr. Eres SÖYLEMEZ (METU, ME) \_\_\_\_\_

**I hereby declare that all information in this document has been obtained and presented in accordance with academic rules and ethical conduct. I also declare that, as required by these rules and conduct, I have fully cited and referenced all material and results that are not original to this work.**

**Kıvanç AZGIN**

## **ABSTRACT**

# **HIGH PERFORMANCE MEMS GYROSCOPES**

Azgin, Kivanç

M. Sc., Department of Electrical and Electronics Engineering

Supervisor: Prof. Dr. Tayfun Akın

February 2007, 151 pages

This thesis reports development of three different high performance, low g-sensitive micromachined gyroscopes having single, double, and quadruple masses. The single mass gyroscope (SMG) is developed for comparison of its performance with the double mass gyroscope (DMG) and quadruple mass gyroscope (QMG). DMG is a tuning fork gyroscope, diminishing the effects of unpredictable g-loadings during regular operation, while QMG is a twin tuning fork gyroscope, developed for a uniform and minimized g-sensitivity. DMG and QMG use novel ring spring connections for merging the masses in drive modes, providing uniform and anti-phase drive mode vibrations that minimize the cross-coupling and the effects of intrinsic and extrinsic accelerations on the scale factor and bias levels of the gyroscopes. The sense mode of each mass of the multi-mass gyroscopes is designed to have higher resonance frequencies than that of the drive mode for possible matching requirements, and these sense modes have dedicated frequency tuning electrodes for frequency matching or tuning. Detailed performance simulations are

performed with a very sophisticated computer model using the ARCHITECT software.

These gyroscopes are fabricated using a standard SOIMUMPs process of MEMSCAP Inc., which provides capacitive gaps of 2  $\mu\text{m}$  and structural layer thickness of 25  $\mu\text{m}$ . Die sizes of the fabricated gyroscope chips are 4.1 mm x 4.1 mm for the single mass, 4.1 mm x 8.9 mm for the double mass, and 8.9 mm x 8.9 mm for the quadruple mass gyroscope. Fabricated gyroscopes are tested with dedicated differential readout electronics constructed with discrete components. Drive mode resonance frequencies of these gyroscopes are in a range of 3.4 kHz to 5.1 kHz. Depending on the drive mode mechanics, the drive mode quality (Q) factors of the fabricated gyroscopes are about 300 at atmospheric pressure and reaches to a value of 2500 at a vacuum ambient of 50 mTorr. Resolvable rates of the fabricated gyroscopes at atmospheric pressure are measured to be 0.109 deg/sec, 0.055 deg/sec, and 1.80 deg/sec for SMG, DMG, and QMG, respectively. At vacuum, the respective resolutions of these gyroscopes improve significantly, reaching to 106 deg/hr with the SMG and 780 deg/hr with the QMG, even though discrete readout electronics are used. Acceleration sensitivity measurements at atmosphere reveal that QMG has the lowest bias g-sensitivity and the scale factor g-sensitivity of 1.02deg/sec/g and 1.59(mV/(deg/sec))/g, respectively. The performance levels of these multi-mass gyroscopes can be even further improved with high performance integrated capacitive readout electronics and precise sense mode phase matching.

Keywords: Gyroscope, MEMS Gyroscope, Tuning Fork Gyroscope, Silicon Micromachining, SOI, g-Sensitivity, Microelectromechanical Systems (MEMS).

## ÖZ

# YÜKSEK PERFORMANSLI MEMS DÖNÜÖLÇERLER

Azgın, Kıvanç

Yüksek Lisans, Elektrik ve Elektronik Mühendisliği Bölümü

Tez Yöneticisi: Prof. Dr. Tayfun AKIN

Şubat 2007, 151 sayfa

Bu tez tek, çift ve dört kütleyle sahip üç değişik yüksek performanslı, düşük g-hassasiyetli dönüölçerin geliştirilmesini anlatmaktadır. Tek kütleli dönüölçer (TKD), çift kütleli dönüölçer (ÇKD) ve dört kütleli dönüölçer (DKD) ile performans karşılaştırması yapmak için geliştirilmiştir. ÇKD, öngörülemeyen g-yüklenmelerinin etkisini azaltan bir diyapazon dönüölçerdir, DKD ise en aza indirilmiş birörnek g-hassasiyeti için geliştirilmiş bir ikiz diyapazon dönüölçerdir. DKD ve ÇKD, karşı etkileşimi ve içsel ve dışsal ivmelerin oranı katsayısıyla çıkış sinyalleri üzerindeki etkilerini en aza indiren zıt fazlı ve birörnek sürüş modu titreşimleri sağlamak için sürüş modunda kütleleri birleştiren yeni halkasal yay bağlantıları kullanmaktadır. Çokkütleli dönüölçerlerin her bir kütlelerinin algılama modlarının rezonans frekansları olası frekans eşleştirme ihtiyacı için sürüş modundan daha yüksek tasarlanmıştır ve bu algılama modlarının frekans eşleştirmek veya ayarlamak için adanmış frekans ayarlama elektrotları vardır. Gelişmiş bilgisayar modelleriyle ARCHITECT yazılımı kullanılarak detaylı performans simülasyonları yapılmıştır.

Bu dönüölçerler, 2 µm sığasal açıklık ve 25 µm yapısal kalınlık sağlayan MEMSCAP şirketinin standart SOIMUMPs işlemiyle üretilmişlerdir. Üretilen dönüölçerlerin yonga boyutları tek kütleli için 4.1 mm x 4.1 mm, çift kütleli için 4.1 mm x 8.9 mm ve dört kütleli dönüölçer için 8.9 mm x 8.9 mm'dir. Üretilen dönüölçerler ayrı bileşenlerden oluşturulan adanmış farksal okuma devreleriyle test edilmişlerdir. Bu dönüölçerlerin sürüş modu rezonans frekansları 3.4 kHz ile 5.1 kHz arasındadır. Sürüş modu mekaniğine bağılı olarak, üretilen dönüölçerlerin atmosferik basınçta sürüş modu kalite faktörleri 300 civarındadır ve 50 mTorr vakum ortamında bu deęer 2500'e kadar çıkmaktadır. Üretilen dönüölçerlerden TKD 0.109 der/sn, ÇKD 0.055 der/sn ve DKD 1.80 der/sn lik dönü hızı farkını ayırıştırabilmektedir. Vakum ortamında bu dönüölçerlerin hassasiyetleri belirgin bir şekilde artmakta ve ayrı okuma devreleri kullanılmasına rağmen TKD için 106 der/saat ve DKD için 780 der/saat'e ulaşmaktadır. Atmosfer basıncında yapılan ivme hassasiyeti ölçümleri DKD'nin 1.02 der/sn/g'lik çıkış g-hassasiyeti ve 1.59(mV/(der/sn))/g'lik orantı katsayısı g-hassasiyeti ile en düşük deęerlere sahip olduğunu göstermektedir. Bu çok kütleli dönüölçerlerin performans seviyeleri, yüksek performanslı tümleşik sığasal okuma devreleri kullanılarak ve hassas algılama modu faz eşlemesiyle daha da iyileştirilebilir.

Anahtar Kelimeler: Dönüölçer, MEMS Dönüölçer, Diyapazon Dönüölçer, Silisyum Mikroişleme, SOI, g-Hassasiyeti, Mikroelektromekanik Sistemler (MEMS)

*To My Dear Mother and Father*

*To My Sweet Sister*

*And*

*To My Love, Mine...*

## **ACKNOWLEDGEMENTS**

First, I would like to thank to my thesis advisor Prof. Dr. Tayfun AKIN not only for his support, guidance, and encouragement, but also, for his friendly and optimistic attitude during this research. It is a privilege for me to work with him. I would also thank to Dr. Said Emre Alper for the very valuable discussions on every detail of the gyroscopes and for cleanroom trainings on microfabrication techniques. His patience, determination and goodwill make him special in my academic life.

Special thanks to Yüksel Temiz for his helps and suggestions in the tests and, before anything, for his friendship. I also thank to Kanber Mithat Silay for the valuable discussions on the tests. Thanks to Mahmud Yusuf Tanrıkulu, Orhan Şevket Akar, İlker Ender Ocak and Ata Tuna Çiftlik for very valuable cleanroom experiences and for their helps in vital problems. I also appreciate the cooperation of Fehmi Civitci in various experimental fields. I would like to thank to all METU MEMS-VLSI Research Group members individually for the nice atmosphere in the laboratory and to METU-MET staff for creating a nice microfabrication environment

Besides, I am very grateful to my mother and father for their invaluable efforts and their dedication throughout my life. I also appreciate my sister for her very valuable support and helps. Finally, memorable thanks to Özgüler Mine Aköner for her understanding, endless patience, support, and love.

This research is funded by State Planning Organization and Turkish Ministry of Defense.

## TABLE OF CONTENTS

PLAGIARISM .....	iii
ABSTRACT .....	iv
ÖZ .....	vi
DEDICATION .....	viii
ACKNOWLEDGEMENTS .....	ix
TABLE OF CONTENTS .....	x
LIST OF TABLES .....	xiii
LIST OF FIGURES .....	xiv
CHAPTERS	
1.INTRODUCTION.....	1
1.1 Gyroscopes.....	3
1.2 Micromachined Gyroscopes.....	13
1.3 Multi-Mass Gyroscope Structures Developed at METU.....	20
1.4 Research Objectives and Thesis Organization.....	24
2.THEORY OF VIBRATORY GYROSCOPES .....	27
2.1 Mechanical Model of Vibratory Microgyroscopes.....	27
2.1.1 Mechanics of the Drive Mode.....	28
2.1.2 Mechanics of the Sense Mode with Coriolis Coupling.....	32
2.2 Electrostatic Actuation and Sensing.....	37
2.3 Flexion Elements.....	43
2.4 Nonlinearity and Noise Sources.....	48
2.4.1 Side Instability .....	48
2.4.2 Electrostatic Levitation .....	51
2.4.3 Acceleration Terms Other Than Coriolis.....	51

2.4.3.1	Static and Fluctuating Accelerations.....	52
2.4.3.2	Rotation Induced Accelerations .....	54
2.4.4	Undercut During Etching .....	56
2.4.5	Operation Temperature .....	58
2.5	Summary .....	59
3.	DESIGN AND FABRICATION OF THE PROPOSED GYROSCOPES .....	60
3.1	Flexion Elements of the Proposed Gyroscopes.....	60
3.2	The Coupling Mechanism .....	62
3.3	Brownian Noise Estimation .....	67
3.4	FEM Modal and Misses-Stress Analysis .....	69
3.5	ARCHITECT Models of Proposed Gyroscopes .....	73
3.6	Fabrication .....	83
3.7	Summary .....	85
4.	TEST RESULTS OF FABRICATED GYROSCOPES.....	86
4.1	Required Test Arrangements.....	86
4.1.1	Post Processing of the Fabricated Gyroscopes.....	87
4.1.2	Resonance Characterization of Drive and Sense Modes.....	89
4.1.2.1	Resonance Characteristics of Single Mass Gyroscope (SMG) .....	89
4.1.2.2	Resonance Characteristics of Double Mass (Tuning Fork) Gyroscope (DMG) .....	92
4.1.2.3	Resonance Characteristics of Quadruple Mass (Twin Tuning Fork) Gyroscope (QMG) .....	96
4.1.3	Readout Electronics .....	101
4.1.4	Self Resonance Loop and Test Setups .....	104
4.2	Test Results with Performance Characteristics of SMG, DMG and QMG ... .....	107
4.2.1	Performance Characteristics of SMG.....	108
4.2.1.1	Test Results of SMG at Atmospheric Ambient.....	108
4.2.1.2	Test Results of SMG at Vacuum Ambient.....	116
4.2.2	Performance Characteristics of DMG .....	119
4.2.2.1	Test Results of DMG at Atmospheric Ambient.....	120
4.2.2.2	Test Results of DMG at Vacuum Ambient.....	127

4.2.3	Performance Characteristics of QMG .....	130
4.2.3.1	Test Results of QMG at Atmospheric Ambient.....	130
4.2.3.2	Test Results of QMG at Vacuum Ambient.....	137
4.3	Summary of Tests and Conclusions.....	140
5.	CONCLUSIONS AND FUTURE WORK .....	143
6.	REFERENCES.....	148

## LIST OF TABLES

Table 3.1: Estimated rate equivalent Brownian noise of the SMG, DMG and QMG .....	68
Table 3.2: The frequencies of the resonant mode shapes of the single mass gyroscope. ....	69
Table 3.3: The frequencies of the resonant mode shapes of the double mass gyroscope. ....	70
Table 3.4: The frequencies of the resonant mode shapes of the quadruple mass gyroscope. ....	72
Table 4.1: Performance specifications of the single-mass gyroscope in atmospheric pressure and in vacuum. Vacuum ambient decreases the noise floor and increases the resolution due to the increased Q factor and decreased Brownian type noise. ....	119
Table 4.2: Performance specifications of the double-mass gyroscope in atmospheric pressure and in vacuum. ....	130
Table 4.3: Performance specifications of the quadruple mass gyroscope in atmospheric pressure and in vacuum. ....	140
Table 4.4: Performance comparison of the three gyroscopes with single, double and quadruple mass(es). Increasing the number of masses and the symmetry of the gyroscope topologies decreases the g-sensitivity but also decreases the resolvable rate at atmospheric pressure. ....	141

## LIST OF FIGURES

Figure 1.1: Coriolis effect; the bowling ball which slides over a rotating frictionless disk surface.....	4
Figure 1.2: Rotating disk with the nonlinear friction characteristics which allows the ball move with a constant velocity with respect to the slot.....	5
Figure 1.3: Velocity differentials of the ball together with their directions.....	6
Figure 1.4: A single degree-of-freedom gyroscope, which is the <i>rate gyroscope</i> . .....	8
Figure 1.5: Structure of a two DOF gyroscope with Cardan suspension, which is called the <i>torque-free gyroscope</i> . .....	9
Figure 1.6: A conventional 2 DOF gyroscope.....	10
Figure 1.7: The precession of the gyro proof mass which is suspended with a vibrating frame fixed to the rotating disc.....	11
Figure 1.8: A high aspect ratio ring gyroscope with its operational structure [14]. .....	14
Figure 1.9: Schematic diagram of the BEI GyroChip by Systron Donner Inertial Division, showing the drive and sense modes of the twin tuning forks [15].....	15
Figure 1.10: Mechanical model of the tuning fork gyro reported by Bosch GMBH [17].....	15
Figure 1.11: Analog Devices' monolithic gyroscope including the gyro structure and necessary electronics integrated on a single chip [20]. .....	17

Figure 1.12: Fabrication process sequence of a vacuum packaged low noise micromachined silicon gyroscope with glass substrate, developed by Seoul National University [23].	19
Figure 1.13: 3-D model of the single mass gyroscope developed in this research	21
Figure 1.14: 3-D model of the tuning fork gyroscope with the symmetrically anchored ring spring between the vibrating masses.	22
Figure 1.15: The model of the twin-tuning-fork gyroscopes with the ring spring for drive mode coupling of the proof masse.	23
Figure 2.1: A unit electrostatic forcing element which is called the “Varying Overlap-Area Type Finger”.	39
Figure 2.2: A unit electrostatic sensing element which is called the “Varying Gap Type Finger”.	42
Figure 2.3: Double sided and double folded spring.	44
Figure 2.4: Force and moment distribution on the double sided and double folded spring loaded in x-direction.	45
Figure 2.5: The single sided double folded spring, which has the connections on the same side.	47
Figure 2.6: Lateral forces in a VOA type finger set: Green, yellow and blue lines represent $F_{\text{Spring}}$ , $F_{\text{Electrostatic}}$ and $F_{\text{NET}}$ , respectively. In (a), a stable operation is simulated where the net force is below 0N for a reasonable displacement margin. However in (b), the finger is not stable because the net force is above 0N even there is no deflection.	49
Figure 2.7: The effect of DC acceleration on the proof mass of the gyroscope.	53
Figure 2.8: Illustration of the effect of centripetal acceleration on the sense axis. This acceleration term is proportional to the location radius and the input rate squared.	54
Figure 2.9: Illustration of the rotational acceleration induced tangential acceleration.	55
Figure 2.10: The force distribution on the surface of a tapered beam with finite deflection amount.	57

Figure 3.1:	The single sided folded springs (green structures) used in the single and double mass gyroscopes.....	61
Figure 3.2:	Same spring type used in the quadruple mass gyroscopes.....	62
Figure 3.3:	(a) The deformed and undeformed ring spring and (b) the angle dependent force-moment relations.....	63
Figure 3.4:	The drive mode shape snapshot of the double mass gyroscope.....	70
Figure 3.5:	The top view of the drive mode snapshot of the quadruple mass gyroscope. ....	71
Figure 3.6:	The stress simulation result of the single mass gyroscope an accelerative shock of 10000g.....	73
Figure 3.7:	Final schematic of the SMG including all the structural components like the springs, anchors, proof mass, varying overlap are and varying gap type fingers and their electrical connections.....	75
Figure 3.8:	Detailed schematic of the SMG including all the basic elements taken from the Architect Libraries.....	76
Figure 3.9:	Final schematic of the DMG, which includes a modified form of the schematic of the SMG with the ring spring coupling mechanism in the middle. This schematic also includes the biasing of the sense finger sets and the driving source.....	77
Figure 3.10:	One of the hierarchical masses of the DMG.....	78
Figure 3.11:	The folded spring subelement, which has the blue symbol in top level schematics. ....	79
Figure 3.12:	Hierarchical schematic of the sense finger sets together with the holding jig, which is a rigid mass. ....	80
Figure 3.13:	Layout of the DMG generated by the Designer tool of CoventorWare. This layout includes all the active subelements with exact dimensions and positions.....	81
Figure 3.14:	The effect of undercut which is taken into account with the help of the precise position and dimension equations in the model. The undercut in (a) is $1.25\mu\text{m}$ while the undercut in (b) is $0.25\mu\text{m}$ . ....	81

Figure 3.15: Small signal rate simulation result of the single mass gyroscope. Green signal is the drive mode vibration of 10 $\mu$ m, the purple line is the input rate and the blue signal is the sense mode vibration. ....	82
Figure 3.16: The fabrication steps of the commercial SOI-MUMPs process of MEMSCAP <sup>®</sup> Inc. including the material legend at the bottom. ....	84
Figure 4.1: Undercut amount during vapor HF etching, reported by MEMSCAP Inc.[35]. ....	87
Figure 4.2: (a) DRIE Etched epitaxial layer over the substrate, (b) oxide residues (black) between the substrate and the epitaxial layer. ....	88
Figure 4.3: SEM image of the released structure. ....	88
Figure 4.4: The test setup is represented with switches to illustrate the procedure clearly. ....	90
Figure 4.5: The drive mode resonance characteristics of the SMG, switches at U1D1. ....	90
Figure 4.6: Sense mode resonance characteristics: (a) Sense finger set, switches at U3D3 with 26V DC polarization voltage and (b) Frequency tuning finger set, switches at U2D2 with 30.5V DC polarization voltage. ....	91
Figure 4.7: Coupling from drive mode to sense mode at drive resonance, switches at U1D3 and U1U3. ....	91
Figure 4.8: Resonance test setup illustration of the DMG. ....	92
Figure 4.9: The drive mode resonance characteristics of the DMG, switches at U1D1. ....	93
Figure 4.10: Plot of Vibration Amplitude ( $\mu$ m pp) versus Driving Voltage and Resonance Frequency for the DMG drive mode. ....	93
Figure 4.11: Sense mode resonance characteristics of the first mass of the DMG: (a) Sense finger set, switches at U3D3 with 19.5V DC polarization voltage and (b) Frequency tuning finger set, switches at U2D2 with 23.5V DC polarization voltage. ....	94
Figure 4.12: Coupling from drive mode to sense mode at drive resonance, switches at U1D3 and U1U3 for both of the masses. ....	95
Figure 4.13: Matched quality factor data of the first (a) and second (b) mass of the DMG. ....	96

Figure 4.14: Resonance test setup illustration of the QMG.....	96
Figure 4.15: The drive mode resonance characteristics of the QMG, switches at U3D3. ....	97
Figure 4.16: Plot of Vibration Amplitude ( $\mu\text{m pp}$ ) versus Driving Voltage and Resonance Frequency for the QMG drive mode.....	97
Figure 4.17: The drive mode resonance characteristics of the QMG, switches at U4D3. ....	98
Figure 4.18: Mismatched quality factor data of the sense modes of the upper, lower, right and left proof masses, with their respective locations.....	99
Figure 4.19: Electromechanical coupling from drive mode to sense mode at drive resonance, switches at U3D1 and U3U1 for all of the masses. ....	100
Figure 4.20: Labels of the sense sets of the SMG (a), DMG (b), and QMG (c). ..	101
Figure 4.21: Buffer, gain and differential amplifier stages connected to the sense finger sets. ....	102
Figure 4.22: AM demodulator, low-pass filter and a +40dB gain stage, extracting the DC rate signal from the raw signal output of the differential amplifier set. ....	102
Figure 4.23: Gold plated PCB package, supporting gyro structures up to 10 mm x 10 mm in size with proper readout chip connections and substrate biasing. ....	103
Figure 4.24: Single (a), double (b) and quadruple (c) mass gyroscopes bonded to the gold-plated packages which are connected to the boards of the resistive type buffers. ....	103
Figure 4.25: Main test board including the gyroscope, buffers, AC couplers, optional gain set, differential amplifiers, and the AM Demodulator.....	104
Figure 4.26: The test setup including an oscilloscope for signal monitoring and phase data extraction, a signal generator for drive mode excitation, a power supply, a multimeter to collect the rate output data, a rate table with RS-232 communication, and, a PC to control the rate table, to store the collected rate data and drive mode frequency data while maintaining the self resonance loop. ....	105

Figure 4.27: Control schematic running on AgilentVee.....	106
Figure 4.28: Circuit board fixed to another apparatus for in-line and off-centered placement of the sense mode to the centripetal acceleration. ....	107
Figure 4.29: The output of the differentially amplified sense mode resistive buffers of the SMG in response to a sinusoidal rate input at 10 Hz with an amplitude of $2\pi$ deg/sec.....	109
Figure 4.30: The four main signals probed on the gyroscope; the driving signal (yellow), the sensed signal from drive mode (green), the differentially amplified sense output (blue) and the DC rate signal (magenta).....	110
Figure 4.31: The bias drift (a) and the Root Allan Variance curve (b) of the SMG.....	111
Figure 4.32: Rate output of the SMG under a constant angular acceleration of $1\text{deg}/\text{sec}^2$ for centered (a) and off-centered (b) positioning. The average scale factor of the gyroscope is $10.1\text{ mV}/(\text{deg}/\text{sec})$ for zero g-loading and $10.2\text{ mV}/(\text{deg}/\text{sec})$ for a loading of $4.44\text{g}$ with nonlinearities of $0.03\%$ and $0.04\%$ respectively. ....	112
Figure 4.33: Plot of scale factor versus angular rate input of the SMG under the same constant angular acceleration of $1\text{deg}/\text{sec}^2$ for centered (a) and off-centered (b) positioning. ....	114
Figure 4.34: Output bias of the SMG for different sense mode acceleration loadings.....	115
Figure 4.35: The bias drift (a) and the Root Allan Variance curve (b) of the SMG at vacuum. ....	117
Figure 4.36: Rate output and scale factor data plots of the SMG at vacuum under a constant angular acceleration of $1\text{deg}/\text{sec}^2$ while the gyroscope is centered. The scale factor of the gyroscope is $8.9\text{ mV}/(\text{deg}/\text{sec})$ for zero g-loading. ....	118
Figure 4.37: The output of the twice differentially amplified sense mode resistive buffers of the DMG in response to a sinusoidal rate input at 10 Hz with an amplitude of $2\pi$ deg/sec.....	120
Figure 4.38: The four main signals probed on the gyroscope; the driving signal (yellow), the sensed signal from drive mode (green), the differentially amplified sense output (blue) and the DC rate signal (magenta).....	121

Figure 4.39: The bias drift and the Root Allan Variance curve of the DMG, which correspond to a bias instability of 200deg/hr and an angle random walk of 5.47deg/√hr. ....	122
Figure 4.40: Rate output of the DMG under a constant angular acceleration of 1deg/sec <sup>2</sup> for centered (a) and off-centered (b) positioning. The average scale factor of the gyroscope is measured to be 6.4 mV/(deg/sec) for zero g-loading and 7.5 mV/(deg/sec) for a loading of 4.44g with nonlinearities of 0.05 % and 0.31, respectively. ....	124
Figure 4.41: Plot of scale factor versus angular rate input of the DMG under the same constant angular acceleration of 1deg/sec <sup>2</sup> for centered (a) and off-centered (b) positioning. ....	125
Figure 4.42: The output voltage of the DMG at rest with linear accelerations of 0g, -1g and 1g in the sense mode. ....	126
Figure 4.43: The bias drift (a) and the Root Allan Variance curve (b) of the DMG, corresponding to a bias drift and an angle random walk of 1028deg/hr and 6.7 deg/√hr, respectively. ....	128
Figure 4.44: Rate output and scale factor data plots of the DMG at vacuum under a constant angular acceleration of 1deg/sec <sup>2</sup> while the gyroscope is centered. The scale factor of the gyroscope is 11.8 mV/(deg/sec) for zero g-loading together with 0.03% nonlinearity. ....	129
Figure 4.45: The output of sense modes resistive buffers, which are differentially amplified in three stages, of the QMG in response to a sinusoidal rate input at 10 Hz with an amplitude of 2π deg/sec. ....	131
Figure 4.46: The four main signals probed on the gyroscope; the driving signal (yellow), the sensed signal from drive mode (green), the differentially amplified sense output (blue) and the DC rate signal (magenta). ....	132
Figure 4.47: The bias drift and the Root Allan Variance curve of the DMG, which correspond to a bias instability of 1.8deg/sec (6485 deg/hr) and an angle random walk of 43.2 deg/√hr. ....	133
Figure 4.48: Rate output of the QMG under a constant angular acceleration of 1deg/sec <sup>2</sup> for both centered (a) and off-centered (b) positioning. ....	134

Figure 4.49: Plot of scale factor versus angular rate input of the QMG under the same constant angular acceleration of $1\text{deg}/\text{sec}^2$ for centered (a) and off-centered (b) positioning. ....	136
Figure 4.50: The output of the DMG at rest with linear accelerations of $1g$ magnitude applied along the four sides of the gyroscope, corresponding to the angles of $0^\circ$ , $90^\circ$ , $180^\circ$ , and $270^\circ$ .....	137
Figure 4.51: The bias drift and the Root Allan Variance curve of the QMG at vacuum, corresponding to a bias drift and an angle random walk of $780\text{deg}/\text{hr}$ and $10.0\text{deg}/\sqrt{\text{hr}}$ , respectively.....	138
Figure 4.52: Rate output and scale factor data plots of the QMG at vacuum under a constant angular acceleration of $1\text{deg}/\text{sec}^2$ while the gyroscope is centered. The scale factor of the gyroscope is $9.2\text{mV}/(\text{deg}/\text{sec})$ for zero g-loading with $0.02\%$ nonlinearity. ....	139

# **CHAPTER 1**

## **INTRODUCTION**

In today's technology, miniaturization is one of the key factors boosting the motivation of research and development throughout the world. Increasing importance of energy resources on the planet, rising demand in mobile devices and developing space technology enforce development of less power consuming, less specific, more applicable, more reliable, more efficient, lighter, and resultantly smaller forms of currently used devices.

Especially, the invention of the transistors has opened the door of a new epoch of miniaturization. Subsequently, today, developing IC (integrated circuit) fabrication techniques become able to fit one transistor in the size that of a few thousands of atoms. The gathered know-how on the fabrication techniques eventually formed a springboard for inventions of micro scale machines.

Today, various micro electromechanical systems (MEMS) have been realized in many fields with a great diversity. Among these, inertial sensors obtained their reputation with their high performance, high reliability, and very small size. In particular, their small dimensions and low power consumption widened the application areas of inertial sensors. Presently, they have been used in navigation of air and marine vehicles and in various stabilization systems. Additionally, today's advancements in fabrication techniques and novel designs enabled much more reliable and sensitive inertial MEMS sensors which find application areas like

tracking control and rollover detection systems in cars, and even in high-g military munitions and in crash tests.

There have been various types of inertial MEMS sensors designed, realized, and mass produced since 1970's [4]. These inertial sensors are divided into two main branches as micro gyroscopes (angular velocity sensors) and micro accelerometers (linear acceleration sensors) owing to their different sensing domains and different working principles. The operational performance of micro accelerometers, due to their simpler mechanical and electronic structures, have reached to an adequate level that these sensors are widely used in afore-mentioned inertial sensor applications. On the other hand, there are exceptional micromachined gyroscopes with reported performance levels approaching 10 degree per hour (deg/hr), aiming tactical grade applications [18]. However, the performance levels of micro gyroscopes are not at the required levels for long-term and strategic navigation applications. Thus, conventional mechanical, laser and fiber optic gyroscopes are still in service in particular areas. Among the reasons of their relatively low performance compared to the conventional gyroscopes, the leading ones are complex mechanical operation principles together with complex electronics, lower "structural dimension" to "fabrication tolerance" ratios, and few fine tuning possibilities. Yet, their promising applicability to a much wider span, which is a consequence of their small size, creates a dense motivation in development of MEMS gyroscopes.

MEMS gyroscopes are classified into four grades depending on their performance characteristics. Rate-grade gyroscopes are the lowest performance gyroscopes and almost all of the MEMS gyroscopes meet this performance level. Tactical-grade is the second performance level which requires a scale factor accuracy better than 0.1% with a bias drift of 150 deg/hr or less [27]. There are some high performance micro-machined gyroscopes that meet these performance levels. The third and fourth performance levels are navigational-grade and strategic-grade, respectively, and their performance criteria are not met by today's microgyroscopes, but with conventional mechanical, fiber optic, and laser gyroscopes. For the MEMS gyroscopes to catch up with the performance levels of these very high performance gyroscopes above, their mechanical and electronic components should be carefully designed and their

fabrication must be absolutely well optimized. Especially the mechanical structure should be analyzed in detail and new perspectives should be created for error minimization while increasing the sensitivity. This thesis reports a detailed investigation of electromechanical error sources in MEMS gyroscopes and proposes completely realized novel single and multi-mass gyroscope topologies which minimize the deviations in scale factor and output bias under static accelerations, together with low mechanical noise and stable drive mode vibration frequencies.

The organization of this chapter is as follows; Section 1.1 includes a brief introduction to gyroscopes with their basic operation principles. Section 1.2 gives an overview of micro-machined gyroscopes with the examples in the literature. Section 1.3 summarizes possible mechanical and structural error sources affecting the micro machined gyroscopes and introduces the single mass, the double mass tuning fork, and the coupled twin tuning fork type micro-machined gyroscope structures developed in this research. Finally, Section 1.5 presents the research objectives and the organization of the thesis.

## ***1.1 Gyroscopes***

Gyroscope is defined as an angular velocity sensor, working on the basic principle of conservation of momentum. Momentum is, conceptually, the tendency of a body to continue moving in its direction of motion, which is a natural consequence of Newton's First Law. If the body is in zero-force and zero-moment state, the sum of momentums of all atoms on this body is constant and when a force or a couple (moment) is applied on the body, the direction and/or the magnitude of the linear and/or angular momentum of this body changes. Angular momentum is, basically, the moment of the momentum. Angular momentum of a body is, then, the sum of the moments of the instantaneous momentums of each atom with respect to a point in the body [1].

Analysis of motion with respect to a noninertial reference frame is another aspect of gyroscopes. In noninertial frames, conservation of energy and conservation of momentum still applies, with extra terms of fictitious forces. Figure 1.1 shows the

linear motion of a bowling ball over a frictionless disc rotating with an angular velocity of “ $\omega$ ”. With respect to the stationary observer, the ball is just sliding over the disc with a constant linear velocity, without being disturbed by the rotation of the disc. But the observer fixed to the disc perceives a different motion, as if an unknown force is accelerating the ball in the opposite direction of rotation while it is approaching the edge of the disc. The dashed curve on the disk is the trajectory that the moving observer perceives, while the ball is moving in a linear path with respect to the stationary one. This phenomena is called the *Coriolis Effect* and the acceleration that the rotating observer presumes is the *Coriolis Acceleration*.

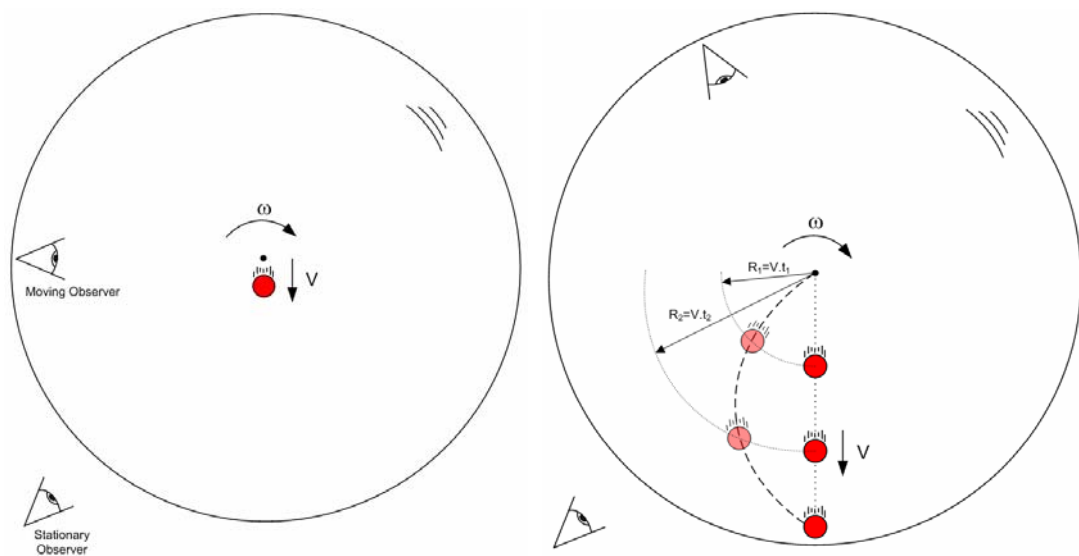


Figure 1.1: Coriolis effect; the bowling ball which slides over a rotating frictionless disk surface.

The reason of this illusion is the rotating looking direction of the moving observer. Thus, the linear motion is perceived as if the ball is accelerating with a rotary motion while there is no force or moment (on the frictionless disk surface) which would deflect the direction of the ball. The angular momentum of the ball remains constant with respect to the stationary observer.

On the other hand, if the ball is subject to some kind of motional restriction on the moving frame, the Coriolis acceleration becomes observable by the stationary observer, too. For this, the same bowling ball example can be modified. To illustrate,

the ball is assumed to be moving in a slot on that same disk. The slot is passing right through the center of the disk and has a friction characteristics that the ball can move with a constant velocity with respect to the slot when the disk rotates with an angular velocity of  $\omega$ . Figure 1.2 shows the rotating disk with the nonlinear friction characteristics which allows the ball move with a constant velocity with respect to the slot.

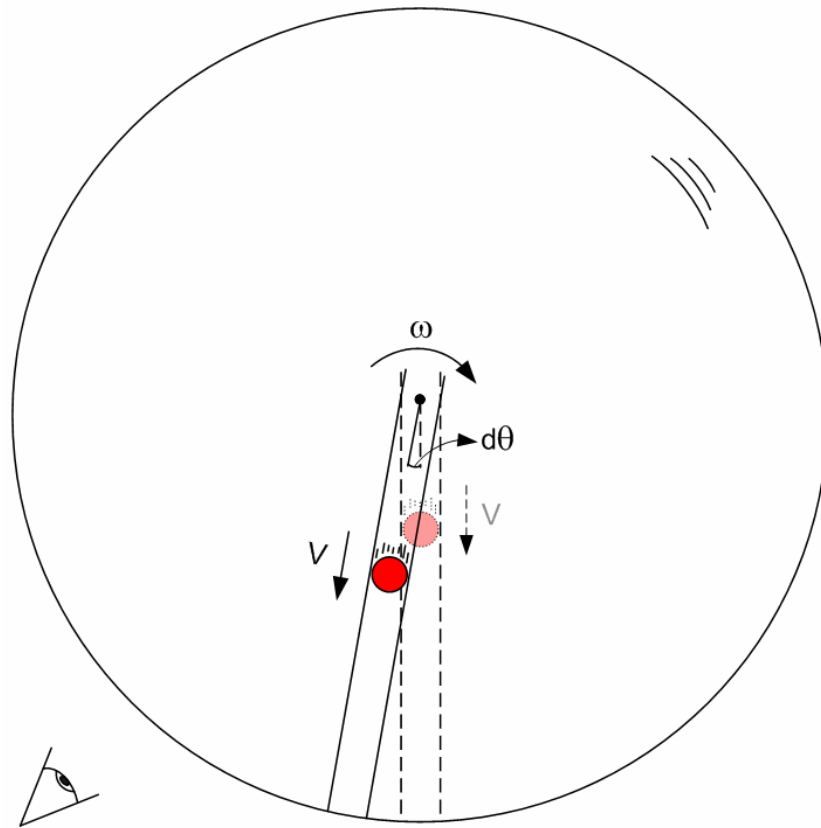


Figure 1.2: Rotating disk with the nonlinear friction characteristics which allows the ball move with a constant velocity with respect to the slot.

The constant velocity of the ball gives us a simpler case to investigate the situation. While the disk is rotating, the direction of the slot and the ball-to-origin distance changes. The change in slot direction directly changes the linear velocity direction of the ball in the slot, while the magnitude of this velocity is constant. The change in ball-to-origin distance causes the ball rotate with a higher tangential velocity. Thus, there are two velocity components that are changing along the same acceleration direction. Figure 1.3 shows the velocity differentials of the ball together with their

directions. The green vectors are the change of the direction of the radial velocity in the slot and the magnitude change of the tangential velocity of the ball [1]. Taking the differential by dividing the terms by “dt”,

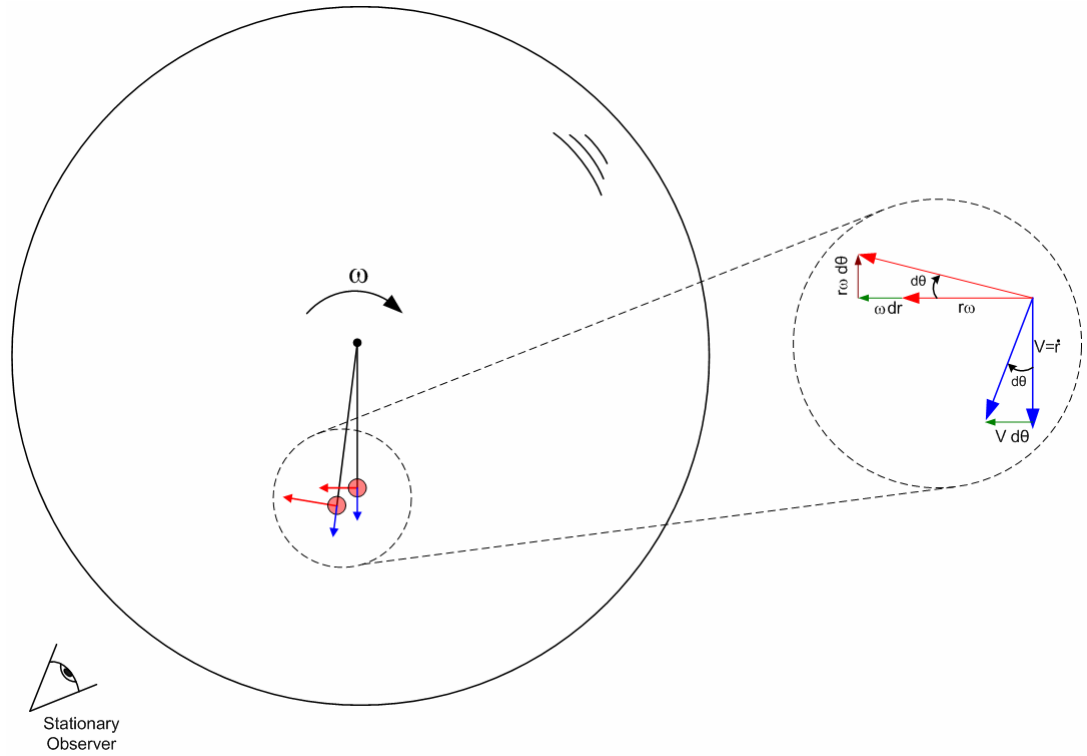


Figure 1.3: Velocity differentials of the ball together with their directions.

$$a_{Coriolis} = \omega \frac{dr}{dt} + V \frac{d\theta}{dt} \quad (1.1)$$

These two accelerations are summed and called Coriolis acceleration. This summing is because of the resultant single force, acting on the ball by the slot wall.

Since,

$$\frac{dr}{dt} = V \quad (1.2.a)$$

$$\frac{d\theta}{dt} = \omega \quad (1.2.b)$$

The Coriolis acceleration is then,

$$a_{Coriolis} = 2.\omega.V \quad (1.3)$$

The brown vector on Figure 1.3 is the centripetal acceleration, which is the result of the direction change of the tangential velocity.

$$a_{Coentripetal} = r.\omega.\frac{d\theta}{dt} = r.\omega^2 \quad (1.4)$$

These equations are valid for only if the ball is moving along the radial direction. For a general motion, Coriolis acceleration is defined as,

$$\vec{a}_{Coriolis} = 2.\vec{\omega} \times \vec{V} \quad (1.5)$$

Here, a determined acceleration term is stated, which should be a result of finite real force which is;

$$\vec{F} = m.\vec{a}_{Coriolis} \quad (1.6)$$

Since the acceleration is already determined;

$$\vec{F} - m.\vec{a}_{Coriolis} = 0 \quad (1.7)$$

Where  $-m.\vec{a}_{Coriolis}$  is an inertial term which has a magnitude of force and a direction opposite to the Coriolis acceleration. According to the D'Alembert's Principle [1], this term can be taken as a fictitious inertia force acting on the mass. For the case of Coriolis acceleration, the fictitious Coriolis force is;

$$\vec{F}_{Coriolis} = -2.m.(\vec{\omega} \times \vec{V}) \quad (1.8)$$

Equation 1.8 reveals another key of Coriolis force; in a rotating disk,  $\vec{\omega}$  is always perpendicular to the rotation plane which is the disk surface, and  $\vec{V}$  is always in the

rotation plane. Thus, the cross product of these terms leads to a vector of Coriolis force, which is always perpendicular to  $\vec{V}$  and on the rotation plane, meaning the location and direction of the ball is not important.

For a gyroscope on the rotating frame, same equations are valid. Especially Equation 1.6 is the basis of all spinning and vibrating gyroscope theories. What makes a spinning or a vibrating mass an angular velocity sensor is the induced Coriolis forces on each and every particle on their proof mass.

Spinning mass gyroscopes are the oldest type rate sensors. Their dynamics is quite complicated owing to the three dimensional vector algebra utilized on a noninertial frame [2]. Figure 1.4 shows a single D.O.F. (degree of freedom) gyroscope, which is called the *rate gyroscope*.

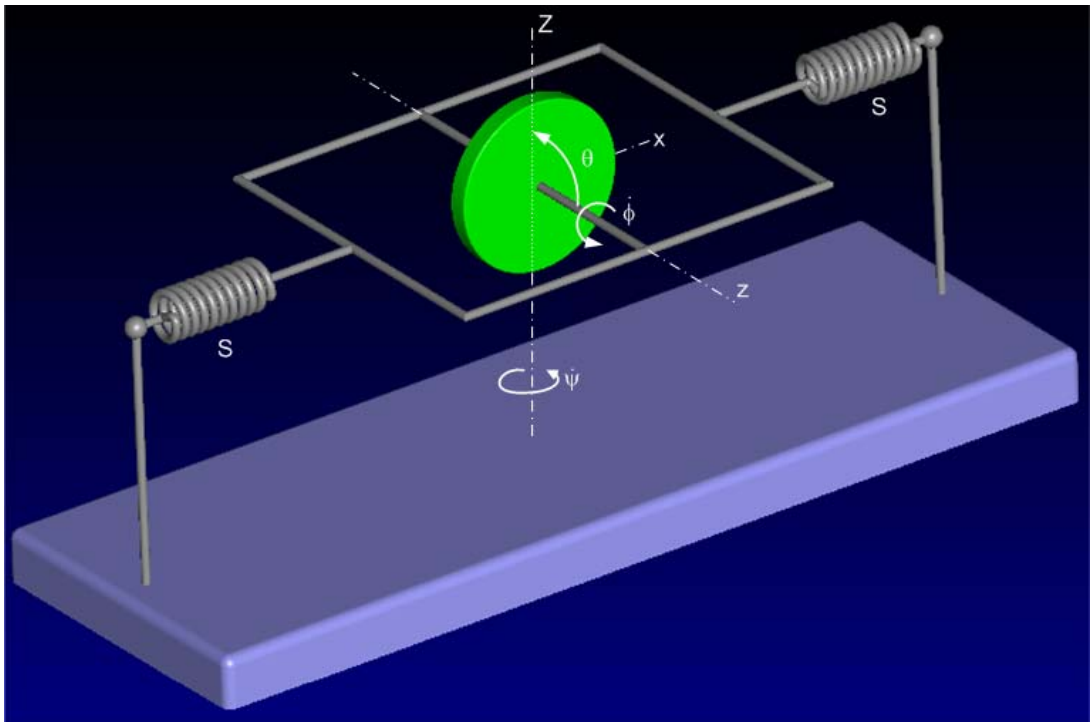


Figure 1.4: A single degree-of-freedom gyroscope, which is the *rate gyroscope*.

Derivation of all dynamics equations of this gyroscope is beyond the scope of this thesis, but the governing equation for a single DOF gyro is worth to mention. The rate gyroscope is composed of a rotating disk spinning on a frictionless bearing and

connected to a rigid frame. This frame is supported by torsional springs and dampers (not shown). For a spin velocity of  $\dot{\phi}$  with a frame angular rate of  $\dot{\psi}$ , the required torque on the springs can be calculated by;

$$M_x = I(\dot{\psi} \times \dot{\phi}) \quad (1.9)$$

This moment is supplied by the torsional springs present. The rotational rate of the rigid frame decides the amount of the torque applied by the springs, which eventually gives the rate data.

Besides the single DOF rate gyroscopes, in short-term applications, passive 2-DOF gyroscopes are used as well. Figure 1.5 shows the structure of a 2-DOF gyroscope with Cardan suspension, which is called the *torque-free gyroscope*.

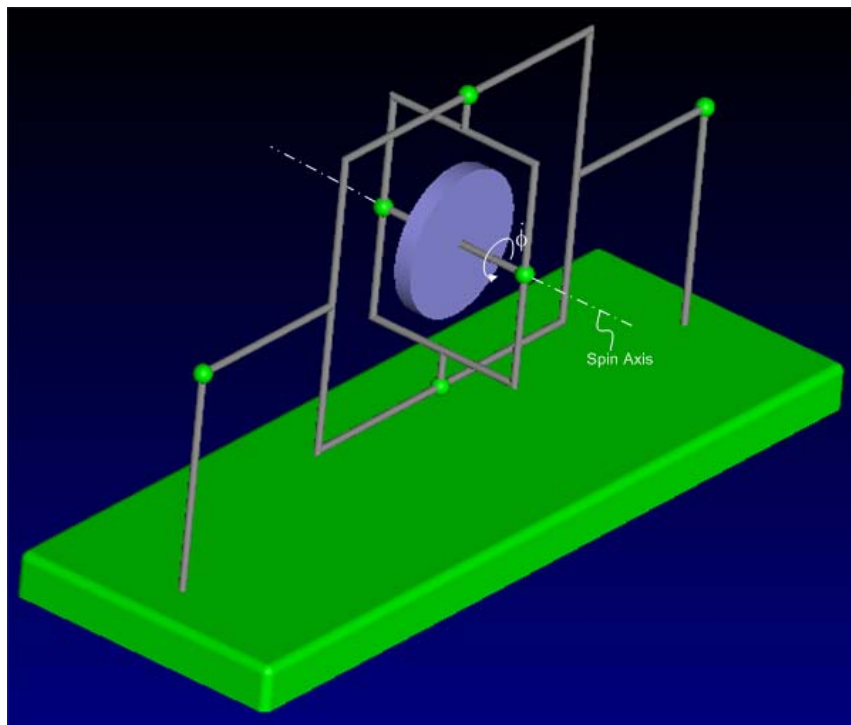


Figure 1.5: Structure of a two DOF gyroscope with Cardan suspension, which is called the *torque-free gyroscope*.

The reason for this alias is that the spinning mass, suspended by a frame-in-frame structure, does not change its spin direction even rapid and complicated rotations are

applied to the frame. This is because the frame cannot apply a torque to the rotor in any direction provided that there is no friction. In practice, the amount of friction decides the reliable operation period for that gyroscope. With adequate bearings, these type of gyroscopes are used in missile technologies owing to their relatively low cost, easier implementation, and torque-free operation. Using a torque-free gyro, the missile is not affected by the reactive torques generated by the force feedback system of advanced spinning mass gyroscopes. Figure 1.6 shows a conventional advanced 2-DOF gyroscope, which has 2 sensitive axes. The stator coils of the AC actuator on the outermost cage is the main feedback actuator, which stabilizes the spin direction with respect to the gyro casing. The potentiometer on the opposing side of the cage obtains the angle of precession data of the spinning mass, which is fed into a controller. This type of spinning gyroscopes with feedback mechanism need to be implemented on relatively massive systems, like turret or tower stabilization, in order to be able to neglect the effects of active feedback mechanism on the rest of the vehicle body.

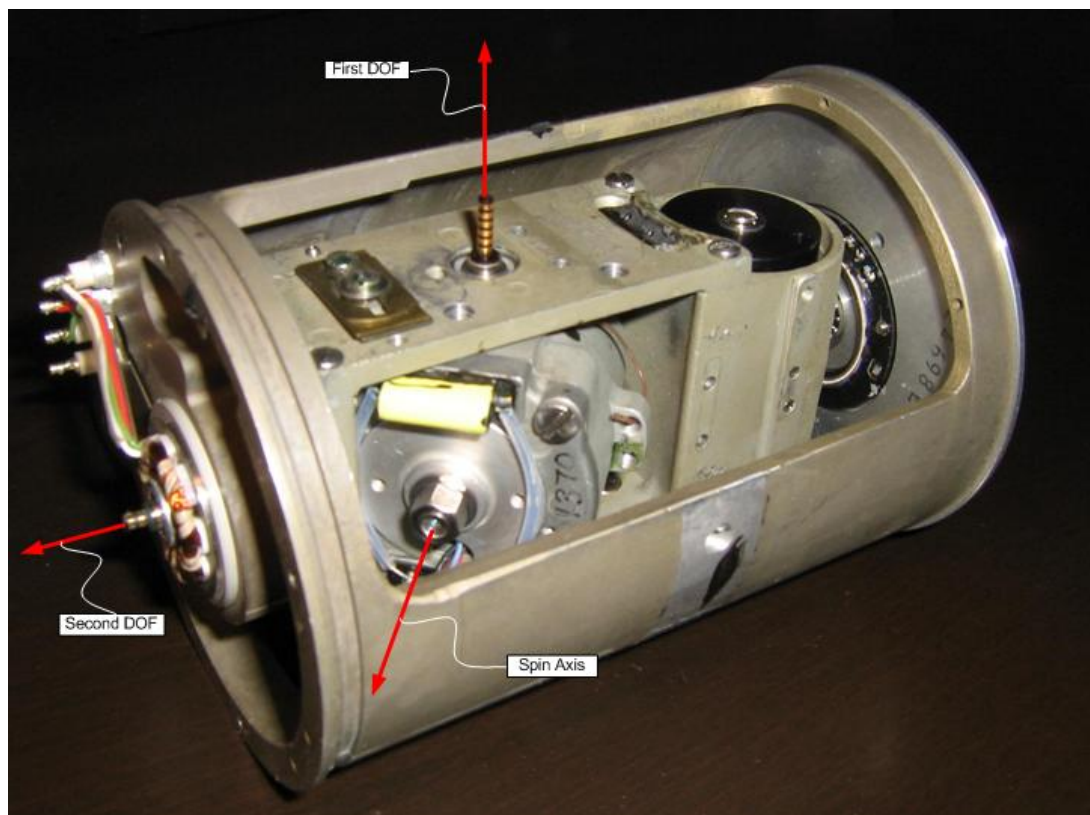


Figure 1.6: A conventional 2 DOF gyroscope.

Apart from the idea of a spinning mass, a vibrating mass is also subjected to the Coriolis force if suspended accordingly. In fact, if there is a vibration together with a rotation, a precession is inevitable. This idea can be utilized for different gyroscope structures on a new operational basis, which is called the vibratory gyroscope.

Vibratory gyroscopes operate in a simpler basis relative to the spinning mass gyroscopes. As mentioned before, if a mass has a finite linear velocity with respect to a rotating frame and if the rotation of the frame is disturbing this line of motion, Coriolis force is the resulting interaction between the frame and the mass. This situation is valid for a vibrating mass, too. Additionally, for vibrating masses, the induced Coriolis force is also a fluctuating force and causes a secondary vibration. Figure 1.7 shows the precession of the gyro proof mass which is suspended with a vibrating frame fixed to the rotating disc.

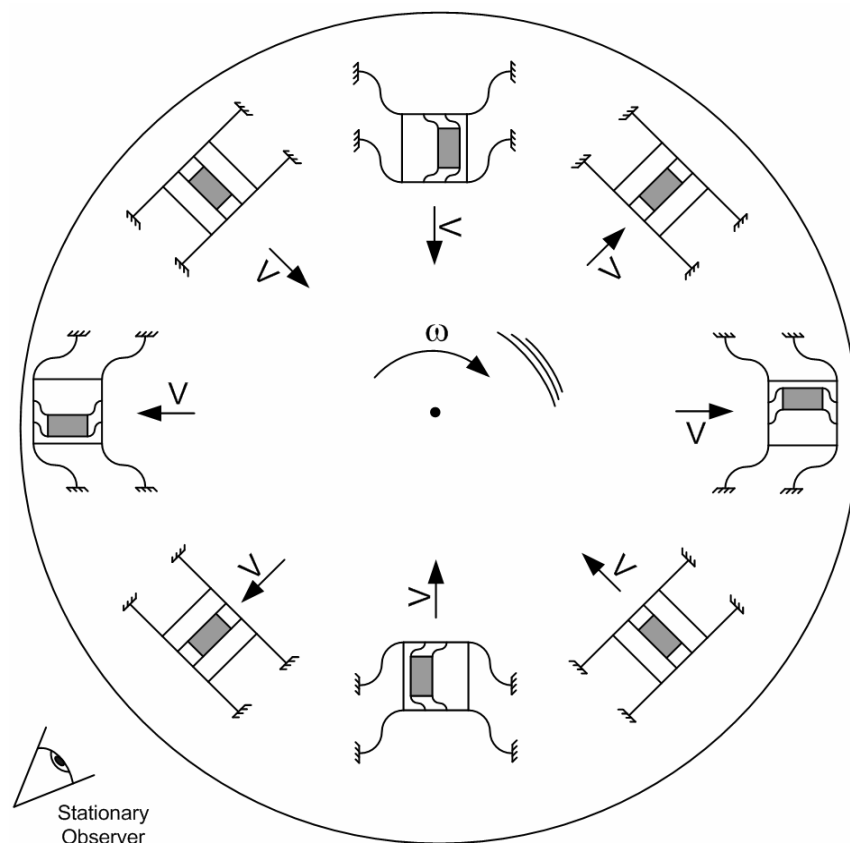


Figure 1.7: The precession of the gyro proof mass which is suspended with a vibrating frame fixed to the rotating disc.

Depending on the instantaneous velocity vector of the mass, the direction and the magnitude of the precession change in the direction opposite to the Coriolis acceleration as a consequence of the D'Alembert's principle. Additionally, the induced Coriolis force is always perpendicular to the driving vibration axis with a magnitude of,

$$a_{Coriolis} = -2.\omega.V.Sin(\omega_v.t) \quad (1.10)$$

Where  $\omega$  is the rotational velocity, V is the maximum vibration velocity, and  $\omega_v$  is the drive mode vibration frequency.

Sensing the input rate is usually realized by sensing the amount of secondary vibration amplitude, which is driven by the induced Coriolis force above. However, the ratio of the secondary (sense mode) vibrations to the primary (drive mode) vibrations due to Coriolis force is very small, and thus, a reliable decoupling should be utilized between these modes.

In MEMS gyroscopes, decoupling of the sense and the drive modes can be realized by only in-plane flexion elements and supporting frames, designs of which are the key factors for a high performance vibrating micro-machined gyroscope. Additionally, with this type of gyroscopes, there is no need for a rotating mass or for a three-dimensional structure, which enable the implementation of such gyroscopes using various micro-machining techniques. Their very low mass-in-motion (proof mass) enables force-feedback control without a significant moment fluctuation on the gyroscope itself. In this thesis, the design and operational details of these micro-machined vibrating gyroscopes are presented.

## ***1.2 Micromachined Gyroscopes***

Developments in both fabrication methods and operational approaches have caused an effective mutual positive feedback, resulting in a diverse research background on micro gyroscopes with a great diversity. Additionally, the developing accelerometer research has also formed a firm know-how on the mechanical, electronic and control systems of the micromachined gyroscopes which are actually Coriolis accelerometers [4]. In conventional mechanical gyroscopes, the Coriolis acceleration of each atom is inherently integrated on a spinning mass. This lumped force is sensed using a simple feedback system or just by measuring the angular displacement of the mass. However, since the operational lifetime of rotating MEMS structures is very short due to wearing problems, another periodic motion; the vibration is utilized for small sized mechanisms. First micro gyroscopes were inspired from the conventional spinning gyroscopes, with a small modification of rotationally vibrating mass instead of a gimbaled spinning mass [5]. Due to very coarse fabrication techniques available for three dimensional topologies, performance levels of these mechanically complex structures were not very promising. Afterwards, it was realized that planar and radially symmetric structures were much more reliable and easier to operate for torsional vibrations. Various planar microgyroscopes have been reported which are vibrating rotationally. Bosch [6] and HSG-IMIT [7] have reported gyroscopes utilizing torsional vibrations. The gyroscope reported by Bosch was intended for automotive applications with a resolution of 0.4 deg/sec. The performance of the gyroscope reported by HSG-HMIT was far better (18 deg/hr) for military applications. NASA JPL [8] and Berkeley Sensor and Actuator Center (BSAC) [9] also reported different gyroscope structures with torsional vibration.

Parallel to the torque-based rotationally resonating microgyroscopes, force-based linearly vibrating micro gyroscopes are also researched. The promising potential of linear proof mass actuation has created a dense motivation on the research of various linear mechanisms. Among these, vibrating beam gyroscopes are the first reported ones with linear actuation [10-[11]. Another very different and novel microgyroscope possessing a linear mass motion is the ring gyroscope [12-[13].

Figure 1.8 shows a high aspect ratio ring gyroscope with its operational structure [14]. The in-plane vibration modes of the ring structure have been utilized for an inherently coupled drive mechanism. But the narrow limits on the drive vibration amplitude and low sense output because of the small sensing areas detained further improvements on this structure.

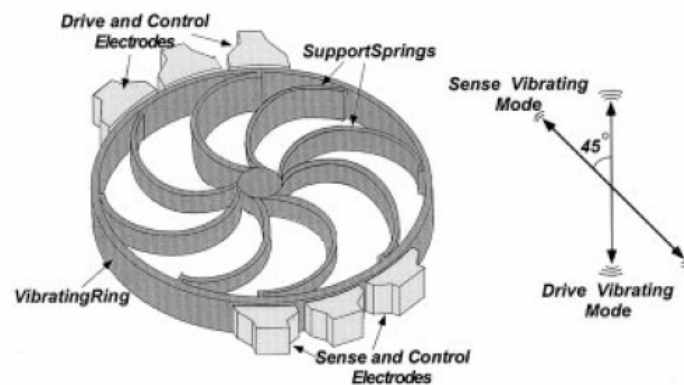


Figure 1.8: A high aspect ratio ring gyroscope with its operational structure [14].

There is an important point about vibrating beam and the ring gyroscopes: they both have a united mass and spring structure, i.e., the springs of the mechanism also forms the proof mass. This fusion adds an advantage of smaller size and easier operation but decreases the performance of the overall sensor because of the high mechanical and electrical noise parameters compared to the low output signals. Solution to this drawback is separating the proof-mass, sense, drive, and the flexion elements as discrete structures. This approach enables more independent and more parametric improvements of the overall system. Various structures are reported with different levels of separation [4]. On the other hand, microgyroscopes are affected not only by the self induced Coriolis force, but also by the other parameters like linear accelerations and process variations, which could be eliminated using mechanisms including more than one proof mass. Tuning fork structures are this kind of original mechanisms which are rejecting the common mode errors like accelerations and process variations if appropriate resonance mode is utilized for rate sensing . In fact, a tuning fork structure is basically composed of a pair of resonating beams in opposite phases. These beams will be affected by the applied accelerations and by some other types of interferences at the same level. Since the tines are exactly same

but only vibrating oppositely, the difference of their output signals would be inherently filtering out the afore-mentioned complications. Figure 1.9 shows the schematic diagram of the GyroChip of BEI Systron Donner Inertial Division, showing the drive and sense modes of the twin tuning forks [15].

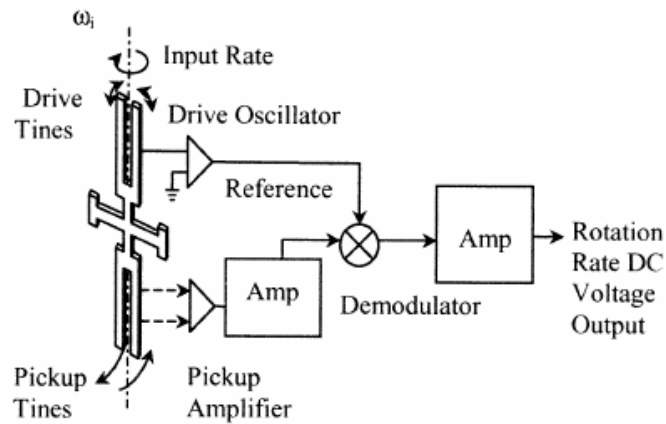


Figure 1.9: Schematic diagram of the BEI GyroChip by Systron Donner Inertial Division, showing the drive and sense modes of the twin tuning forks [15].

Different gyroscope structures have been reported which are also classified as tuning fork owing to their working principles even their structures are far different from a tuning fork. The common approach in these gyroscopes is using an appropriate mechanical coupling for the drive modes of two identical gyroscopes. Draper Labs. [16] and Bosch GmbH [17] reported double mass tuning fork gyroscopes with a resolution better than 0.2deg/sec. Figure 1.10 shows the mechanical model of the tuning fork gyro reported by Bosch GMBH [17].

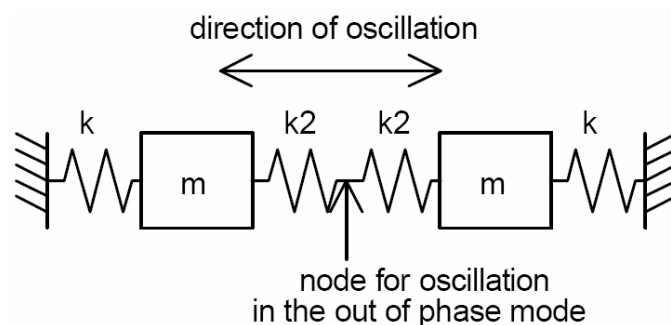


Figure 1.10: Mechanical model of the tuning fork gyro reported by Bosch GMBH [17].

Decreasing the linear acceleration sensitivity (g-sensitivity) is an important advantage of tuning fork gyroscopes, as mentioned before. However, the g-sensitivity of other gyroscope types, especially the laser, fiber optic and conventional mechanical gyroscopes are very low owing to their working principles, and usually their g-sensitivity is not counted as a performance criterion. On the other hand, MEMS based suspended mass vibratory gyroscopes are very sensitive to the constant accelerations due their “Coriolis Accelerometer” type sensing scheme, being very crucial for some applications. Considering this deficit, BAE Systems [18] and Honeywell [19] have reported two different tuning fork gyroscopes with a g-sensitivity lower than 10deg/hr/g. These gyroscopes are intended for military applications and they are survivable in gun-shock applications with a shock acceleration of about 10000g.

Analog Devices also reported a monolithic twin-mass gyroscope with a g-sensitivity of 0.2 deg/sec/g and a resolution of 50 deg/hr [20]. The differential readout schemes and appropriate tuning fork characteristic of the above designs compensate the g-sensitivity deficit of the MEMS gyroscopes, without a resolution or linearity loss. Figure 1.11 shows the Analog Devices’ monolithic gyroscope including the gyro structure and necessary electronics integrated on a single chip.

In microgyroscopes, apart from the working principle, the means of actuation is also very crucial in the design of the sensor. This is because the driving force is always an essential but problematic factor owing to its effects on other parts of the sensor system. Various actuation approaches have been reported that are employing magnetic, electrostatic and piezoelectric forces. Among these, electrostatic actuation is proven to be the most appropriate method for micro scale resonators owing to its simplicity, robustness, reliability and linearity. Electrostatic actuation mechanisms also can serve as sensing or tuning structures with minor modifications, which enables practical error reduction and undesired coupling avoidance. Varying overlap area and varying gap type electrostatic comb structures are the most frequent actuating and sensing structures employed in gyroscope designs [21]. The linear force-deflection characteristics of varying overlap area fingers allow a wide span of vibration amplitude in drive mode of the gyroscopes. Varying gap type fingers are

usually used for capacitive sensing and sense mode frequency tuning owing to their quadratic force-displacement characteristics. Optical [24] and piezoresistive [25] sensing approaches are also reported but the highest performance and reliability is obtained by electrostatic (capacitive) type sensing elements.

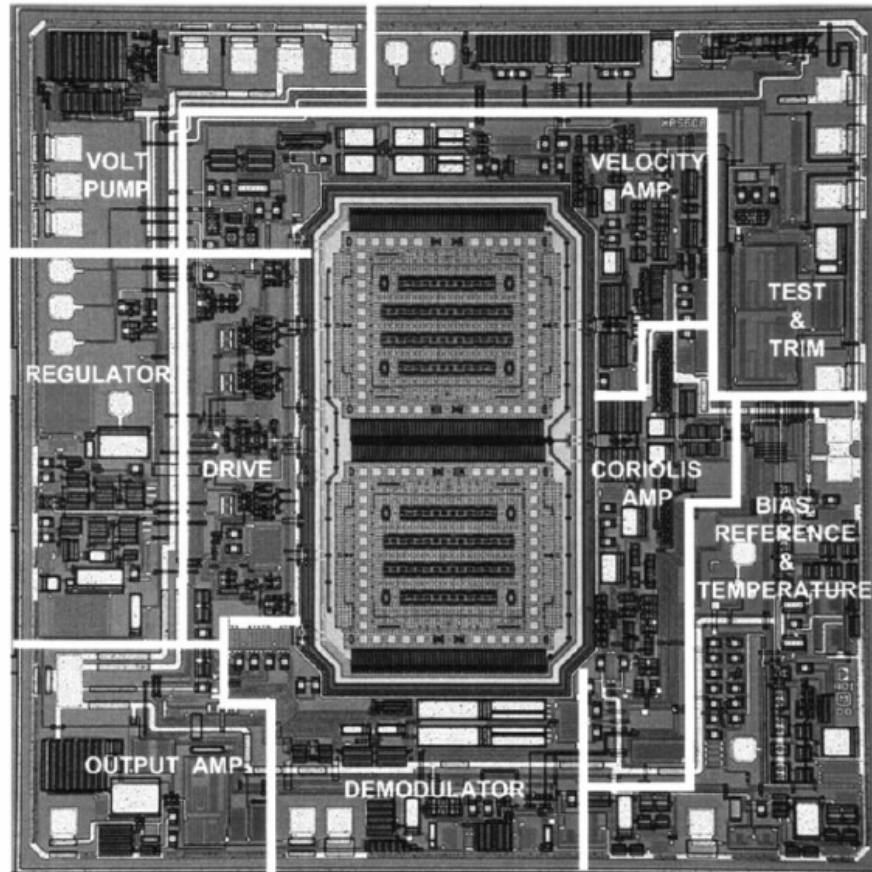


Figure 1.11: Analog Devices' monolithic gyroscope including the gyro structure and necessary electronics integrated on a single chip [20].

The regular operation of the proof mass, the flexion elements and the actuation mechanisms mentioned up to now depends on one vital step, the fabrication sequence, which is the most crucial topic in MEMS devices. The vitality of the fabrication process is due to the dependency of the overall design on the restrictions of the fabrication technique used. To illustrate, the amount of the proof mass and the capacitance of electrostatic sets depend on the allowable structural thickness, the resonance characteristics of the drive mode depends on the material used for the flexion elements and the electrical coupling between the sense and the drive mode

depends on the resistance of the structure together with the supporting substrate. Even the mechanism itself requires a modification to fit in the process limitations. Since the fabrication is the determining step in the production, the gyroscope structure and the fabrication process should be fully compatible.

There have been reported single-crystal silicon [22], electroplated nickel [13], single-crystal quartz [15], silicon-on-insulator (SOI) [7] and surface micromachined gyroscopes [6] which are fabricated using very different micromachining techniques like Deep Reactive Ion Etching (DRIE), photoresist mold electroplating, wet etching and Reactive Ion Etching (RIE).

Besides, among the structural materials, its adjustable resistance, high reliability in long term fluctuating loadings (very low fatigue failure characteristics), already developed process know-how and the even orientation dependency of its elastic constant makes silicon the most convenient structural material for MEMS gyroscopes.

Additionally, the supporting material, which is called the substrate, should also be compatible with the structural material of the gyroscope. SOI technology inherently includes a structural layer and a substrate both composed of single crystal silicon with a thin insulating layer in between. The advantage of the SOI structures is low thermally induced internal stresses owing to the close thermal expansion coefficients.

Glass is another promising substrate material with its strong bonding ability to silicon and its thermal expansion coefficient close to that of silicon. Figure 1.12 shows the fabrication process sequence of a vacuum packaged low noise micromachined silicon gyroscope with glass substrate, developed by Seoul National University [23].

To conclude, the increasing demand in flashing developments of consumer electronics and military applications boost the research motivation on mobile navigation and micro scale inertial sensors. Moreover, by taking the advantage of the developing fabrication techniques and interface circuitry together with the novel

mechanisms suggested, performance grades of microgyroscopes are improving while they are getting much cheaper and smaller.

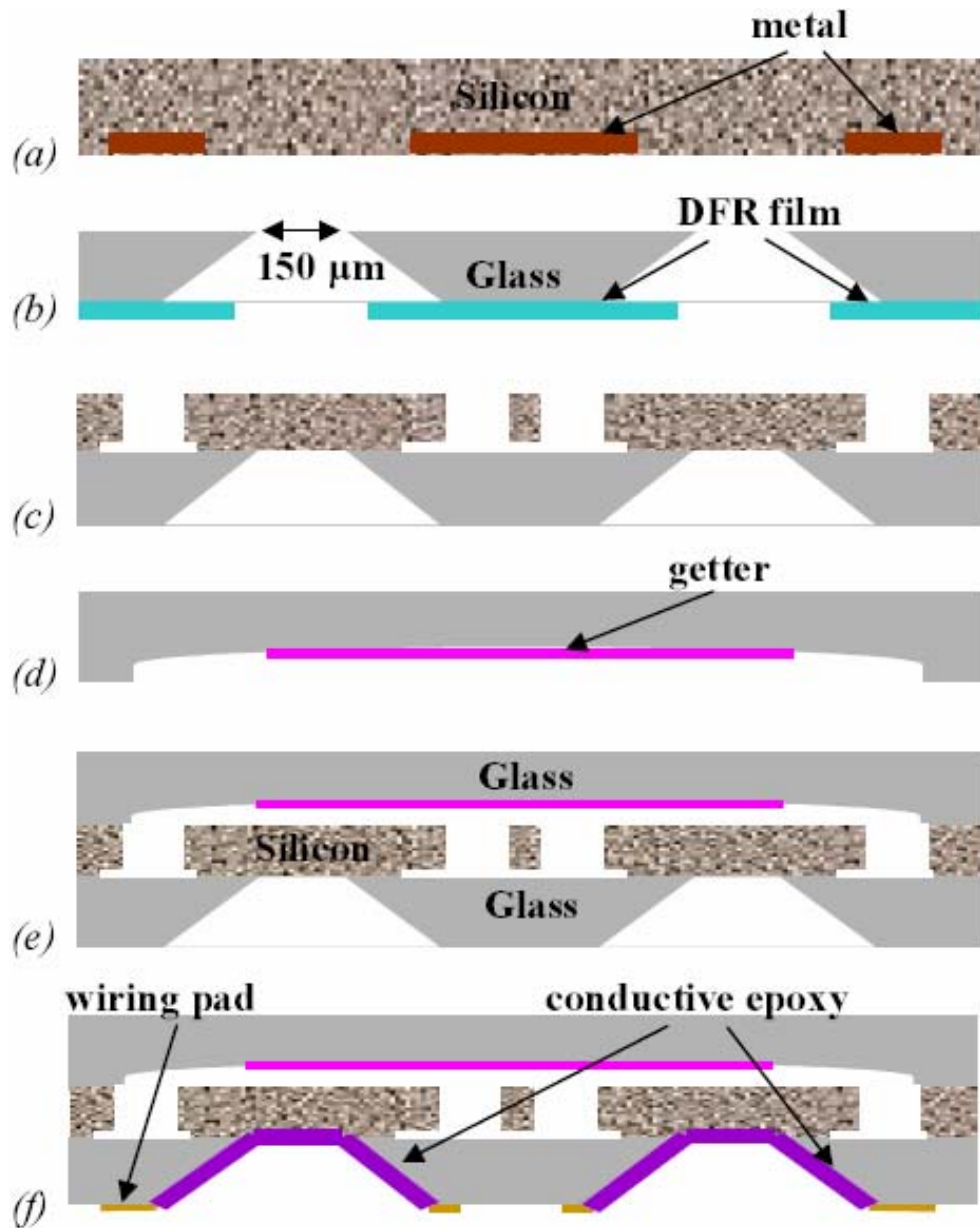


Figure 1.12: Fabrication process sequence of a vacuum packaged low noise micromachined silicon gyroscope with glass substrate, developed by Seoul National University [23].

Yet, the vitality of the perfect fusion in the design, production and control of a microgyroscope reveals the need for improved electromechanical designs and higher precision microfabrication techniques together with improved interface and control electronics in order to increase the sensitivity and reliability of these miniature rate sensors.

### ***1.3 Multi-Mass Gyroscope Structures Developed at METU***

At METU, various gyroscope structures have been realized using different fabrication techniques [26-[33]. These were symmetric and decoupled type single mass vibratory gyroscopes. With the improvements in the flexion elements and supporting topology of these gyroscopes, resolutions better than 30deg/hr have been reached [32]. The balanced and firm mechanical structure together with the precise micromachining techniques with DRIE and sensitive interface electronics have major credit in this performance improvement.

Although resolutions of some of these designs were better than 30deg/hr, the acceleration sensitivity of these topologies was not promising owing to their single-mass structures. The main reason of the g-sensitivity of single mass gyroscopes is the varying gap type capacitive fingers used. These finger sets have a capacitance change under deflections ( $\partial C/\partial x$ ) which is not linear but quadratic. Thus, under a g-loading, the gap of these sets either increase or decrease depending on the loading direction, which results in bias drift and scale factor shift. Despite of the fact that the differential readout schemes suppress the g-dependency of the scale factor under small accelerations, this readout technique worsen the output bias voltage of the sensor if a tuning fork structure is not present.

Moreover, the g-survivability of reported gyroscopes is also very low because of the very sensitive interfaces with  $\pm 2.5V$  DC supplies. Under high g-loadings, suspended sense fingers become unstable and tend to touch to the stationary sets which are directly connected to the sensitive interfaces. This phenomenon is called pull-in. Because of the relatively high polarization voltage applied to the vibrating sense sets, the sensitive interface electronics get damaged. Depending on the biasing technique used, a high current may also pass through the interface, resulting in localized melting or welding of the silicon structure. These problems in previous gyroscope readout schemes lead utilization of resistively biased sense finger sets.

The work in this thesis reports the design, fabrication, characterization and performance tests of three novel gyroscope structures with single, double and quadruple masses.

In the first phase of this research, a single mass and a tuning fork gyroscope is designed with a rigid frame-in-frame structure. Figure 1.13 shows the 3-D model of the single mass gyroscope developed in this research. The sense mode mechanisms of these gyroscopes are designed to be very similar except very minor modifications, in order to extract the improvement in the g-sensitivity and resolution of the gyroscopes.

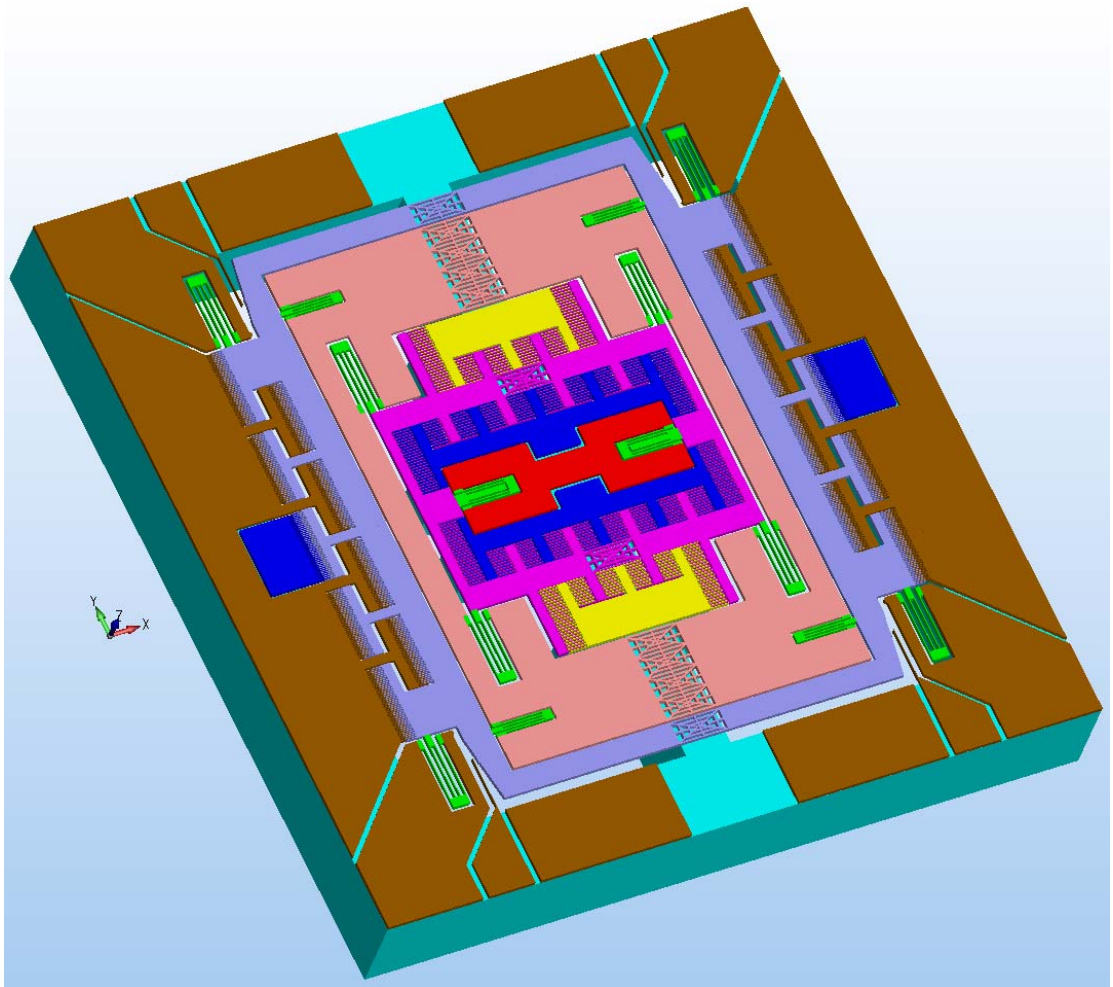


Figure 1.13: 3-D model of the single mass gyroscope developed in this research

In the tuning fork, a very novel coupling mechanism is employed for linear drive mode vibrations together with minimum frequency fluctuation under large amplitude variations while sustaining the exactly opposite displacement phases of the twin masses [34]. The mechanism is a ring shaped spring anchored along the diametric axis which is orthogonal to the main vibration axis. The structure of this coupling mechanism enforced all the frequencies of the structural mode shapes be higher than the frequency of drive mode. Figure 1.14 shows the 3-D model of the tuning fork gyroscope with the symmetrically anchored ring spring between the vibrating masses.

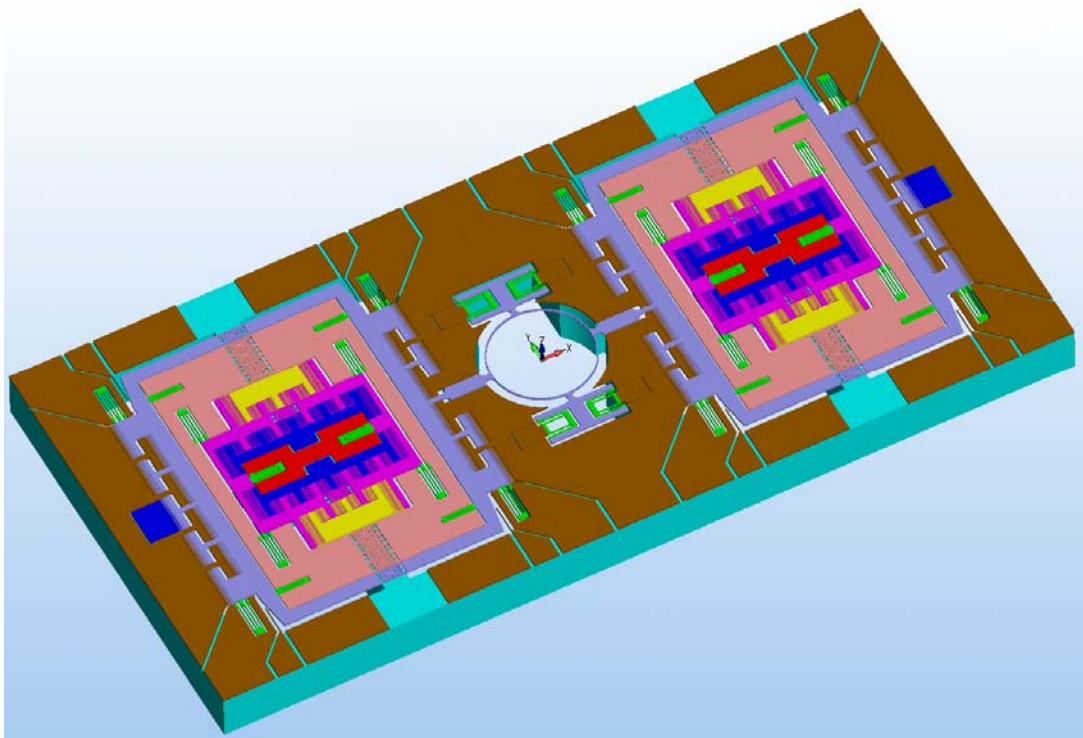


Figure 1.14: 3-D model of the tuning fork gyroscope with the symmetrically anchored ring spring between the vibrating masses.

In the second phase, the drawbacks of the tuning fork design are eliminated by an original quadruple mass gyroscope composed of twin tuning forks working mutually. The goal was to remove asymmetry of the coupling mechanism used in the above tuning fork and make the structure absolutely g-insensitive in all three directions. For this, two of the tuning forks are merged orthogonally with a single ring shaped

coupling spring. Figure 1.15 shows the model of the twin-tuning-fork gyroscopes with the ring spring for drive mode coupling of the proof masses.

In the twin-tuning fork gyroscope, the number of drive mode finger sets is maximized for minimum driving voltages. For all these three gyroscopes, the substrate under the vibrating masses is completely removed except the walls for anchor islands.

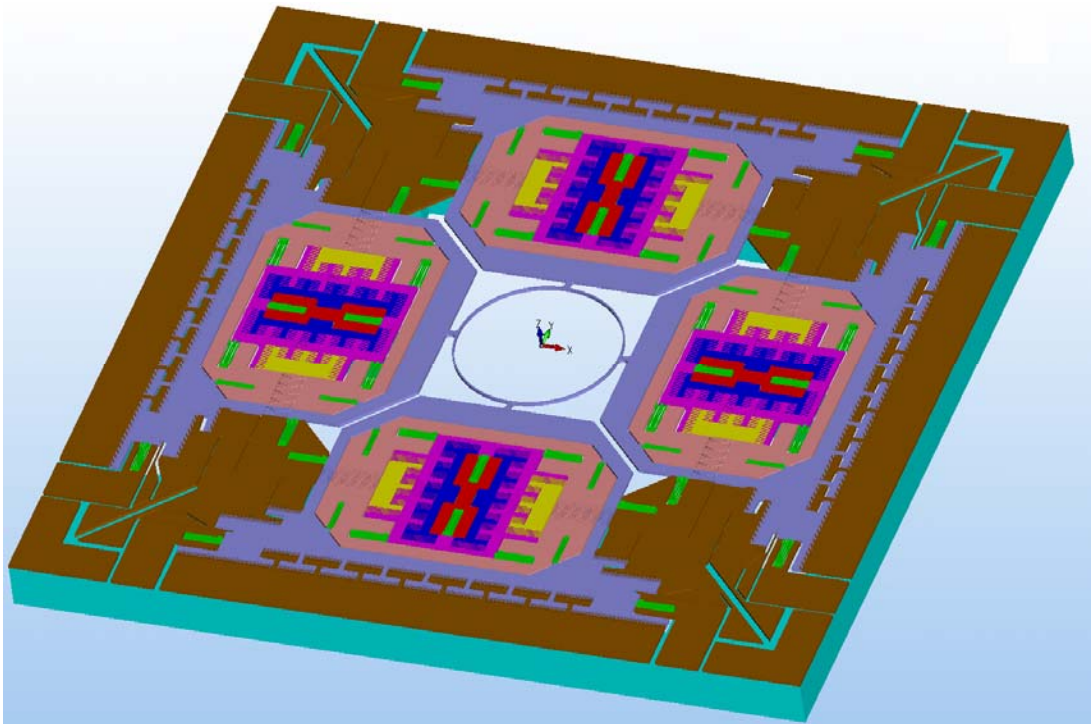


Figure 1.15: The model of the twin-tuning-fork gyroscopes with the ring spring for drive mode coupling of the proof masse.

The gyroscopes were designed to be fabricated using a commercial SOI-MEMS process of MEMSCAP<sup>®</sup> Inc. which is composed of an optimized double-sided DRIE of an SOI wafer with 25 $\mu$ m epitaxial thickness and 400 $\mu$ m substrate thickness.

During performance tests, a resistive type interfacing is used for improved g-survivability. Since the sense structures of these gyroscopes are designed to be very similar for a better performance comparison under similar g-loadings, the improvements in the g-immunities of these gyroscopes become much sharper.

## ***1.4 Research Objectives and Thesis Organization***

The goal of his research is to develop high performance micromachined angular rate sensors with low g-sensitivity and high g-survivability. Designed and realized rate sensors consist of a single mass gyroscope for performance comparison, a double mass tuning fork gyroscope with a novel coupling mechanism and a quadruple mass twin tuning fork gyroscope with the improved coupling mechanism. The specific objectives of this research are as follows:

1. Analysis of mechanical error sources in MEMS gyroscopes, which are classified as vibration coupling via the flexion elements, electrostatic actuation nonuniformities, electrostatic levitation, drift of operational frequency, effects of static linear accelerations and effects of temperature changes.
2. Electromechanical design of a single mass gyroscope with a frame-in-frame topology in order to minimize the errors created by the sources mentioned above. The design should consist of even distribution of supporting flexion elements, separated sense and varying gap type frequency tuning electrode sets and maximum number of drive electrodes for an improved performance characteristics. This design should also enable simple modifications and be compatible with commercial SOI-MEMS process of MEMSCAP Inc.
3. Electromechanical design and development of a novel tuning fork structures with an original coupling mechanism introducing linear drive mode resonance together with minimum frequency fluctuation under large vibration amplitude variations while keeping the masses in exactly opposite displacement phases. The supporting spring structures, electrostatic actuation mechanisms, the capacitive sensing sets and the fabrication tolerances should be considered for a firm tuning fork gyroscope.
4. Performance simulations of these tuning forks in Saber ARCHITECT environment. The resonance characteristics of the modes, matching

polarization voltages, the effect of undercut and an estimate of sensitivity are conducted.

5. Characterization and performance tests of the fabricated gyroscopes in terms of rate sensitivity, linearity, scale factor, bias stability, angle random walk and g-sensitivity. The performance specifications of the gyroscopes with different mechanical topologies should be compared especially in terms of g-sensitivity.

Organization of this thesis and the content summary of the following chapters are presented below:

Chapter 2 gives brief information on the governing equations of the vibrating micromachined gyroscopes together with their working principles, including the resonance characteristics, flexion elements, the electrostatic finger sets, and the damping mechanisms. This chapter also presents a detailed investigation on the mechanical error sources and gives possible solutions.

Chapter 3 gives detailed design procedure of the single mass (SMG), double mass (DMG) and the quadruple mass (QMG) gyroscopes. The design details of the supporting elements, the novel coupling mechanisms and the electrostatic drive and sense finger sets are presented together with the FEM simulations including modal and stress analysis. This chapter also gives detailed information about the fabrication technique used.

Chapter 4 presents the tests setups used for the characterization and performance tests of the fabricated gyroscopes. In this chapter, the designed PCB packages and the test PCB together with the external self resonance loop is presented. The rate table setup for the g-sensitivity tests is also explained. Then the performance characteristics of the SMG, DMG and QMG together with the tests results are given for both atmospheric pressure and for vacuum ambient.

Finally, Chapter 5 summarizes this research and gives the conclusions extracted from the obtained test results. Moreover, this chapter gives a road map for further research on multi-mass micromachined gyroscopes.

## **CHAPTER 2**

### **THEORY OF VIBRATORY GYROSCOPES**

In this chapter, the theory of the micromachined resonating gyroscopes is presented. In a micromachined gyroscope, the mutual interaction between the mechanical and the electrical elements of the overall sensor system requires a multi disciplinary study of their electromechanical design aspects. Section 2.1 presents the governing equations of the mechanical model of the drive and sense modes with the Coriolis coupling under the given angular rate. This model also includes the DC acceleration terms together with the Coriolis acceleration induced on the sense mode. Section 2.2 introduces the electromechanical structural parts that are used in the proposed gyroscope structures and also presents the transduction of applied voltage to the applied force from electrical domain to mechanical domain. In this section, the sense mode basics of the capacitive sensing are also presented. Section 2.3 introduces the mechanical parameters of the proposed gyroscope structures. Section 2.4 presents the noise and nonlinearity sources in micromachined vibratory gyroscopes. Finally, Section 2.5 gives a summary of this chapter.

#### ***2.1 Mechanical Model of Vibratory Microgyroscopes***

In all resonating micromachined gyroscopes, a driving mechanism in order to retain the resonance of the proof mass, a sense mode structure to pick the Coriolis coupling and a proper suspension avoiding coulomb friction are essential. Since the fabrication techniques allow a single piece of moveable structure, the mechanical decoupling of drive and sense modes is also very vital for the sake of the bias

stability and resolution of the rate sensor. The coupling between these modes creates an unpredictable bias shift at the output of the gyroscope as if there is a constant angular rate and increases the mechanical noise. Basically, for decoupling the drive and sense modes, i.e., isolating the drive mode vibration of the proof mass from the sense mode Coriolis accelerometer, the degree of freedoms of these two modes are designed to be orthogonal and fully force-symmetric and moment-symmetric. Since the Coriolis force on a linearly vibrating mass is to be measured and since the vibration axis and the Coriolis force is always orthogonal on the rotating frame, the proof mass should be 2-DOF. But the drive and sense electrode jigs should be 1-DOF and especially the sense electrode jigs should be immune to the resonating mass in drive mode and be only sensitive to the induced Coriolis perpendicular to the drive mode vibration of the proof mass. In this subsection, the sense and drive modes are analyzed separately. Decoupling mechanism of the modes will be mentioned while presenting the flexion elements.

### 2.1.1 Mechanics of the Drive Mode

The structure of the drive mode is a simple mass-spring-damper system. The mass “ $m_D$ ” of the drive mode includes the proof mass and the drive jigs, the lumped spring parameter “ $k_D$ ” is the resultant spring effect of the present flexion elements in drive mode, and the damper “ $c_D$ ” is the structural damping added on the viscous air damping affecting all the mass in drive mode vibration, i.e.,  $m_D$ . For such a single DOF damped system, the governing equation of free vibration is,

$$m_D \ddot{x} + c_D \dot{x} + k_D x = 0 \quad (2.1a)$$

$$\ddot{x} + \frac{c_D}{m_D} \dot{x} + \frac{k_D}{m_D} x = 0 \quad (2.1b)$$

and can be expressed in a more suitable form for further derivations as,

$$\ddot{x} + 2\xi\omega_{n_D}\dot{x} + \omega_{n_D}^2 x = 0 \quad (2.2)$$

where,

$$\omega_{n_D} = \sqrt{\frac{k_D}{m_D}} \quad (2.3)$$

$$\xi_D = \frac{c_D}{2\sqrt{k_D.m_D}} \quad (2.4)$$

which are the natural free vibration frequency ( $\omega_{n_D}$ ) and the ratio of effective damping to the critical damping of the drive mode ( $\xi_D$ ), respectively. The solution of Equation 2.2 for an arbitrary initial condition depends on the amount of damping present in the system. For  $\xi$  values greater than or equal to 1, the system does not oscillate for a complete cycle for any kind of initial condition. But for  $\xi < 1$ , the oscillations can be observed for relevant initial conditions. In case of  $\xi < 1$ , the oscillation frequency of the system also depends on the value of  $\xi$  as,

$$\omega_{d_D} = \omega_{n_D} \sqrt{1 - \xi_D^2} \quad (2.5)$$

In this equation  $\omega_{d_D}$  is the damped natural frequency of drive mode resonator. This resonator is only dissipating energy stored in the initial conditions since the system is not excited externally.

In the case of the forced vibration, the equations change adding the driving harmonic excitation with a frequency of  $\omega$ ,

$$m_D\ddot{x} + c_D\dot{x} + k_D x = F_0 \cos(\omega t) \quad (2.6)$$

Arranging the terms as in Equation 2.2 and 2.6,

$$\ddot{x} + 2\xi_D \omega_{n_D} \dot{x} + \omega_{n_D}^2 x = \frac{F_0}{k_D} \omega_{n_D}^2 \cos(\omega t) \quad (2.7)$$

Transient solution of this differential equation is not important for the operation of a microgyroscope because a steady resonance is required in the drive mode. The steady-state solution of this differential equation is,

$$X_{Drive}(t) = \frac{F_0 / k_D}{1 - \frac{\omega^2}{\omega_{n_D}^2} + i.2.\xi_D \frac{\omega}{\omega_{n_D}}} e^{i.\omega.t} \quad (2.8)$$

This is the time-domain response of the drive mode resonator to an excitation of  $F_0.e^{i.\omega.t}$  applied electrostatically. If the system is driven by a constant DC force of  $F_0$ , the deflection would be,

$$x = \frac{F_0}{k_D} \quad (2.9)$$

So, this deflection is amplified with a factor of,

$$|H(\omega)| = \frac{1}{\sqrt{\left(1 - \frac{\omega^2}{\omega_{n_D}^2}\right)^2 + \left(2.\xi_D \frac{\omega}{\omega_{n_D}}\right)^2}} \quad (2.10)$$

together with a phase;

$$\phi = -\tan^{-1} \left( \frac{2.\xi_D \frac{\omega}{\omega_{n_D}}}{1 - \frac{\omega^2}{\omega_{n_D}^2}} \right) \quad (2.11)$$

The quality factor (Q) of a resonator is defined as the maximum amplification factor of  $|H(\omega)|$  and this parameter is very important for the characterization of the resonators. The resonance peak is reached when the system is excited at a frequency of,

$$\omega_{Res_D} = \omega_{n_D} \sqrt{1 - 2\xi_D^2} \quad (2.12)$$

The quality factor is then found to be,

$$|H|_{\max} = Q_D = \frac{1}{2\xi_D \sqrt{1 - \xi_D^2}} \quad (2.13)$$

with the phase,

$$\phi_{H_{\max}} = -\tan^{-1} \left( \sqrt{\frac{1 - 2\xi_D^2}{\xi_D^2}} \right) \quad (2.14)$$

Equation 2.12 and 2.14 mean that increasing damping decreases both the frequency at maximum response and the phase difference. In the case of drive mode resonance, assumption of light damping leads the assumption of resonance at  $\omega_{n_D}$ . Thus, the quality factor can be estimated as,

$$Q_{D\xi \ll 1} \cong \frac{1}{2\xi_D} = \frac{\sqrt{k_D m_D}}{c_D} \quad (2.15)$$

Hence, the vibration amplitude is,

$$X \cong \frac{F_0}{k_D} Q_{D\xi \ll 1} \quad (2.16)$$

and the phase,

$$\phi_{H_{\max}} \cong -\tan^{-1}(\infty) = -\frac{\pi}{2} \quad (2.17)$$

But when the high performance criteria of the micromachined gyroscopes are considered, the damping effects on the sensor structure become remarkable. In the following sections, these effects will also be presented in detail.

### 2.1.2 Mechanics of the Sense Mode with Coriolis Coupling

In the vibration equations up to now, the mass is the total vibrating mass in the drive mode including the proof mass and the drive finger sets. Same equations of motion are valid for the sense mode also, with different mass, spring and damping. However, the driving force is not an external force, but the induced Coriolis force and the other inertial forces on the sense mode.

For the sake of clarity, the mass motion of the microgyroscope can be assumed a planar motion on a noninertial rotating frame of reference with an angular velocity of  $\vec{\Omega}$ , an angular acceleration of  $\dot{\vec{\Omega}}$  and a linear acceleration of  $\vec{a}_{NIF}$ . The displacement of a particle “P” on this “noninertial reference frame” can be expressed with respect to an “inertial reference frame” as the vector sum of the displacement of this point with respect to the noninertial frame and the displacement of this noninertial frame itself,

$$\vec{r}_{P_{IF}} = \vec{r}_{NIF} + \vec{r}_{P_{NIF}} \quad (2.18)$$

The time derivative of the above displacement vector is,

$$\dot{\vec{r}}_{P_{IF}} = \dot{\vec{r}}_{NIF} + (\dot{r}_{x,P_{NIF}} \mathbf{i} + \dot{r}_{y,P_{NIF}} \mathbf{j}) + (r_{x,P_{NIF}} \dot{\mathbf{i}}_{NIF} + r_{y,P_{NIF}} \dot{\mathbf{j}}_{NIF}) \quad (2.19)$$

This can be written in the form of,

$$\vec{v}_{P_{IF}} = \vec{v}_{NIF} + \dot{\vec{r}}_{P_{NIF}} + \vec{\Omega} \times \vec{r}_{P_{NIF}} \quad (2.20)$$

The reason of adding the cross product term is that the directional unit vectors of the noninertial frame are not stationary but rotating. Since the motion of point P is defined with respect to the noninertial frame, these rotating unit vectors should also be taken into account. Same kinematics is valid for the time derivative of the velocity vector of point P.

$$\dot{\vec{v}}_{P_{IF}} = \dot{\vec{v}}_{NIF} + \frac{d}{dt} (\dot{\vec{r}}_{P_{NIF}} + \vec{\Omega} \times \vec{r}_{P_{NIF}}) + \vec{\Omega} \times (\dot{\vec{r}}_{P_{NIF}} + \vec{\Omega} \times \vec{r}_{P_{NIF}}) \quad (2.21)$$

Rearranging the terms,

$$\underbrace{\vec{a}_{P_{IF}}}_{\substack{\text{Acc. of } P \\ \text{w.r.t.} \\ \text{inertial} \\ \text{reference} \\ \text{frame}}} = \underbrace{\vec{a}_{NIF}}_{\substack{\text{Acc. of} \\ \text{noninertial} \\ \text{frame} \\ \text{w.r.t.} \\ \text{inertial} \\ \text{reference} \\ \text{frame}}} + \underbrace{\vec{a}_{P_{NIF}}}_{\substack{\text{Acc. of } P \\ \text{w.r.t.} \\ \text{noninertial} \\ \text{reference} \\ \text{frame}}} + \underbrace{\dot{\vec{\Omega}} \times \vec{r}_{P_{NIF}}}_{\substack{\text{Angular Acc.} \\ \text{induced} \\ \text{Tangential} \\ \text{Acceleration} \\ \text{of } P}} + \underbrace{\vec{\Omega} \times \dot{\vec{r}}_{P_{NIF}}}_{\substack{\text{Magnitude} \\ \text{change in} \\ \text{Tangential} \\ \text{Velocity} \\ \text{of } P}} + \underbrace{\vec{\Omega} \times \dot{\vec{r}}_{P_{NIF}}}_{\substack{\text{Direction} \\ \text{change in} \\ \text{Linear} \\ \text{Velocity} \\ \text{of } P}} + \underbrace{\vec{\Omega} \times (\vec{\Omega} \times \vec{r}_{P_{NIF}})}_{\substack{\text{Centripetal} \\ \text{Acceleration} \\ \text{of } P}} \quad (2.22)$$

Coriolis Acceleration

Equation 2.22 summarizes all the acceleration terms of a moving particle on a noninertial frame with respect to an inertial one. The induced forces on the particle P is then,

$$\vec{F}_{P_{IF}} = m_P \vec{a}_{NIF} + m_P \vec{a}_{P_{NIF}} + m_P (\dot{\vec{\Omega}} \times \vec{r}_{P_{NIF}}) + m_P (2 \vec{\Omega} \times \dot{\vec{r}}_{P_{NIF}}) + m_P (\vec{\Omega} \times (\vec{\Omega} \times \vec{r}_{P_{NIF}})) \quad (2.23)$$

The fictitious force terms are,

$$\vec{F}_{P_{IF}} - m_P \vec{a}_{NIF} - m_P \vec{a}_{P_{NIF}} - m_P (\dot{\vec{\Omega}} \times \vec{r}_{P_{NIF}}) - m_P (2 \vec{\Omega} \times \dot{\vec{r}}_{P_{NIF}}) - m_P (\vec{\Omega} \times (\vec{\Omega} \times \vec{r}_{P_{NIF}})) = 0 \quad (2.24)$$

As can be noted, these terms include  $\vec{\Omega}$  as well as the time derivative of  $\vec{\Omega}$  and dot squared  $\vec{\Omega}$ . Among these, only the Coriolis acceleration is linearly proportional to

$\vec{\Omega}$  and independent of the position vector  $\vec{r}$ . So, a gyroscope sensing only the Coriolis acceleration and rejecting others will be reliable for rate sensing and be immune to the fluctuations in the input rate and the effects of different settling radii. Another advantage of Coriolis force is that this force is always perpendicular to both the velocity and the rate vectors, as a result of the cross product present. By means of this property, a mass vibrating in a determined line can be converted into a gyroscope with some arrangements, and, this idea forms the basic theory behind the micromachined vibratory gyroscopes.

One should also keep in mind that the force in Equation 2.23 is a “real” force with respect to the stationary frame of reference and it has fictitious counterparts when they are considered in the rotation noninertial frame, with exactly opposite directions. One of those is the Coriolis force with respect to the moving frame,

$$\vec{F}_{Coriolis, P_{NIF}} = -2.m_p.\vec{\Omega} \times \dot{\vec{r}}_{P_{NIF}} \quad (2.25)$$

Up to now, the motion of a particle moving on a noninertial frame is considered. To shift from the particle kinematics to the sensor kinematics, relevant substitutions should be carried out. Thus, the mass of the particle  $m_p$  can be considered as the proof mass  $m_{PM}$  and the  $\dot{\vec{r}}_{P_{NIF}}$  in Equation 2.25 is nothing but the velocity of the resonating proof mass in the afore-mentioned drive mode,

$$\dot{X}_{Drive}(t) = \frac{F_0/k_D}{1 - \frac{\omega_D^2}{\omega_{n_D}^2} + i.2.\xi_D \frac{\omega_D}{\omega_{n_D}}} i.\omega_D.e^{i.\omega_D.t} = i.\omega_D.X_{Drive}(t) \quad (2.26)$$

Meaning that,

$$\dot{X} \cong \frac{F_0}{k_D} \omega_D.Q_{D\xi \ll} \quad (2.27)$$

with the phase,

$$\phi_{H_{\max}} \cong \frac{\pi}{2} - \frac{\pi}{2} = 0 \quad (2.28)$$

Equation 2.27 states that the magnitude of the proof mass velocity is proportional to the driving frequency and drive mode quality factor as well as the excitation magnitude. Equation 2.28 reveals that at resonance, the velocity and the forcing excitation are in phase.

On the other hand, the input rate may also be a sinusoidal, i.e.,

$$\Omega(t) = \Omega_0 \cos(\omega_\Omega t) \quad (2.29)$$

Substituting Equations 2.27 and 2.29 in Equation 2.25,

$$F_{Coriolis,PM_{NIF}} = -2.m_{PM}.\Omega_0 \cos(\omega_\Omega t) \cdot \frac{\omega_D.Q_D}{k_D} F_0 \cos(\omega_D t) \quad (2.30)$$

Rearranging terms,

$$F_{Coriolis,PM_{NIF}} = \frac{-F_0.m_{PM}.\Omega_0.\omega_D.Q_D}{k_D} (\cos((\omega_D + \omega_\Omega)t) + \cos((\omega_D - \omega_\Omega)t)) \quad (2.31)$$

As can be noted, there are two driving terms with different frequencies. These two forces should be taken as the driving term for the sense mode resonator. Modifying Equation 2.8 for the sense mode and substituting Equation 2.31,

$$X_{1,Sense}(t) = \frac{-m_{PM} \cdot Q_D}{k_D k_S} \frac{F_0 \cdot \Omega_0 \cdot \omega_D}{1 - \frac{(\omega_D + \omega_\Omega)^2}{\omega_{n_s}^2} + i \cdot 2 \cdot \xi_S \frac{\omega_D + \omega_\Omega}{\omega_{n_s}}} e^{i(\omega_D + \omega_\Omega)t} \quad (2.32a)$$

$$X_{2,Sense}(t)_2 = \frac{-m_{PM} \cdot Q_D}{k_D k_S} \frac{F_0 \cdot \Omega_0 \cdot \omega_D}{1 - \frac{(\omega_D - \omega_\Omega)^2}{\omega_{n_s}^2} + i \cdot 2 \cdot \xi_S \frac{\omega_D - \omega_\Omega}{\omega_{n_s}}} e^{i(\omega_D - \omega_\Omega)t} \quad (2.32b)$$

Magnitudes of these sense mode vibrations are,

$$X_{1,Sense} = \frac{-m_{PM} \cdot Q_D}{k_D k_S} \frac{F_0 \cdot \Omega_0 \cdot \omega_D}{\sqrt{\left(1 - \frac{(\omega_D + \omega_\Omega)^2}{\omega_{n_s}^2}\right)^2 + \left(2 \cdot \xi_S \frac{\omega_D + \omega_\Omega}{\omega_{n_s}}\right)^2}} \quad (2.33a)$$

$$X_{2,Sense} = \frac{-m_{PM} \cdot Q_D}{k_D k_S} \frac{F_0 \cdot \Omega_0 \cdot \omega_D}{\sqrt{\left(1 - \frac{(\omega_D - \omega_\Omega)^2}{\omega_{n_s}^2}\right)^2 + \left(2 \cdot \xi_S \frac{\omega_D - \omega_\Omega}{\omega_{n_s}}\right)^2}} \quad (2.33b)$$

Equation 2.32 is a general form of the sense mode vibration amplitudes, which are linearly independent. In case of constant input rate, i.e.,  $\omega_\Omega = 0$ , the separated equation simplifies to,

$$X_{Sense} = \frac{2m_{PM} \cdot Q_D}{k_D k_S} \frac{F_0 \cdot \Omega_0 \cdot \omega_D \cdot \omega_{n_s}^2}{\sqrt{(\omega_{n_s}^2 - \omega_D^2)^2 + (2 \cdot \xi_S \cdot \omega_D \cdot \omega_{n_s})^2}} \quad (2.34)$$

The corresponding phase difference would be,

$$\phi_{Sense} = -\tan^{-1} \left( \frac{2 \cdot \xi_S \cdot \frac{\omega_D}{\omega_{n_S}}}{1 - \frac{\omega_D^2}{\omega_{n_S}^2}} \right) \quad (2.35)$$

In the above equation, if  $\omega_{n_S}$  is adjusted to be equal to  $\omega_D$ , which is called “matching”, maximum sense mode vibration amplitude would be achieved. Together with the light damping assumption, the sense mode amplitude becomes,

$$X_{Sense} = \frac{2F_0 \cdot m_{PM} \cdot Q_D \cdot Q_S \cdot \Omega_0 \cdot \omega_D}{k_D k_S} \quad (2.36)$$

But the case of maximum sense mode vibration amplitude diminishes the bandwidth of the gyroscope because the frequency tolerances in Equations 2.33a and 2.33b are lost. On the other hand, mismatched operation causes sensitivity drop, which is a common trade-off between sensitivity and bandwidth. Additionally, the characteristics of the sense and control electronics are also very important because the direction of the rate and the magnitude is extracted by comparing the drive mode and sense mode outputs. Thus, the external electronics become much more deterministic on the overall sensor system. The above equations only give the main kinematics of the mechanical gyroscope structure. A complete analysis together with the control and interface electronics should be carried out for a realistic performance analysis.

## ***2.2 Electrostatic Actuation and Sensing***

Basically, two conductive substances that have different charge distributions and different voltages always attract or repel each other in order to minimize the stored electrostatic energy. This can be explained more clearly if a bungee-jumper is

considered. When the jumper is released, he is accelerating down and the stored potential energy is being converted to kinetic energy and dissipated through the air viscosity. The gravitational force applied to the jumper is actually the derivative of the potential energy of the jumper with respect to the distance traveled, i.e.,

$$F_g = \frac{\partial(m \cdot g \cdot h)}{\partial(h)} = m \cdot g \quad (2.37)$$

In the case of electrostatic force, the electrostatic force is the derivative of the stored capacitive energy,

$$F_e = \frac{1}{2} \cdot \frac{\partial C}{\partial(x, y, z)} \cdot V^2 \quad (2.38)$$

where the C is the capacitance in between,

$$C = \frac{\varepsilon \cdot A}{d} \quad (2.39)$$

and V is the voltage difference. For the sinusoidal actuation, the voltage is applied is,

$$V = -V_p + V_{ac} \cdot \sin(\omega t) \quad (2.40)$$

The terms in the driving voltage are the constant potential and the sinusoidal voltage added on top of it.

In micromachining, the most applicable way of forming variable capacitors is forming high aspect ratio capacitive fingers. There are mainly 2 types of these finger structures; varying overlapping area type and varying gap type. Figure 2.1 shows a unit electrostatic forcing element which is called the “Varying Overlap-Area Type Finger Set”. Main advantages of this type fingers are that they permit high displacements due to their compact structure and their capacitance change with changing displacement is linear. However, their capacitance change per unit

deflection is small. So, this type of finger sets are usually utilized for driving the proof mass.

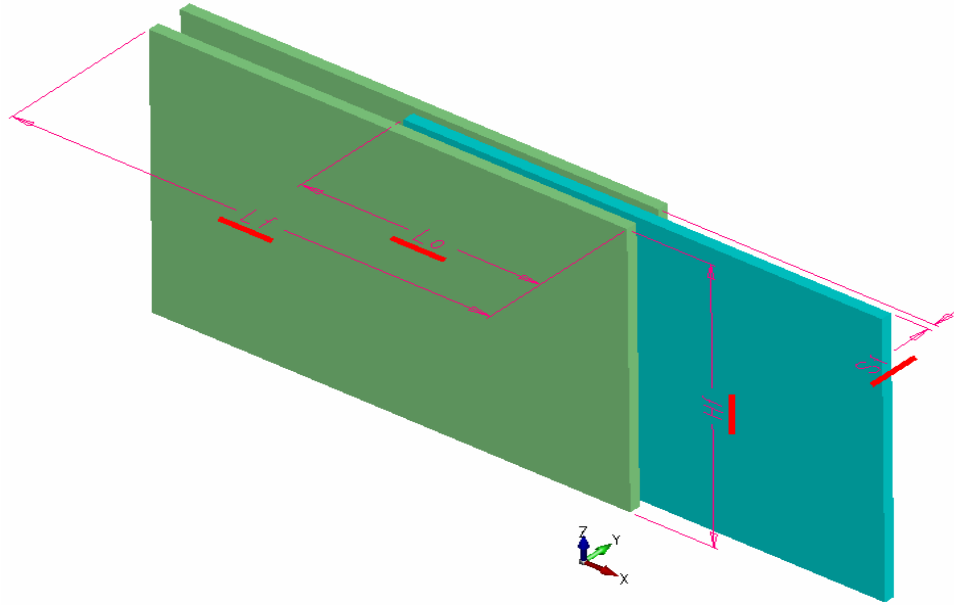


Figure 2.1: A unit electrostatic forcing element which is called the “Varying Overlap-Area Type Finger”.

Main parameters in the varying overlap area (VOA) type fingers are;

$L_f$  = Finger Length

$L_o$  = Finger Overlap Length

$H_f$  = Finger Height

$S_f$  = Finger to Finger Distance

$\alpha$  = Fringing Field Correction Factor

Among these parameters, only the fringing field correction factor is an empirical parameter which depends on the shape and thickness of the structure. Substituting the given parameters in the Equation 2.37,

$$C = \alpha \cdot \epsilon_o \cdot \left[ \frac{\overbrace{(L_o \pm x) \cdot (H_f - z)}^A}{\underbrace{(S_f + y)}_d} \right] + \alpha \cdot \epsilon_o \cdot \left[ \frac{\overbrace{(L_o \pm x) \cdot (H_f - z)}^A}{\underbrace{(S_f - y)}_d} \right] \quad (2.41)$$

And if a potential difference is applied to the comb fingers, the system tries to maximize the capacitance. So a force will be induced in the direction which will increase the capacitance and decrease the electrostatic energy. The derivative of the electrostatic energy is related with the force through this relation. For the VOAs, the driving force is in the x direction. Since the finger set is symmetrical in the z and y axes, the net force component is in the x direction. The magnitude of this force component is then,

$$F_e^x = \pm \alpha \cdot \epsilon_0 \cdot \frac{1}{2} \cdot \left[ \frac{(H_f - z)}{(S_f + y)} + \frac{(H_f - z)}{(S_f - y)} \right] \cdot (V_{ac} \cdot \sin(\omega t) - V_p)^2 \quad (2.42)$$

where,

$$(V_{ac} \cdot \sin(\omega t) - V_p)^2 = V_{ac}^2 \cdot \sin^2(\omega t) + V_p^2 - 2 \cdot V_p \cdot V_{ac} \cdot \sin(\omega t) \quad (2.43)$$

Arranging terms,

$$(V_{ac} \cdot \sin(\omega t) - V_p)^2 = \left( \frac{V_{ac}^2}{2} + V_p^2 \right) - 2 \cdot V_p \cdot V_{ac} \cdot \sin(\omega t) - \left( \frac{V_{ac}^2}{2} \cdot \cos(2 \cdot \omega t) \right) \quad (2.44)$$

Combining Equations 2.40 and 2.42,

$$F_e^x = \pm \alpha \cdot \epsilon_0 \cdot \frac{1}{2} \cdot \left[ \frac{(H_f - z)}{(S_f + y)} + \frac{(H_f - z)}{(S_f - y)} \right] \cdot \left[ \left( \frac{V_{ac}^2}{2} + V_p^2 \right) - 2 \cdot V_p \cdot V_{ac} \cdot \sin(\omega t) - \left( \frac{V_{ac}^2}{2} \cdot \cos(2 \cdot \omega t) \right) \right] \quad (2.45)$$

Deflections in the y and z directions are assumed to be zero to extract the electrostatically induced force in only x-direction. In practice, the deflections in both y and z are present and cause different problems which will be mentioned later. Assuming no deflection in y and z,

$$F_e^x = K \cdot \left[ \left( \frac{V_{ac}^2}{2} + V_p^2 \right) - 2 \cdot V_p \cdot V_{ac} \cdot \sin(\omega t) - \left( \frac{V_{ac}^2}{2} \cdot \cos(2 \cdot \omega t) \right) \right] \quad (2.46)$$

where,

$$K = \alpha \cdot \varepsilon_0 \cdot \frac{H_f}{S_f} \quad (2.47)$$

At this point, it is observed that there are three main force components,

$$\text{DC Term:} \quad F_{e,DC}^x = K \cdot \left( \frac{V_{ac}^2}{2} + V_P^2 \right) \quad (2.48)$$

$$\text{Primary Driving Term:} \quad F_{e,fx1}^x = -K \cdot 2 \cdot V_P \cdot V_{ac} \cdot \text{Sin}(\omega t) \quad (2.49)$$

$$\text{Secondary Driving Term:} \quad F_{e,fx2}^x = -K \cdot \left( \frac{V_{ac}^2}{2} \cdot \text{Cos}(2 \cdot \omega t) \right) \quad (2.50)$$

These forces have different excitation frequency. DC term is a constant force proportional to the square of the applied DC and AC voltages magnitudes. Primary term is the main driving term used in the design of the gyroscopes. The advantage of this forcing component is that the force generated is linearly proportional to the applied DC and AC voltage magnitudes and right in phase with the applied AC voltage. Secondary driving term is the final component at the twice the frequency of the input AC signal. Since the magnitude of this component is limited to the magnitude of the AC signal, the peak-to-peak input voltage should be quite high for appropriate drive vibration. There is only one advantage of this component which is the rejection of electrical coupling if the DC voltage is set 0V and the mode frequency is twice the driving signal frequency. The primary term is, as stated before, the main driving term. In order to filter out the higher frequency component, the springs can be adjusted just by setting the resonant frequency of the resonator to the primary excitation frequency. As a result, dc term and secondary driving term become negligible under the large amplitude of resonating mass.

Same electrostatic derivations are also valid for the varying gap type sense finger sets. Figure 2.2 shows a unit electrostatic sensing element which is called the “Varying Gap Type Finger”.

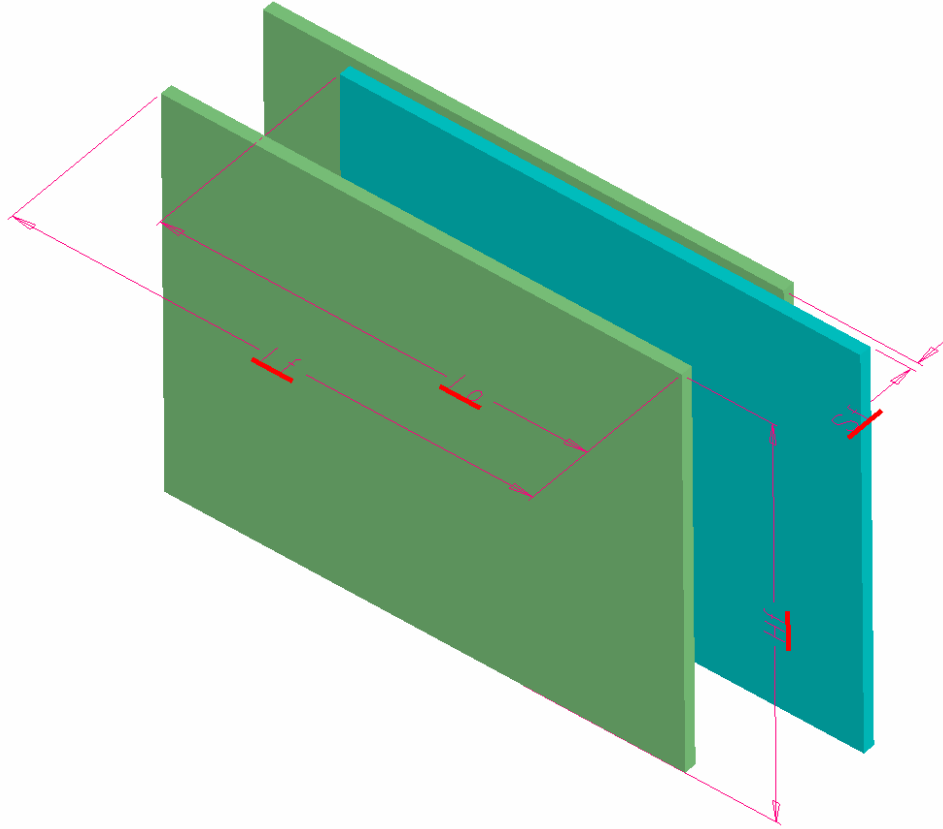


Figure 2.2: A unit electrostatic sensing element which is called the “Varying Gap Type Finger”.

The static forcing in the sense mode is,

$$F_{sense}^y = \alpha \cdot \epsilon_0 \cdot \frac{1}{2} \cdot (L_o \pm x) \cdot (H_f - z) \left( \frac{1}{(S_f + y)^2} - \frac{1}{(d_a - y)^2} \right) \cdot V^2 \quad (2.51)$$

Assuming the variations in the  $y$  is negligible in the presence of the  $d_g$  and  $d_a$ , and given that  $d_a$  is 9 times larger than  $d_g$ , the net force in the sense mode can be approximated as,

$$F_{sense}^y = \alpha \cdot \varepsilon_0 \cdot \frac{1}{2} \cdot (L_o \pm x) \cdot (H_f - z) \frac{1}{(S_f + y)^2} \cdot V^2 \quad (2.52)$$

This serves as a negative spring in the sense mode and allows sense mode resonance frequency to be adjusted. This phenomenon is utilized in the dedicated frequency tuning electrode sets.

The sense mode electromechanical dynamics are also dependent on this phenomenon. Additionally, the capacitance change in the sense mode is approximated as;

$$\frac{\partial C}{\partial x} = -\alpha \cdot \varepsilon_0 \cdot \frac{H_f \cdot L_o}{d_g^2} \quad (2.53)$$

This capacitance dependency is then used for sensing the Coriolis acceleration induced displacements. Depending on the readout scheme, the sense mode capacitor is then biased using resistive or a capacitive impedance to measure the small variations on the sense mode.

### ***2.3 Flexion Elements***

The suspension structures of the vibratory micromachined gyroscope are one of the most important structural parts because their shape and rigidity decides the operational frequency, sensitivity and many other design aspects.

There are various spring structures with different connection possibilities. Among these, two types have distinctive linearity and size properties. The first one is a double folded and double sided type. Figure 2.3 shows the double sided and double folded spring.

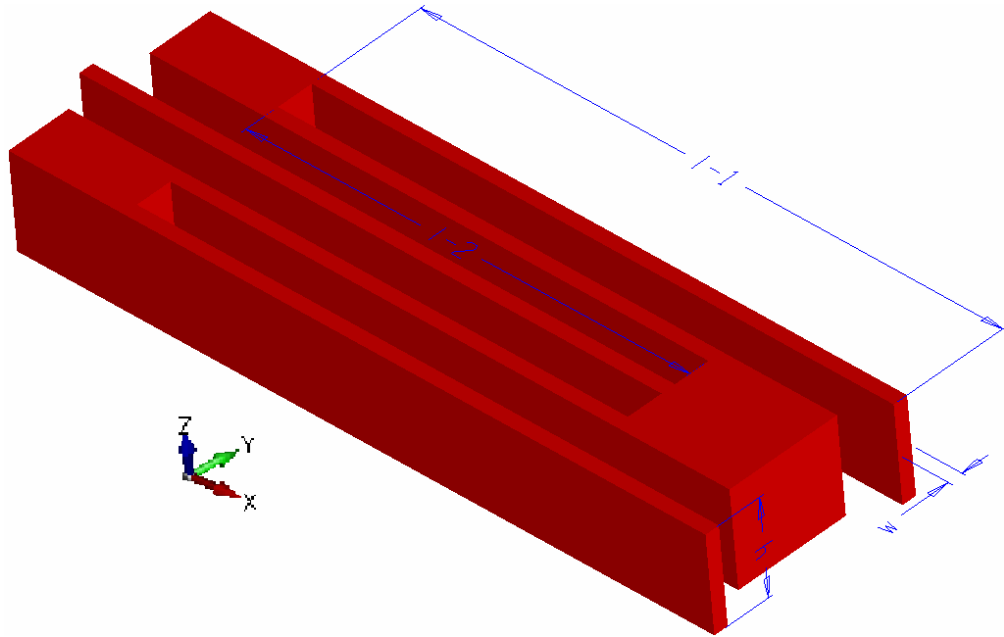


Figure 2.3: Double sided and double folded spring.

This spring is composed of beam elements connected with rigid masses. For a single beam under force and moment loading, the end point deflection angles are,

$$\theta_{Force} = \frac{F \cdot l^2}{2 \cdot E \cdot I} \quad (2.54)$$

$$\theta_{Moment} = \frac{M \cdot l}{E \cdot I} \quad (2.55)$$

The end points of the beams forming the folded spring are parallel to each other and at these ends, the slope is zero. This can be achieved by a force and a moment pair. Combining these, i.e.,

$$\theta_{Load} = \theta_{Moment} \quad (2.56)$$

resulting in,

$$M = \frac{F \cdot l}{2} \quad (2.57)$$

The deflection at one end is then the superposition of deflections of the moment and the load,

$$x = \frac{F \cdot l^3}{3 \cdot E \cdot I} - \frac{M \cdot l^2}{2 \cdot E \cdot I} \quad (2.58)$$

substituting M and I,

$$\frac{F}{x} = k_y = \frac{E \cdot h \cdot w^3}{l^3} \quad (2.59)$$

In the case of folded type spring, since two beams are in series, they are in parallel being serially connected to the single one. So, the overall spring constant is,

$$k_y^{Folded} = E \cdot h \cdot w^3 \cdot \left( \frac{2}{3 \cdot L_1^3 + L_2^3} \right) \quad (2.60)$$

For the double sided and double folded spring, derivation of spring constant in x direction is a bit complicated owing to its nonlinearity. Figure 2.4 shows the force and moment distribution on the double sided and double folded spring loaded in x-direction.

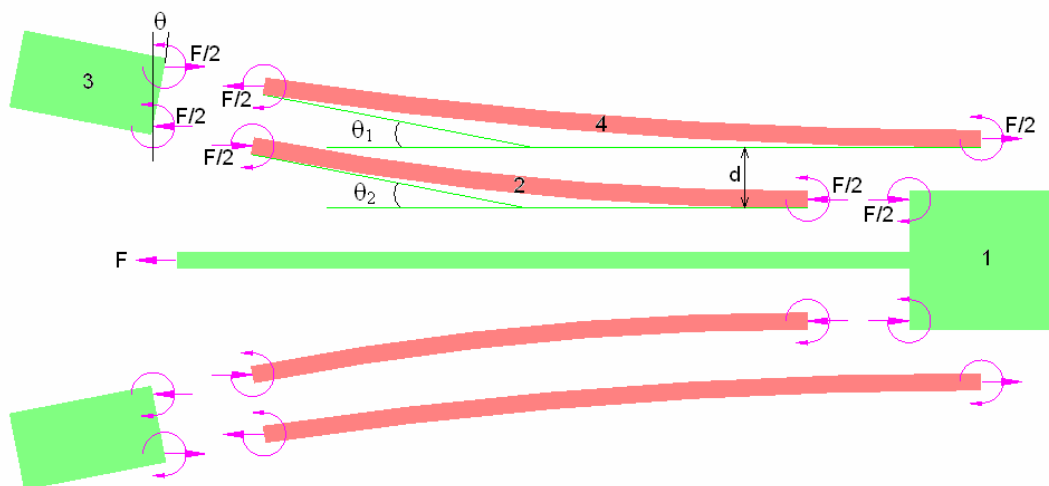


Figure 2.4: Force and moment distribution on the double sided and double folded spring loaded in x-direction.

As can be seen in Figure 2.4, since  $\theta_1$  and  $\theta_2$  are to be equal,

$$\frac{M_1 \cdot L_1}{E \cdot I} = \frac{M_2 \cdot L_2}{E \cdot I} \quad (2.61)$$

For the moment equilibrium for Body-3,

$$M_1 + M_1 \cdot \frac{L_1}{L_2} = \frac{F \cdot d}{2} \quad (2.62)$$

Thus, the moments are found to be,

$$M_1 = \frac{F \cdot d \cdot L_2}{2 \cdot (L_1 + L_2)} \quad (2.63)$$

$$M_2 = \frac{F \cdot d \cdot L_1}{2 \cdot (L_1 + L_2)} \quad (2.64)$$

Determining the unknown moments, the angle  $\theta$  can be easily found,

$$\theta = \frac{F \cdot d \cdot L_1 \cdot L_2}{2 \cdot E \cdot I \cdot (L_1 + L_2)} \quad (2.65)$$

Since  $x = d \cdot \sin \theta$  and  $\sin \theta \cong \theta$  for small  $\theta$ ,

$$x = \frac{F \cdot d^2 \cdot L_1 \cdot L_2}{2 \cdot E \cdot I \cdot (L_1 + L_2)} \quad (2.66)$$

substituting the “I” and rearranging the terms to give a spring constant,

$$k_x^{Folded} = \frac{E \cdot h \cdot w^3 \cdot (L_1 + L_2)}{6 \cdot d^2 \cdot L_1 \cdot L_2} \quad (2.67)$$

This is the vertical spring constant of the “double sided and double folded” spring, which is highly nonlinear and relatively soft. These drawbacks of double sided and double folded spring type is required to be fixed with a slightly different spring which do not have moment imbalance. Figure 2.5 shows the single sided double folded spring, which has the connections on the same side.

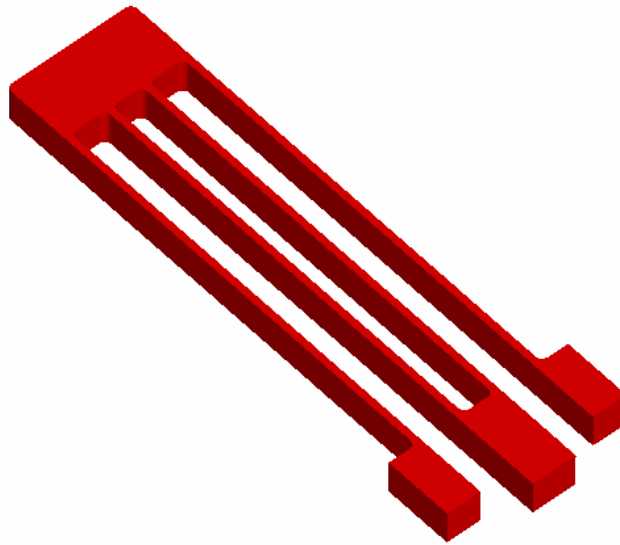


Figure 2.5: The single sided double folded spring, which has the connections on the same side.

This spring type is much stiffer in the vertical axis owing to its fully balanced force and moment equilibrium. The spring constant of this structure is equal to the spring constant of the single guided beam, which is,

$$k_y^{Folded} = \frac{E \cdot h \cdot w^3}{l^3} \quad (2.68)$$

The vertical spring constant is then simply,

$$k_x^{Folded} = \frac{E \cdot h \cdot w}{l} \quad (2.69)$$

This spring type is much stiffer and linear. In the design, all the folded suspension springs are decided to be used this type.

## ***2.4 Nonlinearity and Noise Sources***

In the design of a micromachined gyroscopes structure, some very important aspects are present which should be taken into account for a high performance inertial rate sensor. In this subsection, these aspects are explained including side instability, electrostatic levitation, other acceleration terms, undercut and the temperature variations.

### **2.4.1 Side Instability**

Side instability is an important phenomenon in any kind of electrostatic actuation. It is basically a state of instable electro-mechanic force balance. To illustrate, consider two identical magnets at a distance and a small iron ball right at the middle of these magnets. This is an unstable equilibrium. An infinitesimal motion of the ball results in sticking to one of the magnets. If the ball is suspended with two springs, this instability can be overcome. Same problem arises in the driving combs. In capacitive finger sets, three electrostatic force components are always present, but only a vibration in x direction is required. For the VOA type fingers sets, rotor fingers are almost equally pulled to both sides and if the spring constant in this direction is not sufficient, the rotor fingers will eventually collapse to one side. Considering the structure in Figure 2.1, the electrostatic force in y direction is,

$$F_e^y = \alpha \cdot \varepsilon_0 \cdot \frac{1}{2} \cdot (L_o \pm x) \cdot (H_f - z) \left( \frac{1}{(S_f - y)^2} - \frac{1}{(S_f + y)^2} \right) \cdot V^2 \quad (2.70)$$

together with the mechanical spring force,

$$F_{Spring}^y = k_y \cdot y \quad (2.71)$$

the resultant is,

$$F_{NET}^y = \alpha \cdot \epsilon_0 \cdot \frac{1}{2} \cdot (L_o \pm x) \cdot (H_f - z) \left( \frac{1}{(S_f - y)^2} - \frac{1}{(S_f + y)^2} \right) \cdot V^2 - k_y \cdot y \quad (2.72)$$

Figure 2.6 shows the lateral forces in a VOA type finger set: Green, yellow and blue lines represent  $F_{Spring}$ ,  $F_{Electrostatic}$  and  $F_{NET}$ , respectively.

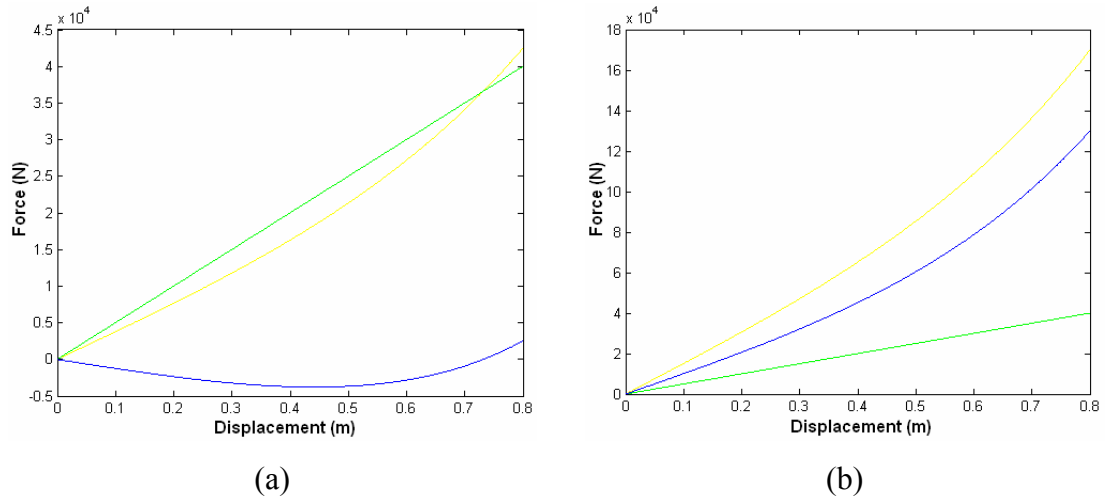


Figure 2.6: Lateral forces in a VOA type finger set: Green, yellow and blue lines represent  $F_{Spring}$ ,  $F_{Electrostatic}$  and  $F_{NET}$ , respectively. In (a), a stable operation is simulated where the net force is below 0N for a reasonable displacement margin. However in (b), the finger is not stable because the net force is above 0N even there is no deflection.

At  $y=0$ , the slope of  $F_{NET}^y$  gives the stability condition of the system. For stable equilibrium, (i.e. the electrostatic force cannot overcome the spring force for an interval of  $x$ ) the voltage applied is assumed constant. So, a constant voltage is applied and the system has deflected some, but pull-in did not occur. For pull-in to take place at that constant voltage, one should externally pull the mass to a point that pull-in occur.

In Figure 2.6 (a), there is no “buffer region” present, so pull-in occurs in an infinitesimal displacement. The model can be summarized as,

$$\frac{\partial F_{NET}^y}{\partial y} = \alpha \cdot \varepsilon_0 \cdot \frac{1}{2} \cdot (L_o \pm x) \cdot (H_f - z) \left( \frac{2 \cdot (S_f - y)}{(S_f - y)^4} + \frac{2 \cdot (S_f + y)}{(S_f + y)^4} \right) \cdot V^2 - k_y \quad (2.73)$$

For stability, the derivative of the net force should be negative,

$$\frac{\partial F_{NET}^y}{\partial y} \Big|_{y \rightarrow 0} = \alpha \cdot \varepsilon_0 \cdot 2 \cdot \frac{(L_o \pm x) \cdot (H_f - z)}{(S_f)^3} \cdot V^2 - k_y \leq 0 \quad (2.74)$$

so, the spring constant in y direction should be at least above value to prevent pull-in right at the beginning of the motion of the system,

$$k_y \geq \alpha \cdot \varepsilon_0 \cdot 2 \cdot \frac{(L_o \pm x) \cdot (H_f - z)}{(S_f)^3} \cdot V^2 \quad (2.75)$$

Equally, for the equivalence point ( $\pm$  turns to  $+$  because pull-in can occur if overlap area increases),

$$\frac{k_y \cdot (S_f)^3}{\alpha \cdot \varepsilon_0 \cdot 2 \cdot V^2 \cdot (H_f - z)} \geq (L_o + x) \quad (2.76)$$

$$x = \frac{k_y \cdot (S_f)^3}{\alpha \cdot \varepsilon_0 \cdot 2 \cdot V^2 \cdot (H_f - z)} - L_o \quad (2.77)$$

Using Equation 2.77, the maximum deflection can be determined without side instability. It should be noted that this result assumes that the rotor fingers are moving in x direction and right at the middle of the stator fingers. For the eccentric case, the worst case should be considered for side instability.

As a matter of fact, the drive mode actuators should be as rigid as possible in the sense direction not only for the side instability problem but also for the minimum cross-coupling and acceleration sensitivity. These aspects are presented in the following subsections in detail.

## **2.4.2 Electrostatic Levitation**

In surface micromachined structures, especially in finger sets that have a conductive substrate right under, the asymmetry in the 3-dimensional capacitive fringing fields cause a net out-of-plane force on the moveable finger sets. Capacitance between stator and ground planes is usually considered to be constant. But because of the suspended mass, the fringing fields between the stator, the substrate and the vibrating mass could change the capacitance in between. If these capacitances are extracted as a function of vertical displacement, it is observed that there is a maximum capacitance elevation which is called as the levitation. Adding the disturbances in the fringing fields caused by the vibration, the level of levitation is not even constant. The effect of levitation on the performance of the overall sensor is high cross coupling resulting in unpredictable output bias.

To solve this problem, the structure of the sensor should be revised. First, if possible, the substrate should be an insulating material. Depending on the process, removing all the substrate material under the moveable parts is a better solution. Maintaining electrostatic-wise symmetric finger sets with physically symmetric structure are the only solutions to the electrostatic comb levitation problem.

## **2.4.3 Acceleration Terms Other Than Coriolis**

As stated before, vibratory gyroscopes are Coriolis accelerometers. Their structures are based on measuring the harmonic displacements caused by the induced Coriolis acceleration. But their suspended structure is not only subject to Coriolis acceleration but also static and angular acceleration induced linear acceleration together with the centripetal ones. In this subsection, the effects of these acceleration terms are presented

### 2.4.3.1 Static and Fluctuating Accelerations

One of the most important and most frequent problems in MEMS gyroscopes is the static acceleration sensitivity. The reason of this problem lies in the application areas of these sensors together with their working principles.

Vibratory MEMS gyroscopes must have a stable operating point, i.e., the average gap spacing of the sense mode varying gap fingers should be constant for a linear and reliable input-rate output-voltage relation. The reason is that the amount of charge pumped to or sucked from the stationary sets highly depends on the gap spacing value of the sense fingers. If the gap spacing is small, the amount of charge increases because of the increased capacitance change.

Under a static acceleration, the sense mode vibration axis shifts, causing the sense finger gaps increase or decrease. If the gyroscope is a single mass one, this shift directly affects the output signal in two ways. Firstly, the output bias changes depending on the level of the component of the acceleration in the sense mode. The bias value increases or decreases if single ended reading is utilized. Secondly, since the DC operating point of the gyroscope is changed, the scale factor changes, which disturbs the linearity.

Fluctuating accelerations or shortly the “external vibrations” have a worse effect on the sensor output. Not only the magnitude but also the frequency of the vibration affects the output error. If this frequency come close to the drive or sense mode resonance, the sensor may become unusable because of the saturated electronic gain stages.

Figure 2.7 shows the effect of DC acceleration on the proof mass of the gyroscope. As can be noticed, the drive mode is also affected. But its negligible if the sense mode is considered because in the sense mode the induced displacement amount is in the order of nanometers and can easily be dominated by an external acceleration.

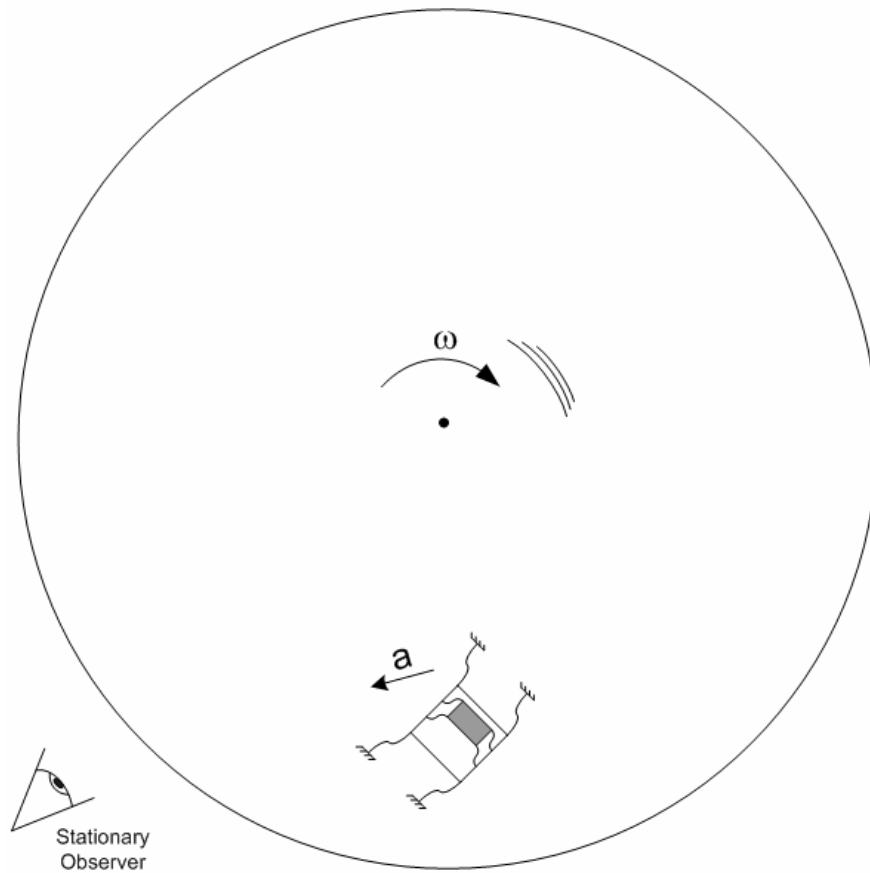


Figure 2.7: The effect of DC acceleration on the proof mass of the gyroscope.

Differential reading schemes suppress this error to a limited extent. In differential reading, the bias response is always positive because of the quadratic character of the sense fingers, i.e., the bias always increase regardless of the direction of the acceleration. Same situation is valid for the scale factor also. Scale factor tends to increase with increasing acceleration magnitude, again regardless of the direction.

The best solution is utilization of even number of masses which work in a determined way. This type of gyroscopes are called “tuning fork”. The basic principle is taking the difference of the sense mode signals of the proof masses working exactly out-of-phase. Thus, effects of all external accelerations are suppressed while the rate signals are amplified. Throughout this thesis, in the design step, two different tuning fork gyroscopes are realized.

### 2.4.3.2 Rotation Induced Accelerations

There are two special acceleration terms that are mentioned in Equation 2.22; the centripetal acceleration and the angular acceleration induced tangential acceleration. These acceleration terms are, just like the Coriolis acceleration, induced by an angular velocity or an angular acceleration. Figure 2.8 shows the illustration of the effect of centripetal acceleration on the sense mode.

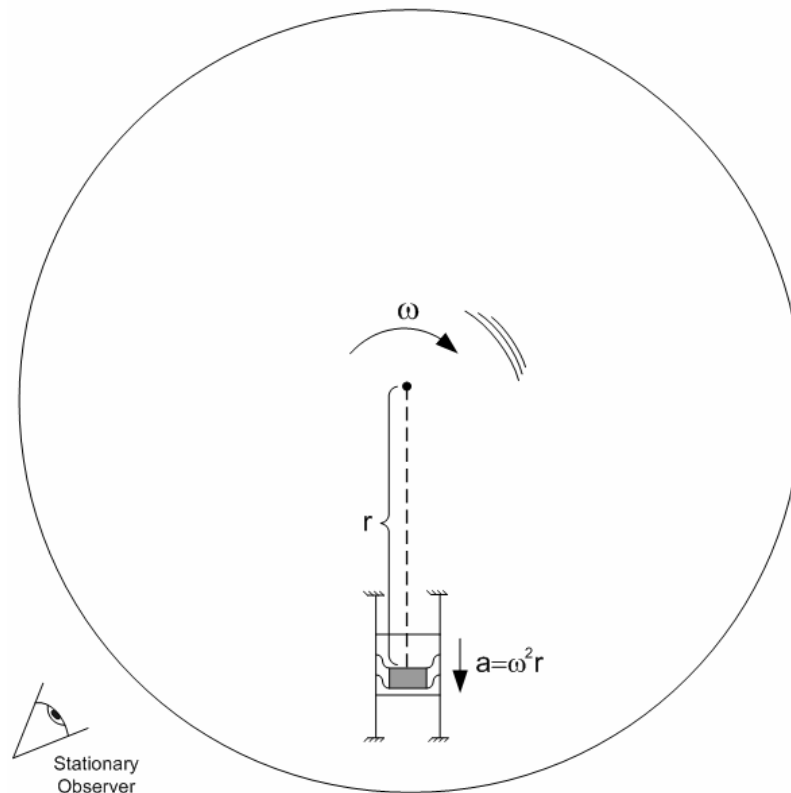


Figure 2.8: Illustration of the effect of centripetal acceleration on the sense axis. This acceleration term is proportional to the location radius and the input rate squared.

In real operation, inertial micromachined gyroscopes are subject to this acceleration at most. Since the radius and the angular velocity may be varying in time, the effect of this term is very random but rate dependent. Thus, the output of the gyroscope will be affected randomly in magnitude. But since the direction of acceleration is always radial and outward, its effect on the rate output and on the scale factor is monotonic.

Another acceleration term induced by the rotational motion is the tangential acceleration which is the result of a rotational acceleration. Figure 2.9 shows the illustration of the rotational acceleration induced tangential acceleration. This term is also proportional to the rotation radius, thus, cannot be predetermined and should be considered as an error source. Additionally, the direction of acceleration is also important because its effect on the output will be different like in the static acceleration case.

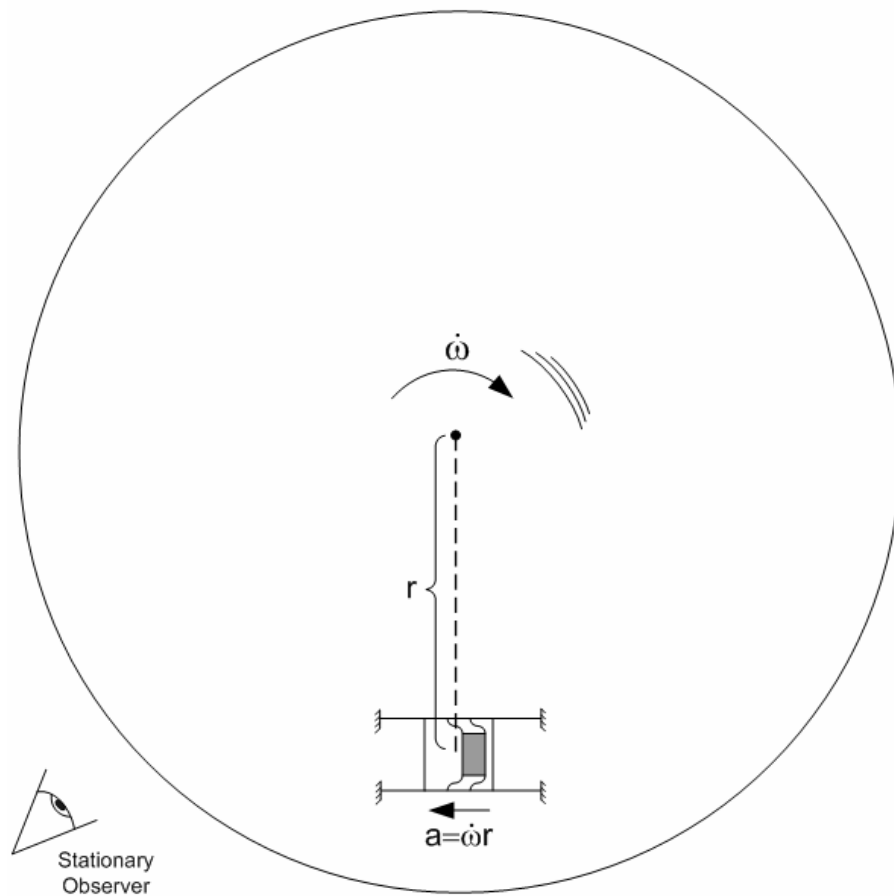


Figure 2.9: Illustration of the rotational acceleration induced tangential acceleration.

Although these acceleration terms are rotation induced, their character is same as the afore-mentioned static and fluctuating accelerations, and can be suppressed with same tuning fork structures together with differential reading.

#### 2.4.4 Undercut During Etching

Flexion elements are, as stated before, one of the most critical structures in the vibratory micromachined gyroscopes. Since part assembly is not possible in MEMS fabrication technologies, the structures are processed with minimum parts. Almost all MEMS gyroscopes are fabricated as a single piece of moving structure. During this fabrication, some process variations and tolerances are present which are specific to the steps in the fabrication. Throughout this fabrication sequence, the undercut amount is the main erroneous phenomenon deciding the precision of the dimensions. Depending on the type of etching or forming, the shape and distribution of the undercut varies. Especially in Deep Reactive Ion Etching (DRIE), the undercut has a tapered shape. This shape is not very important for the proof mass or the finger jigs, but very vital for the finger sets and especially for the flexion elements.

The tapered shape of the drive and sense fingers usually cause an unbalanced electrostatic forcing. The charge distribution over the finger edges highly dependent on the gaps between the edges of the neighboring fingers. The tapered structure causes the charges accumulate on the wider edge, causing a larger force on the upper side. Hence, the driving and sensing fingers inherently creates force imbalance, lightly tilting the overall structure from one side to another during drive mode vibration.

Figure 2.10 shows the force distribution on the surface of a tapered beam with finite deflection amount. The cumulative net reaction force is not at the center of the beam but shifted up depending on the taper angle.

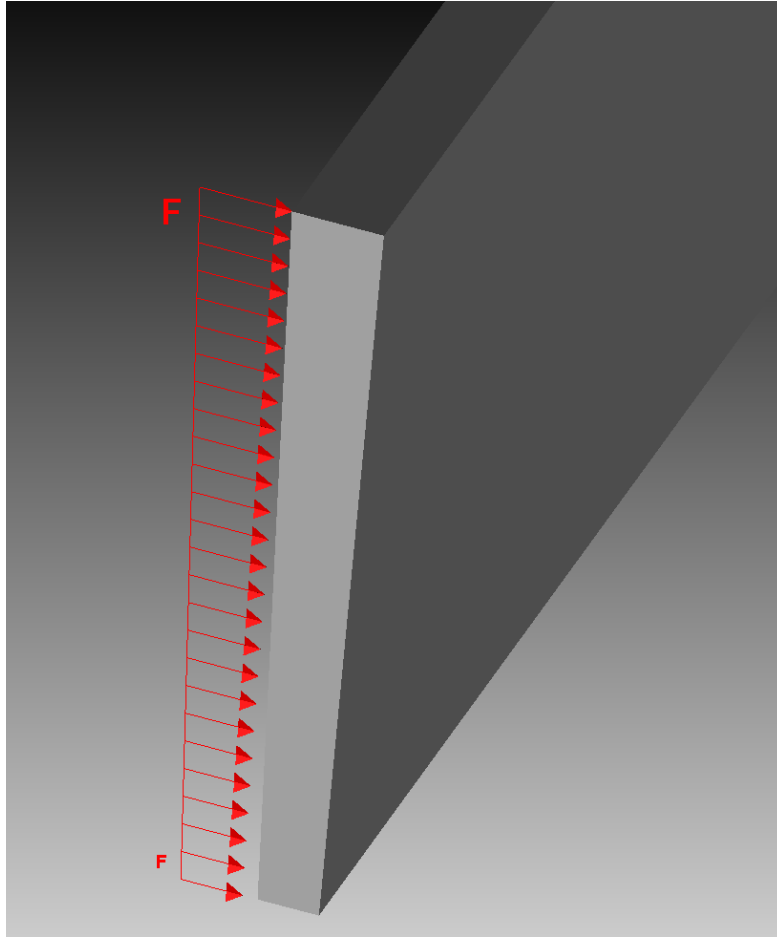


Figure 2.10: The force distribution on the surface of a tapered beam with finite deflection amount.

Another drawback of this tapered cross-section is the uneven stress distribution over the spring elements. Since the thickness of the beam element is decreasing down, the stress amount on the edges also decreases, causing a net spring force which is applied not exactly along the center of gravity of the proof-mass but along an upper plane. Thus, the proof-mass starts yawing or tilting when the resonance is achieved. Hence the output noise increases and run-to-run output bias becomes unstable.

To overcome this problem, the process should be well optimized and some trial structures should be tested. In this thesis, a readily optimized commercial silicon-on-insulator (SOI) process is utilized for minimized process nonuniformities.

## 2.4.5 Operation Temperature

Another important external parameter is the temperature of the overall structure. Temperature has many different effects on the sensor package, mechanical structure and the readout electronics. The temperature dependency of the readout electronics composed of integrated circuits is a more frequent issue that has several ways of control. In micromachined gyroscopes, especially the mechanical structure and the package are affected by the ambient temperature changes and this creates vital problems if the sensor is not designed considering an operational temperature band.

Temperature has two main effects on the overall sensor. One of them is the thermal expansion, which affect the sensitivity of the sensor because of varying finger spacing. Expansion also changes the resonant frequency of the structure by changing the dimensions of the flexion elements. As a result, the sensitivity and the operation point of the gyroscope changes. The other effect of the temperature change is the change of the electrical resistance of the structural material. Especially for the doped silicon, this effect is more evident.

Thermal material compatibility is another concern when the thermal effects are considered. In the process, the substrate, structural material and other materials used should have close thermal expansion coefficients in order to avoid high internal stresses and buckling of flexion elements. In particular, the substrate and the structure material should be similar materials, like in the SOI technology or in the Silicon-On-Glass (SOG) process. Additionally, the bonding materials like the epoxy patch should be used carefully. If possible, one-point affixing should be utilized.

Temperature is one of the primary concerns during the micromachined gyroscope design. Necessary precautions should be taken to avoid the effects of temperature during and after the design and fabrication stages. The characterization of the sensors should also include precise control of temperature for reliability. The calibration of the gyroscopes should also include temperature dependency of sensor output for an improved performance

## ***2.5 Summary***

This chapter presents the basic theory of the vibratory MEMS gyroscopes. In this chapter, the vibration kinematics of the drive and sense mode resonators is investigated in detail. Additionally, the electrostatic transduction in the drive mode is also presented. Moreover, the electrostatic spring effect in the varying gap type finger sets and the capacitance dependency of these sets to small displacements are also derived. The mechanical spring structures are also presented in detail with two different approaches. The cross axis spring constants of these springs are derived and concluded that the single sided folded springs are the best fit for a decoupled micromachined gyroscope. Moreover, the error sources in micromachined gyroscopes are also presented. Especially, the effects of external accelerations, process nonuniformities, and temperature effects are examined with possible solutions proposals.

## **CHAPTER 3**

### **DESIGN AND FABRICATION OF THE PROPOSED GYROSCOPES**

In this chapter, the design details of the fabricated gyroscopes including the mode shapes and their resonance frequencies, stress analysis under the impact shocks of several thousands of g, the design details of the novel coupling mechanism and the architect model of the structures together with the fabrication steps are presented. Section 3.1 presents the placement strategy of flexion elements used in the SMG, DMG and QMG. Section 3.2 introduces the design calculations of the novel coupling mechanism used in DMG and QMG. In Section 3.4 the modal and stress analysis of the gyroscopes are presented. In this section, the shock performance and vibration mode frequencies are given in detail. In section 3.5, the system model of the gyroscopes developed using the CoventorWare ARCHITECT are presented. Section 3.6 presents the SOI-MEMS fabrication technology of MEMSCAP<sup>®</sup> Inc. Finally, Section 3.7 gives a brief summary of the chapter.

#### ***3.1 Flexion Elements of the Proposed Gyroscopes***

As stated in Chapter 2, all the linear flexion elements in the designed gyroscopes are the single sided type folded springs. These springs are used for all the suspension purposes and for the drive-to-sense interactions. Figure 3.1 shows the single sided folded springs used in the single and double mass gyroscopes. Since these folded springs can only be connected from one end, the area of the outer and inner frames

needed to be optimized for minimal spring spacing. For this, the circumferences of the springs are etched forming a 50  $\mu\text{m}$  gap for proper operation.

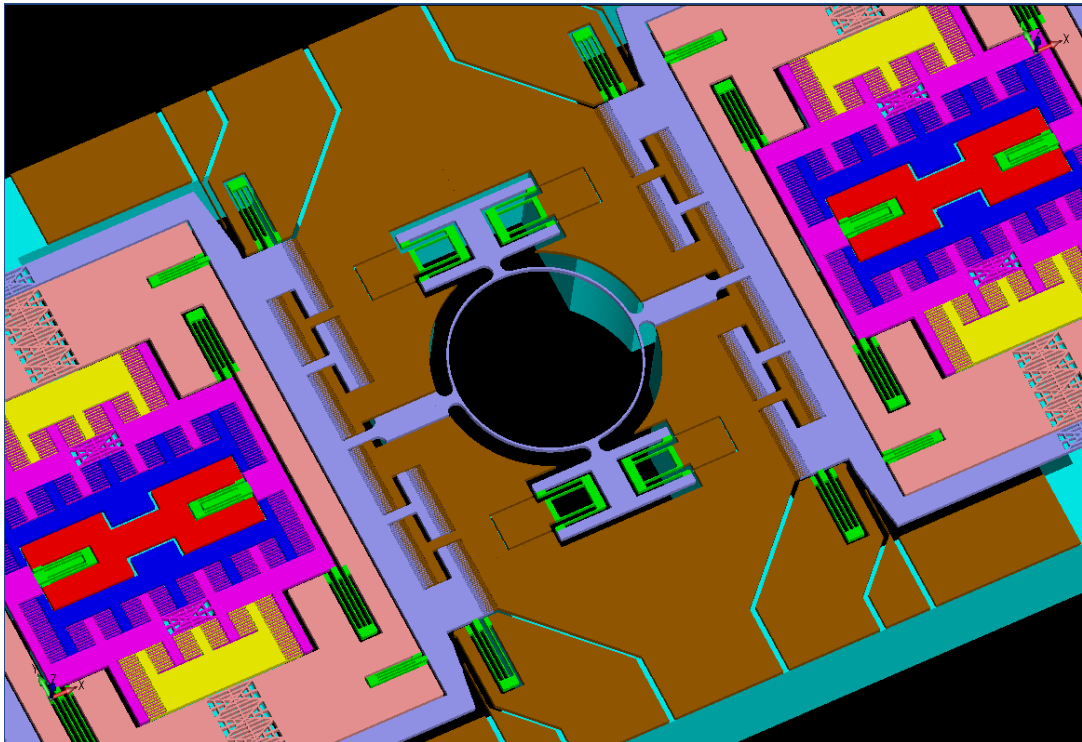


Figure 3.1: The single sided folded springs (green structures) used in the single and double mass gyroscopes.

Additionally, the anchored and cross-connected drive jigs, proof mass and the sense jigs are supported with these springs connected to all four corners for improved decoupling together with suppressed second order effects like frequency doubling and rotational modes.

Figure 3.2 shows the spring locations on the quadruple mass gyroscopes, which are the same type used in the single and double mass gyroscopes. In the quadruple mass gyroscope, the size and the shape of the outer drive jig requires a modification of anchor spring locations. For the balanced drive mode at the lowest modal frequency, these anchor springs are connected to the middle of the drive jigs and to both of the ends of the varying overlapping-area type driving finger sets.

Moreover, all the spring structures are optimized to have the other resonance modes away from the operational mode. In spite of the constant structural thickness which is decided by the fabrication process, the operational modes of all gyroscopes are tuned by fine positioning of the springs and detailed spring constant trials using FEM tools.

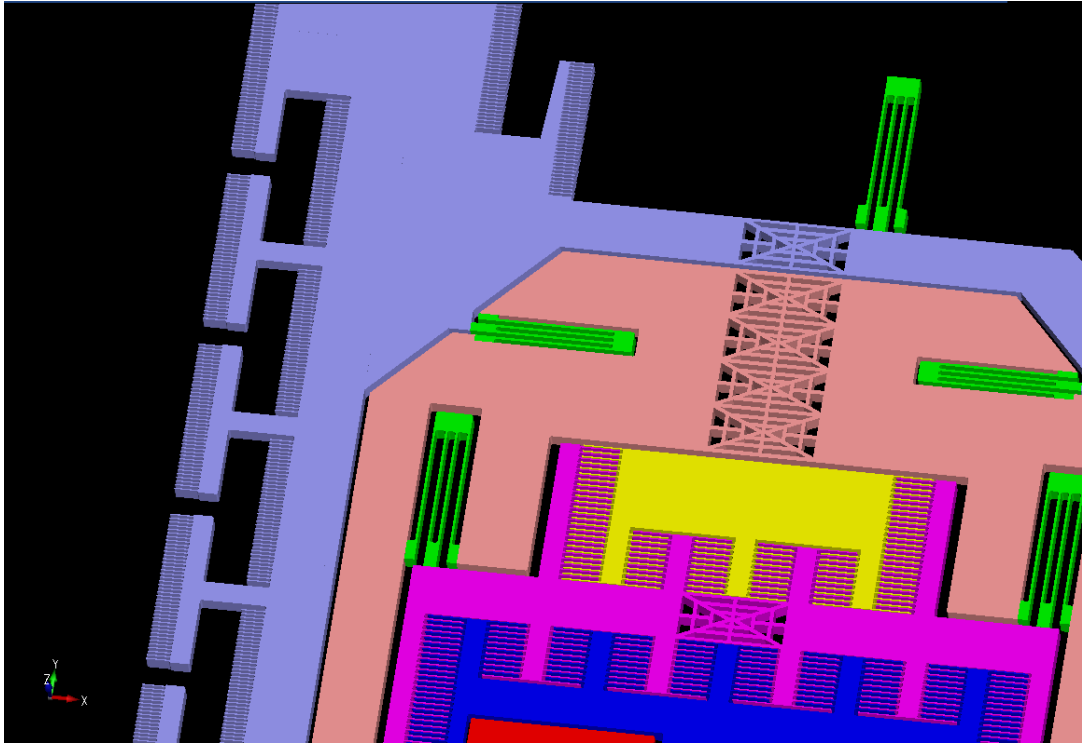


Figure 3.2: Same spring type used in the quadruple mass gyroscopes.

### ***3.2 The Coupling Mechanism***

One of the key factors in multi-mass gyroscopes is the coupling mechanism which synchronizes the individual proof masses. In the scope of this research, a novel ring shaped coupling mechanism is proposed. The main idea of this mechanism is that the thin film ring shaped structures have the ability of inducing orthogonal forces when there is an input forcing. Figure 3.3 shows the deformed and undeformed ring spring together with the position dependent force-moment relations.

For the spring constant estimation of the ring shaped structures, Castigliano's theorem is utilized. This theorem states that the partial derivative of strain energy gives the force or moment in the predetermined direction.

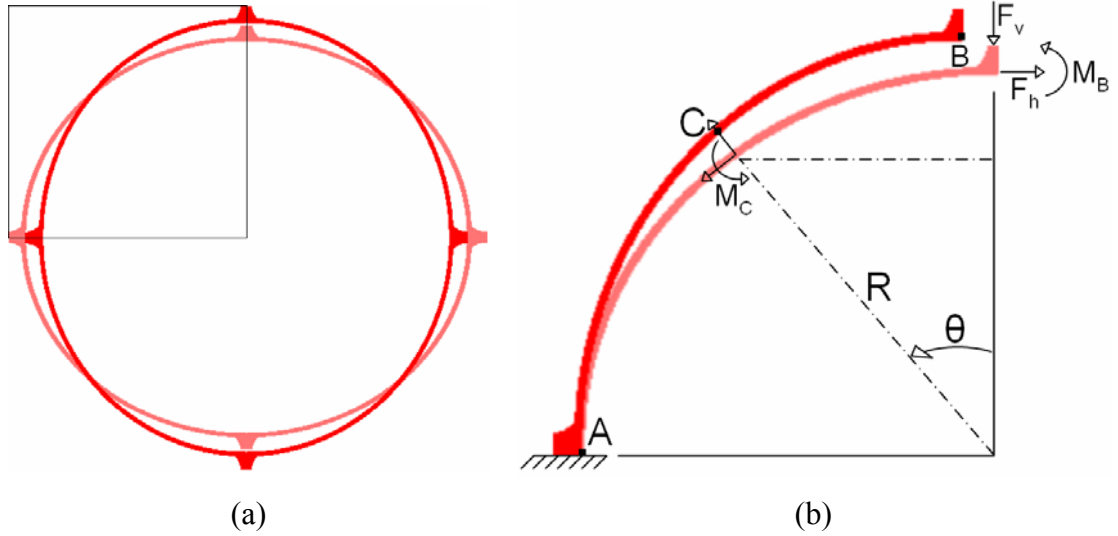


Figure 3.3: (a) The deformed and undeformed ring spring and (b) the angle dependent force-moment relations.

For thin curved beams, the strain energy of tensile and shear forces are negligible when bending is considered. So, the bending energy is considered as the only spring energy present. The moment equilibrium for the BC arc is,

$$\sum M_{BC} = M_C + M_B - F_v \cdot R \cdot \sin\theta - F_h \cdot R \cdot (1 - \cos\theta) = 0 \quad (3.1)$$

thus,

$$M_C = F_v \cdot R \cdot \sin\theta + F_h \cdot R \cdot (1 - \cos\theta) - M_B \quad (3.2)$$

The partial derivatives of  $M_C$  are then,

$$\frac{\partial M_C}{\partial F_v} = R \cdot \sin\theta \quad (3.3a)$$

$$\frac{\partial M_C}{\partial F_h} = R(1 - \cos\theta) \quad (3.3b)$$

$$\frac{\partial M_C}{\partial M_B} = -1 \quad (3.3c)$$

Evaluating the moment integral over the given range in order to find the deflection amount induced by the corresponding excitation;

The vertical force,

$$\delta_v = \frac{1}{E.I} \int_0^L M \cdot \frac{dM}{dF_v} \cdot ds = \frac{1}{E.I} \int_0^{\pi/2} (F_v \cdot R \cdot \sin \theta + F_h \cdot R \cdot (1 - \cos \theta) - M_B) \cdot (R \cdot \sin \theta) \cdot R \cdot d\theta \quad (3.4a)$$

$$\delta_v = \frac{R^2}{E.I} \left( \frac{\pi \cdot F_v R}{4} + \frac{F_h R}{2} - M_B \right) \quad (3.4b)$$

The horizontal force,

$$\delta_h = \frac{1}{E.I} \int_0^L M \cdot \frac{dM}{dF_h} \cdot ds = \frac{1}{E.I} \int_0^{\pi/2} (F_v \cdot R \cdot \sin \theta + F_h \cdot R \cdot (1 - \cos \theta) - M_B) \cdot R \cdot (1 - \cos \theta) \cdot R \cdot d\theta \quad (3.5a)$$

$$\delta_h = \frac{R^2}{E.I} \left( \frac{F_v R}{2} + \left( \frac{3 \cdot \pi}{4} - 2 \right) \cdot F_h R + \left( 1 - \frac{\pi}{2} \right) M_B \right) \quad (3.5b)$$

And the end point moment,

$$\theta_{M_B} = \frac{1}{E.I} \int_0^L M \cdot \frac{dM}{dM_B} \cdot ds = \frac{1}{E.I} \int_0^{\pi/2} (F_v \cdot R \cdot \sin \theta + F_h \cdot R \cdot (1 - \cos \theta) - M_B) \cdot (-1) \cdot R \cdot d\theta \quad (3.6a)$$

$$\theta_{M_B} = \frac{R}{E.I} \left( \frac{\pi}{2} M_B - F_v R + \left( 1 - \frac{\pi}{2} \right) F_h R \right) \quad (3.6b)$$

One should note that the symmetry of the ring results in “0” rotation at point B. So,  $\theta_{M_B} = 0$ . Substituting this in Equations 3.4b, 3.5b and 3.6b,

$$M_B = \frac{2.F_v.R}{\pi} \quad (3.7)$$

$$\delta_v = \left( \frac{\pi}{4} - \frac{2}{\pi} \right) \frac{F_v.R^3}{E.I} \quad (3.8)$$

$$\delta_h = \left( \frac{2}{\pi} - \frac{1}{2} \right) \frac{F_v.R^3}{E.I} \quad (3.9)$$

In the derivations, the quadrant is assumed to be exposed to the half of the loading, i.e.,

$$F_v = \frac{F}{2} \quad (3.9)$$

So, total diameter changes in vertical and horizontal directions are,

$$2.\delta_v = \left( \frac{\pi}{2} - \frac{4}{\pi} \right) \frac{F_v.R^3}{E.I} \quad (3.10)$$

$$2.\delta_h = \left( \frac{4}{\pi} - 1 \right) \frac{F_v.R^3}{E.I} \quad (3.11)$$

As can be noted, the deflection amounts are not same. There is 9% difference between the vertical and horizontal deflections. The difference is not very crucial for the operation of the tuning fork, but can be minimized by distorting the circular structure of the ring into an elliptical one.

The induced stress amount is another concern for the ring design. The maximum stress induced on the ring is,

$$\sigma_{Max} = \frac{M_{Max} \cdot c_{Max}}{I} \quad (3.12)$$

Substituting Equation 3.7 in 3.2,

$$M_C = F_v \cdot R \cdot \left( \sin\theta - \frac{2}{\pi} \right) \quad (3.13)$$

For  $\theta=0$ ,

$$M_C = -\frac{2 \cdot F_v \cdot R}{\pi} = M_B = M_{Max} \quad (3.14)$$

The cross-section of the ring is plain rectangle with a structural thickness of “t” and ring width “w”. The maximum stress is induced at the edge of the ring where,

$$c = \frac{w}{2} \quad (3.15)$$

The moment of inertia of this rectangle is,

$$I = \frac{t \cdot w^3}{12} \quad (3.16)$$

Substituting Equations 3.14, 3.15 and 3.16 in 3.12,

$$\sigma_{Max} = \frac{12 \cdot F_v \cdot R}{\pi \cdot b \cdot d^2} \quad (3.17)$$

This is the maximum stress induced on the rings, concentrated at the inner and outer surfaces of the quadrant end points.

For the fully symmetric loading which is the case of the quadruple mass gyroscope, the spring constant of the thin film becomes direction independent. Using similar

derivation techniques, the spring constant of the symmetrically loaded ring spring is found to be,

$$\delta = \frac{\pi - 2}{4} \frac{F_v \cdot R^3}{E \cdot I} \quad (3.18)$$

The maximum stress induced on the structure is close but less than that of the DMG,

$$\sigma_{Max} < \frac{12 \cdot F_v \cdot R}{\pi \cdot b \cdot d^2} \quad (3.19)$$

Although the force-deflection formulas are accurate for the resonance frequency estimation, the linearity of these springs are highly dependent on the thickness because of the thin film assumption. Thus, the FEM analyses of the overall gyroscopes are also held.

### ***3.3 Brownian Noise Estimation***

Inertial micromachined sensors, including the gyroscopes, operate with a basic principle of measuring displacements which are generated by external forces or moments. These displacements may be very small, i.e. smaller than the diameter of a silicon atom. Even though very high performance and low noise capacitive or magnetic sensing schemes are developed, there is a sensitivity limit for these sensors for temperatures higher than 0 Kelvin. Reason is the nature of the substances used which are composed of continuously vibrating atoms, if it is not at absolute temperature [36]. Brownian noise is the cumulative effect of this unpredictable vibration of the structure and the ambient gas molecules or atoms.

For the micromachined sensors, there are two main Brownian noise sources; the structural material and the surrounding air or gas. These two terms have both damping effects on the system, which is an important parameter for the Brownian noise. The spectral density of such dampers are given by [27],

$$F_n = \sqrt{4 \cdot k \cdot T \cdot b_s} \quad (3.20)$$

where  $k$  is the Boltzmann constant ( $1.38 \times 10^{-23}$  J/K),  $T$  is the temperature of the medium, and  $b_s$  is the damping coefficient effecting the body. The force term in Equation 3.20 has a unit of N/ $\sqrt{\text{Hz}}$ , meaning that the Brownian noise is dependent on the frequency band of interest. Thus, for vibratory MEMS gyroscopes, the rate equivalent Brownian noise at its operational frequency is estimated as,

$$\Omega \approx \sqrt{\frac{k \cdot T}{Q_s \cdot \omega_{Res} \cdot m_s \cdot X_D^2 \cdot (0.01745) \cdot A_g^2}} \quad (3.21)$$

in (deg/sec)/ $\sqrt{\text{Hz}}$ , where  $Q_s$  is the sense mode quality factor,  $\omega_{Res}$  is the drive mode resonance frequency,  $m_s$  is the sense mode effective mass,  $X_D$  is the drive mode vibration amplitude, and  $A_g$  is the angular gain (m<sub>PM</sub>/M<sub>S</sub>). Equation 3.21 states that increasing the quality factor, driving amplitude, frequency of operation, or the angular gain decreases the Brownian noise.

Since this noise is independent of the electronic noise of the readout electronics, estimation of it give the theoretical performance limit for the proposed gyroscopes. Table 3.1 gives the estimated rate equivalent Brownian noise of the SMG, DMG and QMG together with the assumed operational conditions.

Table 3.1: Estimated rate equivalent Brownian noise of the SMG, DMG and QMG

	T	Q	w (Rad/sec)	X (m)	Ag	BN ((Deg/hr)/ $\sqrt{\text{Hz}}$ )
<b>SMG</b>	298	10	10719.11413	1.00E-05	0.75	11.9
<b>DMG</b>	298	5	15880.75086	1.00E-05	0.75	9.7
<b>QMG</b>	298	2	14985.39696	1.00E-05	0.72	12.4

The estimation above assumes operation at atmospheric pressure with a drive mode vibration of 10  $\mu\text{m}$ . At lower pressures, it is evident that the thermo-mechanical Brownian noise will be lower. For the drive mode resonators of the designed gyroscopes, the Quality factor is estimated to be increased by more than two orders of magnitude, decreasing the Brownian noise below 1((Deg/hr)/ $\sqrt{\text{Hz}}$ ). However, the

electronic noise of the external electronics is much higher than the Brownian noise of these structures at atmospheric ambient.

### ***3.4 FEM Modal and Misses-Stress Analysis***

The finite element models of the designed gyroscopes are built using the 3-D design program KeyCreator. The built models are then simulated in the CoventorWare environment. Using the modeler and the simulator, all the low frequency mode shapes are modified and tuned iteratively for a stable operation. Table 3.2 show the final frequency list of the resonant mode shapes of the single mass gyroscope. As stated, the lowest frequency mode is the operational drive mode.

Table 3.2: The frequencies of the resonant mode shapes of the single mass gyroscope.

Mode #	Frequency (Hz)	Generalized Mass (Kg)	Damping
1	3412.39624	2.72E-07	0
2	6380.686035	1.283E-07	0
3	6782.78418	2.06E-07	0
4	8492.87207	9.80E-08	0
5	9414.629883	7.57E-08	0
6	10154.73926	3.91E-08	0
7	13996.54395	4.37E-08	0
8	15874.55176	5.86E-08	0
9	17530.32227	1.92E-07	0
10	17892.17383	7.98E-08	0

Figure 3.4 shows the drive mode shape snapshot of the double mass gyroscope. The symmetry in the anchored springs of the ring mechanism and the even deflection fields prove the proper coupling of the single mass structures.

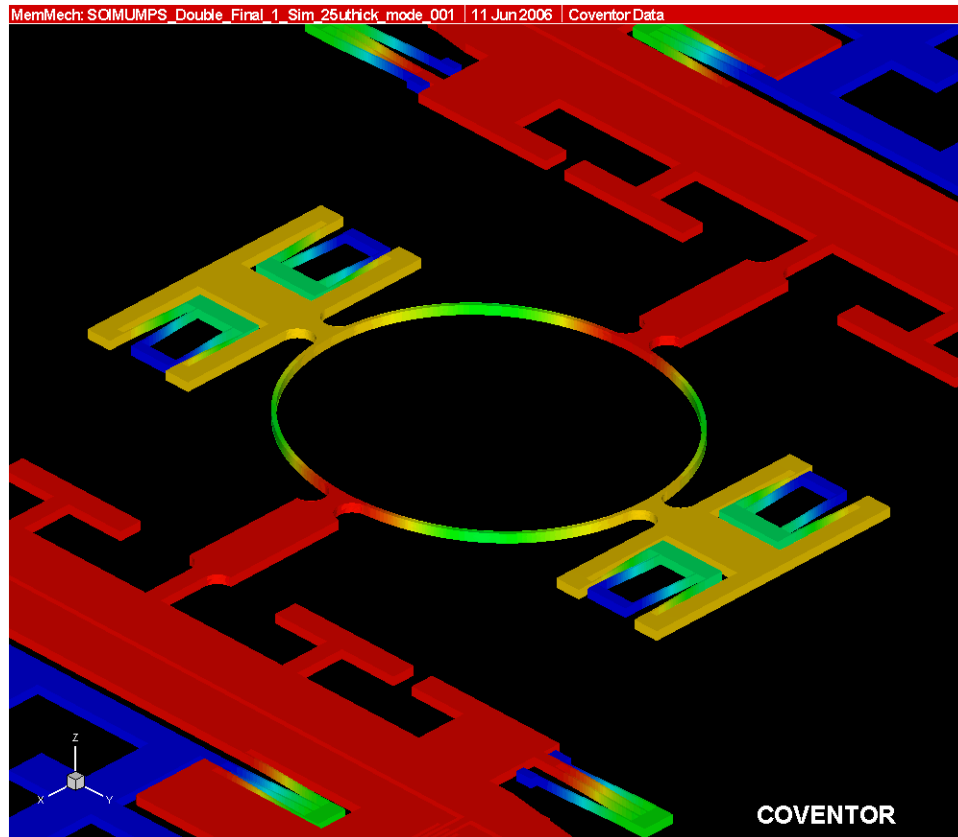


Figure 3.4: The drive mode shape snapshot of the double mass gyroscope.

Table 3.3 shows the frequencies of the resonant mode shapes of the double mass gyroscope. In spite of the increased area, the out-of-plane mode are suppressed leaving the first mode to the operational drive mode.

Table 3.3: The frequencies of the resonant mode shapes of the double mass gyroscope.

Mode #	Frequency (Hz)	Generalized Mass (Kg)	Damping
1	5055.274414	5.560E-07	0
2	6476.939453	1.683E-07	0
3	6477.623535	1.685E-07	0
4	6884.001953	2.071E-07	0
5	6888.526367	2.071E-07	0
6	7989.031738	5.403E-07	0
7	8607.475586	1.341E-07	0
8	8611.37207	1.339E-07	0
9	9601.262695	8.044E-08	0
10	9618.634766	7.548E-08	0

The modal analysis of the quadruple mass gyroscope requires some trial sub-analysis to arrange the frequencies of the out-of-plane and sense modes. Figure 3.5 shows the top view of the drive mode snapshot of the quadruple mass gyroscope.

The folded springs connecting the proof mass to the drive jigs and the color legend indicating the amount of deflections reveal that the drive mode vibration is well guided by the ring mechanism.

The mode shapes of the quadruple mass gyroscope are quite different than each other and their frequencies are closer compared to the double and single mass gyroscopes. The reason is that the number of DOF's are increased with increasing dimensions. Since the structural thickness, which is  $25\ \mu\text{m}$ , is constant, the rigid assumption of the frames and thick beams are degenerated. The reason of the trial frequency adjustments using the simulator is to separate the frequencies for lower coupling and higher reliability.

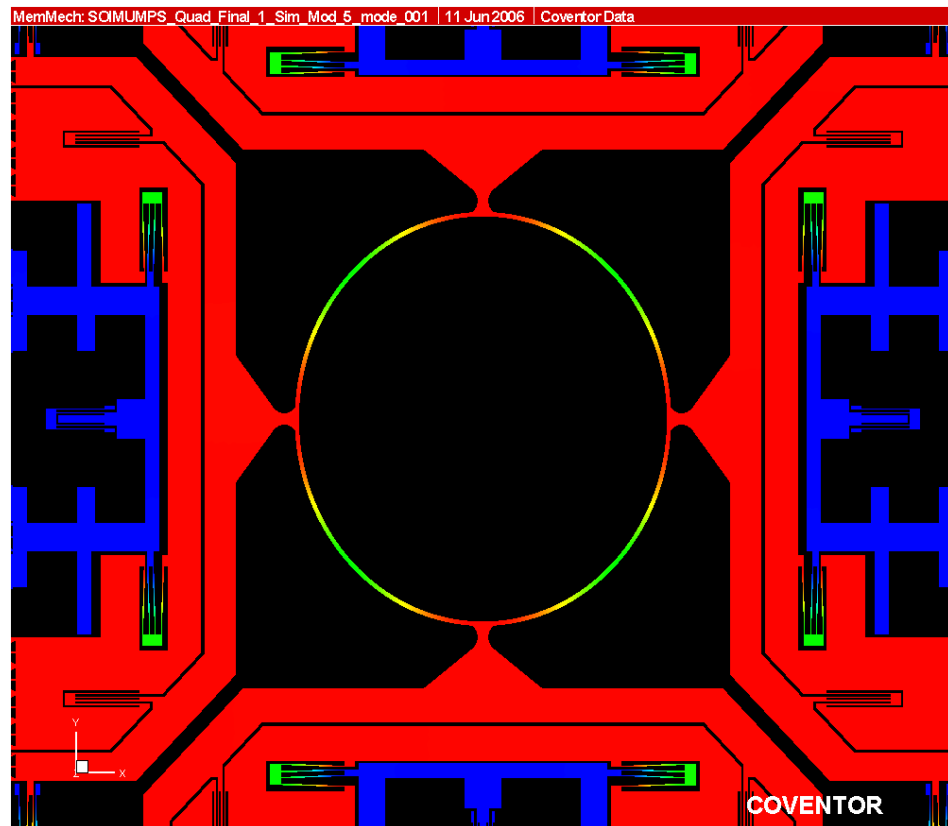


Figure 3.5: The top view of the drive mode snapshot of the quadruple mass gyroscope.

Table 3.4 shows the frequencies of the resonant mode shapes of the quadruple mass gyroscope. The motion in the mode shapes of the first mode, which is the operational drive mode, and the sixth mode are very similar except the phases. Thus, their frequencies are intentionally separated to be on the safe side.

Table 3.4: The frequencies of the resonant mode shapes of the quadruple mass gyroscope.

Mode #	Frequency (Hz)	Generalized Mass (Kg)	Damping
1	4769.50293	1.18E-06	0
2	5117.755371	1.113E-07	0
3	6025.078125	1.80E-07	0
4	6035.066406	1.80E-07	0
5	6039.998535	1.801E-07	0
6	6046.782227	1.80E-07	0
7	6972.088867	1.68E-07	0
8	6972.928711	1.69E-07	0
9	7108.267578	6.46E-07	0
10	7110.369629	6.481E-07	0

In general, the stress levels in low frequency resonators do not reach to the yielding values due to the soft spring structures and relatively high masses. But this may create some problems especially in vibrational and shock accelerations. For this, the gyroscopes are simulated for an acceleration input of 10000g.

Figure 3.6 shows the stress simulation result of the single mass gyroscope during an accelerative shock of 10000g. Although the input shock is quite high, the maximum stress values do not exceed 900MPa, which is far below the yield stress of the silicon of 1700MPa. In the figure, the stress concentrations are lumped on the folded springs, which allow high deformations. Actually, this elasticity relieves the structure and stress distribution throughout the gyroscope topology.

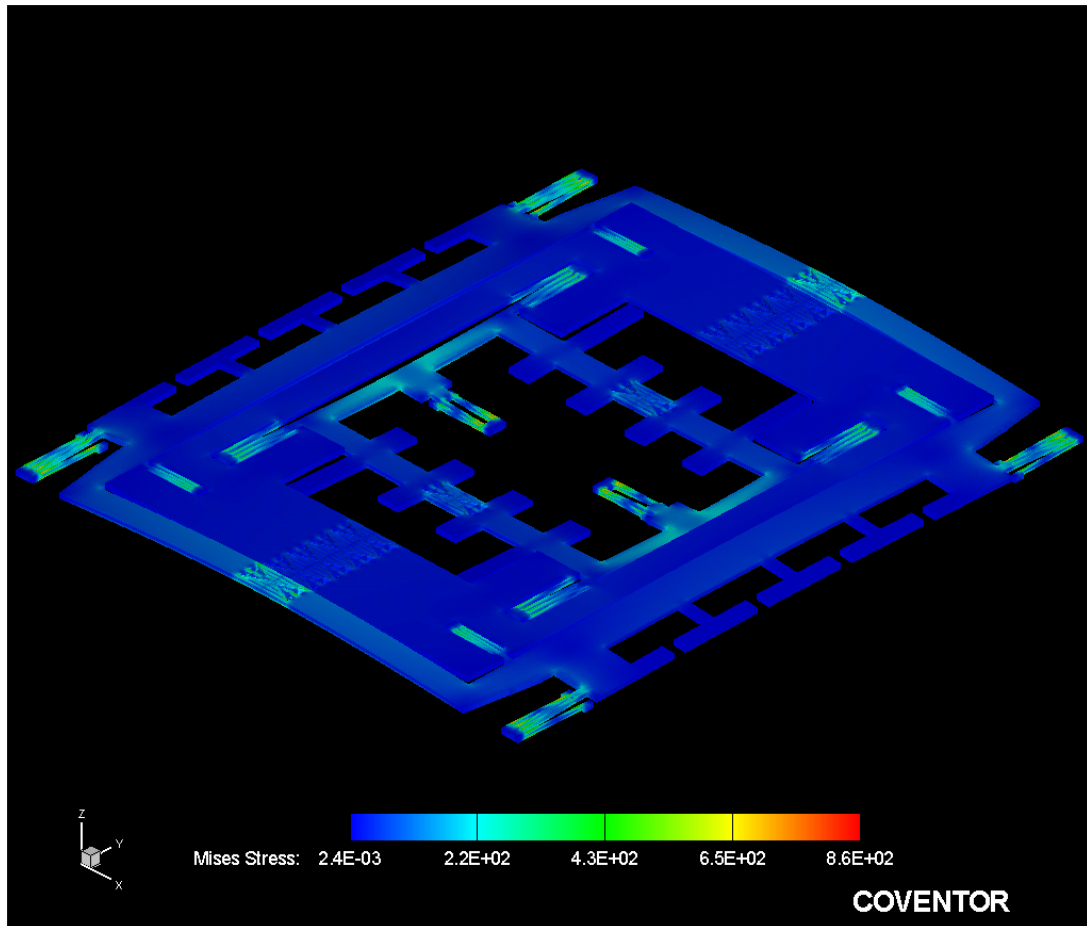


Figure 3.6: The stress simulation result of the single mass gyroscope an accelerative shock of 10000g.

In the double and quadruple mass gyroscopes, the induced stress amounts are much lower because of the increased anchorage springs. These gyroscopes are theoretically immune to accelerations of 20000g magnitude.

### ***3.5 ARCHITECT Models of Proposed Gyroscopes***

After the design stage, the system models of proposed gyroscopes are built in the ARCHITECT environment of CoventorWare software. Architect is a complete environment for the design, simulation and analysis of MEMS systems. The control on the environmental inputs and on the internal parameters of the MEMS structure makes this software tool very suitable for development of high performance micromachined gyroscopes.

Using the Architect, almost all of the gyroscope structures can be parametrically modeled and simulated. The co-simulation ability of the Architect with MATLAB widens the possibilities. In this research, the system modals of the single and double mass gyroscope are built in the Architect environment and the quadruple mass is left as a future study.

Figure 3.7 shows the final schematic of the SMG including all the structural components like the springs, anchors, proof mass, varying overlap area and varying gap type fingers and their electrical connections. This schematic is the main modal of the SMG. The box named “Reference Frame” is the model of the frame that the gyroscope is fixed. This modal has linear acceleration and rotational velocity inputs for all three axes, which are controlled during performance analysis.

In the model schematic of the SMG, the frame-in-frame topology can also be seen. There are three proof masses connected to the outer drive fingers, to the proof mass and to the inner sense fingers present in the upper half of the schematic. All three masses are connected to each other with the blue folded spring symbols. The electrical connections of the finger sets are arranged in the way that the bonding pads are identical to these connections.

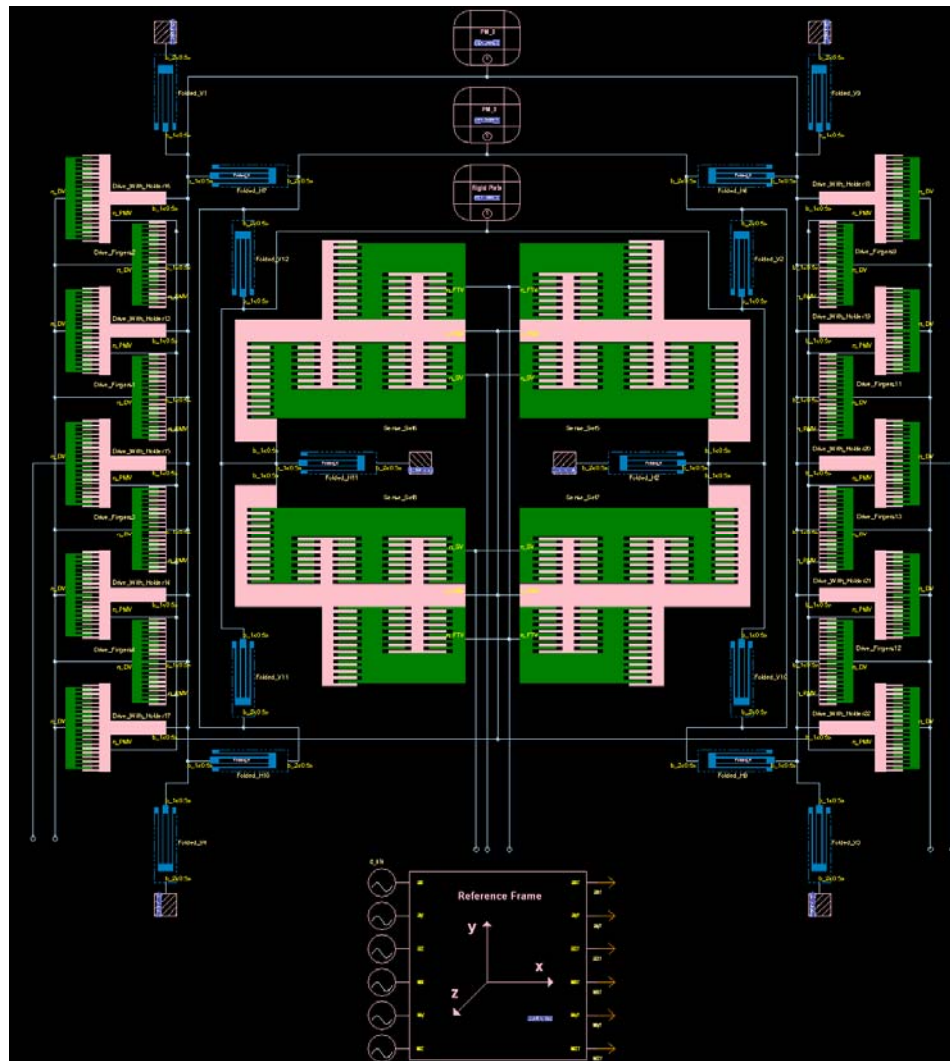


Figure 3.7: Final schematic of the SMG including all the structural components like the springs, anchors, proof mass, varying overlap are and varying gap type fingers and their electrical connections.

The advantages of hierarchical approach become more evident when the primitive model is considered. Figure 3.8 shows the detailed schematic of the SMG including all the basic elements taken from the Architect Libraries. Since the number of connections and individual coordinate and dimension requirements, the model become less efficient considering both simulation time and building time of the schematic. The hierarchical model also include this much detail in a more parametric and repetitive manner.

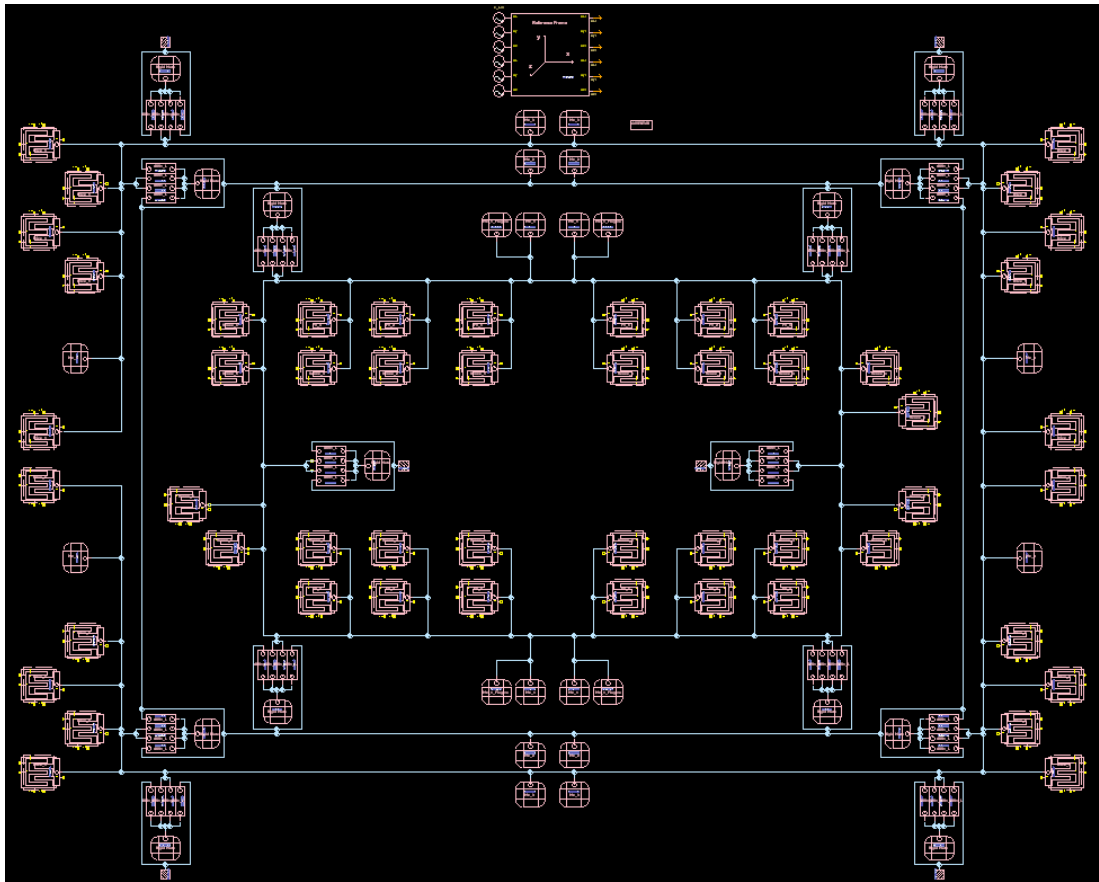


Figure 3.8: Detailed schematic of the SMG including all the basic elements taken from the Architect Libraries.

Figure 3.9 shows the schematic of the DMG, which includes two modified forms of the SMG schematic with the ring spring coupling mechanism in the middle. This schematic also includes the biasing of the sense finger sets and the driving source.

Since the Architect Library does not have a ring or arc shaped spring model, a new spring is added to the library with adequate curve fitting. The curved quarters of the ring spring are approximated using sixth order polynomials with a cumulative error less than 0.1%.

Additionally, there are displacement and angle probes placed to monitor the motion of individual masses. These help not only to see the amount of drive mode vibration amplitude and direction, but also to determine the amount of quadrature error induced because of the electrostatic force imbalances on the outermost frame



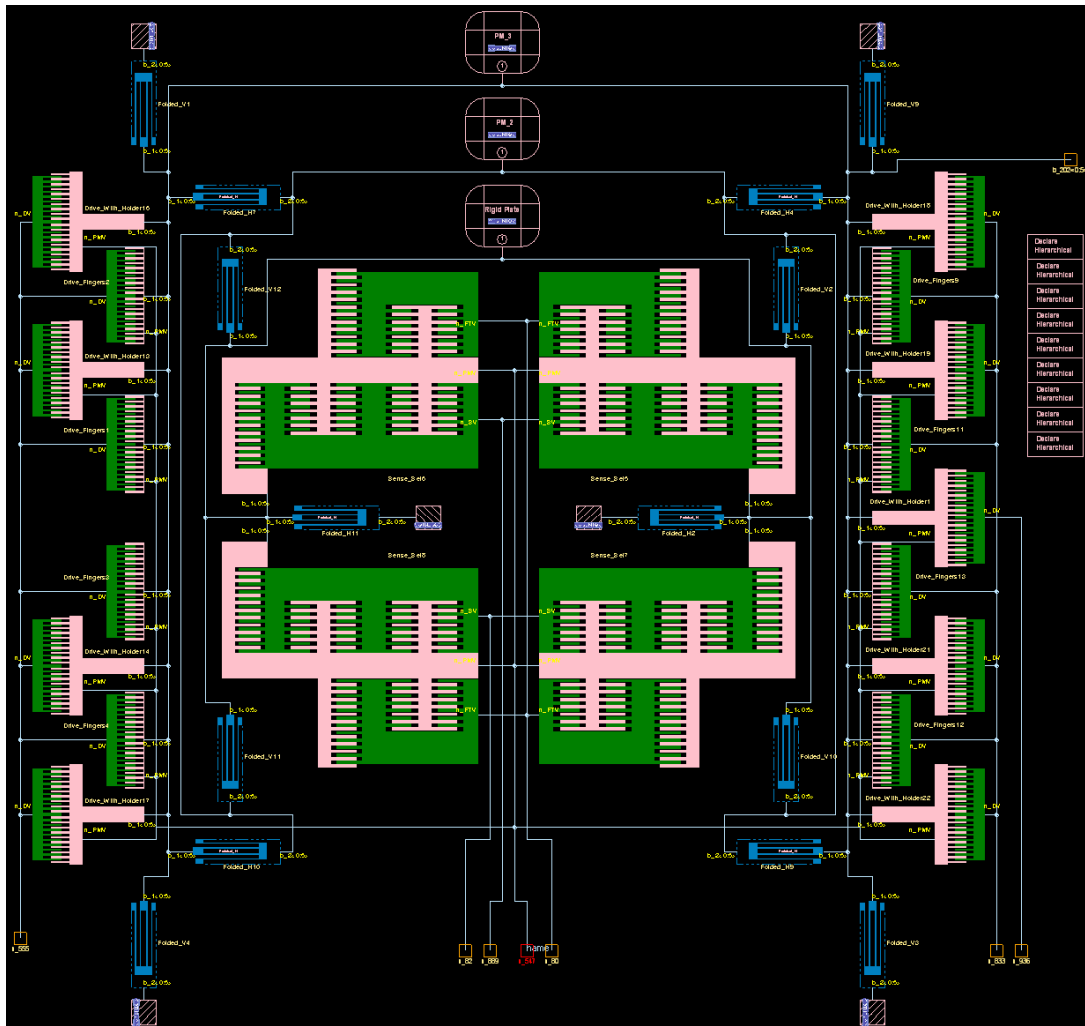


Figure 3.10: One of the hierarchical masses of the DMG.

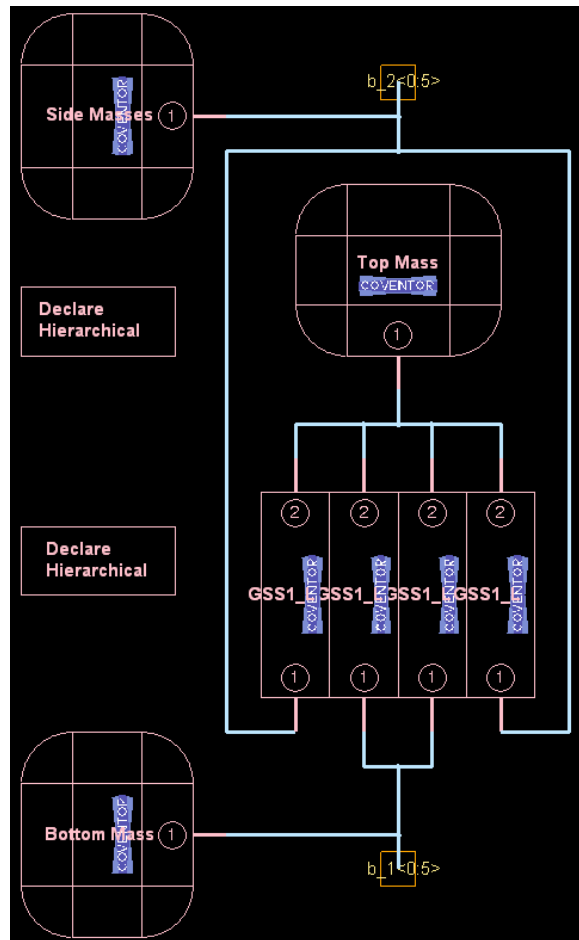


Figure 3.11: The folded spring subelement, which has the blue symbol in top level schematics.

Figure 3.12 shows the hierarchical schematic of the sense finger sets together with the holding jig, which is a rigid mass. In the schematics, the electrical and mechanical contacts have different connections. The mechanical parts are connected via six channel busses for the rotational and translational data in three axes.

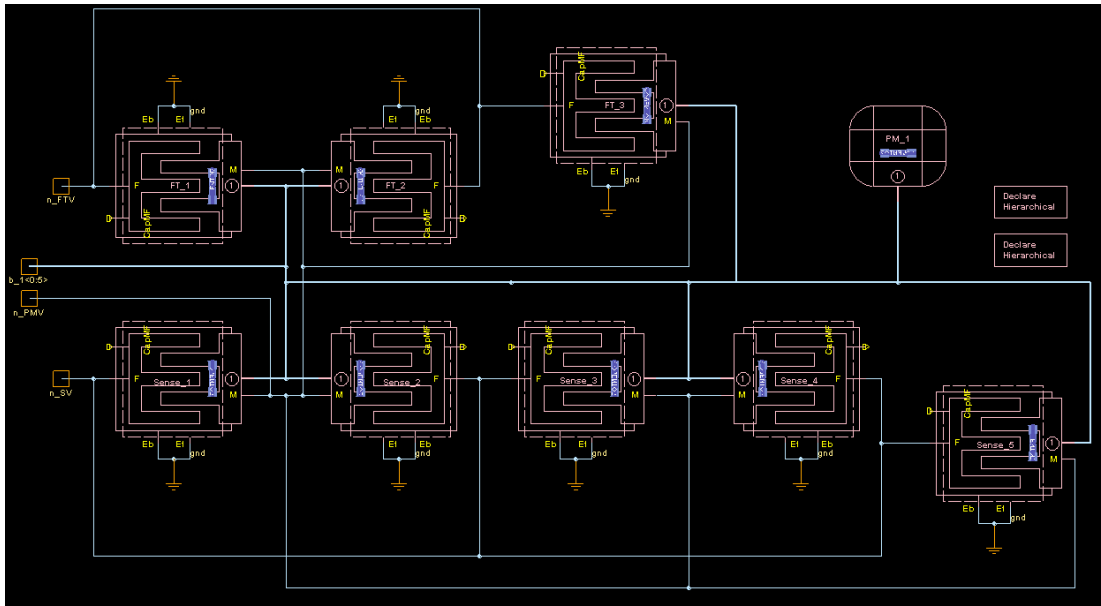


Figure 3.12: Hierarchical schematic of the sense finger sets together with the holding jig, which is a rigid mass.

Figure 3.13 shows the layout of the DMG generated by the Designer tool of CoventorWare. This layout includes all the active subelements with exact dimensions and positions.

As a matter of fact, all the size and position equations of each element are entered into their schematic symbols. These equations also include the effects of undercut during the fabrication. Since these schematics are composed of more than 200 different equations with their modified versions, it is not practical to mention all of them in this dissertation. Additionally, there are more than 90 dimensional, positional and quantitative parameters present in these modals. Although forming these models cost considerable time, the development and characterization of the modeled sensor become much easier and clear with detailed simulations which saves much more time.

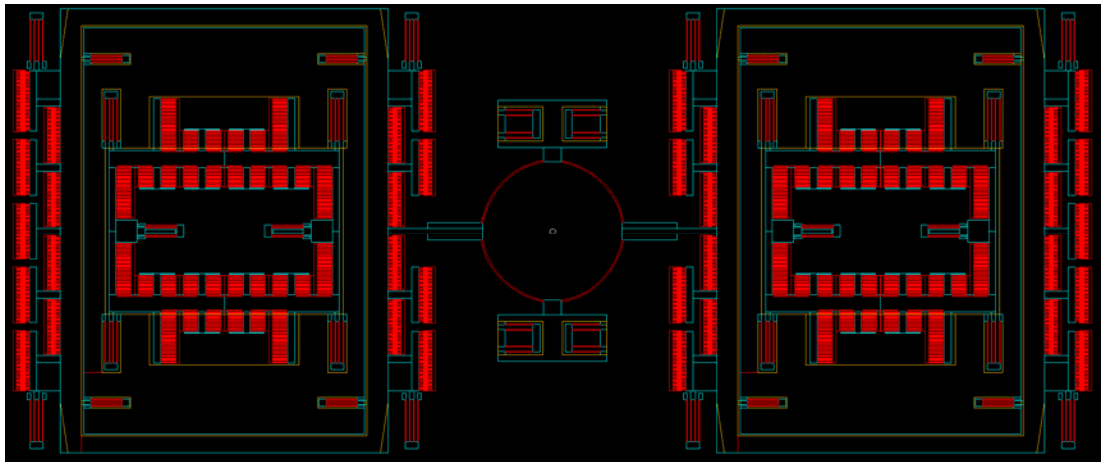


Figure 3.13: Layout of the DMG generated by the Designer tool of CoventorWare. This layout includes all the active subelements with exact dimensions and positions.

One of the key features of the Architect is its ability to simulate the effect of undercut if adequate models are used.

Figure 3.14 shows the effect of undercut which is taken into account with the help of the precise position and dimension equations in the model. This figure shows two layouts generated by the Designer tool.

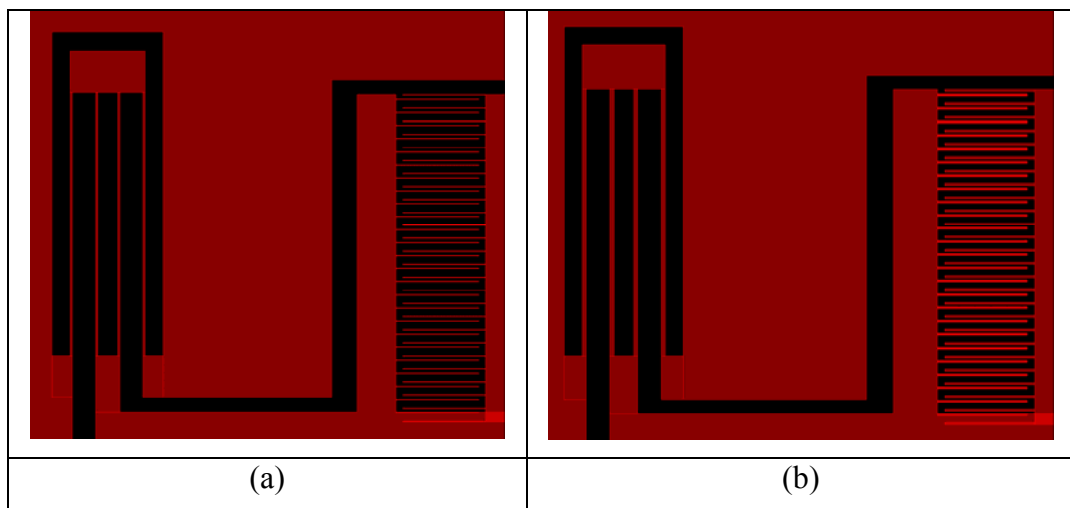


Figure 3.14: The effect of undercut which is taken into account with the help of the precise position and dimension equations in the model. The undercut in (a) is  $1.25\mu\text{m}$  while the undercut in the (b) is  $0.25\mu\text{m}$ .

Since the simulator assumes the structures as they are formed by the Designer, it is better to test the effects of all the parameters on the generated layout using the

Designer tool. In Figure 3.14 (a), the effect of the  $1.25\ \mu\text{m}$  undercut is clearly observable when the spring and the sense finger sets are considered. The undercut amount in Figure 3.14 (b) is only  $0.25\ \mu\text{m}$ . In these models, position and dimension equations are in a mutual interaction. Depending on the amount of undercut or any other dimensional parameter, the positions of all other structural elements are modified.

The ARCHITECT has a developed simulation environment capable of transient, DC operating point, small signal and Monte Carlo simulations. Figure 3.15 shows the small signal rate simulation result of the single mass gyroscope. Green signal is the drive mode vibration of  $10\ \mu\text{m}$ , the purple line is the input rate and the blue signal is the sense mode vibration.

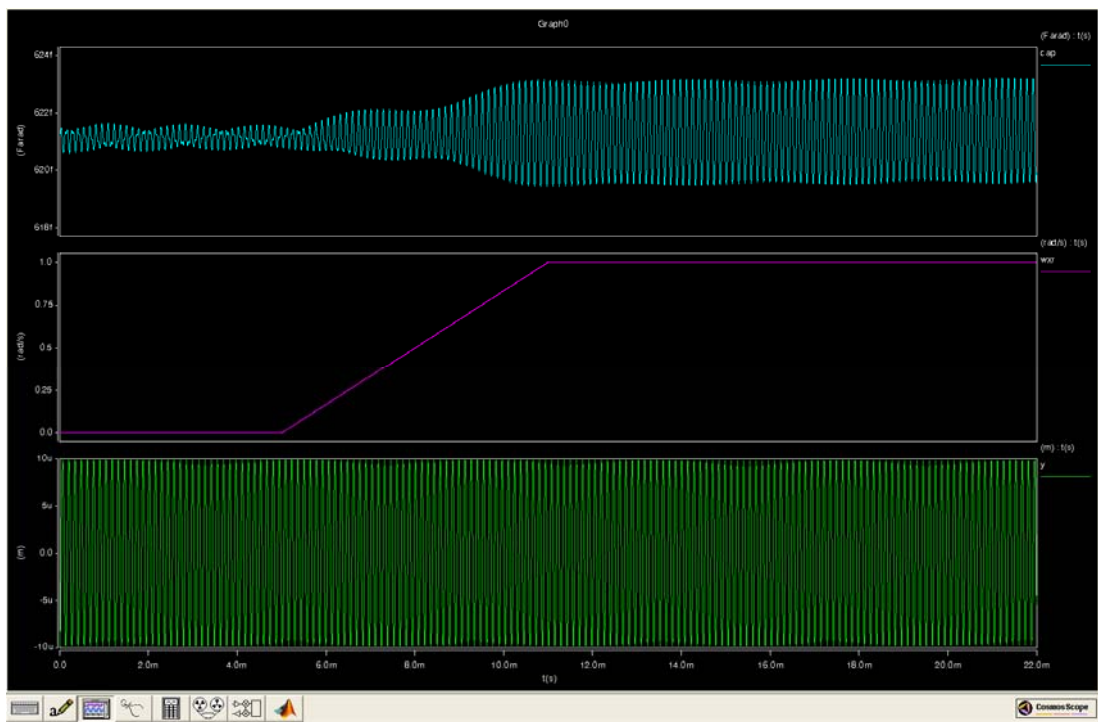


Figure 3.15: Small signal rate simulation result of the single mass gyroscope. Green signal is the drive mode vibration of  $10\ \mu\text{m}$ , the purple line is the input rate and the blue signal is the sense mode vibration.

In this figure, the quadrature vibration and the vibration generated by the Coriolis acceleration are clearly observable. Since the damping coefficients are provided empirically, the sense and drive mode vibration amounts are not exact and needs to

be corrected after the characterizations of the fabricated sensors in atmospheric and vacuum ambient.

As stated before, the architect simulator is capable of running simulations as a submodel in the SIMULINK environment of MATLAB. Just like the hierarchical subelements, a subsystem can be generated and placed in the SIMULINK with adequate connections, which may include the drive and sense connections, the displacements in three dimensions or the frame acceleration and/or rotational velocities. In this thesis, this part is left as a future research topic.

After the design step, using the ARCHITECT, drive and sense mode resonance characteristics are fine tuned. The effects of the tuning voltages are investigated and the frequency gap between the sense and the drive modes of the SMG and DMG are adjusted accordingly. Additionally, sensitivity analysis of the resonance frequency to the undercut and structural thickness are conducted. Depending on these analysis, the layouts of the gyroscopes are finalized.

Although a sophisticated model is built, there are some optimization issues and complete system simulations are left as a future study for the advanced control and readout circuits developed in parallel to this research.

### ***3.6 Fabrication***

In MEMS, fabrication is the one of the limiting factors. The designers should always keep in mind the limitations and constant aspects of the process that will be utilized. The gyroscopes within the scope of this work are designed to be fabricated using a commercial SOI process modified for MEMS applications. The advantages of this fabrication technique can be listed as; the structures can be easily released, all the etching steps are completely optimized and the overall cost of the process for prototype development is very low. Figure 3.16 shows the fabrication steps of the commercial SOI-MUMPs process of MEMSCAP® Inc. including the material legend at the bottom [35].

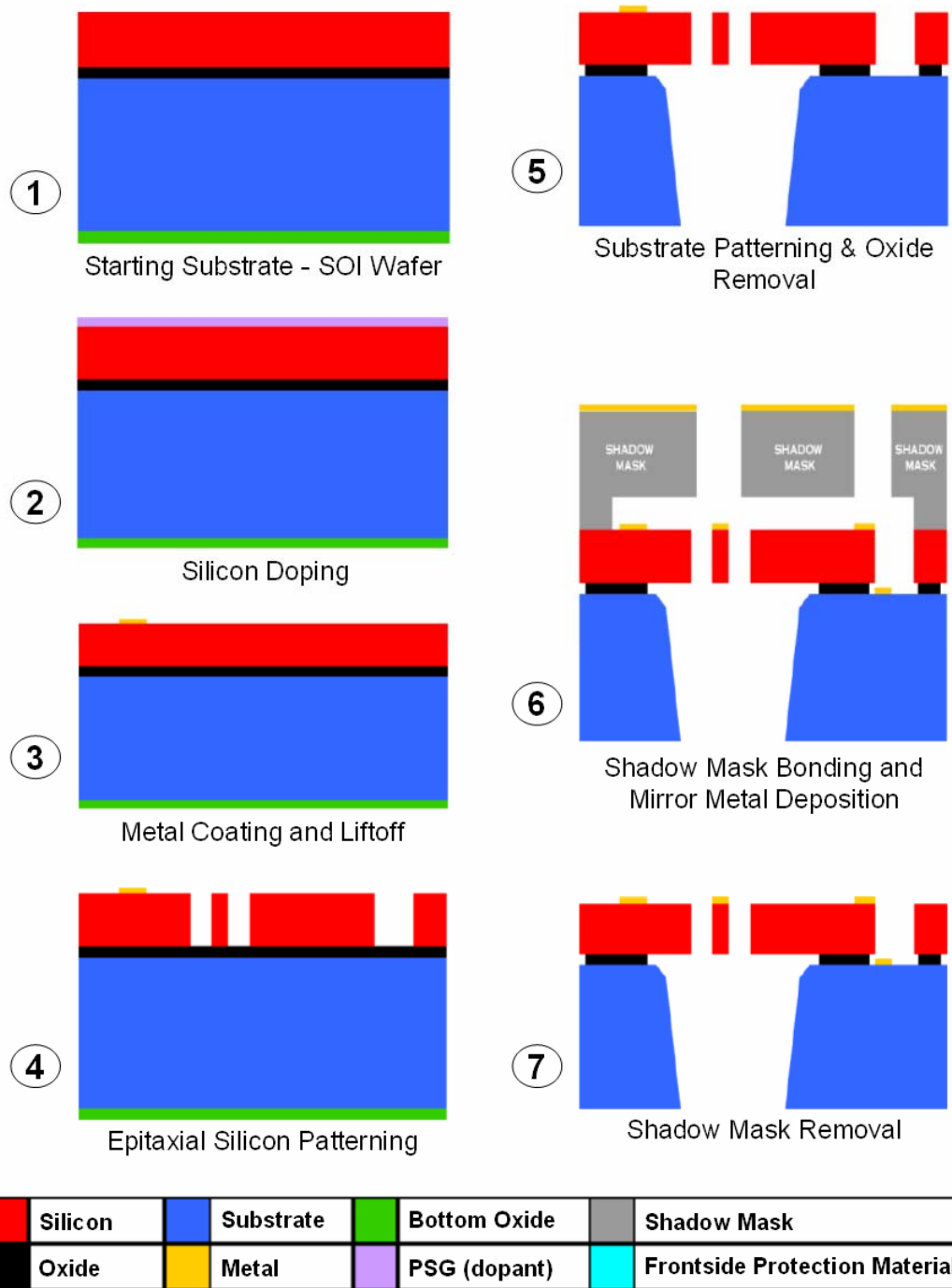


Figure 3.16: The fabrication steps of the commercial SOI-MUMPs process of MEMSCAP<sup>®</sup> Inc. including the material legend at the bottom [35].

This process is mainly composed of a front and back side deep reactive ion etching of the 25  $\mu\text{m}$  thick epitaxial layer and 400  $\mu\text{m}$  thick substrate layer respectively. In order to increase the conductivity of the fabricated structures, the fresh wafers are

doped using PSG before the etching processes. After the dry etch steps, the 1-2  $\mu\text{m}$  thick oxide layer in between is removed in vapor HF. Additionally, the process has two metallization steps for anchored and released parts.

### ***3.7 Summary***

This chapter presents the design details of the fabricated gyroscopes. In this chapter, the necessity of fine frequency adjustments of the mode shapes is explained. Additionally, the Finite Element Simulations for modal and stress parameters are presented with the simulation results. The gyroscopes are simulated to be survivable to accelerative shocks less than 20000g. Moreover, the governing equations of the ring spring is also derived and summarized. The force, moment and deflection relations of two different applications of the ring spring coupling mechanism are investigated. Besides, the ARCHITECT models of the designed gyroscopes are presented in detail. Finally, the SOI-MEMS fabrication technology of MEMSCAP<sup>®</sup> Inc is presented, which is a cheap multi user MEMS project for prototype development.

## **CHAPTER 4**

### **TEST RESULTS OF FABRICATED GYROSCOPES**

This chapter presents the conducted test procedure of the fabricated gyroscopes and the test results, together with the performance specifications of each gyroscope. Measuring the performance parameters, especially g-sensitivity of the gyroscope requires several adjustments and apparatus. Data collection and controlled input generation for the gyroscopes are other important points for robust testing. Section 4.1 presents the required test arrangements for performance characterization of the gyroscopes. Section 4.2 presents test results of the fabricated single mass (SMG), double mass (DMG) and quadruple mass (QMG) gyroscopes with their interpretations. Finally, Section 4.3 summarizes the results of the overall tests and comments on additional aspects required in order to fully characterize an inertial MEMS gyroscope.

#### ***4.1 Required Test Arrangements***

Tests of these fabricated gyroscopes require a procedure with some arrangements utilizing various devices. The received gyroscope structures, because of the frame-in-frame structure mentioned in Chapter 3, are not released and needs to be released before the tests. During the tests of the SOI gyroscopes, one should follow a guideline for a complete characterization. In order to form a sound base while expressing the test results, it is required to mention the setups and approaches used during the tests beforehand. This section describes the post processing of the gyroscope structures, required preliminary resonance tests, designed printed circuit

boards (PCBs) together with gold plated PCB packages for readout electronics, bonding diagrams, custom fixtures, external self resonance loop setup and the rate table control.

#### 4.1.1 Post Processing of the Fabricated Gyroscopes

The residual  $\text{SiO}_2$  layer between the substrate and the epitaxial layer cannot be removed completely after the oxide-etch step in vapor HF conducted at MEMSCAP Inc. The reason is that the oxide removal process of MEMSCAP is a standardized  $1 \mu\text{m}$  oxide removal in HF vapor, with an approximately  $1.8 \mu\text{m}$  undercut. Figure 4.1 shows the undercut amount during HF vapor etching [35]. Thus, the structures were not released when received.

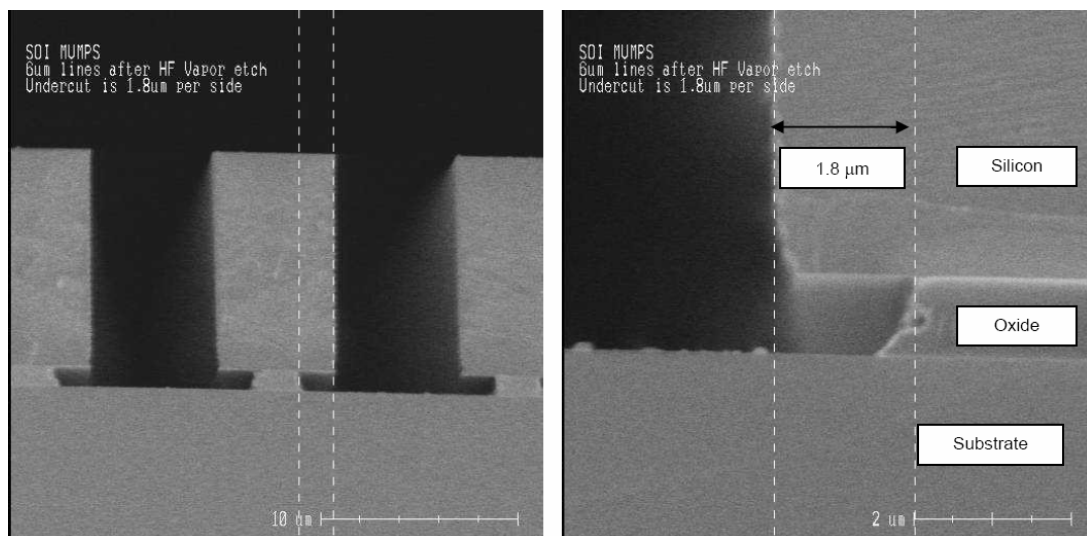


Figure 4.1: Undercut amount during vapor HF etching, reported by MEMSCAP Inc.[35].

For the post process release, the samples are immersed in 48% HF and etched for 4 minutes with soft agitation. This step removes the  $1 \mu\text{m}$  oxide layer between the substrate and the epitaxial layer. After etching the oxide layer, the samples are cleaned in DI water, acetone, and IPA, in the given sequence for 5 minutes each. Finally, in order to dry the samples without sticking, they are cleaned one more time in methanol and then directly put on the  $70^\circ\text{C}$  hot plate. Figure 4.2 illustrates the DRIE etched epitaxial layer over the substrate and the oxide residues (black) right

under the etch hole walls. The proof masses of the released structures are checked one more time if they are free to move or not, using the probe station.

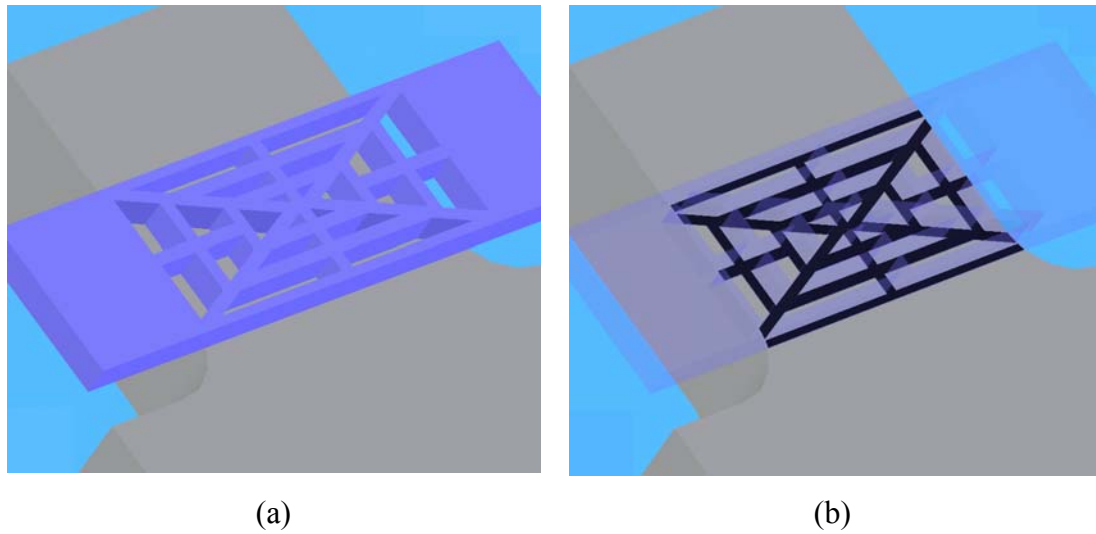


Figure 4.2: (a) DRIE Etched epitaxial layer over the substrate, (b) oxide residues (black) between the substrate and the epitaxial layer.

Figure 4.3 shows the SEM image of the released structure. The etch undercut of the substrate layer usually favors the oxide removal. In order to prevent structural softening, the etch holes are formed using beams connected by truss-shaped links.

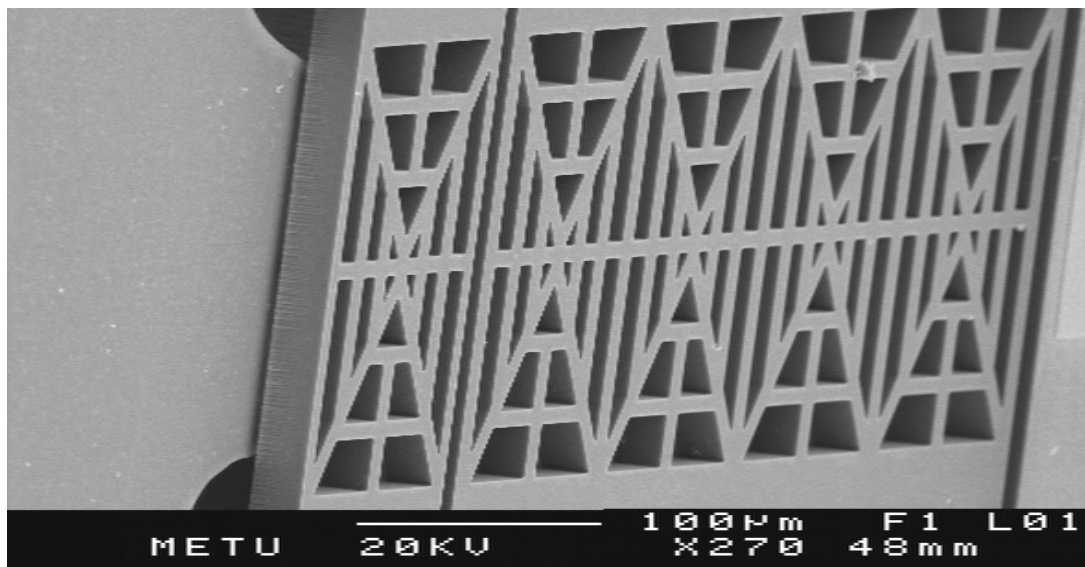


Figure 4.3: SEM image of the released structure.

## **4.1.2 Resonance Characterization of Drive and Sense Modes**

For the rate tests, the resonance frequencies and quality factors of the drive and sense modes are required for each gyroscope. The designed values together with the actual device character give us an idea about the process variations and the quality factor of the resonator. The resonance tests are conducted using the Agilent 4295A Network / Spectrum / Impedance analyzer and a probe station. Depending on the mechanism of the gyroscope, different excitation schemes are applied. In general, the proof mass of the gyroscope and the substrate is biased to a DC voltage. The gyro is driven from one side or two, depending on the mechanism and locations of the drive/sense fingers, and then the electrical gain of the mechanism is extracted by the network analyzer. This gain is composed of the gain of feed-through capacitance together with the gain obtained by the mechanical resonance. In this section, the resonance characteristics of the single, double and quadruple gyroscopes are presented in detail.

### **4.1.2.1 Resonance Characteristics of Single Mass Gyroscope (SMG)**

In order to present the resonance characteristics of the gyroscopes, in Figure 4.4 the test setup is represented with two switches to illustrate the procedure clearly. In the figure, upper switch shows which finger set is driven while the lower switch is indicating which finger set is sensed. The drive resonance characteristics is measured with the upper switch at position “1” and the lower switch at position “1”, shortly  $U_p=1$ ,  $D_{own}=1$ , i.e., U1D1. This representation will be used for further test results also.

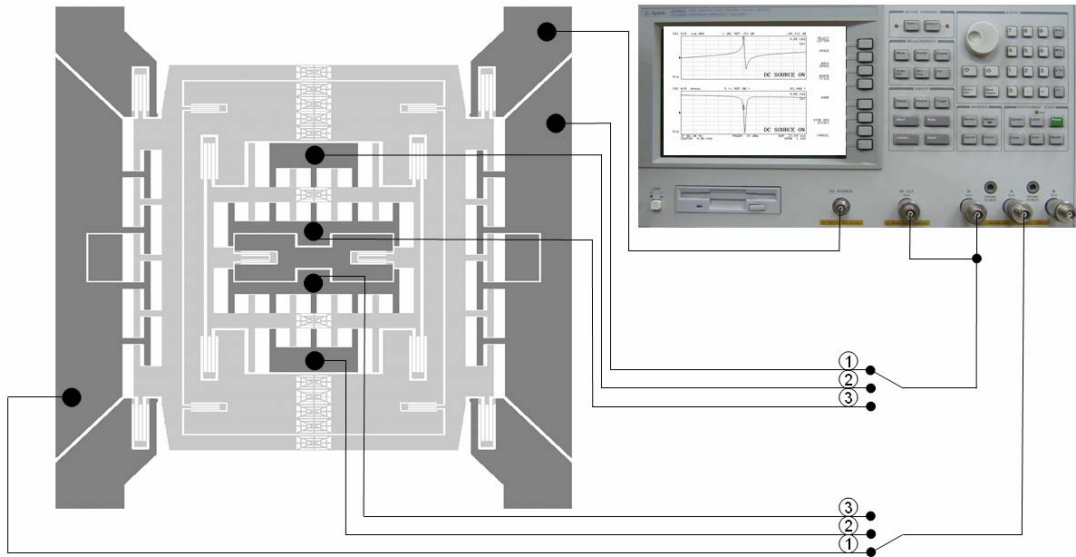


Figure 4.4: The test setup is represented with switches to illustrate the procedure clearly.

Figure 4.5 shows the drive mode resonance characteristics of the SMG, switches at UID1. The quality factor of the drive mode is measured to be 216.

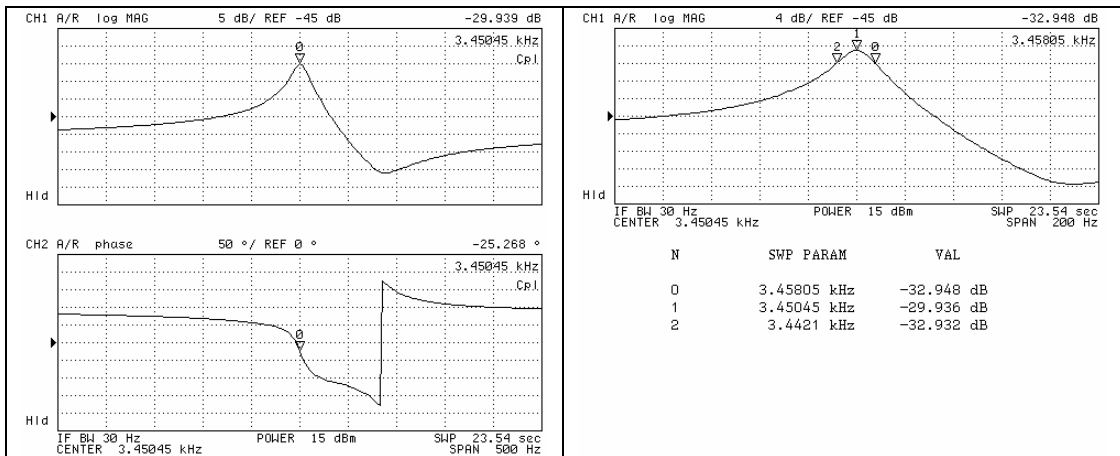


Figure 4.5: The drive mode resonance characteristics of the SMG, switches at UID1.

Figure 4.6 shows the resonance characteristics of the sense mode. The sense mode of the gyroscopes has two sets of fingers; the sense and the frequency tuning (FT) finger sets. Their resonance characteristics give us the possible matching conditions, if required. In the rate tests, gyroscopes will be operated at mismatched condition,

thus, it is reasonable to operate the gyroscope with a -15V DC polarization voltage applied to proof mass with the same voltage applied to the FT sets.

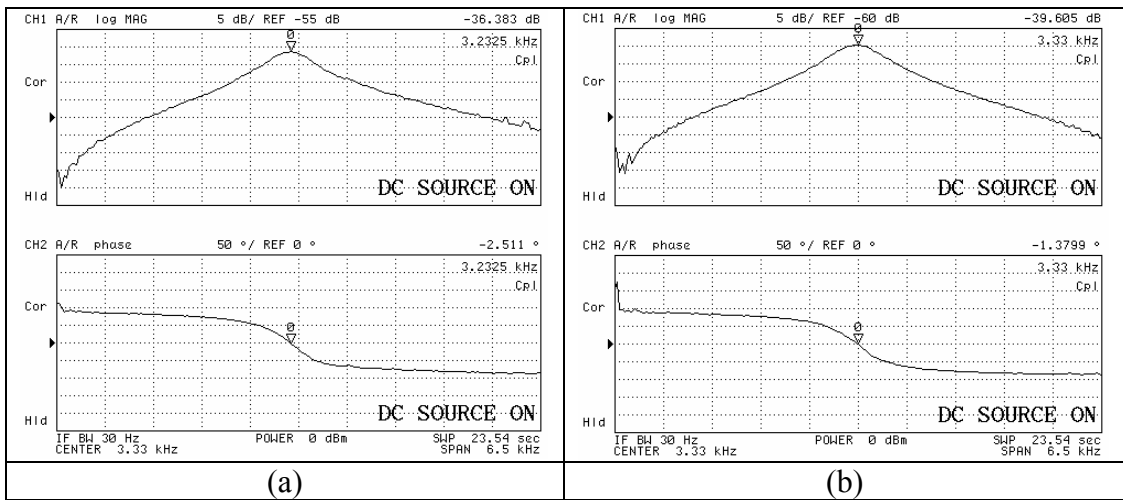


Figure 4.6: Sense mode resonance characteristics: (a) Sense finger set, switches at U3D3 with 26V DC polarization voltage and (b) Frequency tuning finger set, switches at U2D2 with 30.5V DC polarization voltage.

Figure 4.7 shows the total coupling from drive mode to upper and lower sense finger sets, including the electrical and mechanical coupling. From the phase data of the resonance characteristics, it is found that electrical coupling is dominant in the gyroscope since the phases look similar for the opposing sense finger sets.

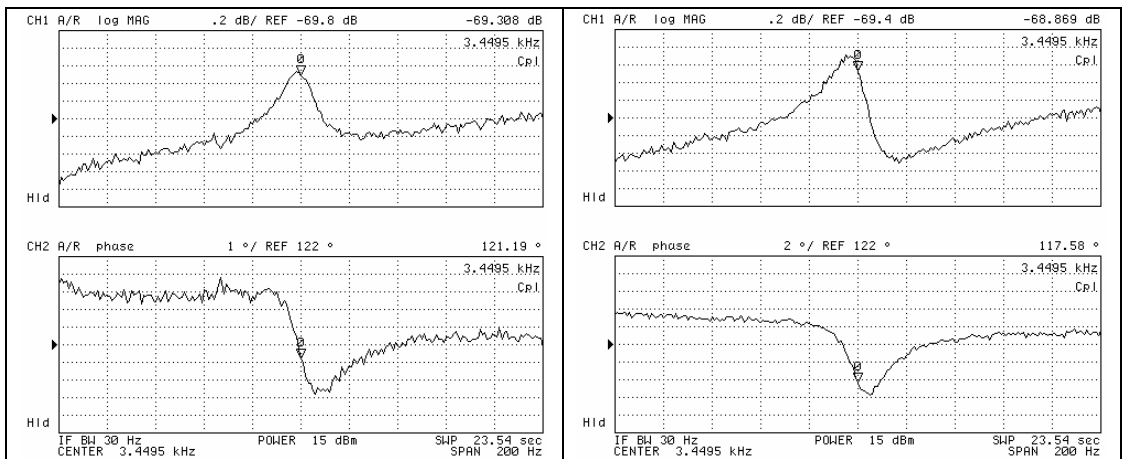


Figure 4.7: Coupling from drive mode to sense mode at drive resonance, switches at U1D3 and U1U3.

### 4.1.2.2 Resonance Characteristics of Double Mass (Tuning Fork) Gyroscope (DMG)

For the resonance tests of the DMG, sense modes of each mass should be characterized separately. Figure 4.8 shows the test setup illustration of the DMG.

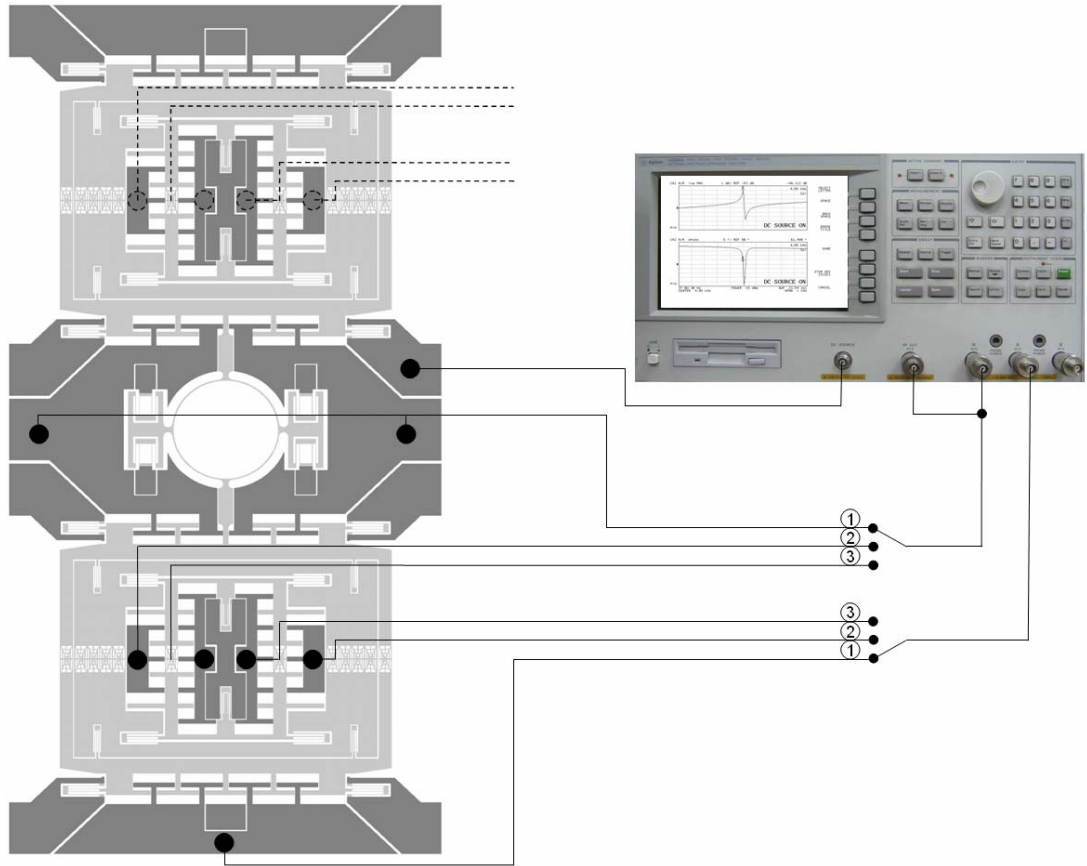


Figure 4.8: Resonance test setup illustration of the DMG.

After the drive mode characterization, the connections for each mass are adjusted accordingly. Figure 4.9 shows the drive mode resonance characteristics of the DMG with switches at U1D1. The quality factor of the drive mode is 303, which is higher than the SMG. The reason of this increase in  $Q$  is the increase in the resonance frequency while the drive sets are kept constant with respect to the resonating mass.

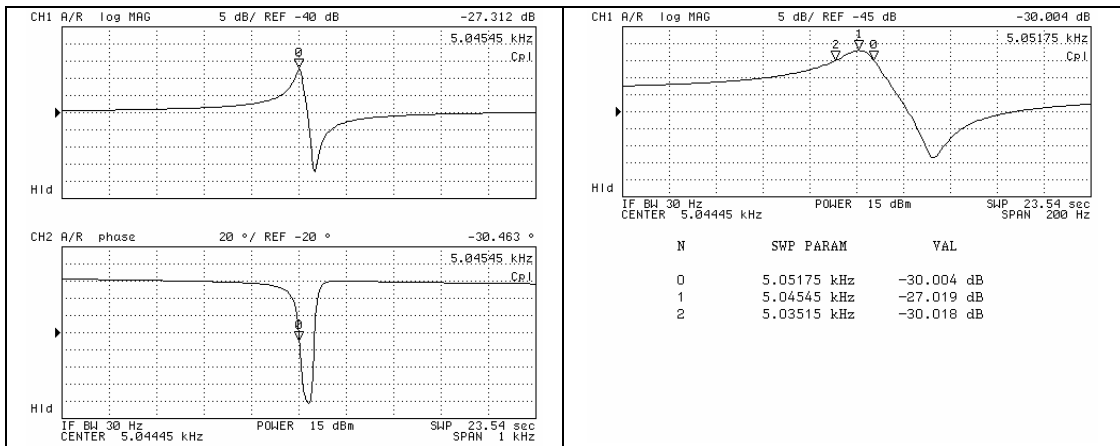


Figure 4.9: The drive mode resonance characteristics of the DMG, switches at U1D1

Stress stiffening of the mechanism is another concern for the drive mode. Figure 4.10 shows the resonance frequency shift in drive mode with increasing vibration amplitude which is linearly related to signal voltage.

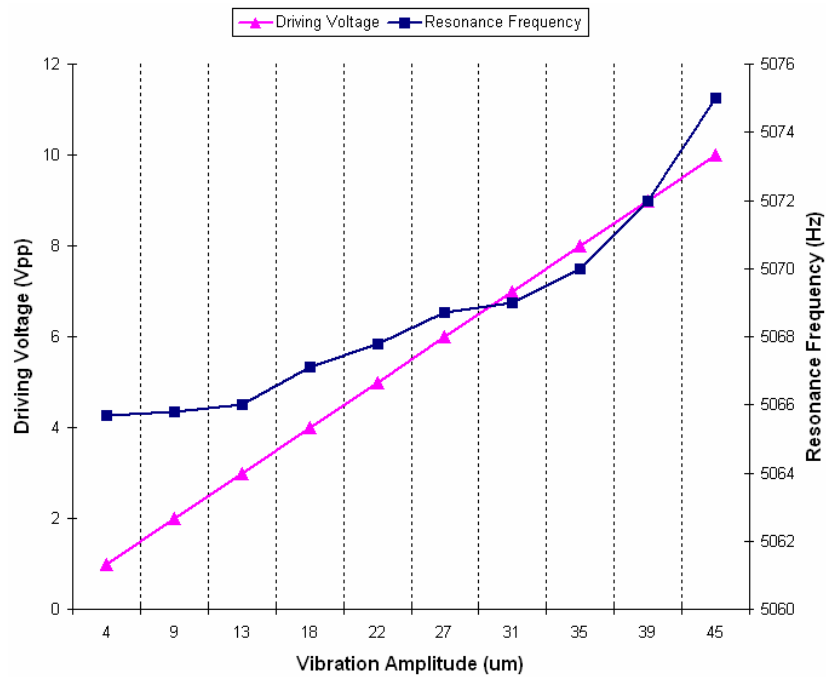


Figure 4.10: Plot of Vibration Amplitude ( $\mu\text{m pp}$ ) versus Driving Voltage and Resonance Frequency for the DMG drive mode.

For the drive mode, the amount of frequency shift is only 9 Hz in a vibration amplitude span of 45  $\mu\text{m}$ , peak-to-peak. This low value of stress stiffening is the result of the low-stress coupling mechanism. This proves that the ring spring in the

middle of the proof masses provides a linear coupling together with a negligible frequency shift in very different vibration amplitudes.

Figure 4.11 shows the sense mode resonance characteristics of the first mass of the DMG. The second mass' resonance characteristics is very close to that of the first. In the rate tests, like the SMG, the gyroscopes will be operated at mismatched condition, thus, it is reasonable to operate the gyroscope with a -15V DC polarization voltage applied to proof mass and FT sets.

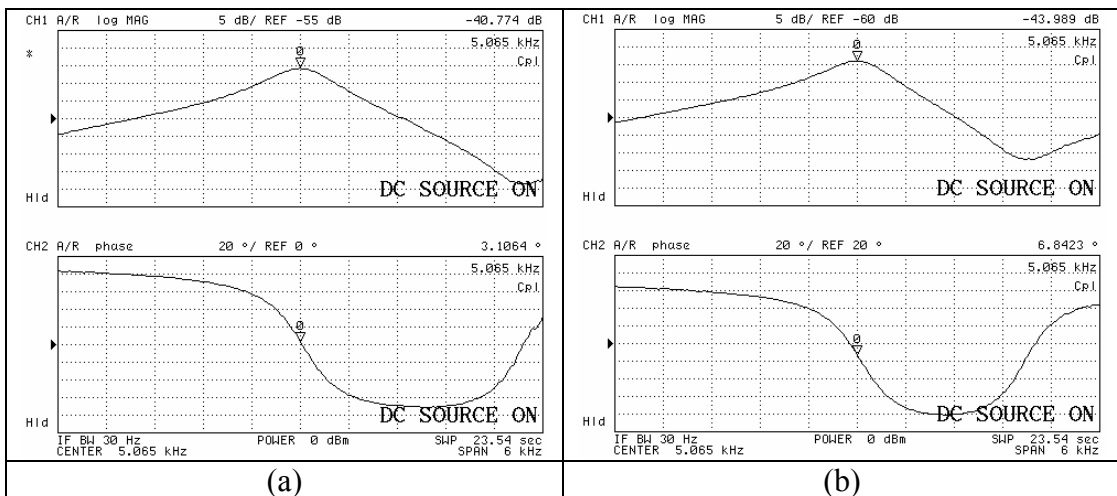


Figure 4.11: Sense mode resonance characteristics of the first mass of the DMG: (a) Sense finger set, switches at U3D3 with 19.5V DC polarization voltage and (b) Frequency tuning finger set, switches at U2D2 with 23.5V DC polarization voltage.

In DMG, as can be seen in Figure 4.12, coupling from drive to sense mode is dominated mechanically. The phases of the opposing sense sets of the same mass are exactly opposite, meaning that the mechanically generated signals are dominant. These electrical and mechanical couplings from drive mode to sense mode heavily depend on the resistance of the gyroscope structure. The reason is that the biasing of the proof mass is affected by this resistance. Usually, because of the high structure resistance, the biasing of the regions that are close to the drive and sense fingers is not very effective. Thus, small charging-discharging currents of the capacitances passing through the proof mass induce voltages, causing electrical coupling. If this is not the case, then mechanical capacitance change due to the quadrature error becomes dominant.

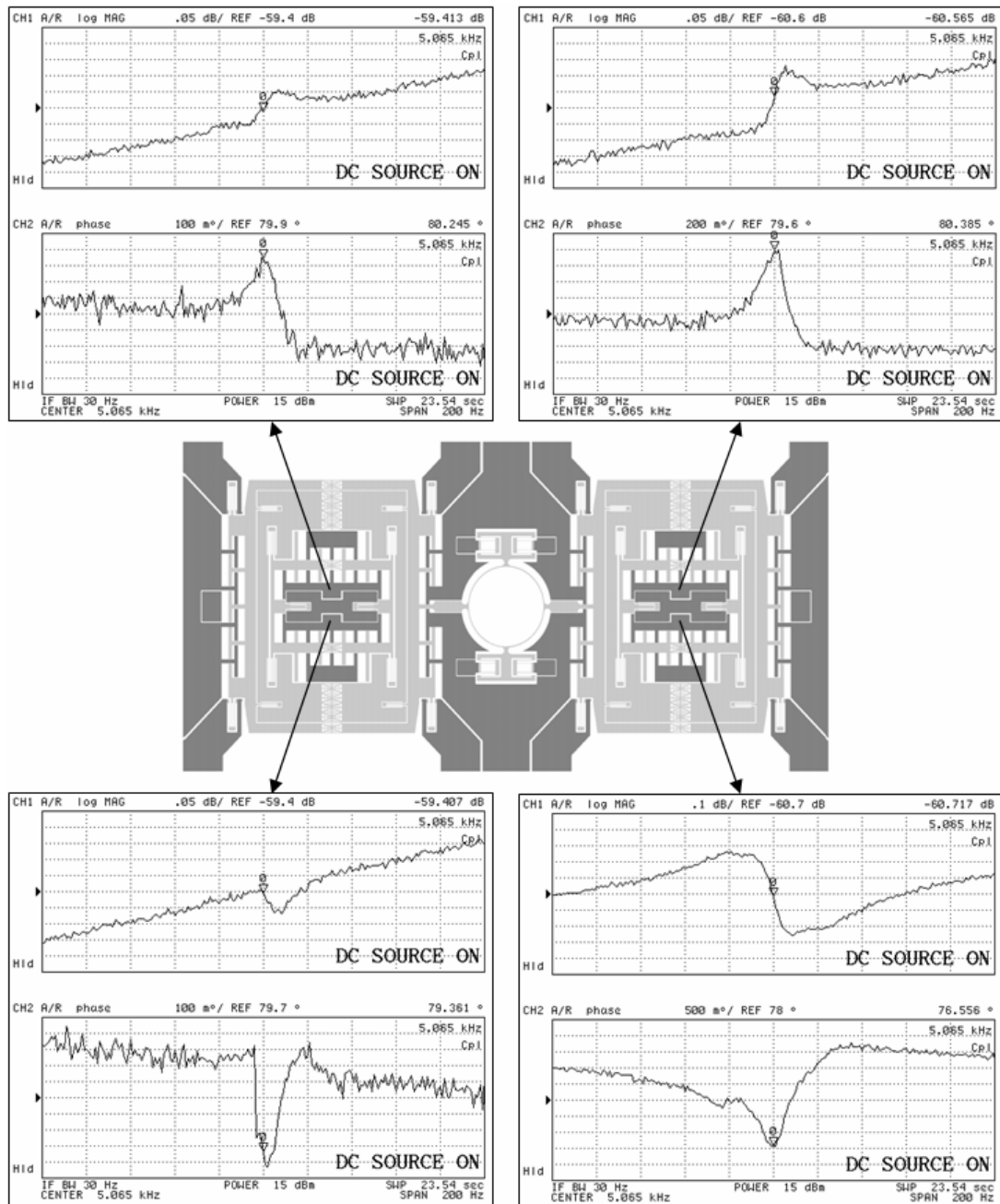


Figure 4.12: Coupling from drive mode to sense mode at drive resonance, switches at U1D3 and U1U3 for both of the masses.

Figure 4.13 shows the sense mode quality factor data of both masses corresponding to a Q factor of 6.7 and 6.9, respectively. The difference between the drive and sense mode quality factors is the long varying gap fingers in the sense mode boosting the damping in sense mode.

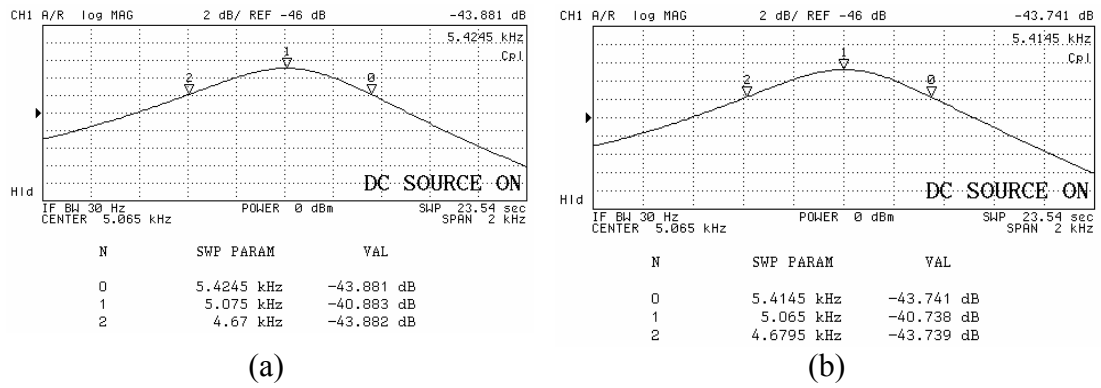


Figure 4.13: Matched quality factor data of the first (a) and second (b) mass of the DMG.

### 4.1.2.3 Resonance Characteristics of Quadruple Mass (Twin Tuning Fork) Gyroscope (QMG)

Figure 4.14 shows the resonance test setup of the QMG. In the tests of the QMG, different driving schemes are also demonstrated.

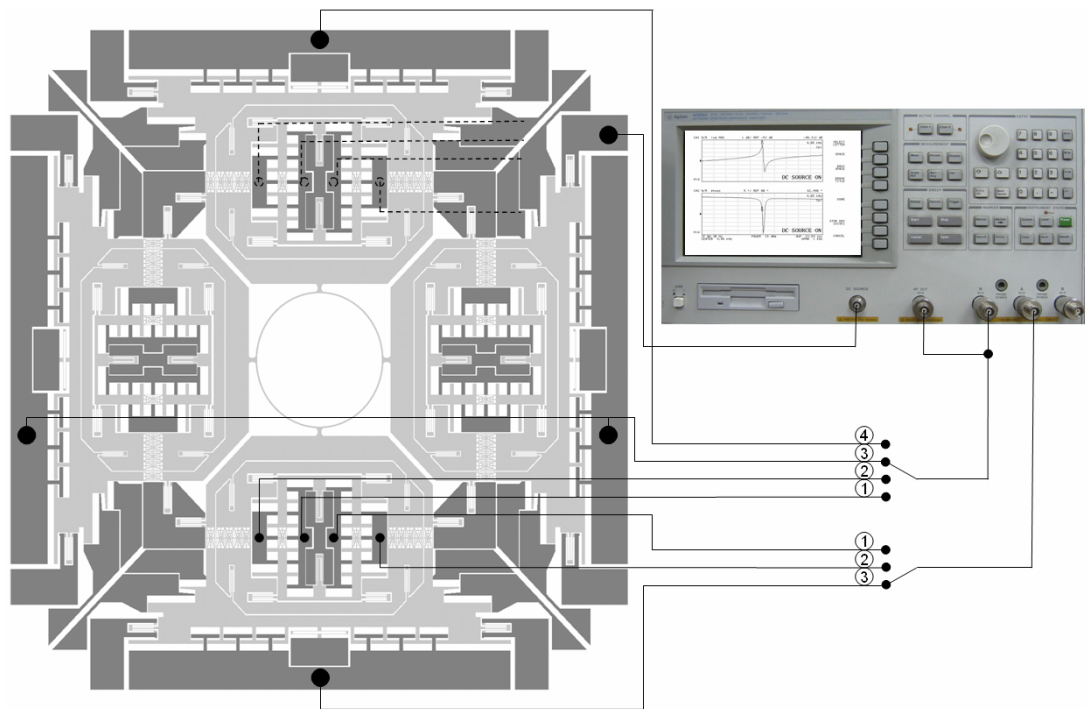


Figure 4.14: Resonance test setup illustration of the QMG.

In the QMG, owing to its mechanism and drive set locations, the excitable modes differ depending on the excitation scheme. For normal operation, the gyroscope will

be driven from the opposing sides, switches at U3D3. Figure 4.15 shows the drive mode resonance characteristics of the QMG for this arrangement. The quality factor of the drive mode is about 86.

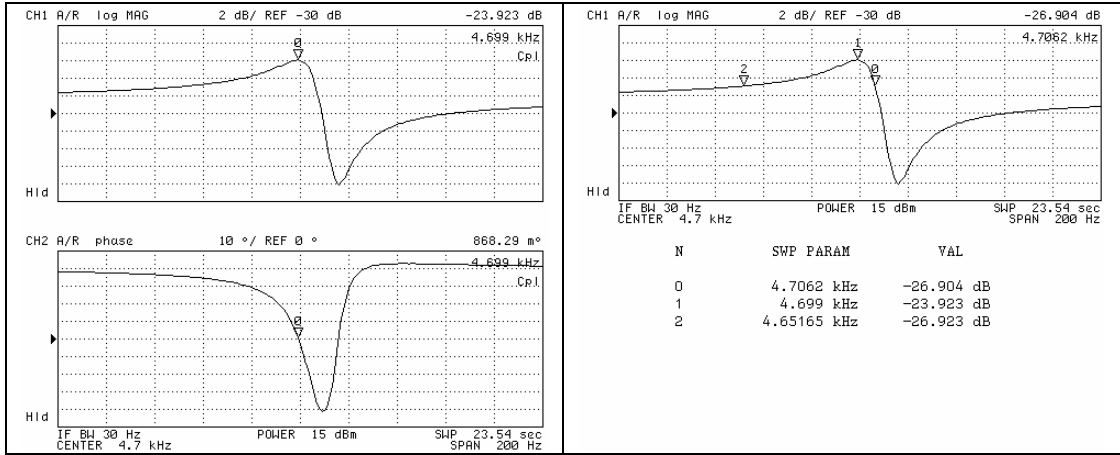


Figure 4.15: The drive mode resonance characteristics of the QMG, switches at U3D3.

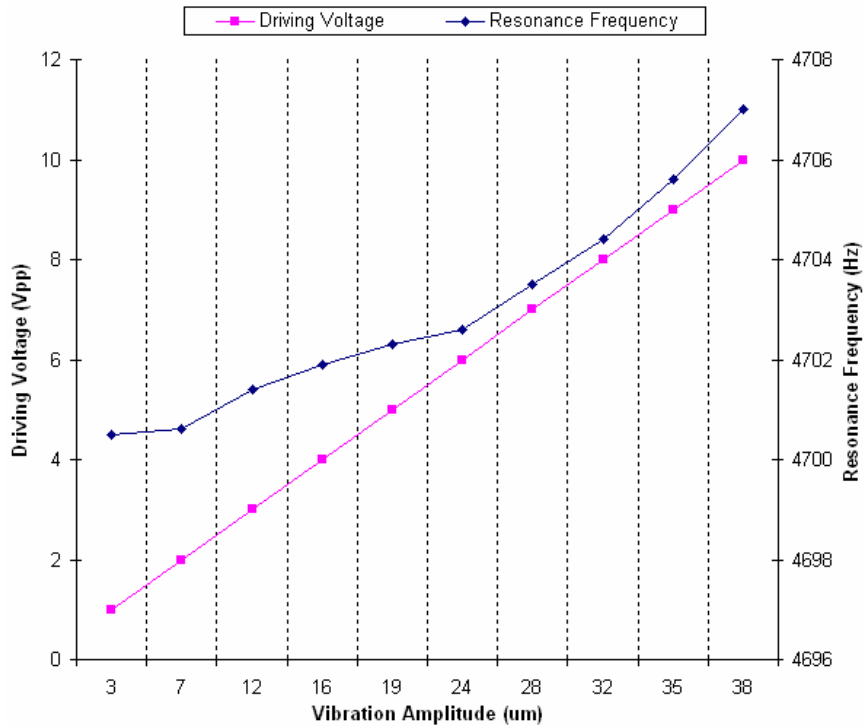


Figure 4.16: Plot of Vibration Amplitude ( $\mu\text{m pp}$ ) versus Driving Voltage and Resonance Frequency for the QMG drive mode.

The coupling mechanism in QMG, like in DMG, is measured to be very linear and low vibration amplitude dependent. Figure 4.16 shows the resonance frequency increase with the increasing drive amplitude with driving voltage ( $V_{pp}$ ).

Figure 4.17 shows the resonance characteristics when the gyroscope is driven from only one drive finger set, switches at U4D3. When driven from single side, the unsymmetrical forces excite other higher frequency modes together with the drive mode, which is the lowest frequency mode. Adjusting operational frequency to the first resonance mode adds robustness to the drive loop for self resonance.

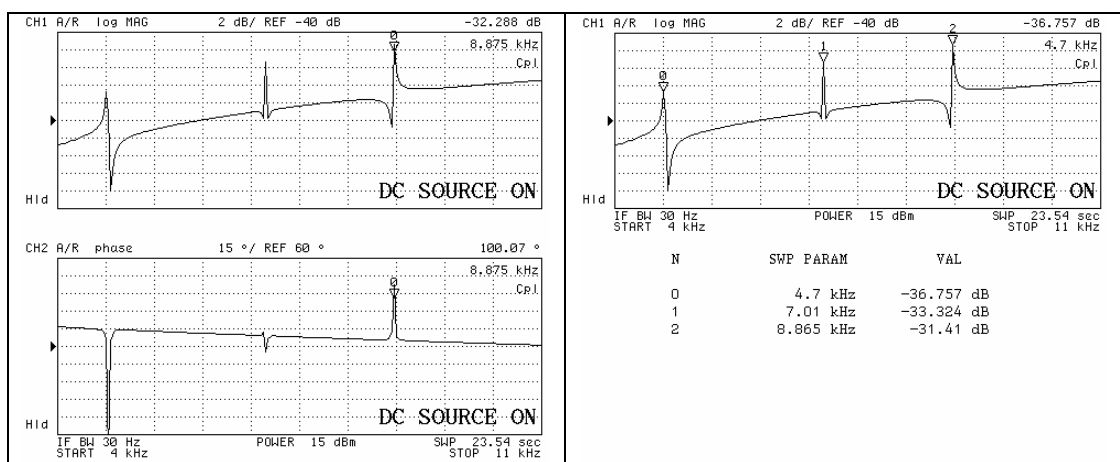


Figure 4.17: The drive mode resonance characteristics of the QMG, switches at U4D3.

Figure 4.18 shows the sense mode quality factor data of the upper, lower, right and left proof masses. The quality factors are 5.3, 5.4, 5.6 and 5.6, respectively. These Q-Factor data are close to that of DMG, because the sense structures are very close to each other.

Actual resonance frequencies of the sense modes are not measurable. This is because the signals generated on the sense fingers need a finite voltage difference to reveal the capacitance change as an induced current. The amount of this potential difference directly decreases the sense mode resonance frequency because of the quadratic manner of the varying gap finger sets. Thus, the designed sense mode resonance characteristics cannot be verified directly using filter analyzers, but can be proven by including this softening effect in the electromechanical spring system of the sense

mode. The resonance characteristics in Figure 4.17 are obtained with a proof mass DC polarization voltage of 15V.

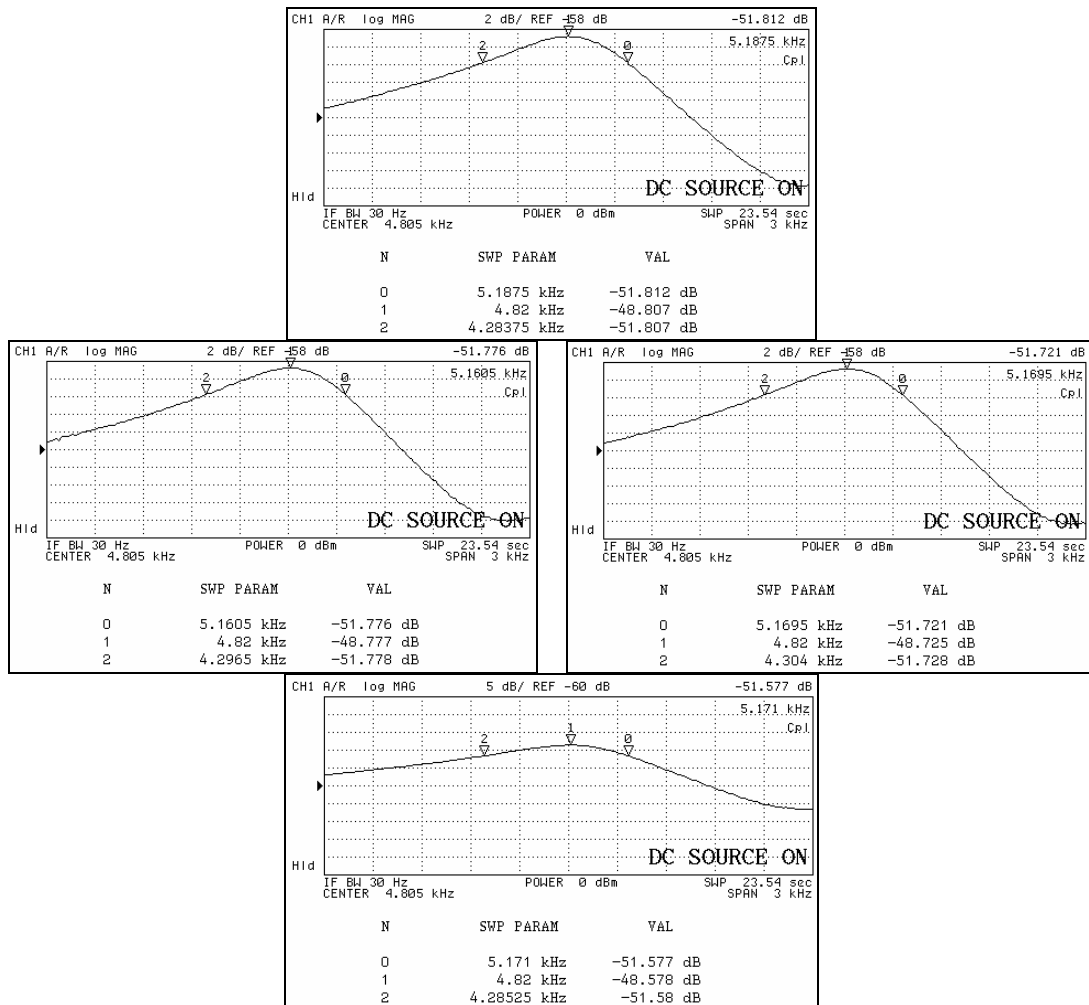


Figure 4.18: Mismatched quality factor data of the sense modes of the upper, lower, right and left proof masses, with their respective locations.

As the last part of the resonance characterization of the QMG, the electromechanical coupling from drive to sense mode is measured. Figure 4.19 shows the electromechanical coupling from drive mode to sense mode at drive resonance. In QMG, the coupling from drive to sense mode is electrically dominated. The reason of this is the high structural resistance. The resistance of a single mass is about  $750\Omega$ , from one proof mass contact to other. It should be noted that there is only 1 pair of folded springs are present between these contacts. If the sense mode fingers are considered, they are 3 folded spring pairs far from the proof mass contact. This

makes 2kΩ. This resistance is large enough for an electro capacitive interaction between the drive mode and sense mode. From the figure, it can be easily noticed that the coupling ratio in horizontal finger sets are lower than the vertical sets. The reason is that during the tests, QMG is driven from top and bottom drive finger sets, causing a larger coupling to the upper and lower sense fingers.

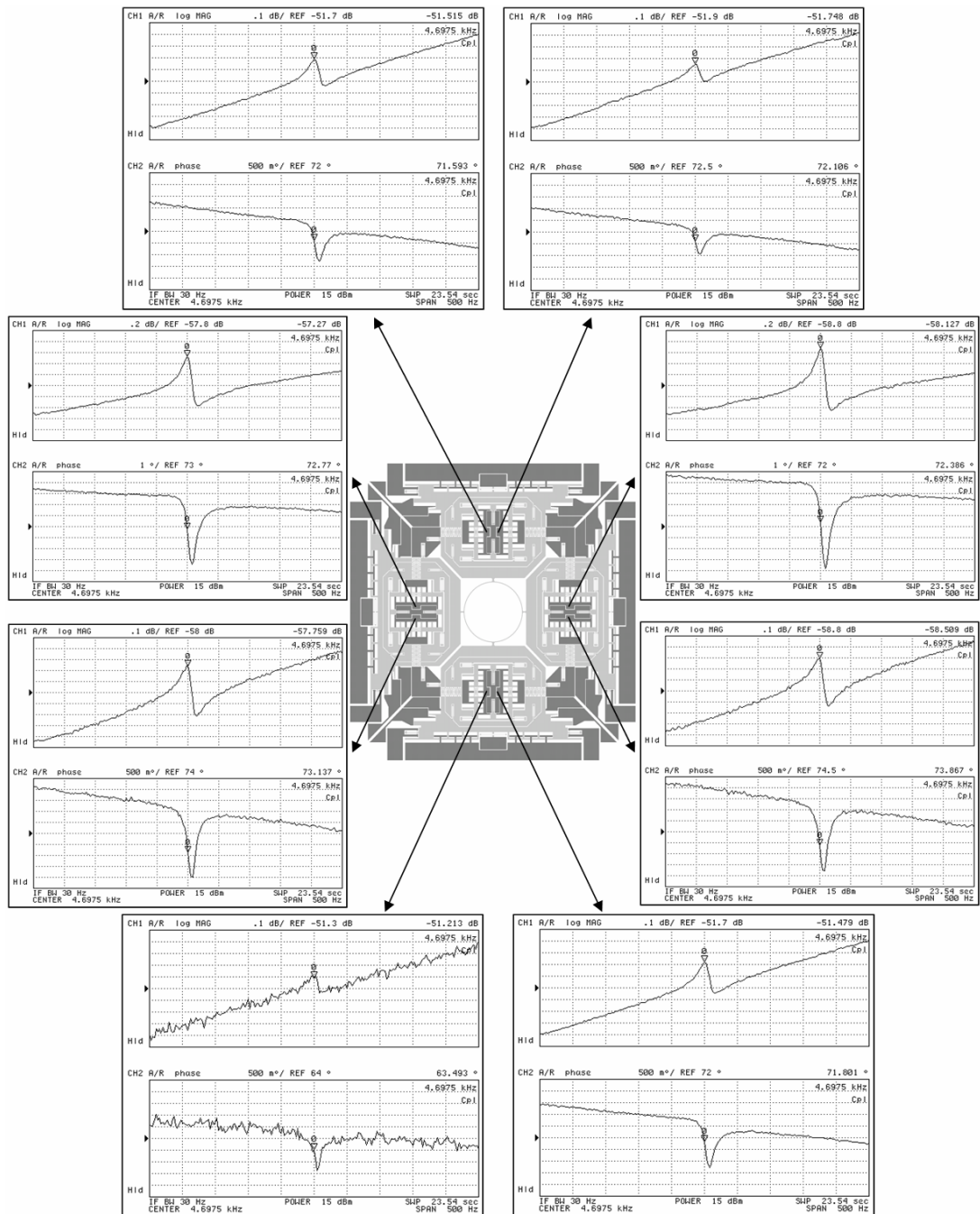


Figure 4.19: Electromechanical coupling from drive mode to sense mode at drive resonance, switches at U3D1 and U3U1 for all of the masses.

### 4.1.3 Readout Electronics

The capacitance change on the sense and drive fingers is sensed by converting the induced current to voltage by biasing the drive pick and sense sets to ground with a lower impedance resistor with respect to the impedance of the parasitic capacitances on the sensed node. This voltage value is then fed to a unity gain buffer. To eliminate the DC offsets, AC couplers are used right after the unity gain buffer outputs. To compensate the level and gain differences caused by process variations, an optional gain set is designed. Moreover, seven instrumentation amplifiers are utilized in a proper connection to reject the common mode electrical coupling, quadrature and offsets at the output of the buffers. The placement is done to be compatible to all the three gyroscopes. Figure 4.20 shows the labels of the sense sets of the SMG, DMG, and QMG.

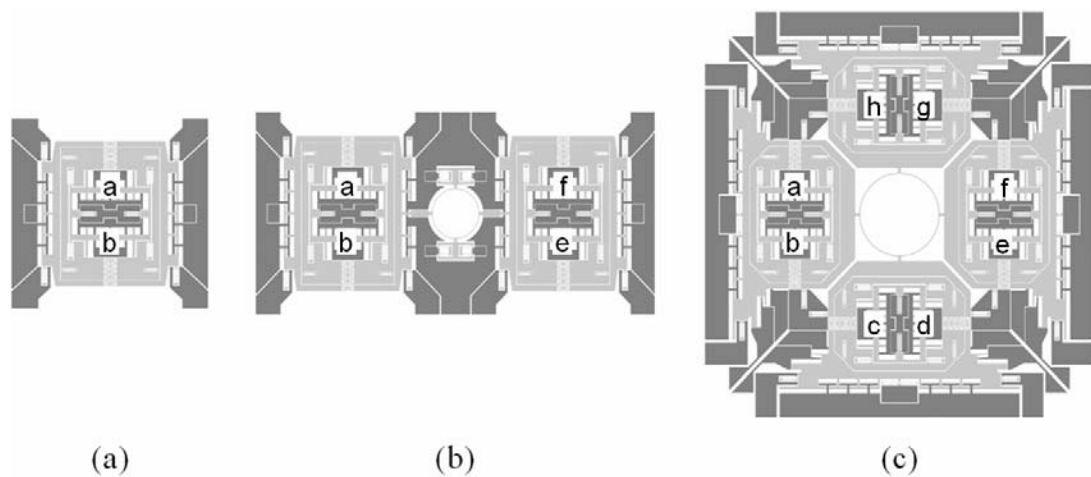


Figure 4.20: Labels of the sense sets of the SMG (a), DMG (b), and QMG (c).

Figure 4.21 shows the buffer, gain and differential amplifier stages connected to the sense finger sets. Depending on the number of masses of the tested gyroscopes, the differential amplifiers are by-passed by jumpers in order to feed the required inputs to the demodulator stage.

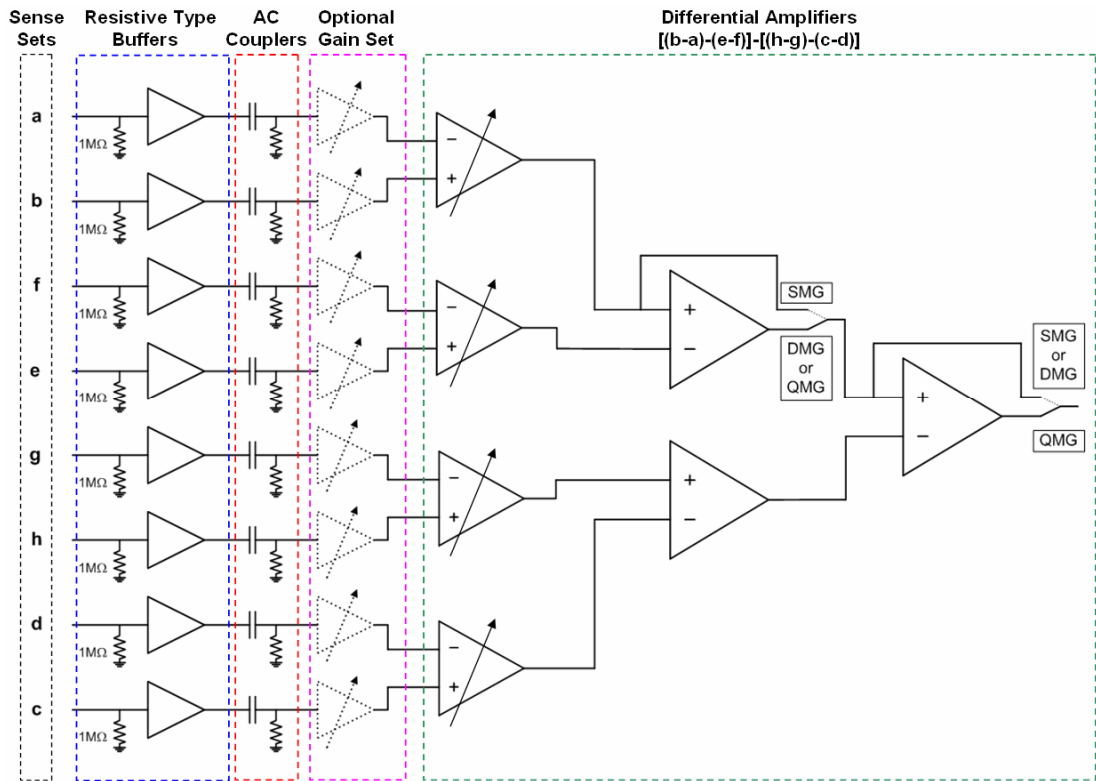


Figure 4.21: Buffer, gain and differential amplifier stages connected to the sense finger sets.

Figure 4.22 shows the AM demodulator, low-pass filter and a +40dB gain stage, extracting the DC rate signal from the raw signal output of the differential amplifier set in the Figure 4.21.

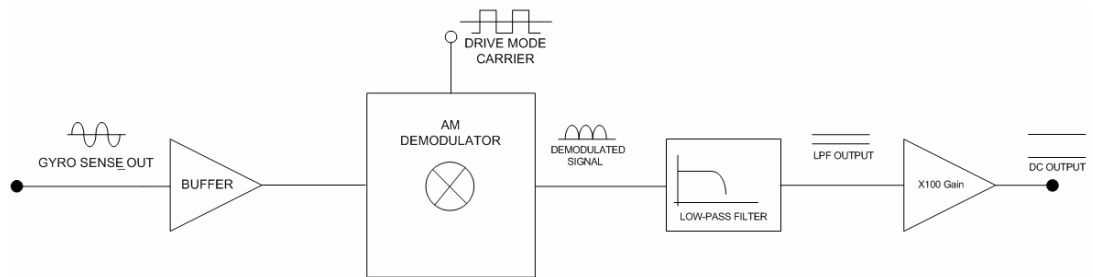


Figure 4.22: AM demodulator, low-pass filter and a +40dB gain stage, extracting the DC rate signal from the raw signal output of the differential amplifier set.

During the design stage of the gyroscopes, the metal pads of the finger sets and the proof masses could not be located evenly because of the process limitations. Different sizes of the gyroscopes also create a problem in finding a standard way of testing. To solve this problem, a standard package and a test circuit is designed.

Figure 4.23 shows the designed gold plated PCB package, supporting gyro structures up to 10 mm x 10 mm in size with proper readout chip connections and substrate biasing. This package is compatible with vacuum packaging using proper vacuum caps and epoxy-patch sealing.

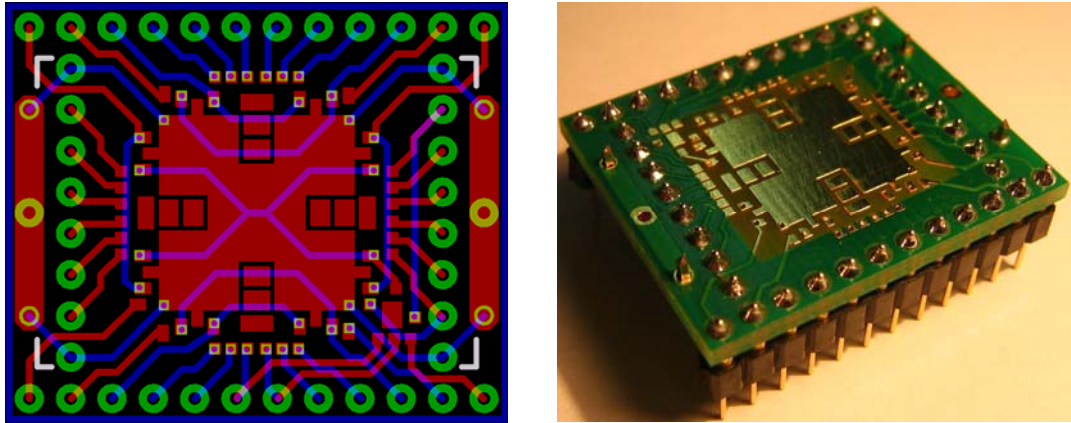


Figure 4.23: Gold plated PCB package, supporting gyro structures up to 10 mm x 10 mm in size with proper readout chip connections and substrate biasing.

The resistively biased sensing sets require an additional PCB for SMD resistors and LF353 op-amps. Figure 4.24 shows the gyroscopes bonded to the gold-plated packages which are connected to the boards of the resistive buffers.

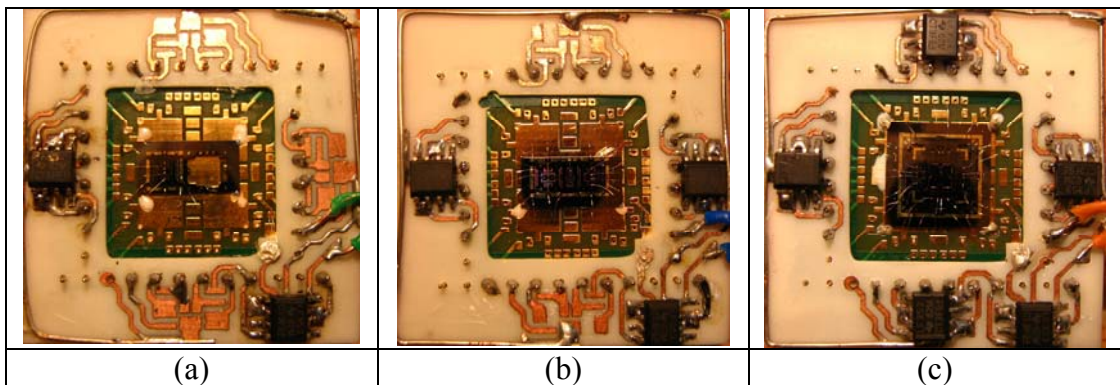


Figure 4.24: Single (a), double (b) and quadruple (c) mass gyroscopes bonded to the gold-plated packages which are connected to the boards of the resistive type buffers.

Figure 4.25 shows the main test board including the gyroscope, buffers, AC couplers, optional gain set, differential amplifiers, and the AM Demodulator. The drive mode

“pick” signals, i.e. the drive mode sense, are directly send out of the board to an outer loop for phase locked driving signal generation and for monitoring purposes.

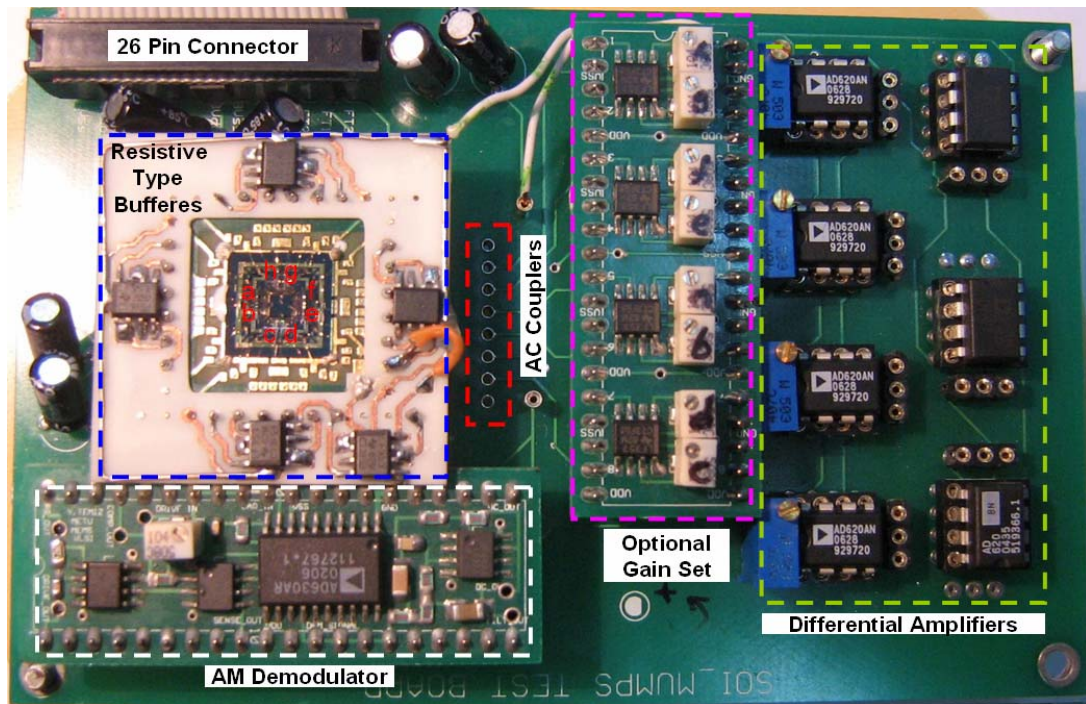


Figure 4.25: Main test board including the gyroscope, buffers, AC couplers, optional gain set, differential amplifiers, and the AM Demodulator.

#### 4.1.4 Self Resonance Loop and Test Setups

Keeping the resonance condition at drive mode is another problem to be solved for repeatable rate tests. This is because the drive mode is right on a blade edge while resonating and tends to diminish or blow up rather than resonate with maximized amplitude. The resonance is a marginal stable point in s-domain, thus, it is not stable and durable without a nonlinear control strategy, which dynamically modifies the root loci of the overall system to follow;

1. The minimum phase in between
2. The maximum amplitude.

Among these, keeping the phase between the sensed signal from the drive mode and the driving signal is a more reliable solution because of the lower fluctuation range and simpler realization. To achieve the phase locked resonance, a computer with AgilentVee software, an HP Infinium oscilloscope and a signal generator is required.

Figure 4.26 shows test setup including an HP Infinium oscilloscope for signal monitoring and phase data extraction, an Agilent 33120A Function / Arbitrary Waveform Generator for drive mode excitation, an Agilent E3631A power supply, an Agilent 34401A multimeter to collect the rate output data, a rate table with RS-232 communication (Ideal Aerosmith 1280, AERO 800 Table Controller), and, a PC to control the rate table, to store the collected rate data and drive mode frequency data while maintaining the self resonance loop.

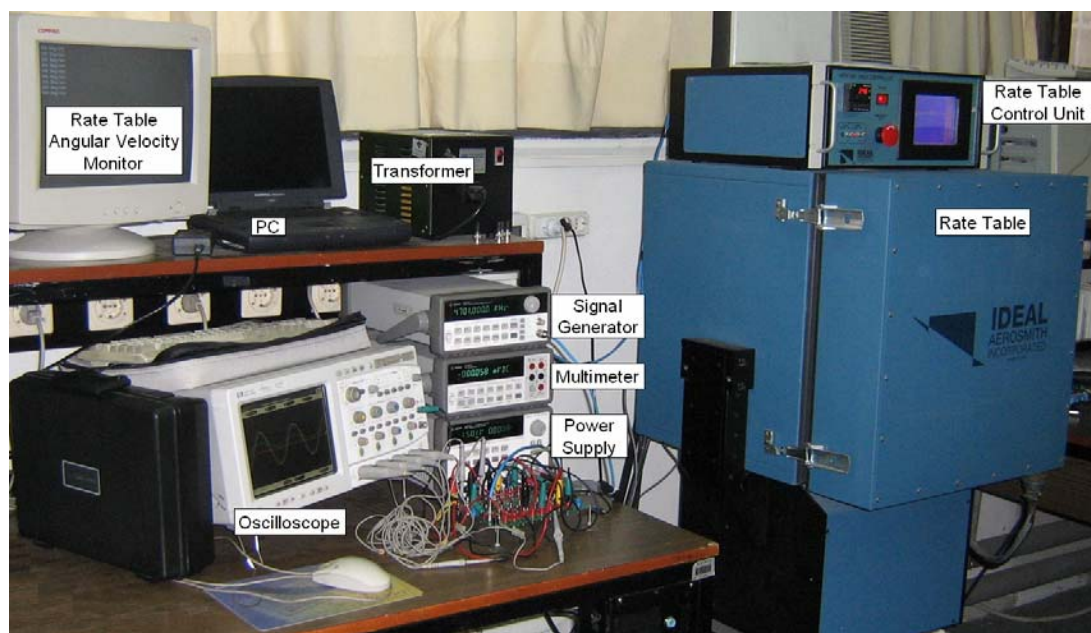


Figure 4.26: The test setup including an oscilloscope for signal monitoring and phase data extraction, a signal generator for drive mode excitation, a power supply, a multimeter to collect the rate output data, a rate table with RS-232 communication, and, a PC to control the rate table, to store the collected rate data and drive mode frequency data while maintaining the self resonance loop.

The self resonance loop is in a form of frequency controlled resonator. The control scheme of a PI controller is utilized in a different manner. The phase between the drive mode excitation signal and the drive mode pick signal is tried to be minimized

with the help of the measurement devices and the AgilentVee software. Figure 4.27 shows the control schematic running on AgilentVee. In the schematic, the period of the driving signal and the phase difference is read from the oscilloscope. The phase difference is usually sensed as the half of the period with a negative sign because of the notation used in oscilloscope. Thus, the error in the phase is calculated as the difference between the phase data and the half of the driving signal period ( $-B*0.5 - A$ ). This error is fed into an accumulator in the AgilentVee for error integration. Since this error is in the order of micro seconds, x10000 amplification is required to pass from time (period) domain to frequency domain. After adding an offset value for a faster convergence to the operational frequency, this frequency data is sent to the signal generator. As a result, the phase difference between the signal at the input and output of the drive mode is kept as small as possible, with a fluctuation of only 0.2 degrees.

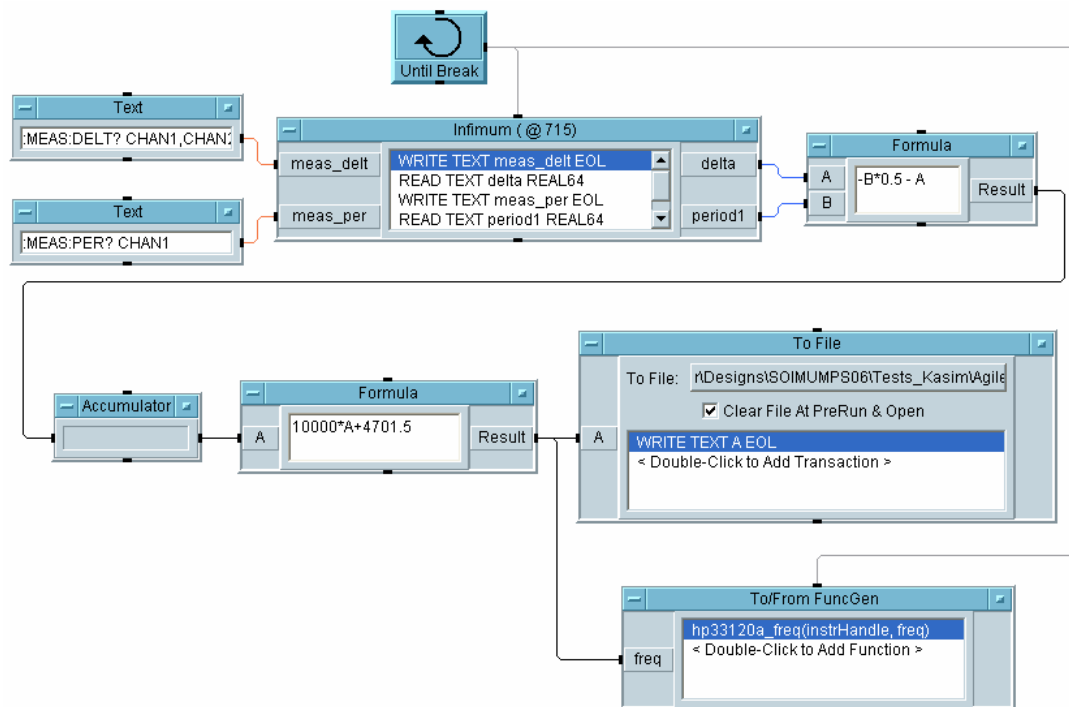


Figure 4.27: Control schematic running on AgilentVee.

There is an angular velocity limit of the rate table, which is  $\pm 1000$ deg/sec. For the rate tests under g-loading, the circuit board is placed 143mm off-centered on the rate table platform. Purpose of this off-centered placement is to induce the maximum

achievable centripetal acceleration on the sense mode, which is about 4.44g at  $\pm 1000$ deg/sec. Figure 4.28 shows the circuit board fixed to another apparatus for in-line and off-centered placement of the sense mode to the centripetal acceleration.

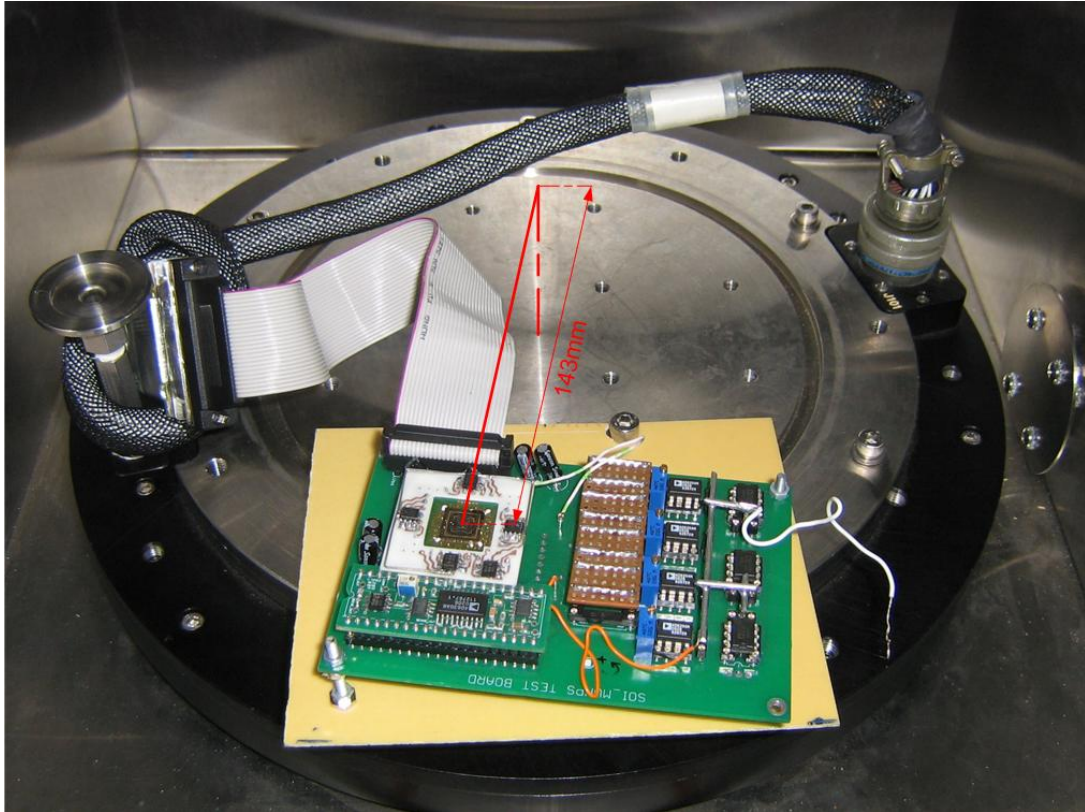


Figure 4.28: Circuit board fixed to another apparatus for in-line and off-centered placement of the sense mode to the centripetal acceleration.

## ***4.2 Test Results with Performance Characteristics of SMG, DMG and QMG***

The performance parameters of the fabricated gyroscopes are extracted from three different test sequences. At first, the quadrature and angular rate sensitivity data of the gyroscopes are extracted from the raw sensor output while the sensor is subject to sinusoidal inputs. This test is conducted without any electronic readout circuitry but only using a spectrum analyzer and the self resonance loop. In the second step, the output bias voltages of the gyroscopes are collected with zero angular rate input for several hours in order to extract the drift and noise parameters. In the third step, the

rate sensitivities of the gyroscopes are measured using the rate table. In these tests, the gyroscopes are fixed right at the center and away from the center to extract both the rate sensitivity and acceleration dependency of this rate sensitivity. The limitations on the number of connections of vacuum setup restrain the test procedure. At vacuum, due to the noise generated on the slip-rings of the gyroscope and bulky rate table setup, bias g-sensitivities and raw sensor output tests could not be done. Thus, at vacuum, the scale factor and the g-dependent scale factor drift tests are held. Additionally, at vacuum, the tests under zero input rate to extract the bias stability and angle random walk are also done.

#### **4.2.1 Performance Characteristics of SMG**

The main design purpose of the single mass gyro is to form a reference to be able to compare and estimate the improvements obtained by increasing the number of sensing masses and increasing the symmetric topology.

In this subsection, the performance parameters of the single mass gyroscope are presented. During the tests, the proof mass voltage is kept at +15V for all three gyroscopes, which corresponds to similar drive-to-sense matching conditions for a better comparison.

##### **4.2.1.1 Test Results of SMG at Atmospheric Ambient**

The raw sensor output of the SMG, which is the final stage in Figure 4.21, is extracted using Agilent 4295A Network / Spectrum / Impedance analyzer. The signal is swept in a band of 50 Hz. Figure 4.29 shows the output of the differentially amplified sense mode resistive buffers of the SMG in response to a sinusoidal rate input at 10 Hz with amplitude of  $2\pi$  deg/sec. The peak at the center is the quadrature coupling from drive mode to sense mode, which gives the rate equivalent quadrature of the gyroscope. The two peaks symmetric to the center peak are the response of the gyroscope structure to a sinusoidal input at  $(\omega-10)$ Hz and  $(\omega+10)$ Hz. Their magnitudes are slightly different due to the frequency gain of the sense mode system. These peaks reveal the raw angular rate sensitivity of the SMG.

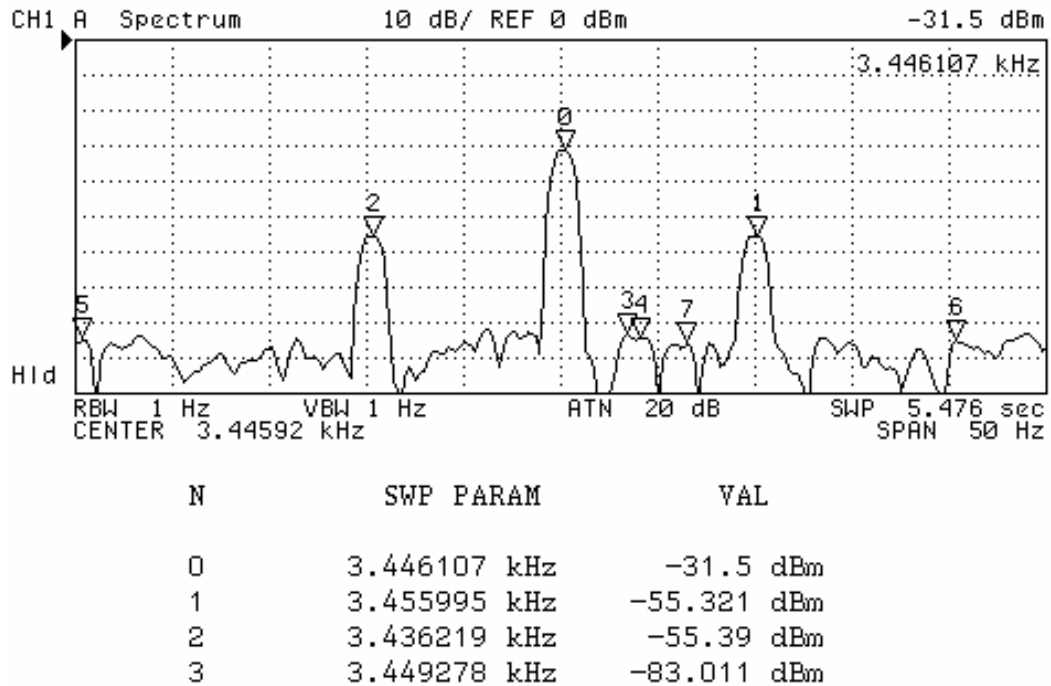


Figure 4.29: The output of the differentially amplified sense mode resistive buffers of the SMG in response to a sinusoidal rate input at 10 Hz with an amplitude of  $2\pi$  deg/sec.

For the SMG, the level of quadrature coupling is about 98.0 deg/sec and the raw angular rate sensitivity is  $60.5 \mu\text{V}/(\text{deg}/\text{sec})$ . These data give the standalone performance of the electromechanical gyroscope structure without external signal processing electronics.

The DC rate signal is obtained utilizing the AM modulator backed filter block. Figure 4.30 shows the four main signals probed on the gyroscope; the driving signal, the sensed signal from drive mode, the differentially amplified sense output and the DC rate signal. During the tests, it is observed that depending on the magnitude and direction of the input rate, the phase of the differential output node is shifting to right or left. Actually, the AM demodulator is evaluating the amount of Coriolis coupling with multiplying the sense mode output with the drive mode output. Thus, depending on the phase and magnitude of the quadrature coupling, a positive or negative bias at the DC rate output is observed.

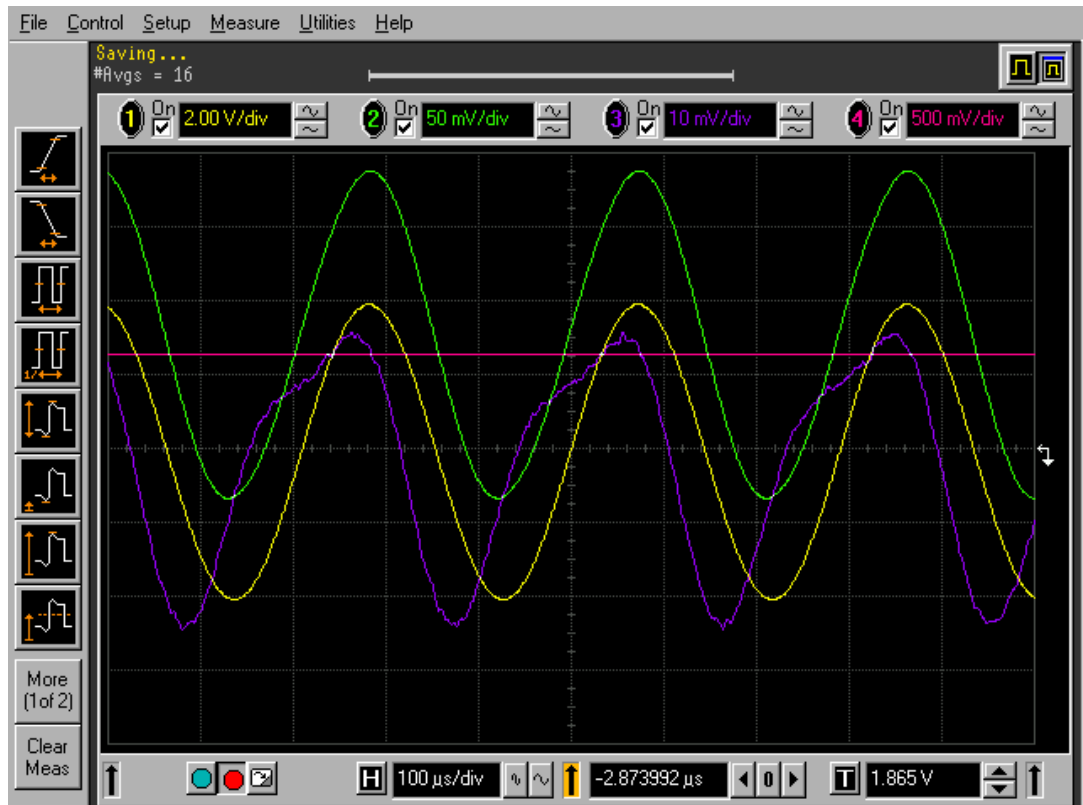
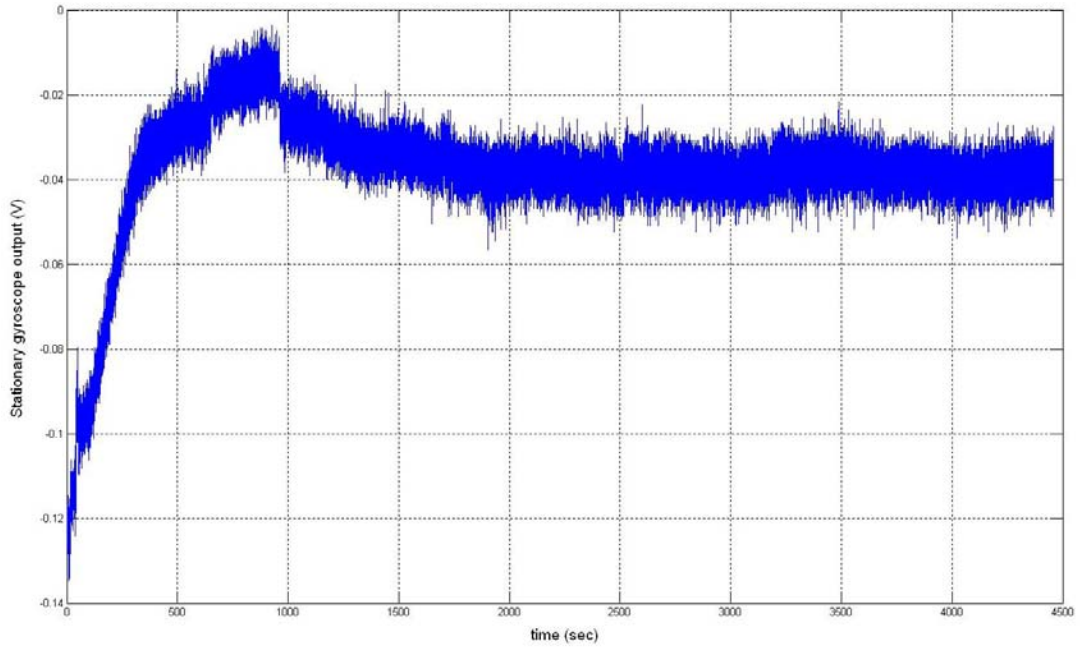
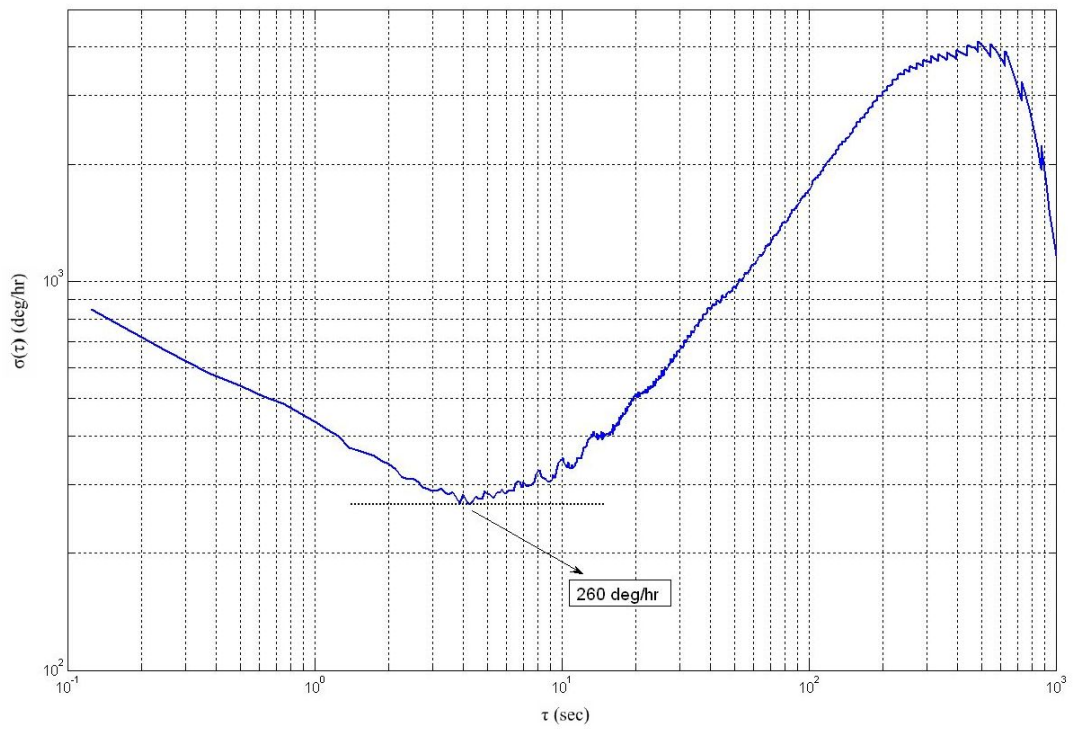


Figure 4.30: The four main signals probed on the gyroscope; the driving signal (yellow), the sensed signal from drive mode (green), the differentially amplified sense output (blue) and the DC rate signal (magenta).

Bias instability is the measure of resolvable rate for the given gyroscope. Angle random walk is related to the integral of the uncorrelated noise at the output. To determine the bias instability and the angle random walk, the gyroscope output is collected for about 1.5 hours. Using the Root Allan Variance method, the bias instability and the angle random walk of the SMG are calculated to be 391deg/hr and 5.2 deg/ $\sqrt{\text{hr}}$ , respectively. Figure 4.31 shows the bias drift and the Root Allan Variance curve of the SMG



(a)

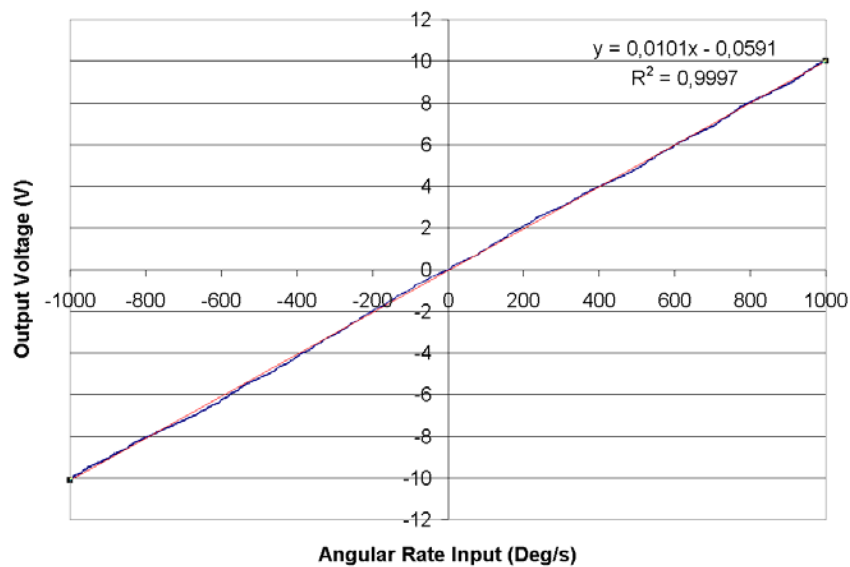


(b)

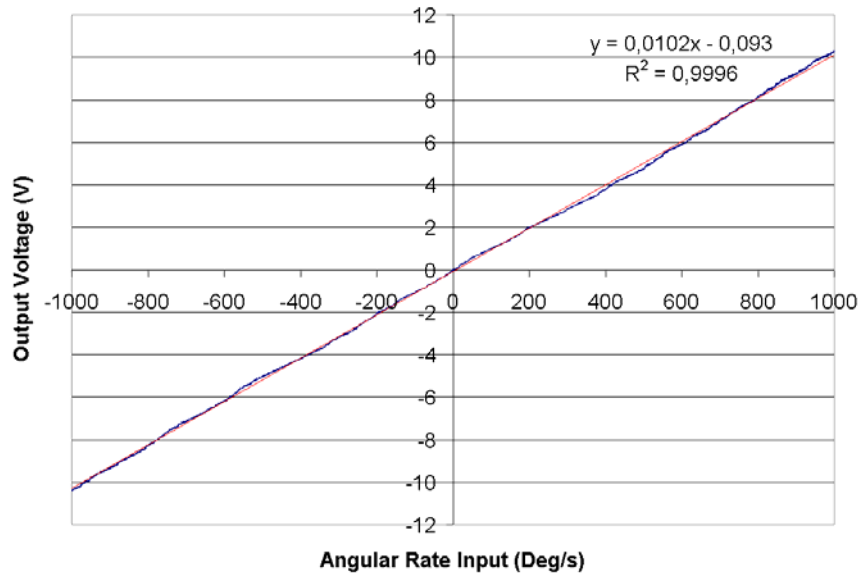
Figure 4.31: The bias drift (a) and the Root Allan Variance curve (b) of the SMG.

SMG is designed to have a dynamic range of  $\pm 1000$  deg/sec with scale factor nonlinearity less than 1.0%.

Figure 4.32 shows the rate output of the SMG under a constant angular acceleration of  $1\text{deg/sec}^2$  for centered and off-centered positioning which induces  $0\text{g}$  and  $4.44\text{g}$  centripetal acceleration on the sense mode resonator. The average scale factor of the gyroscope is  $10.1\text{ mV}/(\text{deg/sec})$  for zero  $g$ -loading and  $10.2\text{ mV}/(\text{deg/sec})$  for a loading of  $4.44\text{g}$  with nonlinearities of  $0.03\%$  and  $0.04\%$ , respectively.



(a)



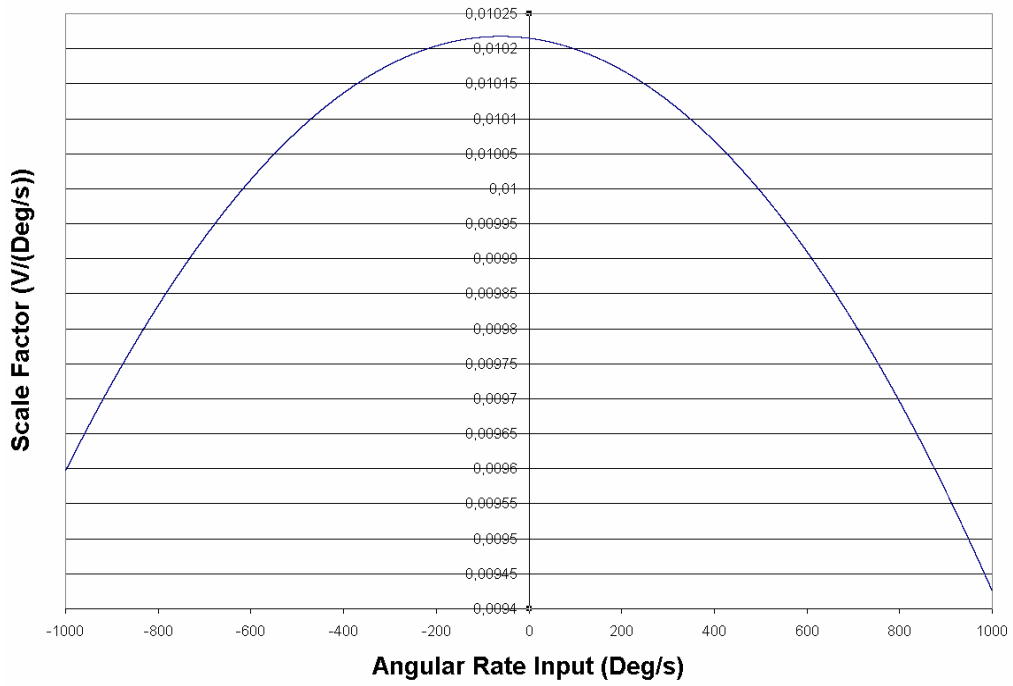
(b)

Figure 4.32: Rate output of the SMG under a constant angular acceleration of  $1\text{deg/sec}^2$  for centered (a) and off-centered (b) positioning. The average scale factor of the gyroscope is  $10.1\text{ mV}/(\text{deg/sec})$  for zero  $g$ -loading and  $10.2\text{ mV}/(\text{deg/sec})$  for a loading of  $4.44\text{g}$  with nonlinearities of  $0.03\%$  and  $0.04\%$  respectively.

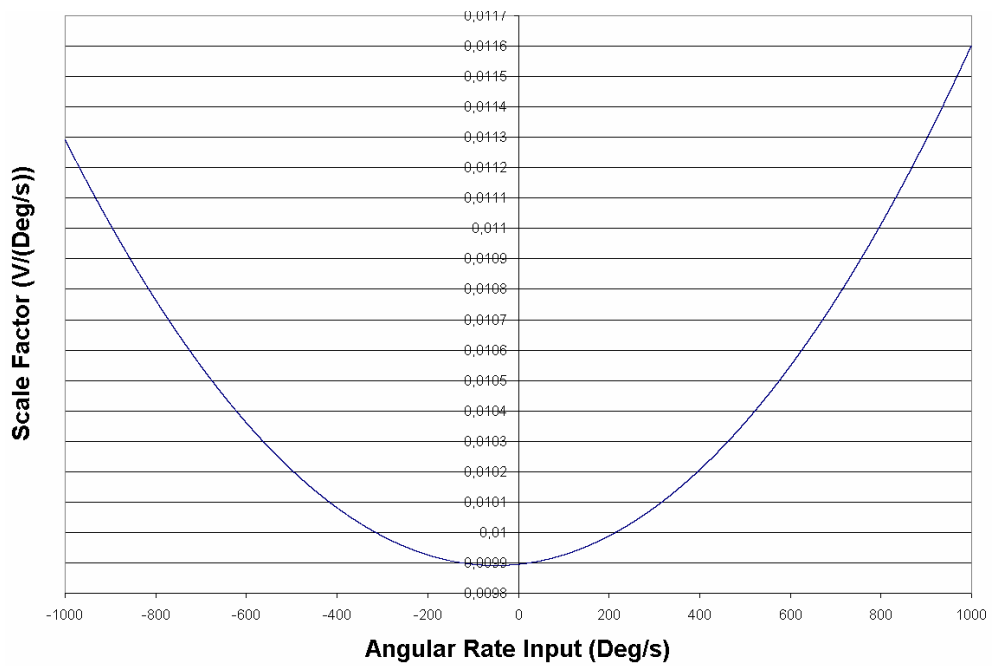
Figure 4.33 gives the plot of scale factor versus angular rate input of the SMG extracted from the scale factor for both centered (a) and off-centered (b) positioning. The g-sensitivity of the scale factor is extracted by measuring the drift of the scale factor with increasing acceleration in conjunction with the acceleration-free rate test.

The reason is that scale factors of gyroscopes are not only dependent on the accelerations but also spring or mass imbalances. Together with the noise and bias drift of the output voltage, it is not quite possible to extract the g-sensitivity of the gyroscope. For this purpose, a third order best-fit for the rate plot is obtained. Thus, the noise on the output is partially suppressed. Taking the derivative of this best-fit yield a parabola, this gives the trend of the scale factor with varying rate input. Since this procedure is followed for both the centered and off-center rate tests, effect of static acceleration on the output can be extracted.

For SMG, the acceleration-free scale factor deviation and acceleration induced scale factor deviation have completely different plots, which reveal a scale factor g-sensitivity of  $3.85(\text{mV}/(\text{deg}/\text{sec}))/\text{g}$ .



(a)



(b)

Figure 4.33: Plot of scale factor versus angular rate input of the SMG under the same constant angular acceleration of  $1\text{deg}/\text{sec}^2$  for centered (a) and off-centered (b) positioning.

Another performance parameter related to external acceleration loadings is the bias drift acceleration sensitivity. The test of this parameter consists of measuring the zero input rate output voltage of the sensor while the sense mode is subject to static

accelerations. Figure 4.34 shows the output bias of the SMG for different sense mode acceleration loadings. In the plot, an interesting and important detail is present. For a single mass gyroscope with differential readout circuitry, the rate output always increases under a static loading in the sense mode, if the fingers are exactly symmetric. The direction of the loading is not important. The reason of this lies in the quadratic character of the sense mode varying capacitances. Under a g-loading, a new equilibrium condition is set up with different sense finger gap spacing values. Since the increase in the gap spacing of one side is equal to the decrease in the gap spacing in the other side, the cumulative capacitance change is always positive. Thus, the output bias always increases under a g loading, if the sense sets are perfectly centered. In the case of the SMG, the sense modes are not perfectly centered due to process nonuniformities. Since there is only the differential reading present aiming to decrease the g-sensitivity, the bias g-sensitivity of the SMG is about 1.94 (deg/sec)/g.

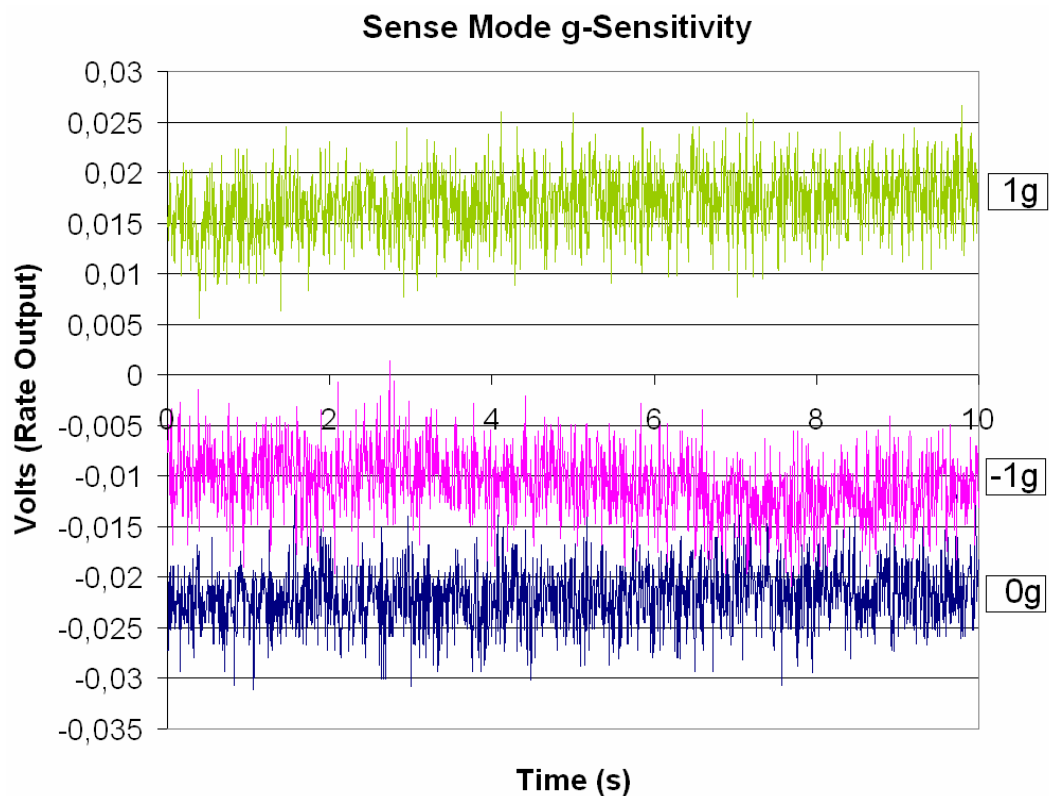
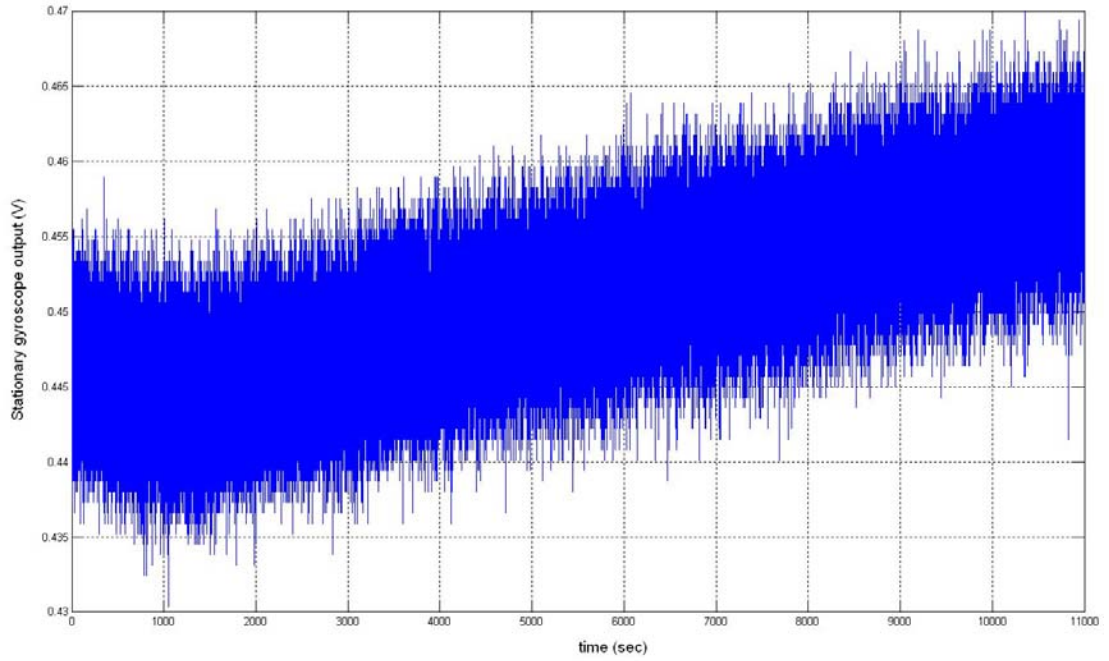


Figure 4.34: Output bias of the SMG for different sense mode acceleration loadings.

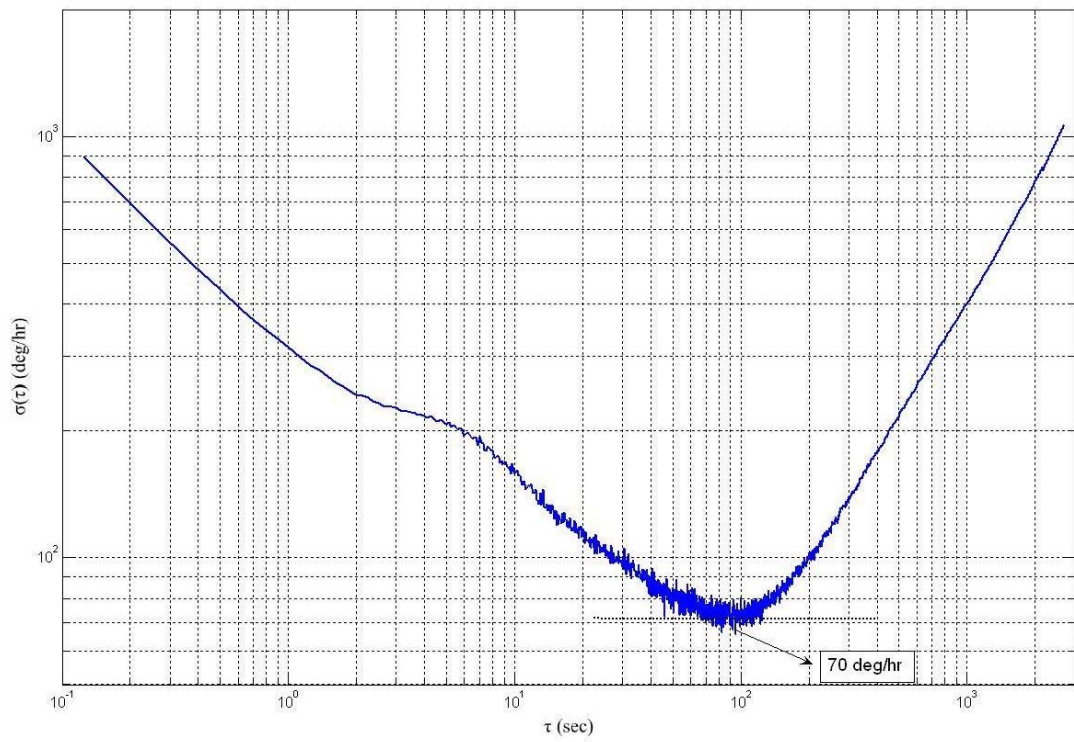
#### 4.2.1.2 Test Results of SMG at Vacuum Ambient

At vacuum, the required driving voltages and vibration amplitudes are much lower, which is a result of the increased Q factor. So, in general, the vacuum ambient increases the resolution and decreases the noise of the sensor. Figure 4.35 shows the bias drift and the Root Allan Variance curve of the SMG at vacuum. At vacuum, the bias instability and angle random walk of the SMG are measured to be 106 deg/hr and 4.8 deg/ $\sqrt{\text{hr}}$ , respectively.

Figure 4.36 gives the rate output and scale factor data plots of the SMG at vacuum under a constant angular acceleration of 1deg/sec<sup>2</sup>, while the gyroscope is centered on the rate table. The scale factor of the gyroscope is 8.9 mV/(deg/sec) for zero g-loading. The gyroscope has a very minute scale factor drift in the span of  $\pm 1000$  deg/sec in a linear manner due to the nonlinearities in the readout circuitry.

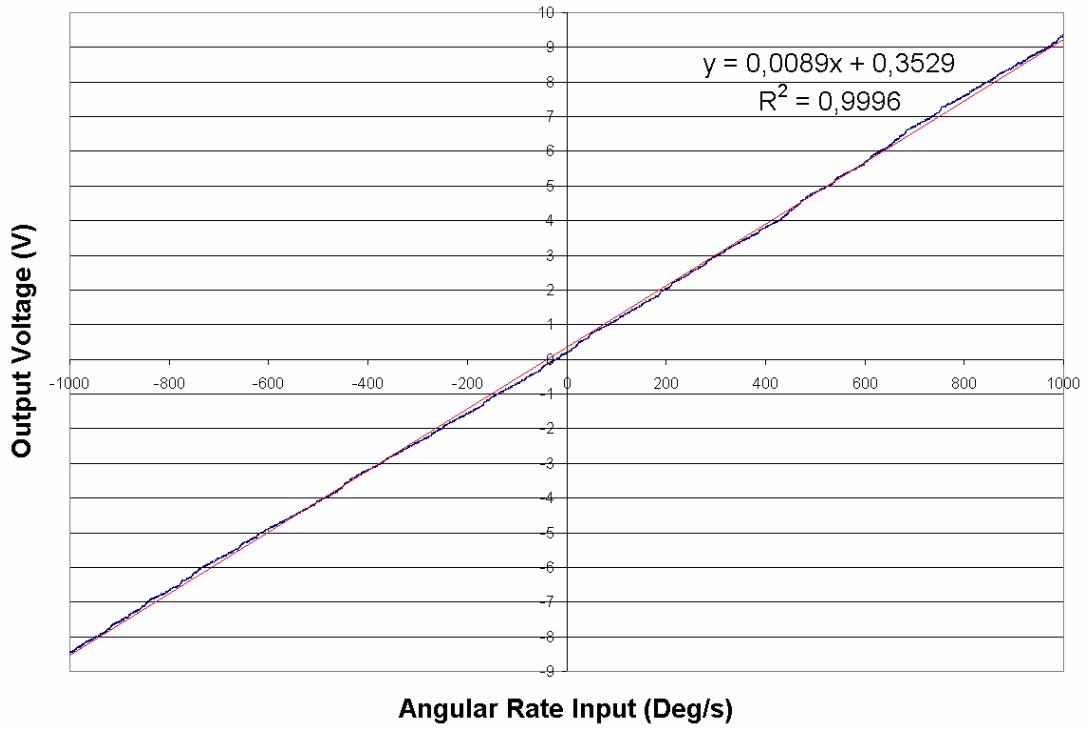


(a)

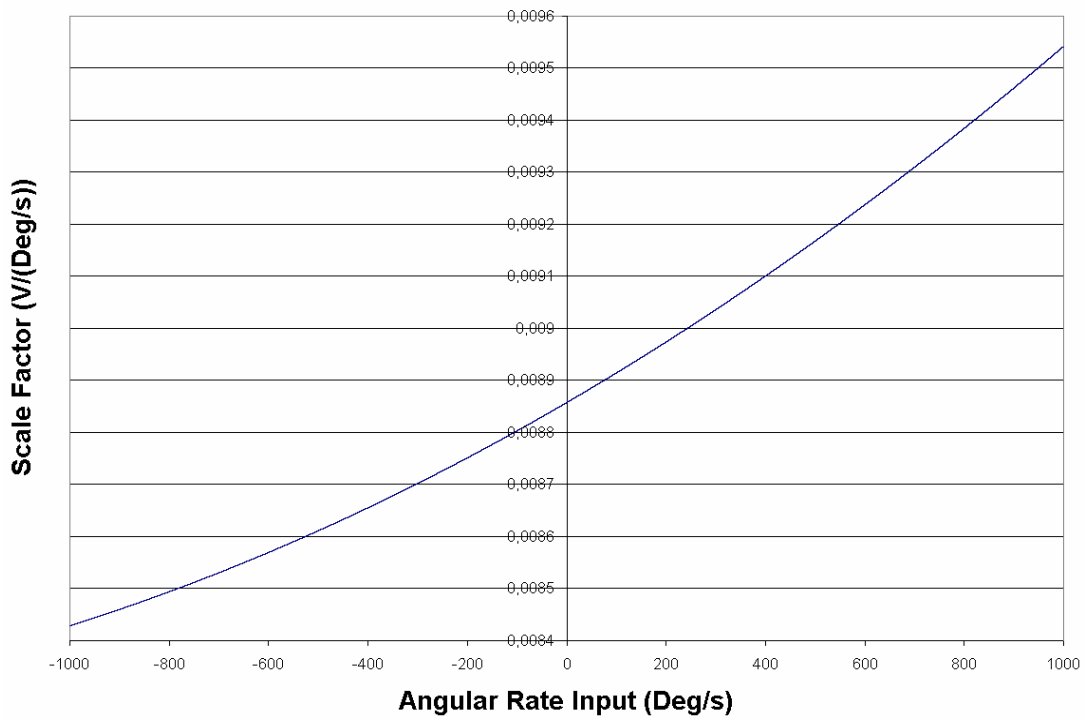


(b)

Figure 4.35: The bias drift (a) and the Root Allan Variance curve (b) of the SMG at vacuum.



(a)



(b)

Figure 4.36: Rate output and scale factor data plots of the SMG at vacuum under a constant angular acceleration of  $1\text{deg}/\text{sec}^2$  while the gyroscope is centered. The scale factor of the gyroscope is  $8.9\text{ mV}/(\text{deg}/\text{sec})$  for zero g-loading.

Finally, Table 4.1 presents overall performance specifications of the single-mass gyroscope in atmospheric pressure and in vacuum. Vacuum ambient decreases the noise floor and increases the resolution due to the increased Q factor and decreased Brownian noise.

Table 4.1: Performance specifications of the single-mass gyroscope in atmospheric pressure and in vacuum. Vacuum ambient decreases the noise floor and increases the resolution due to the increased Q factor and decreased Brownian type noise.

	Single Mass Gyroscope	
	Atmosphere	Vacuum
Drive Mode Resonance Frequency	3446 Hz	3451 Hz
Drive Mode Vibration Amplitude	16.8 $\mu\text{m}$	-
Drive Mode Quality Factor	216	-
Scale Factor	10.1mV/( $^{\circ}$ /s)	8.9 mV/( $^{\circ}$ /s)
R <sup>2</sup> nonlinearity	0.03 %	0.04 %
Bias Instability	391 $^{\circ}$ /hr	106 $^{\circ}$ /hr
Angle Random Walk	5.2 $^{\circ}$ / $\sqrt{\text{hr}}$	4.8 $^{\circ}$ / $\sqrt{\text{hr}}$
Bias g-sensitivity	1.94 ( $^{\circ}$ /s)/g	-
Scale Factor g-sensitivity	3.85 (mV/( $^{\circ}$ /s))/g	-
Raw Angular Rate Sensitivity	60.5 $\mu\text{V}$ /( $^{\circ}$ /s)	-
Rate Equivalent Quadrature	98.0 $^{\circ}$ /s	-
Frequency Margin For 40 $\mu\text{m}$	8 Hz	-

#### 4.2.2 Performance Characteristics of DMG

The twin tuning fork topology of the DMG aims to decrease the g-sensitivity of the SMG. The inherent out-of-phase driving capability of the topology brings reliability in tests.

In this subsection, the performance parameters of the double mass gyroscope are presented. During the tests, the proof mass voltage is kept at +15V for the gyroscopes, which corresponds to similar drive-to-sense matching conditions for a better comparison. Since the structure is symmetric, single piece and uniform, the frequency mismatch is assumed to be negligible.

### 4.2.2.1 Test Results of DMG at Atmospheric Ambient

Figure 4.37 shows the output of the twice differentially amplified sense mode resistive buffers of the DMG in response to a sinusoidal rate input at 10 Hz with amplitude of  $2\pi$  deg/sec. This spectrum reveals that DMG has a level of quadrature coupling of 413.4 deg/sec and raw angular rate sensitivity about  $45.6 \mu\text{V}/(\text{deg}/\text{sec})$ .

Quadrature error has several sources which may be added up to or subtracted from each other. In the case of DMG, the mechanical and electrical coupling has added up because of the phase. Hence the quadrature error increased with respect to the SMG.

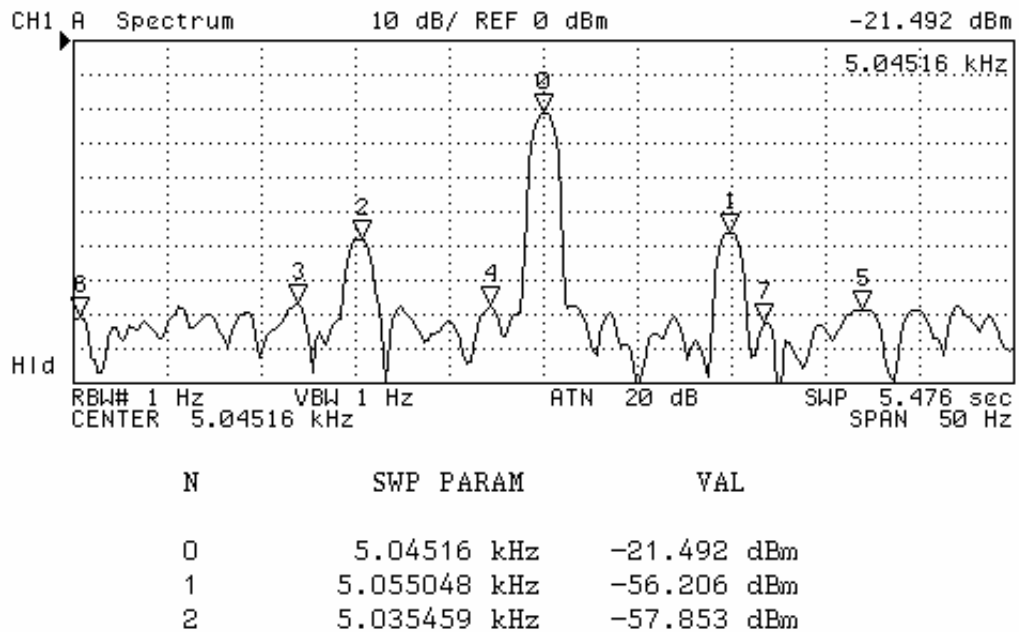


Figure 4.37: The output of the twice differentially amplified sense mode resistive buffers of the DMG in response to a sinusoidal rate input at 10 Hz with an amplitude of  $2\pi$  deg/sec.

Figure 4.38 shows the four main signals probed on the DMG; the driving signal, the sensed signal from drive mode, the differentially amplified sense output and the DC rate signal. The glitches on the differentially amplified sense output are due to the coupling from modulator circuitry. A portion of the quadrature error is the result of this coupling. Differential reading cannot overcome this problem because of the asymmetric PCB topology, which causes a minute coupling from the demodulator to the sensor outputs.

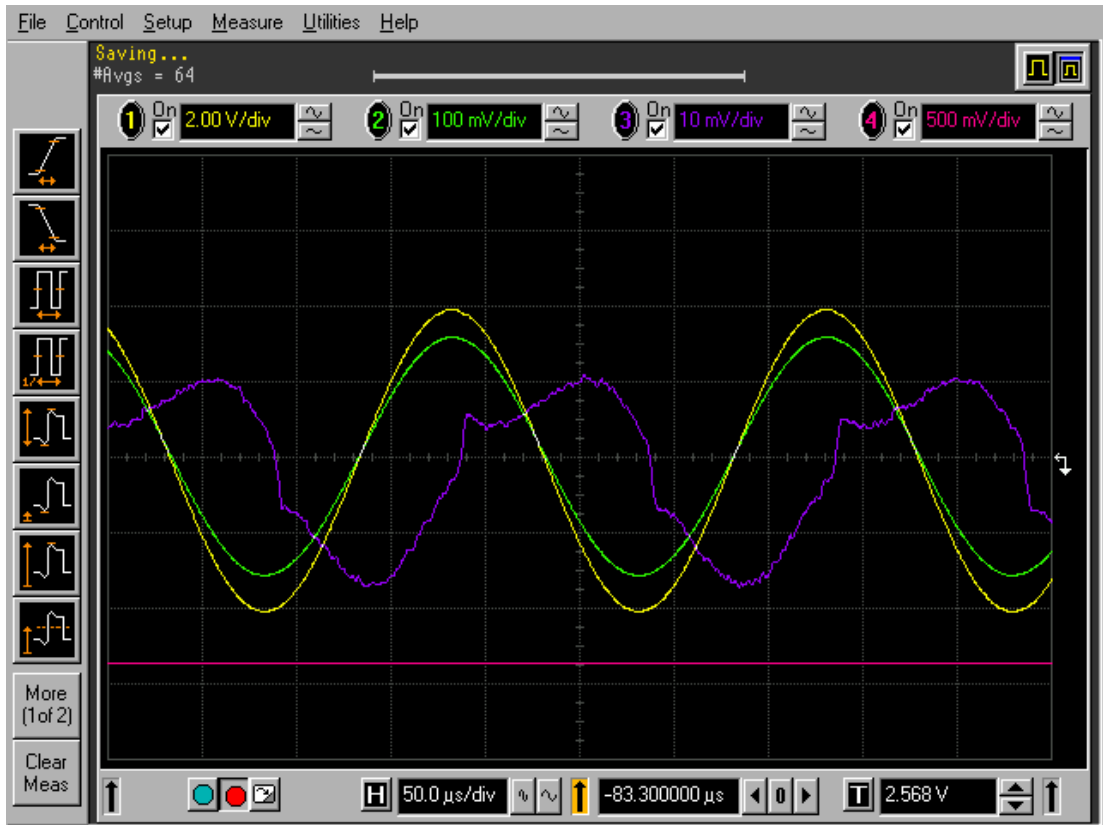
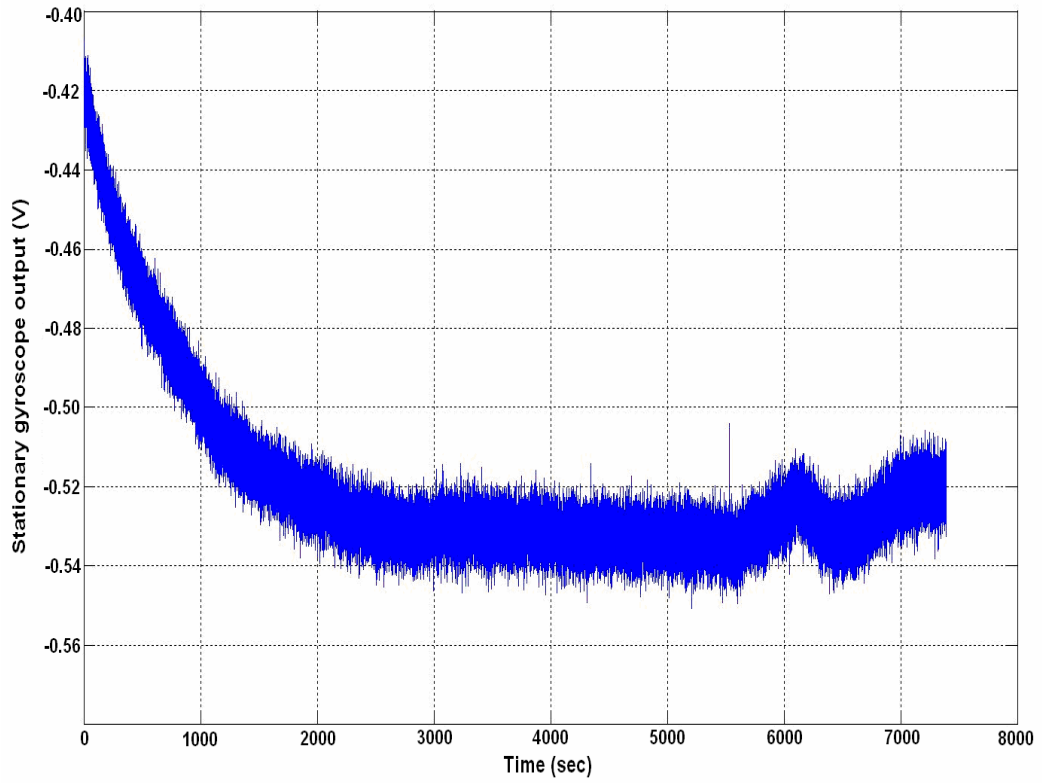
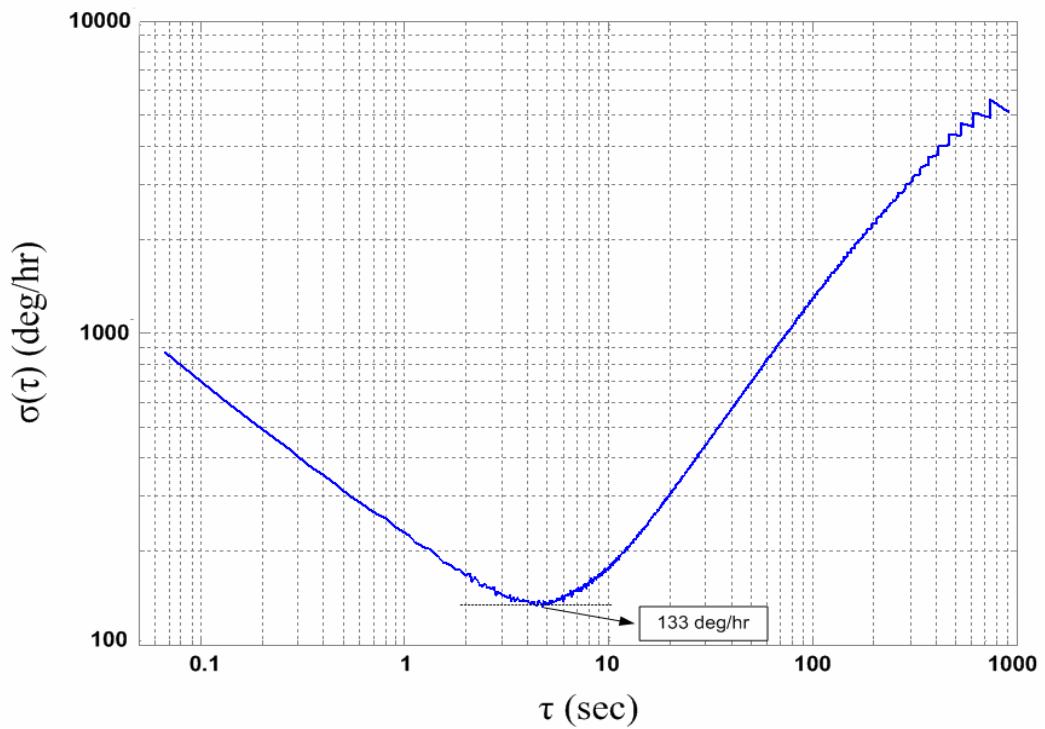


Figure 4.38: The four main signals probed on the gyroscope; the driving signal (yellow), the sensed signal from drive mode (green), the differentially amplified sense output (blue) and the DC rate signal (magenta).

Noise performance and resolution of the double mass gyroscope is measured to be similar to that of the SMG. This means that the mechanical performance of the coupling mechanism used does not affect the performance of the gyroscope, which is a proof of merit. Figure 4.39 shows the bias drift and the Root Allan Variance curve of the DMG, which correspond to a bias instability of 200deg/hr and an angle random walk of 5.47deg/ $\sqrt{\text{hr}}$ .



(a)



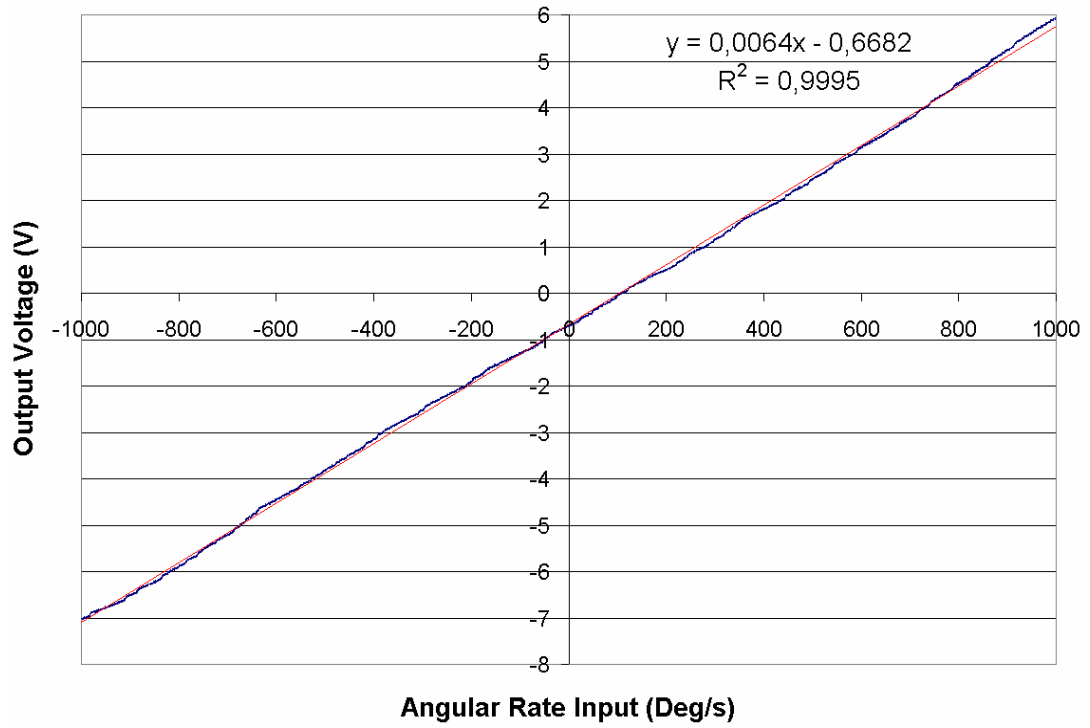
(b)

Figure 4.39: The bias drift and the Root Allan Variance curve of the DMG, which correspond to a bias instability of 200deg/hr and an angle random walk of 5.47deg/ $\sqrt{\text{hr}}$ .

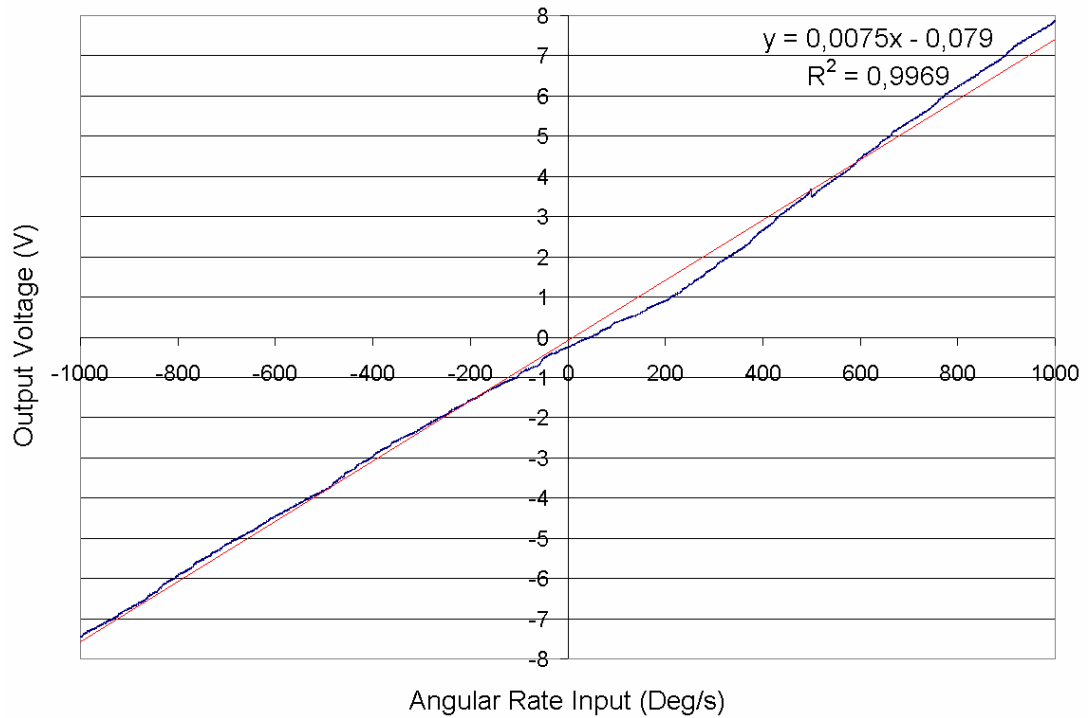
Since the sense mode structure and the proof mass of the DMG is very similar to that of the SMG, the same dynamic range and nonlinearity parameters of the SMG are applied. Figure 4.40 shows the rate output of the DMG under a constant angular acceleration of  $1\text{deg}/\text{sec}^2$  for both centered and off-centered positioning. The average scale factor of the gyroscope is measured to be  $6.4\text{ mV}/(\text{deg}/\text{sec})$  for zero g-loading and  $7.5\text{ mV}/(\text{deg}/\text{sec})$  for a loading of  $4.44\text{g}$  with nonlinearities of  $0.05\%$  and  $0.31\%$ , respectively.

The increase in the nonlinearity in off-centered test is supposed to be due to a hysteric mechanical problem on the gyroscope. Especially the deviation in the linearity between  $0\text{deg}/\text{sec}$  and  $500\text{deg}/\text{sec}$  and the glitch at about this angular velocity reveals the afore-mentioned hysteric problem, possibly due to a very small etch defect.

It is measured that the variation of scale factor of the DMG is very different than that of the SMG. Figure 4.41 shows the plot of scale factor versus angular rate input of the DMG under the same constant angular acceleration of  $1\text{deg}/\text{sec}^2$  for centered and off-centered positioning. In both of these plots, the ends of the parabolas rise up, meaning that the scale factor drift is increasing with increasing g-loading. Besides, the acceleration dependent scale factor drift is  $2.16\text{ (mV}/(\text{deg}/\text{sec}))/\text{g}$ , which is close to the half that of the SMG.

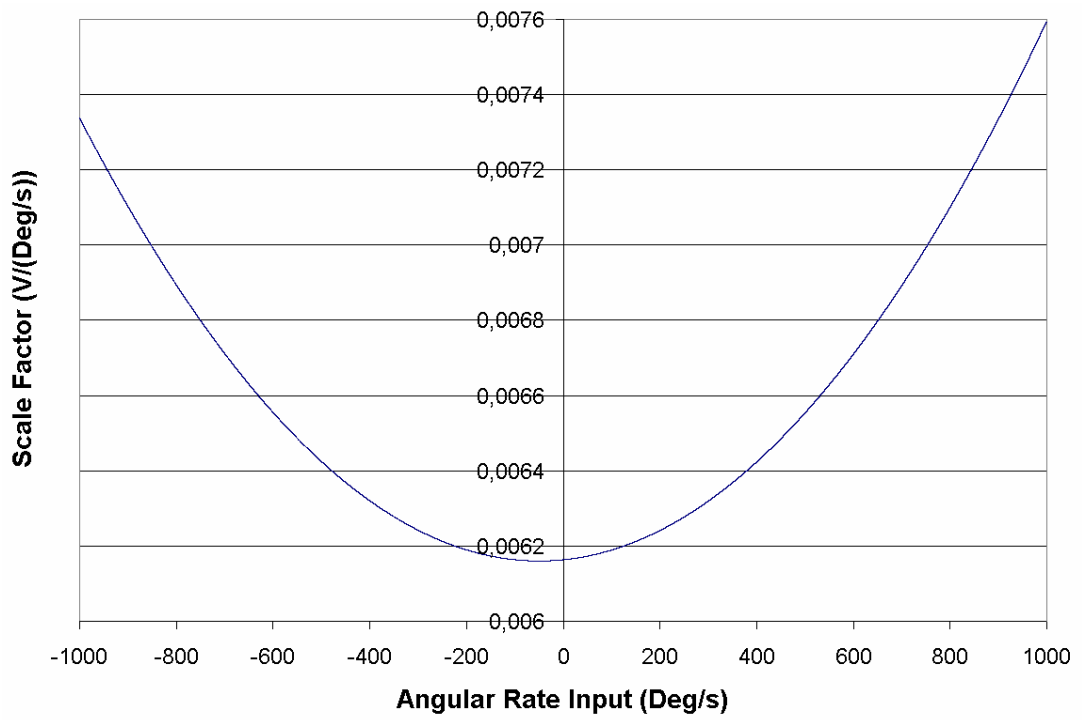


(a)

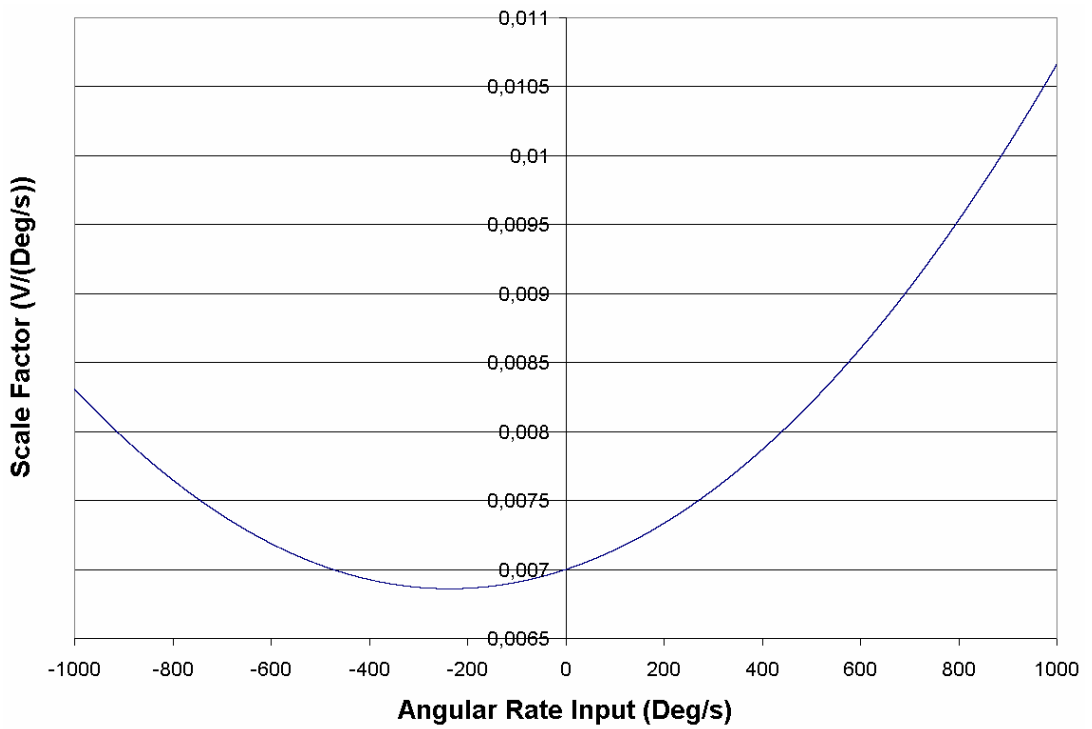


(b)

Figure 4.40: Rate output of the DMG under a constant angular acceleration of  $1 \text{ deg/sec}^2$  for centered (a) and off-centered (b) positioning. The average scale factor of the gyroscope is measured to be  $6.4 \text{ mV}/(\text{deg/sec})$  for zero g-loading and  $7.5 \text{ mV}/(\text{deg/sec})$  for a loading of  $4.44g$  with nonlinearities of  $0.05\%$  and  $0.31\%$ , respectively.



(a)



(b)

Figure 4.41: Plot of scale factor versus angular rate input of the DMG under the same constant angular acceleration of  $1\text{deg}/\text{sec}^2$  for centered (a) and off-centered (b) positioning.

The g-test results of the DMG are also better than the SMG. Figure 4.42 shows the output voltage of the DMG at rest with linear accelerations of 0g, -1g and 1g in the sense mode, corresponding to a bias g-sensitivity of 1.67(deg/sec)/g.

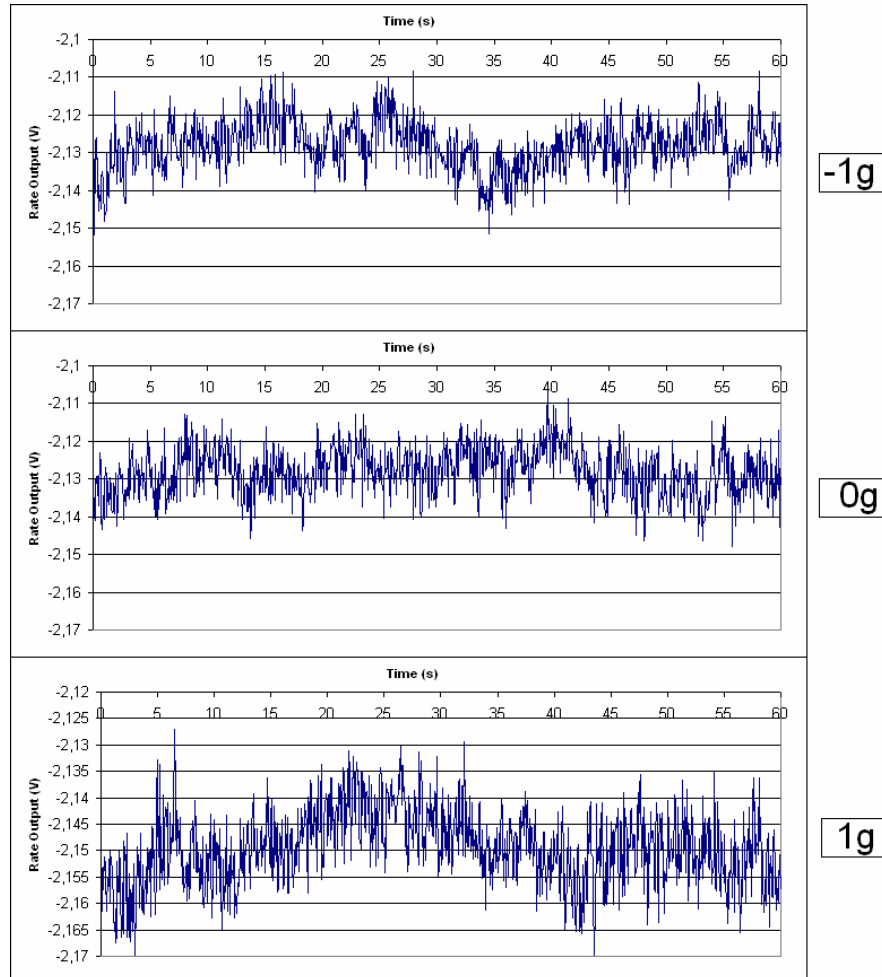


Figure 4.42: The output voltage of the DMG at rest with linear accelerations of 0g, -1g and 1g in the sense mode.

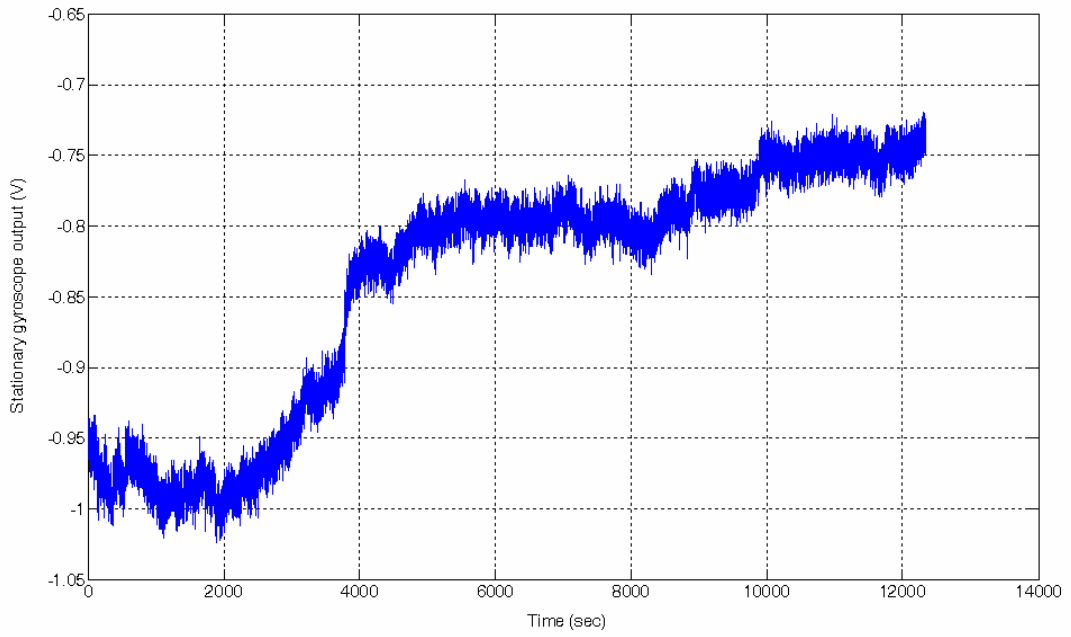
Although the g-sensitivity of the bias is decreased with respect to SMG, this value is still high compared to the tuning fork gyroscopes in the literature. The possible reasons are low performance readout electronics and the mismatched operation conditions together with the high vibration amplitude.

#### 4.2.2.2 Test Results of DMG at Vacuum Ambient

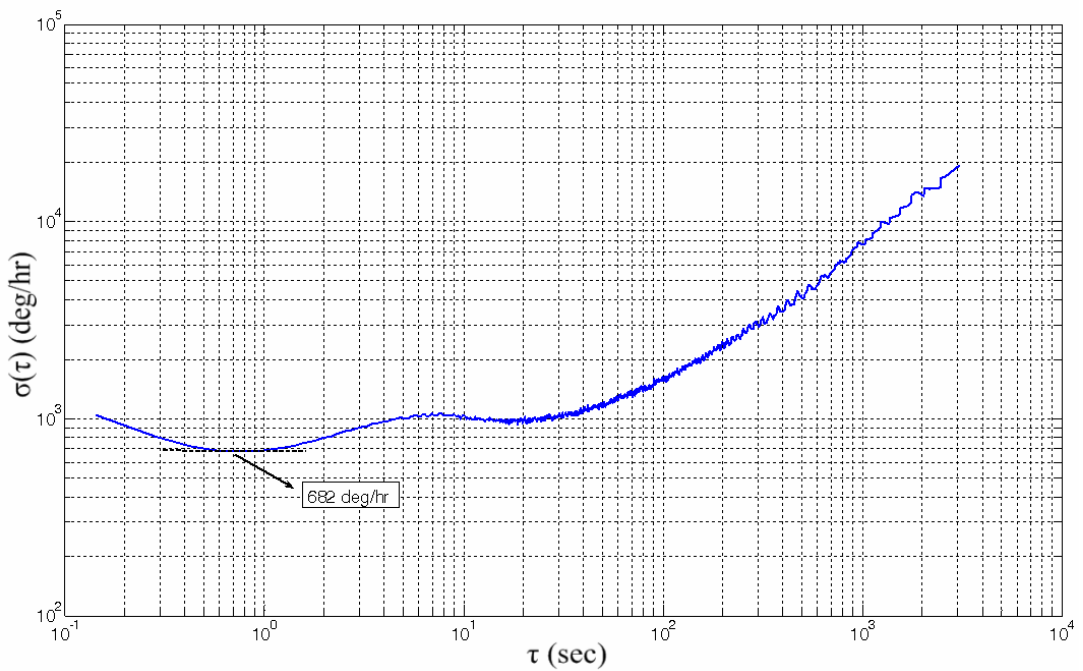
Although all the performance parameters of the DMG at vacuum is expected to be better than that of atmospheric pressure, bias instability and angle random walk of the output on a zero rate input is higher than the atmospheric ambient.

Figure 4.43 shows bias drift and the Root Allan Variance curve of the DMG, corresponding to a bias drift and an angle random walk of 1028deg/hr and 6.7deg/ $\sqrt{\text{hr}}$ , respectively. The non-ideal temperature control, process variations on the chip itself or a process nonuniformity.

Figure 4.44 shows the rate output and the scale factor data plots of the DMG at vacuum under a constant angular acceleration of 1deg/sec<sup>2</sup> while the gyroscope is centered. The scale factor of the gyroscope is 11.8 mV/(deg/sec) for zero g-loading. The asymmetry in the drive-to-sense coupling is possibly due to the fabrication nonuniformities or nonuniform structural electronic resistance.

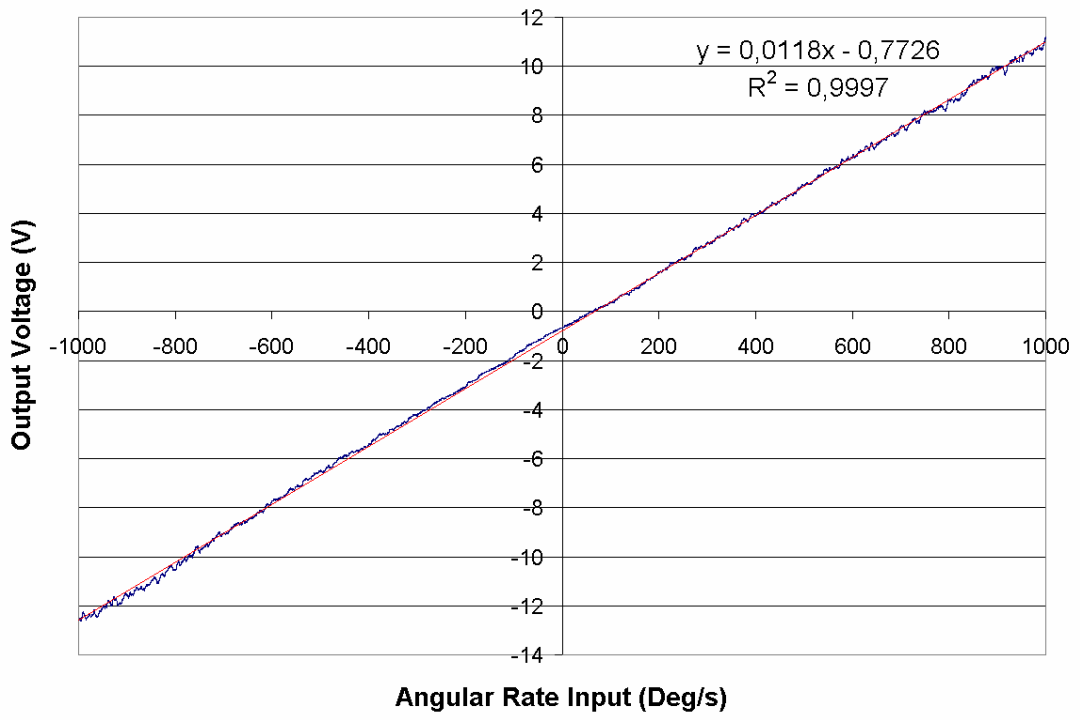


(a)

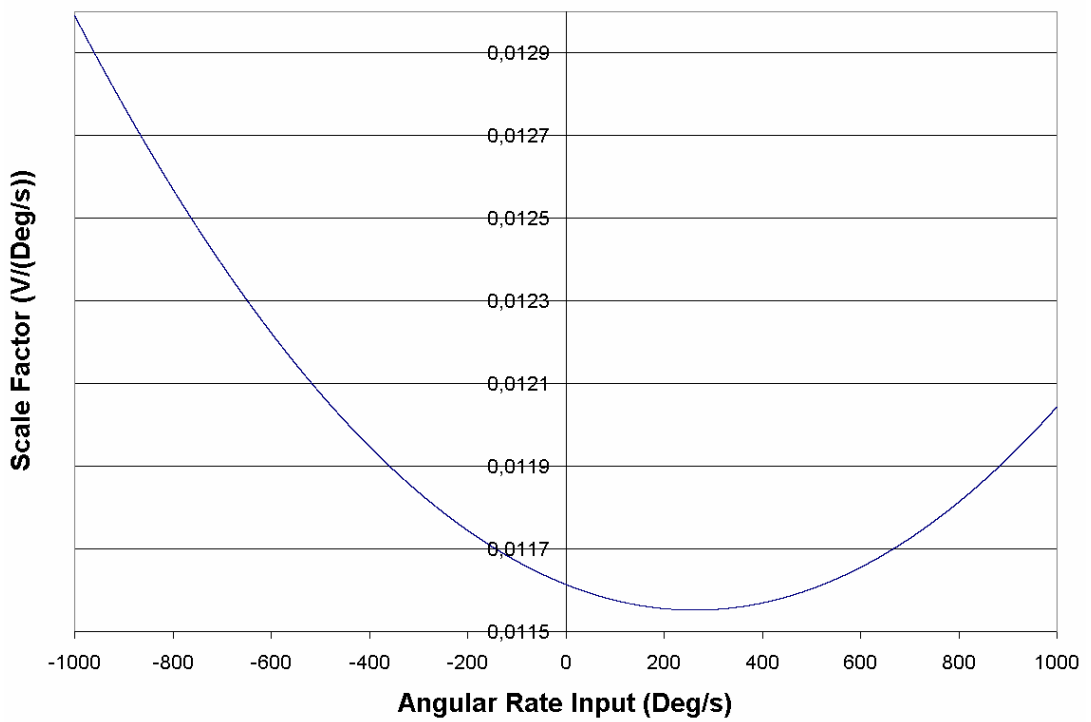


(b)

Figure 4.43: The bias drift (a) and the Root Allan Variance curve (b) of the DMG, corresponding to a bias drift and an angle random walk of 1028deg/hr and 6.7 deg/ $\sqrt{\text{hr}}$ , respectively.



(a)



(b)

Figure 4.44: Rate output and scale factor data plots of the DMG at vacuum under a constant angular acceleration of  $1 \text{ deg/sec}^2$  while the gyroscope is centered. The scale factor of the gyroscope is  $11.8 \text{ mV}/(\text{deg/sec})$  for zero g-loading together with 0.03% nonlinearity.

Finally, Table 4.2 presents overall performance specifications of the double-mass gyroscope in atmospheric pressure and in vacuum. Vacuum ambient decreases the nonlinearities due to the decreased vibration amplitude but also decreased the resolution and increased the angle random walk, possibly due to process non-uniformities.

Table 4.2: Performance specifications of the double-mass gyroscope in atmospheric pressure and in vacuum.

	Double Mass Gyroscope	
	Atmosphere	Vacuum
Drive Mode Resonance Frequency	5045 Hz	5058 Hz
Drive Mode Vibration Amplitude	12.6 $\mu\text{m}$	-
Drive Mode Quality Factor	303	-
Scale Factor	6.4 mV/(°/s)	11.8 mV/(°/s)
R <sup>2</sup> nonlinearity	0.05 %	0.03 %
Bias Instability	200 °/hr	1028.65 °/hr
Angle Random Walk	5.47 °/ $\sqrt{\text{hr}}$	6.7 °/ $\sqrt{\text{hr}}$
Bias g-sensitivity	1.67 (°/s)/g	-
Scale Factor g-sensitivity	2.16 (mV/(°/s))/g	-
Raw Angular Rate Sensitivity	45.6 $\mu\text{V}/(^\circ/\text{s})$	-
Rate Equivalent Quadrature	413.4 °/s	-
Frequency Margin For 40 $\mu\text{m}$	9 Hz	-

### 4.2.3 Performance Characteristics of QMG

QMG is designed to diminish the asymmetry problems in the DMG due to its twin tuning fork topology together with the decreased g-sensitivity.

In this subsection, the performance parameters of the quadruple mass gyroscope are presented. During the tests, the proof mass voltage is kept at +15V. Besides, all seven differential amplifiers are utilized for complete differential sensing.

#### 4.2.3.1 Test Results of QMG at Atmospheric Ambient

Figure 4.45 shows the output of sense mode resistive buffers, which are differentially amplified in three stages, of the QMG in response to a sinusoidal rate input at 10 Hz

with an amplitude of  $2\pi$  deg/sec. This spectrum reveals that QMG has a level of quadrature coupling at 273.3 deg/sec and raw angular rate sensitivity about 131.8  $\mu\text{V}/(\text{deg}/\text{sec})$  at atmospheric ambient.

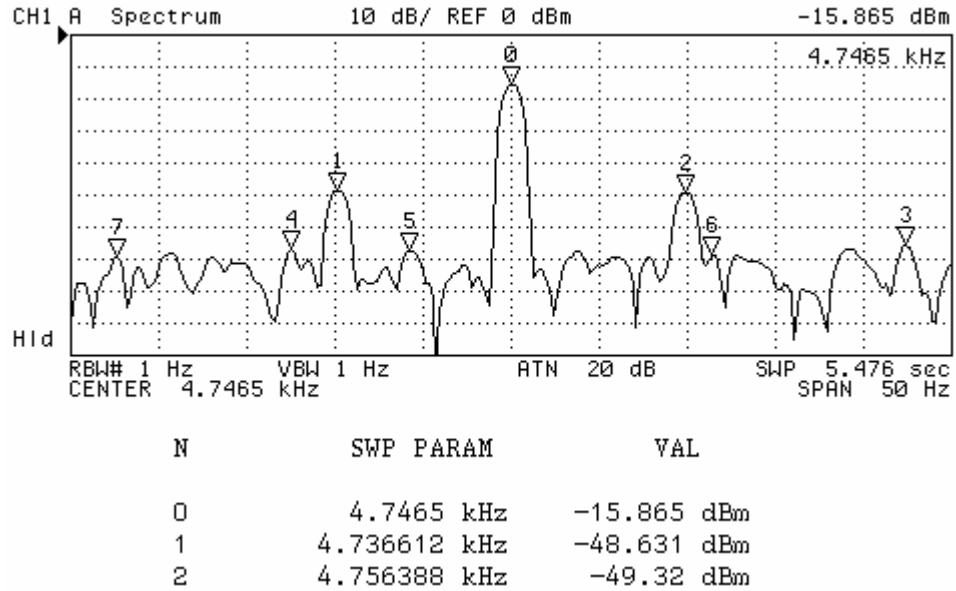


Figure 4.45: The output of sense modes resistive buffers, which are differentially amplified in three stages, of the QMG in response to a sinusoidal rate input at 10 Hz with an amplitude of  $2\pi$  deg/sec.

Figure 4.46 shows the four main signals probed on the QMG; the driving signal, the sensed signal from drive mode, the differentially amplified sense output and the DC rate signal. The singularities (glitches) on the differentially amplified sense output are due to the coupling from modulator circuitry. A portion of the quadrature error is the result of this coupling.

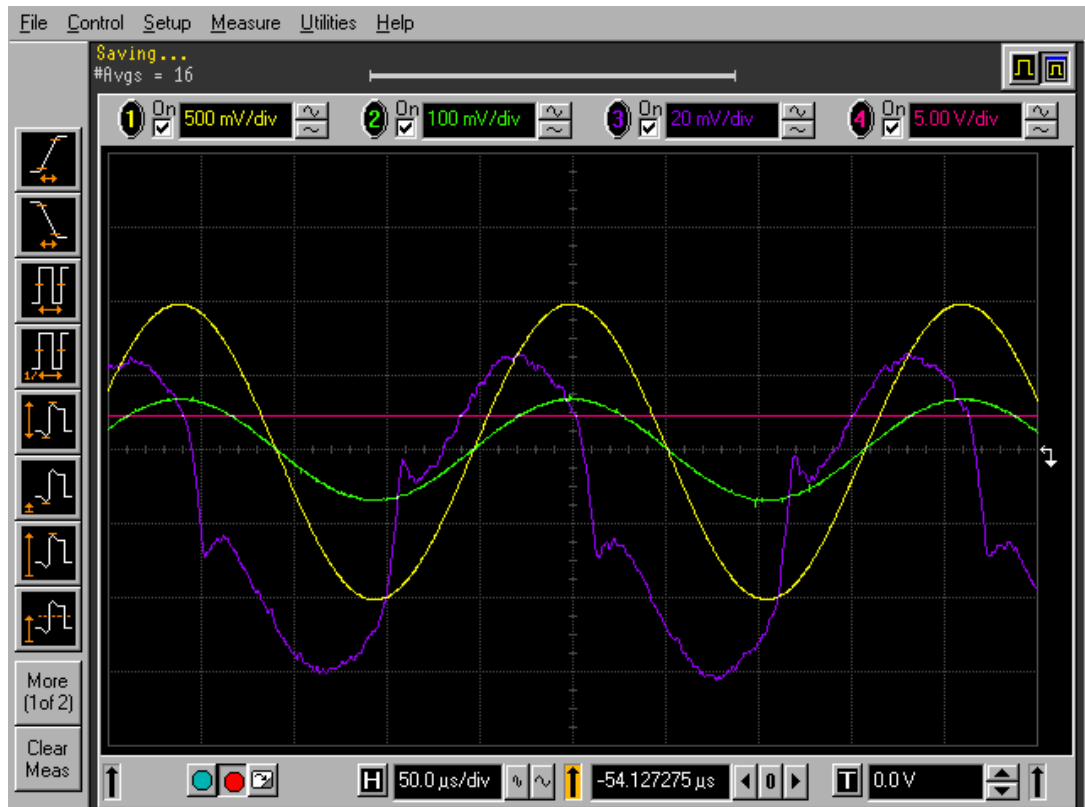
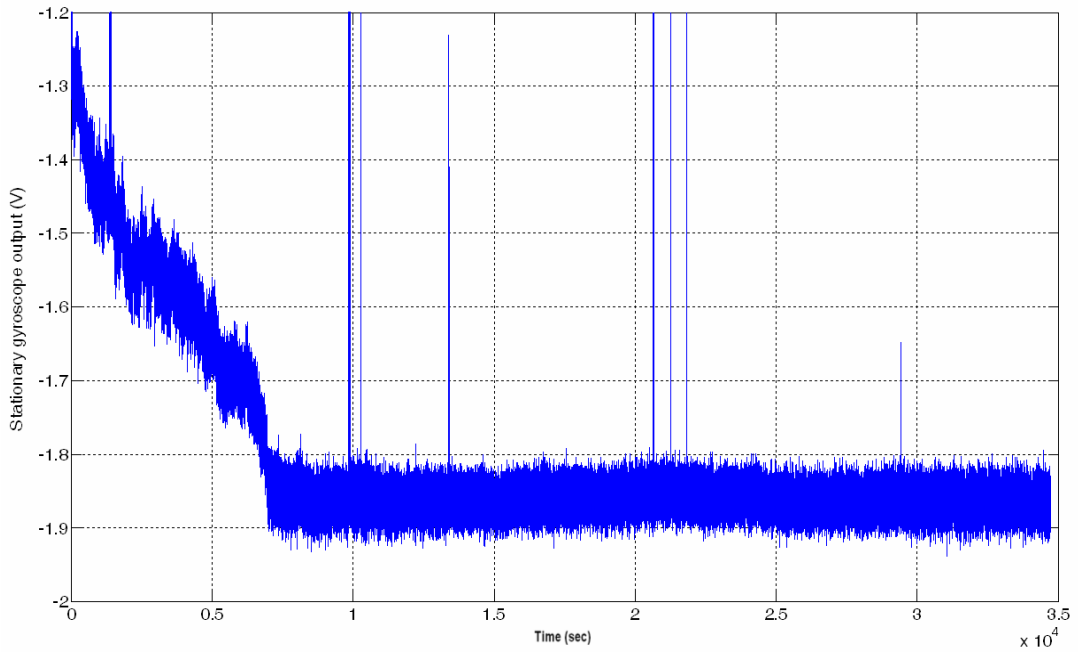
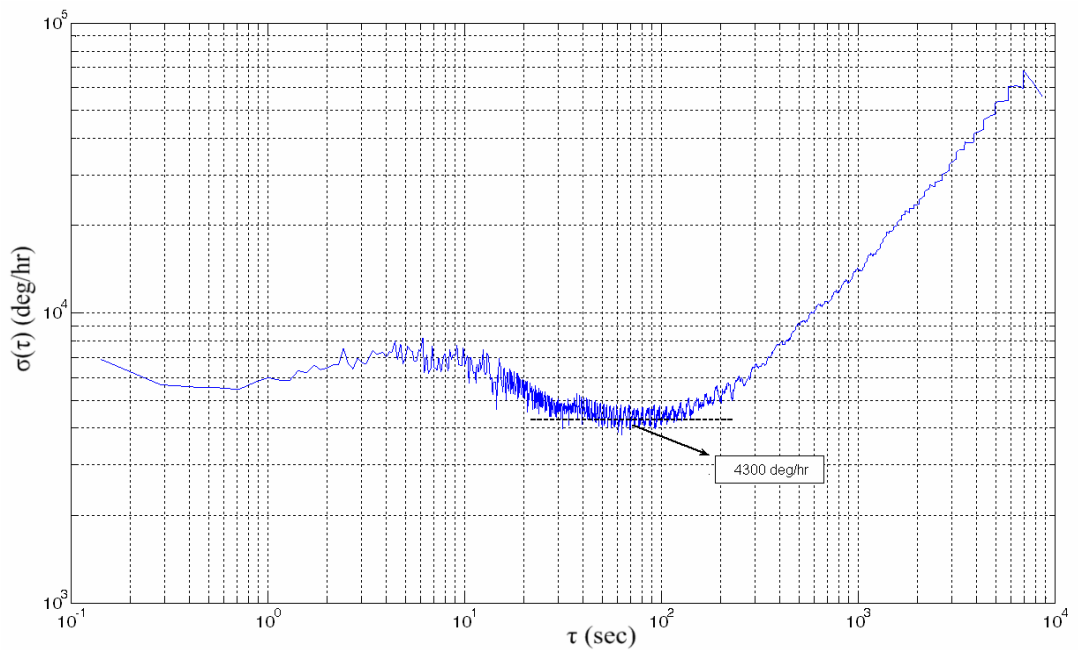


Figure 4.46: The four main signals probed on the gyroscope; the driving signal (yellow), the sensed signal from drive mode (green), the differentially amplified sense output (blue) and the DC rate signal (magenta).

The symmetric coupling mechanism with 4 separate masses decreases the noise performance and resolution due to the large sensor area with process variations and very high damping coefficient compared to the double mass and single mass gyroscope. Figure 4.47 shows the bias drift and the Root Allan Variance curve of the DMG, which correspond to a bias instability of 1.8 deg/sec (6485 deg/hr) and an angle random walk of 43.2 deg/ $\sqrt{\text{hr}}$ .



(a)

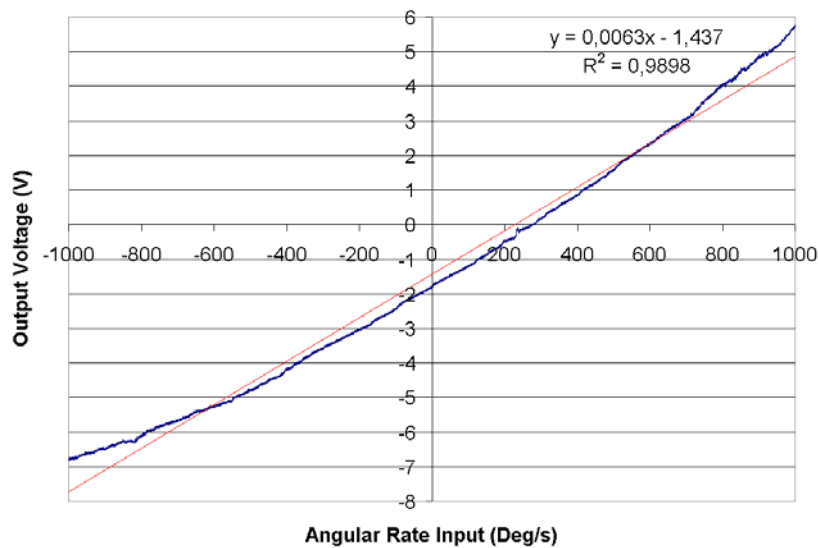


(b)

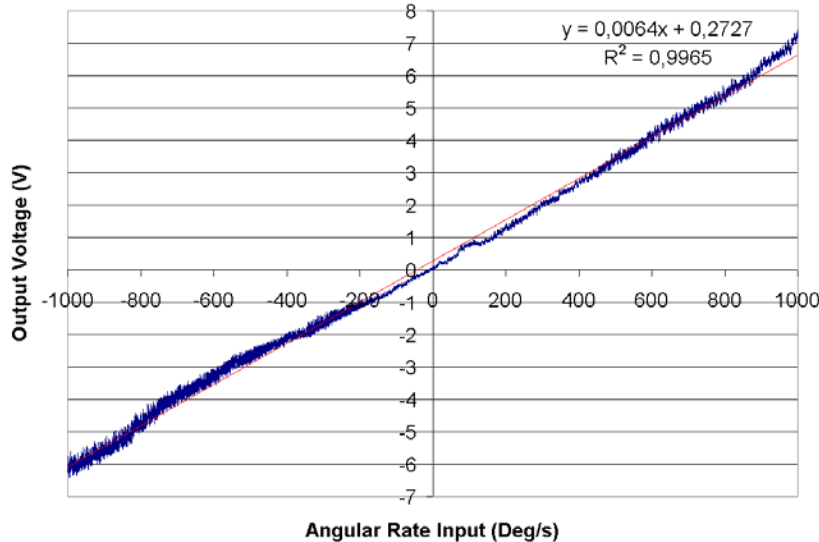
Figure 4.47: The bias drift and the Root Allan Variance curve of the DMG, which correspond to a bias instability of 1.8deg/sec (6485 deg/hr) and an angle random walk of 43.2 deg/ $\sqrt{\text{hr}}$ .

Since the sense mode structure and the proof mass of all three gyroscope structures are very similar, the same dynamic range and nonlinearity parameters are applied. Figure 4.48 shows the rate output of the QMG under a constant angular acceleration

of  $1 \text{ deg/sec}^2$  for both centered and off-centered positioning. The average scale factor of the gyroscope is measured to be  $6.3 \text{ mV}/(\text{deg/sec})$  for zero g-loading and  $9.2 \text{ mV}/(\text{deg/sec})$  for a loading of  $4.44\text{g}$  with nonlinearities of  $1.02 \%$  and  $0.35$ , respectively. The nonlinear character of the QMG at atmospheric pressure is due to its large die size and high damping coefficients. The off-centered positioning of the QMG affected stability negatively. This is possibly due to the different damping coefficients on each mass and slightly different sense mode resonance frequencies.



(a)



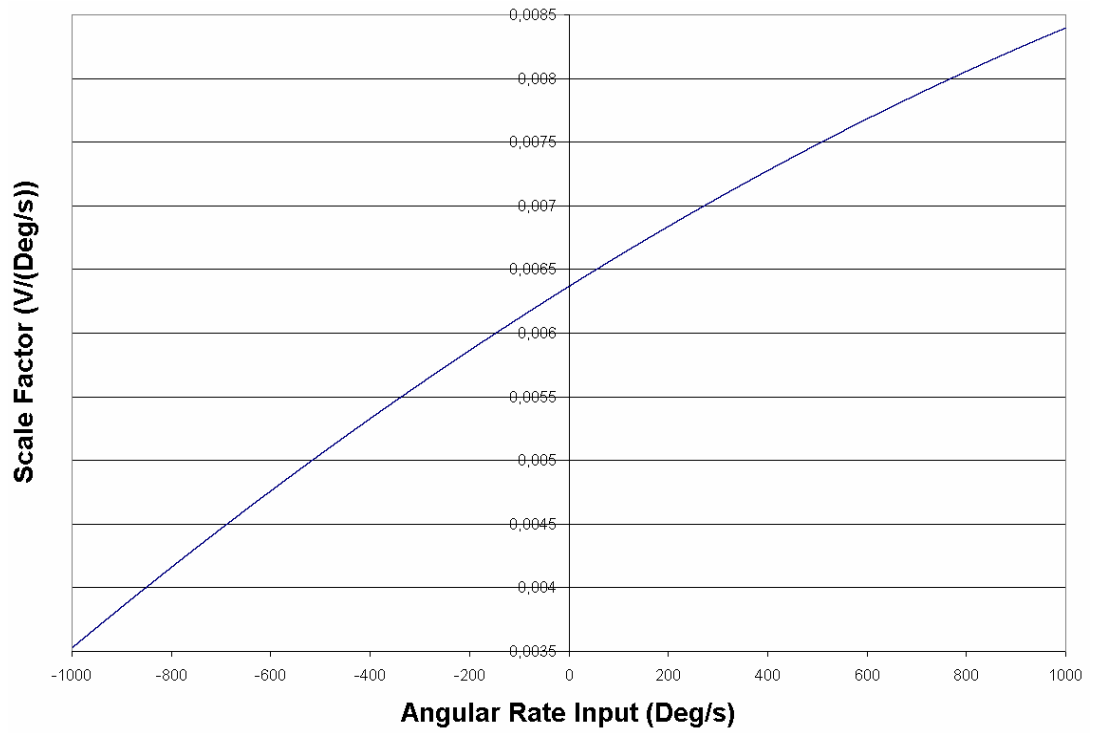
(b)

Figure 4.48: Rate output of the QMG under a constant angular acceleration of  $1 \text{ deg/sec}^2$  for both centered (a) and off-centered (b) positioning.

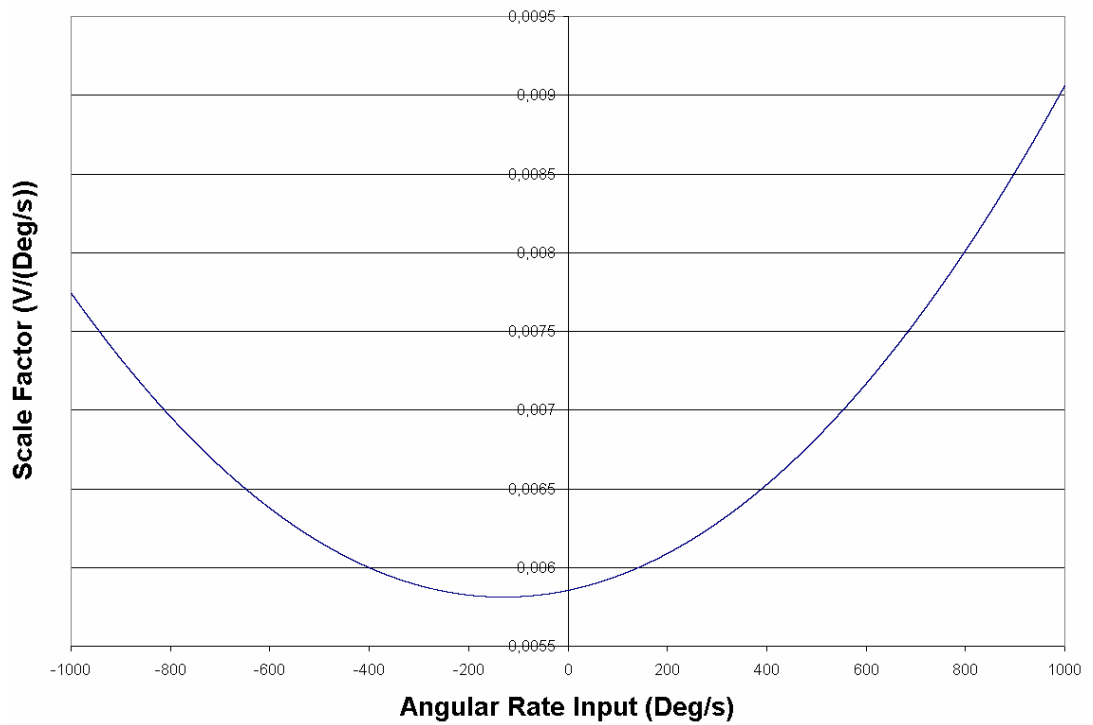
Figure 4.49 shows the plot of scale factor versus angular rate input of the QMG under the same constant angular acceleration of  $1\text{deg}/\text{sec}^2$  for centered and off-centered positioning. In centered test, the scale factor tends to increase with increasing rate input. This behavior means either the proof masses are not exactly centered and the decreased Coriolis coupling from drive mode cannot overcome this minute shift of proof masses, or a mechanical obstacle is present which is not detectable by microscope investigation. However, the acceleration dependent scale factor drift is  $1.59\text{ (mV}/(\text{deg}/\text{sec}))/\text{g}$ , which is about 70 % that of DMG and 40 % that of the SMG.

The QMG has the lowest bias g-sensitivity among the three gyroscopes. Figure 4.50 shows the output of the DMG at rest with linear accelerations of  $1\text{g}$  magnitude applied along the four sides of the gyroscope, corresponding to the angles of  $0^\circ$ ,  $90^\circ$ ,  $180^\circ$ , and  $270^\circ$ . The corresponding bias g-sensitivity is  $1.02(\text{deg}/\text{sec})/\text{g}$ .

The decrease in the bias g-sensitivity of the QMG is highly due to the odd-symmetric coupling mechanism in the drive mode together with the fully differential processing of resistively biased buffer signals.



(a)



(b)

Figure 4.49: Plot of scale factor versus angular rate input of the QMG under the same constant angular acceleration of  $1 \text{ deg/sec}^2$  for centered (a) and off-centered (b) positioning.

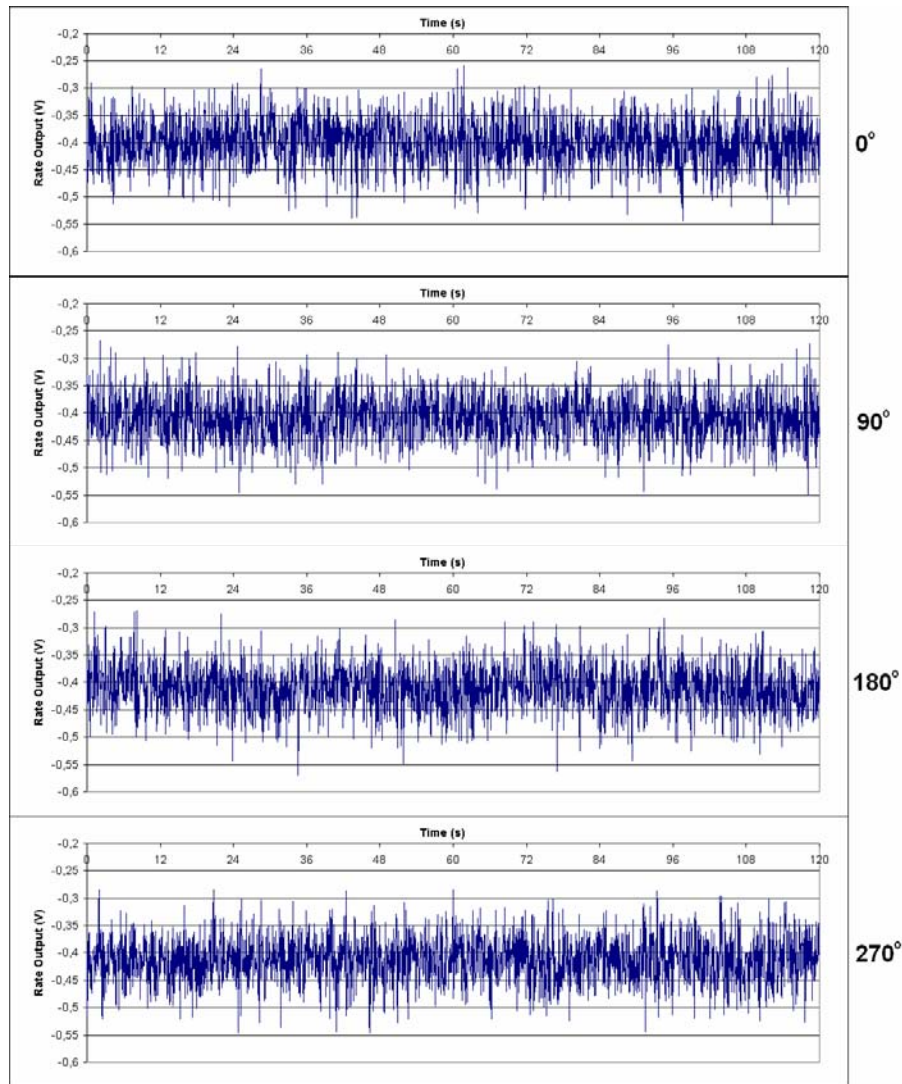
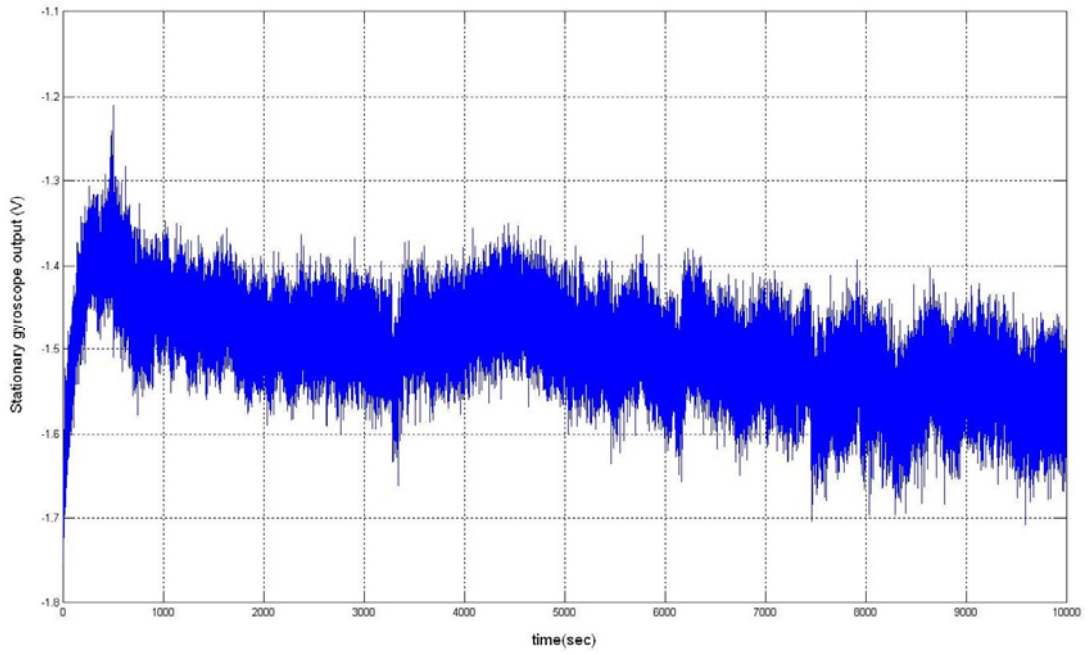


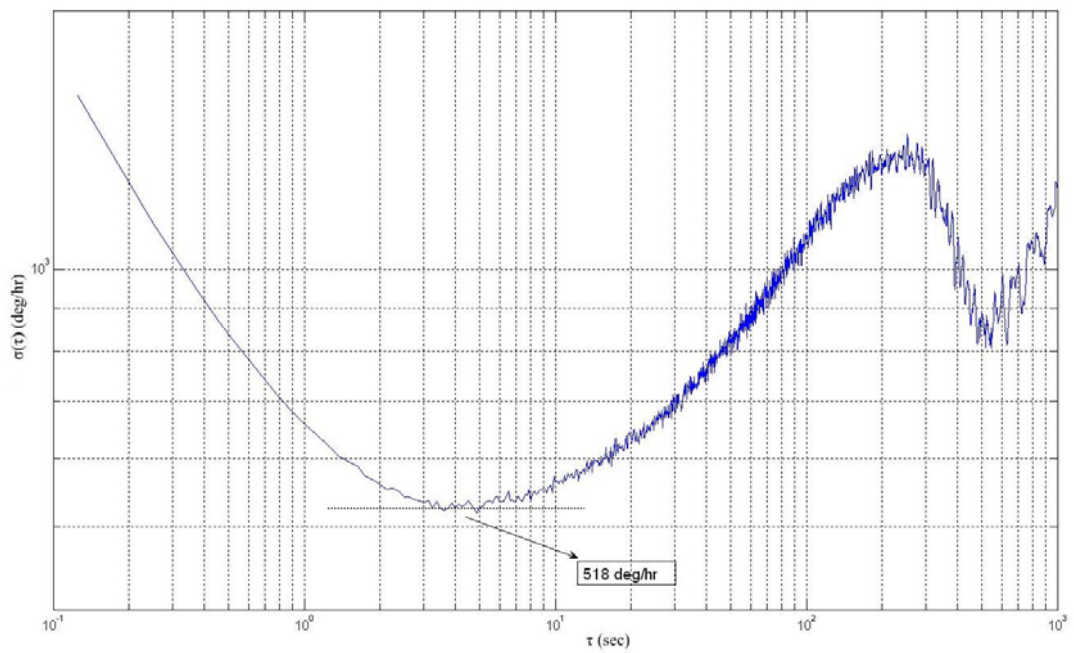
Figure 4.50: The output of the DMG at rest with linear accelerations of 1g magnitude applied along the four sides of the gyroscope, corresponding to the angles of  $0^\circ$ ,  $90^\circ$ ,  $180^\circ$ , and  $270^\circ$ .

### 4.2.3.2 Test Results of QMG at Vacuum Ambient

As expected, the bias instability and angle random walk of the output to a zero rate input is much lower than the atmospheric ambient. Figure 4.51 shows bias drift and the Root Allan Variance curve of the QMG at vacuum, corresponding to a bias drift and an angle random walk of  $780\text{deg/hr}$  and  $10.0\text{deg}/\sqrt{\text{hr}}$ , respectively. The lowered viscous air damping provided by the vacuum ambient and increased thermal stability due to less number of air particles in convection and conduction, plays an important role in this noise improvement.



(a)

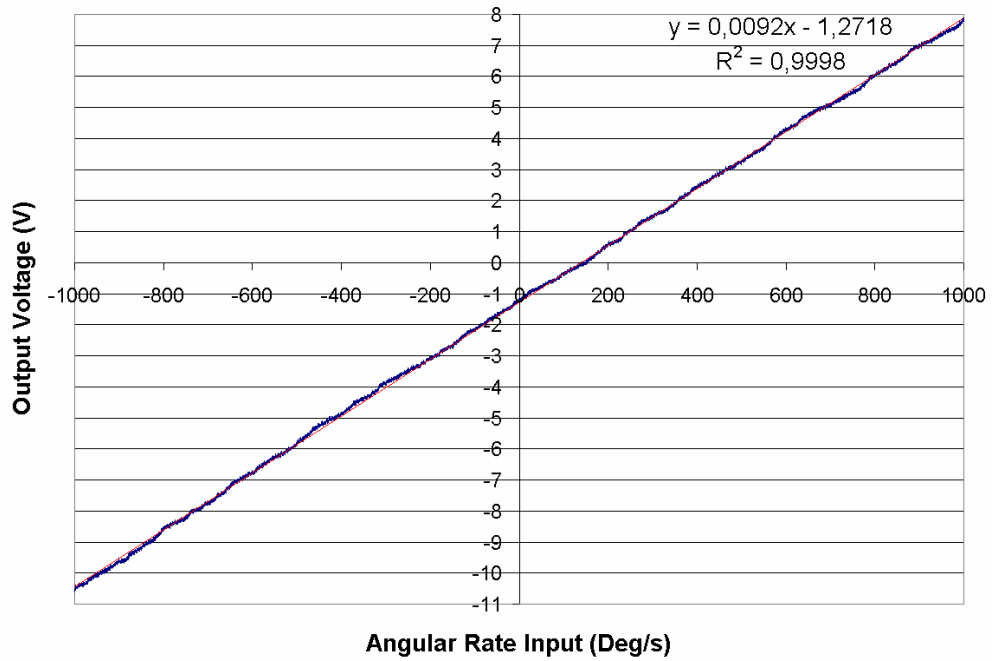


(b)

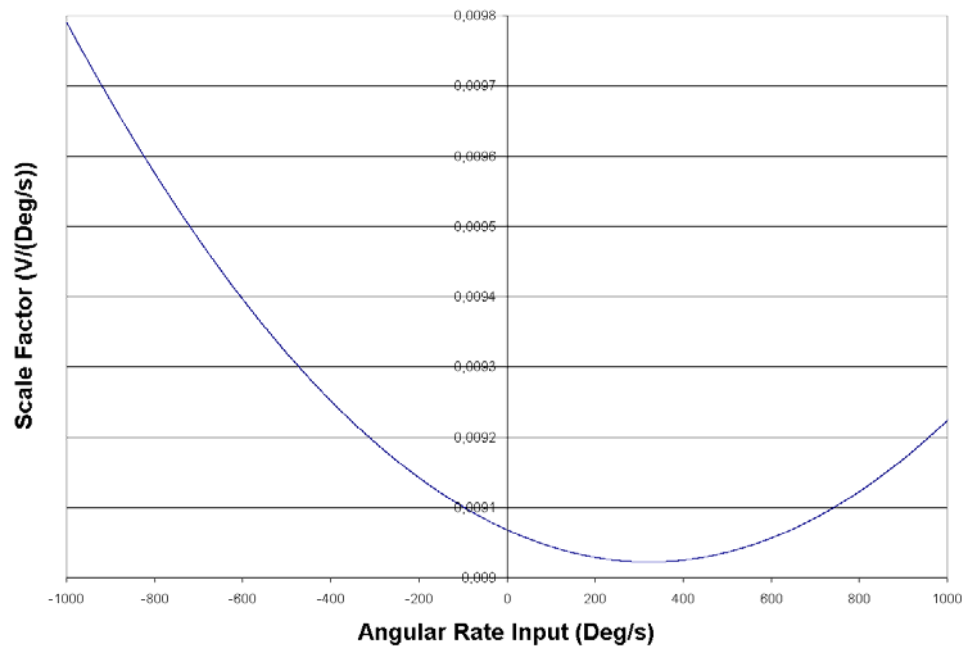
Figure 4.51: The bias drift and the Root Allan Variance curve of the QMG at vacuum, corresponding to a bias drift and an angle random walk of 780deg/hr and 10.0deg/ $\sqrt{\text{hr}}$ , respectively.

Figure 4.52 shows the rate output and scale factor data plots of the QMG at vacuum under a constant angular acceleration of 1deg/sec<sup>2</sup> while the gyroscope is centered. The scale factor of the gyroscope is 9.2 mV/(deg/sec) for zero g-loading with 0.02%

nonlinearity. The asymmetry in the drive-to-sense coupling is possibly due to the fabrication nonuniformities or nonuniform structural electronic resistance throughout the relatively large gyroscope chip.



(a)



(b)

Figure 4.52: Rate output and scale factor data plots of the QMG at vacuum under a constant angular acceleration of  $1 \text{ deg/sec}^2$  while the gyroscope is centered. The scale factor of the gyroscope is  $9.2 \text{ mV}/(\text{deg/sec})$  for zero g-loading with 0.02 % nonlinearity.

Finally, Table 4.3 presents overall performance specifications of the quadruple-mass gyroscope in atmospheric pressure and in vacuum. Vacuum ambient decreases the nonlinearities due to the decreased vibration amplitude and increases the resolution with a low angle random walk. Additionally, the quad-mass gyroscope is proven to be an effective structure for decreasing the g-sensitivity

Table 4.3: Performance specifications of the quadruple mass gyroscope in atmospheric pressure and in vacuum.

	Quadruple Mass Gyroscope	
	Atmosphere	Vacuum
Drive Mode Resonance Frequency	4747 Hz	4719 Hz
Drive Mode Vibration Amplitude	2.4 $\mu\text{m}$	-
Drive Mode Quality Factor	86	-
Scale Factor	6.3 mV/( $^{\circ}$ /s)	9.2 mV/( $^{\circ}$ /s)
R <sup>2</sup> nonlinearity	1.00 %	0.02 %
Bias Instability	6485.67 $^{\circ}$ /hr	780 $^{\circ}$ /hr
Angle Random Walk	43.2 $^{\circ}$ / $\sqrt{\text{hr}}$	10.0 $^{\circ}$ / $\sqrt{\text{hr}}$
Bias g-sensitivity	1.02 ( $^{\circ}$ /s)/g	-
Scale Factor g-sensitivity	1.59 (mV/( $^{\circ}$ /s))/g	-
Raw Angular Rate Sensitivity	131.8 $\mu\text{V}$ /( $^{\circ}$ /s)	-
Rate Equivalent Quadrature	273.3 $^{\circ}$ /s	-
Frequency Margin For 40 $\mu\text{m}$	6 Hz	-

### 4.3 Summary of Tests and Conclusions

In this chapter, the characterization and performance tests of fabricated vibrating micromachined gyroscopes which have both single and multiple masses together with novel mechanical drive mode coupling mechanisms are presented. The tests are conducted using resistive biasing with external self resonance and control loops. The test procedure revealed the scale factor, nonlinearity, bias instability (resolution), angle random walk (integrated noise), bias and scale factor g-sensitivity together with the rate equivalent quadrature and raw angular rate sensitivity of the gyroscopes at atmospheric ambient. Among these, scale factor, nonlinearity, bias instability and angle random walk parameters of these gyroscopes are tested also at vacuum. The results of these tests revealed some important facts about g-sensitivity of vibratory

micromachined gyroscopes and verified the advantages of multi-mass gyroscopes with differential readout scheme.

Table 4.4 summarizes the performance parameters of the developed gyroscopes, both at atmospheric and vacuum ambient. Depending on the number of masses and the number of sense electrodes, the driving amplitude is adjusted for similar scale factor for all three gyroscopes. Since the employed drive mechanisms and the optimized folded springs allow up to 50  $\mu\text{m}$  of peak-to-peak vibration amplitude with minute frequency shift, the tests are held at different vibration amplitudes for different structures without a significant performance fluctuation from structure to structure.

Table 4.4: Performance comparison of the three gyroscopes with single, double and quadruple mass(es). Increasing the number of masses and the symmetry of the gyroscope topologies decreases the g-sensitivity but also decreases the resolvable rate at atmospheric pressure.

	SMG		DMG		QMG	
	ATM	VAC	ATM	VAC	ATM	VAC
Drive Mode Resonance Frequency (Hz)	3446	3451	5045	5058	4747	4719
Drive Mode Vibration Amplitude ( $\mu\text{m}$ )	16.8	-	12.6	-	2.4	-
Drive Mode Quality Factor	216	-	303	-	86	-
Scale Factor ( $\text{mV}/(^{\circ}/\text{s})$ )	10.1	8.9	6.4	11.8	6.3	9.2
$R^2$ nonlinearity (%)	0.03	0.04	0.05	0.03	1.00	0.02
Bias Instability ( $^{\circ}/\text{hr}$ )	391	106	200	1029	6486	780
Angle Random Walk ( $^{\circ}/\sqrt{\text{hr}}$ )	5.2	4.8	5.5	6.7	43.2	10.0
Bias g-sensitivity ( $(^{\circ}/\text{s})/\text{g}$ )	1.94	-	1.67	-	1.02	-
Scale Factor g-sensitivity ( $(\text{mV}/(^{\circ}/\text{s}))/\text{g}$ )	3.85	-	2.16	-	1.59	-
Raw Angular Rate Sensitivity ( $\mu\text{V}/(^{\circ}/\text{s})$ )	60.5	-	45.6	-	131.8	-
Rate Equivalent Quadrature ( $^{\circ}/\text{s}$ )	98.0	-	413.4	-	273.3	-
Frequency Margin For 40 $\mu\text{m}$ (Hz)	8	-	9	-	6	-

The resolutions of the gyroscopes are highly dependent on the driving mechanism and on the ambient pressure. Increasing the number of masses dramatically affect the resolution of the overall sensor, as expected. The reason of this is the impossibility of and exact quality factor matching of all the sensing masses manually, causing a phase mismatch and additional noise. Additionally, increased number of differential amplifiers adding additional noise in a cascaded manner and different drive mode vibration amplitudes the gyroscopes aiming a comparable scale factor similarity are other parameters that affects the performance of the gyroscopes. Thus, the SMG has the best resolution, at about 391deg/hr in atmospheric ambient. At vacuum, the

resolutions of the gyroscopes are improved due to the decreased viscous air friction which is a major phase source in the sense mode. The SMG has reached a resolution level of 106deg/hr at vacuum.

Same consideration is valid for the quadrature error in the gyroscopes. Increasing the number of sensing masses increases the quadrature error because of the minute phase differences between the masses, resulting in higher offset at the output of the gyroscopes.

However, contrary to the decrease in the resolution, the performances of the gyroscopes are improved in the g-sensitivity manner if multiple masses are utilized. Comparing the SMG, DMG and QMG, QMG has the lowest scale factor and bias shift caused by the intentionally induced acceleration in its sense direction. The measured bias g-sensitivity value of the QMG is about 1.02 (deg/sec)/g and the scale factor g-sensitivity is about 1.59 (mV/(deg/sec))/g, which have improved the g-sensitivity of the SMG by about 100%.

The vacuum performance of the gyroscopes are measured to be much better considering the resolution and the angle random walk, but due to the setup restrictions, the g-tests of the fabricated gyroscopes cannot be done and left for future research. During the tests, it is verified that decreasing g-sensitivity and quadrature while improving the resolution is possible at vacuum ambient together with adequate frequency and phase tuning structures.

In conclusion, the performance tests of designed and fabricated single and multi-mass micromachined gyroscopes are successfully accomplished. The double and quadruple mass gyroscopes are verified to be decreasing the g-sensitivity compared to single mass gyroscopes. The tradeoff between the g-sensitivity and the resolution, is also presented and verified with adequate performance tests. Improving the readout and control electronics together with utilization of active frequency tuning loop would yield better results for the given structures.

## CHAPTER 5

### CONCLUSIONS AND FUTURE WORK

The research reported in this dissertation comprises the development of multi-mass high performance micro-machined gyroscopes. The proposed multi-mass gyroscopes utilize a novel ring-spring coupling mechanism minimizing the drive mode non-linearities and deviations from exactly opposite resonance phases. Within the scope of this research three different micro-machined gyroscopes are designed and fully characterized. These gyroscopes have single, double and quadruple mass structures to compare the g-sensitivity levels with increasing number of masses. The designed gyroscopes are fabricated using commercial SOI-MUMPs process of MEMSCAP<sup>®</sup> Inc. Moreover, special test setups are implemented for self-resonance operation of the drive mode resonator and g-sensitivity tests. Additionally the performance characteristics of these three different gyroscope designs are obtained in both atmospheric and vacuum ambient.

Based on the results obtained from this study following conclusions are drawn:

1. The electromechanical dynamics of single and multi-mass gyroscopes are investigated. Especially the drive mode mechanics of tuning-forks are studied for minimal cross-coupling and resonance non-linearity with maximum linear and rotational acceleration immunity. It is concluded that the effects of external linear accelerations, inherent centripetal forces and tangential accelerations caused by unpredictable rotational accelerations on the sense and drive modes of the gyroscope can only be minimized by multi-mass

structures. However, in multi-mass resonators the harmony among the masses turns out to be a vital point in their design. It was observed that in the previously designed tuning-fork structures the peak resonance frequency is highly dependent on the driving amplitude because of the rigid and non-optimized coupling structures. To overcome these problems a new ring-shaped, highly linear coupling mechanism is devised.

2. To further advance this study, three novel micro-machined gyroscopes are designed including different applications of the afore-mentioned coupling mechanism. The simplest structure was a single mass gyroscope serving as a reference to compare the performances of multi-mass gyroscopes. This gyroscope has all the fundamental structural design aspects including fully symmetric and evenly distributed stress-free suspension springs, frame-in-frame type drive jig, proof mass and sense jig arrangement, dedicated varying gap type frequency tuning and sense finger sets, varying overlap-area type drive finger sets allowing high vibration amplitudes. In the double mass type gyroscope two single mass structures are connected via the aforementioned coupling mechanism forming a tuning fork structure. This structure is more robust to linear and rotational accelerations, has more stable drive mode resonance with an improved sensitivity with differential read-out. But, in spite of the low g-sensitivity the asymmetric effect of the accelerations on the drive and sense axes causes non-uniform direction-dependent g-immunity. To overcome this problem a quadruple mass structure is proposed with modified version of the original single mass structures connected using the fully symmetric ring spring. For effective use of area, the shapes of the drive jig, proof mass and sense jig are modified together with the locations of the suspension springs. This sophisticated design has the advantage of uniform and lower g-sensitivity, more stable drive mode resonance and maximized sensitivity with differential read-out.
3. The designs of the gyroscopes are compatible with a well optimized SOI process which has 25  $\mu\text{m}$  structural thickness and 2  $\mu\text{m}$  capacitive gaps with back side substrate removal with an additional post-processing of wet oxide

etching. The single, double and quadruple mass gyroscopes occupy an area of 4.1 mm x 4.1 mm, 4.1 mm x 8.9 mm, and 8.9 mm x 8.9 mm respectively.

4. Preliminary resonance tests are followed by the full performance tests done with the released gyroscope prototypes that are hybrid connected to resistively biased unity gain buffer-connected operational amplifiers. For these tests special gold electroplated package PCBs and a mainboard PCB, to which all the other sub-circuits are connected, are designed and manufactured. In addition, an external drive loop is set up for controllable drive mode frequency and amplitude in self-resonance.
5. The performance characteristics of the released single, double and quadruple mass gyroscopes are determined by using the designed mainboard PCB and the external self-resonance loop. For this, a series of tests are performed with and without angular rate application in order to measure the raw angular rate sensitivity, bias instability, angle random walk, rate equivalent quadrature error, scale factor,  $R^2$  non-linearity, bias g-sensitivity, scale factor g-sensitivity and drive mode frequency stability.
6. The performance tests are held in both atmospheric and vacuum ambient. In these tests it is shown that bias g-sensitivity and scale factor g-sensitivity are decreased by 50% by the quadruple-mass gyroscope compared to the single mass one. Despite the poor read-out electronics, the single mass gyroscope reached a resolution of 106deg/hr at vacuum ambient, with an  $R^2$  non-linearity less than 0.05%. The resolution of the double and quadruple mass gyroscopes increases due to the poor output matching. Nevertheless, at vacuum their resolutions are better than 0.3deg/sec. Furthermore, during these tests the performance of the proposed ring-spring coupling mechanism is observed. The peak resonance frequency of all the three gyroscopes deviates less than 10 Hz in a vibration amplitude span of 0-44  $\mu\text{m}$  peak-to-peak.

Although the major g-sensitivity problem of the previous gyroscope structures are solved and double and quadruple mass gyroscopes are designed there still remains need for further research for improving the overall performance of MEMS gyroscopes. Below some topics that should be further researched are explained:

1. The mechanical offset that is present in the sense mode of the multi-mass structures should be minimized by proper control methods for effective differential read-outs. By means of this, the g-sensitivity and the non-linearity of the gyroscopes can be further improved.
2. For higher rate sensitivity and lower drive mode vibration amplitudes, capacitive type interface circuits should be utilized. Moreover, the externally implemented drive mode self-resonance loop should be implemented in single chip ICs together with the input buffers to minimize the effects of uncorrelated noise on the signal lines.
3. For multi-mass gyroscopes the scale factor and bias offset of individual masses should be automatically corrected and matched for an effective angular rate output extraction.
4. The drive and sense modes of the gyroscopes should be electrically isolated but mechanically connected for the minimum quadrature error on each mass. For this, appropriate electrical isolation techniques should be researched, like trench filling or oxidative insulation.
5. The cross-axis sensitivity of the quadruple mass gyroscope can be further decreased by placing additional electrodes on the lower surface of the proof masses and subtracting the sensed rate data from these electrodes from the main signal. Furthermore, the structure can be optimized as a novel three-axes gyroscope.

In conclusion, the demonstration of high performance gyroscopes with low g-sensitivity using multi-mass structures is achieved in this research. Even with the poor read-out electronics and external resonance loops, the measured performances of the fabricated gyroscopes show that multi-mass gyroscope structures with a well-optimized coupling mechanism improves the immunity to induced accelerations while preserving the other performance criteria. Moreover, it is foreseen that the proposed multi-mass gyroscopes can be advanced for higher number of sensitive axes.

## REFERENCES

- [1] J. L. Meriam and L.G. Kraige, "Engineering Mechanics Volume 2: Dynamics," Fourth Edition, John Wiley & Sons, New York, 1998.
- [2] Irving H. Shames, "Engineering Mechanics, Statics and Dynamics," Fourth Edition, Prentice Hall, New Jersey, 1996.
- [3] P. Ferdinand Beer and E. Russell Johnston Jr, "Mechanics of Materials," Second Edition, Mc Graw Hill, London, 1992.
- [4] N. Yazdi, F. Ayazi, and K. Najafi, "Micromachined Inertial Sensors," Proc. of the IEEE, Vol. 86, No. 8, pp. 1640-1659, August 1998.
- [5] P. Greiff, B. Boxenhorn, T. King, and L. Niles, "Silicon Monolithic Micromechanical Gyroscope," Tech. Dig. 6th Int. Conf. Solid-State Sensors and Actuators (Transducers'91), San Fransisco, NY, pp. 966-968, June 1991.
- [6] K. Funk, H. Emmerich, A. Schilp, M. Offenber, R. Neul, and F. Larmer, "A Surface Micromachined Silicon Gyroscope Using a Thick Polysilicon Layer," Proc. IEEE Micro Electro Mechanical Systems Workshop (MEMS'99), Orlando, FL, pp. 57-60, January 1999.
- [7] W. Geiger, W. U. Butt, A. Gaißer, J. Frech, M. Braxmaier, T. Link, A. Kohne, P. Nommensen, H. Sandmaier, and W. Lang, "Decoupled Microgyros and the Design Principle DAVED," Sensors Actuators A, vol. 95, pp. 239-249, 2002.
- [8] W. C. Tang, "Micromechanical Devices at JPL for Space Exploration," Proc. IEEE Aerospace Conf., Aspen, CO, pp. 461-470, March 1998.
- [9] T. Juneau, A. P. Pisano, and J. H. Smith, "Dual Axis Operation of a Micromachined Rate Gyroscope," Tech. Dig. 9th Int. Conf. Solid-State Sensors and Actuators (Tranducers'97), Chicago, IL, pp. 883-886, June 1997.
- [10] H. Yang, M. Bao, H. Yin, and S. Shen, "A Novel Bulk Micromachined Gyroscope Based on a Rectangular Beam-Mass Gyroscope," Sensors Actuators A, vol. 96/2-3, pp. 145-151, February 2002.
- [11] R. Voss, K. Bauer, W. Ficker, T. Gleissner, W. Kupke, M. Rose, S. Sassen, J. Schalk, H. Seidel, and E. Stenzel, "Silicon Angular Rate Sensor for Automotive Applications with Piezoelectric Drive and Piezoresistive Readout," Tech. Dig. 9th Int. Conf. Solid-State Sensors and Actuators (Transducers'97), Chicago, IL, pp. 879-882, June 1997.

- [12] M. W. Putty, "A Micromachined Vibrating Ring Gyroscope," Ph.D. Dissertation, The University of Michigan, 1995.
- [13] S. Chang, M. Chia, P. Castillo-Borelley, W. Hidgon, Q. Jiang, J. Johnson, L. Obedier, M. Putty, Q. Shi, D. Sparks, and S. Zarabadi, "An Electroformed CMOS Integrated Angular Rate Sensor," *Sensors Actuators A*, vol. 66, pp. 138-143, April 1998.
- [14] F. Ayazi and K. Najafi, "A HARPSS Polysilicon Vibrating Ring Gyroscope," *J. Microelectromechanical Sys.*, Vol. 10, No. 2, pp. 169-179, June 2001.
- [15] A. M. Madni, L. E. Costlow, S. J. Knowles, "Common Design Techniques for BEI GyroChip Quartz Rate Sensors for Both Automotive and Aerospace/Defense Markets," *IEEE Sensors*, Vol. 3, No. 5, pp.569-578, October 2003.
- [16] J. Bernstein, S. Cho, A. T. King, A. Kourepenis, P. Maciel, and M. Weinberg, "A Micromachined Comb-Drive Tuning Fork Rate Gyroscope," *Proc. of IEEE Micro Electro Mechanical Systems Workshop (MEMS'93)*, Fort Lauderdale, FL, pp. 143-148, February 1993.
- [17] M. Lutz, W. Golderer, J. Gerstenmeier, J. Marek, B. Maihofer, S. Mahler, H. Munzel and U. Bischof, "A Precision Yaw Rate Sensor in Silicon Micromachining," *Tech. Dig. 9th Int. Conf. Solid-State Sensors and Actuators (Transducers'97)*, Chicago, IL, pp. 847-850, June 1997.
- [18] A. Gripton, "The Application and Future Development of a MEMS SiVSG® for Commercial and Military Inertial Products," *IEEE Position Location and Navigation Symp. (PLANS'02)*, Palm Springs, CA, pp. 28-35, April 2002.
- [19] D. Karnick, G. Ballas, L. Koland, M. Secord, T. Braman, and T. Kourepenis, "Honeywell Gun-Hard Inertial Measurement Unit (IMU) Development," *IEEE Position Location and Navigation Symp. (PLANS'04)*, Monterey, CA, pp. 49-55, April 2004.
- [20] J. A. Geen, S. J. Sherman, J. F. Chang, and S. R. Lewis, "Single-Chip Surface Micromachined Integated Gyroscope with 50/spl deg/h Allan Deviation," *J. Solid State Cct.*, Vol. 37, No. 12, pp. 1860-1866, December 2002.
- [21] B. E. Boser, "Electronics for Micromachined Inertial Sensors," *Tech. Dig. 9th Int. Conf. Solid-State Sensors and Actuators (Transducers'97)*, Chicago, IL, pp. 1169-1172, June 1997.
- [22] S. S. Baek, Y. S. Oh, B. J. Ha, S. D. An, B. H. An, H. Song, and C. M. Song, "A Symmetrical Z-Axis Gyroscope with a High Aspect Ratio Using Simple and New Process," *Proc. IEEE Micro Electro Mechanical Systems Workshop (MEMS'99)*, Orlando, FL, pp. 612-617, January 1999.

- [23] J.-Y. Lee, S.-H. Jeon, H.-K. Jung, H.-K. Chang, and Y.-K. Kim, "Vacuum Packaged Low Noise Gyroscope with Sub mdeg/s/ $\sqrt{\text{Hz}}$  Resolution," Proc. IEEE Micro Electro Mechanical Systems Workshop (MEMS'05), Miami, FL, pp. 359-362, January 2005.
- [24] O. Degani, D. J. Seter, E. Socher, S. Kaldor, and Y. Nemirowsky, "Optimal Design and Noise Consideration of Micromachined Vibrating Rate Gyroscope with Modulated Integrative Differential Optical Sensing," J. Microelectromechanical Sys., Vol. 7, No. 3, pp. 329-338, September 1998.
- [25] S. Zhaohui, C. Xuemeng, H. Shusen, W. Yuelin, J. Jiwei, and L. Xinxin, "A High-Sensitivity Piezoresistive Gyroscope with Torsional Actuation and Axially-Stressed Detection," Proc. IEEE Sensors Conf., Toronto, Canada, pp. 457-460, October 2003.
- [26] S. E. Alper, "Silicon Surface Micromachined Gyroscope Using MEMS Technology," M.Sc. Thesis, Middle East Technical University, 2000.
- [27] S. E. Alper, "MEMS Gyroscopes For Tactical-Grade Inertial Measurement Applications," Ph.D. Dissertation, Middle East Technical University, 2005.
- [28] S. E. Alper and T. Akin, "A Symmetric Surface Micromachined Gyroscope with Decoupled Oscillation Modes," Sensors and Actuators A, Vol. 97-98C, pp. 337-348, April 2002.
- [29] S. E. Alper and T. Akin, "A Symmetrical and Decoupled Nickel Microgyroscope on Insulating Substrate," Sensors and Actuators A, Vol. 115, pp. 336-350, September 2004.
- [30] S. E. Alper and T. Akin, "A Single-Crystal Silicon Symmetrical and Decoupled MEMS Gyroscope on an Insulating Substrate," J. Microelectromechanical Systems, Vol. 14, No. 4, pp. 707-717, August 2005.
- [31] S. E. Alper, K. M. Silay , and T. Akin, "A Low-Cost Rate-Grade Nickel Microgyroscope," Sensors and Actuators A: Physical, Vol. 132, Issue 1, pp. 171-181, November 2006
- [32] S. E. Alper, K. M. Silay , and T. Akin, "Tactical-Grade Silicon-on-Glass Gyroscope with Very-Small Quadrature Coupling," Proc. of the 20th European Conf. on Solid-State Transducers (Eurosensors XX), Gothenburg, Sweden, pp. M2B-P3, September 2006
- [33] S. E. Alper, K. Azgin, and T. Akin, "High-Performance SOI-MEMS Gyroscope with Decoupled Oscillation Modes" 19th IEEE Int. Conf. on Micro Electro Mechanical Systems (MEMS 2006), Istanbul, TURKEY, January 2006.
- [34] K. Azgin, Y. Temiz, and T. Akin, "An SOI-MEMS Tuning Fork Gyroscope With Linearly Coupled Drive Mechanism" 20th IEEE Int. Conf. on Micro Electro Mechanical Systems (MEMS 2007), Kobe, JAPAN, January 2007.

- [35] Keith Miller, Allen Cowen, Greg Hames and Busbee Hardy, "SOIMUMP's Design Handbook, a MUMPs® Process", Revision 4.0.
- [36] T. B. Gabrielson, "Mechanical-Thermal Noise in Micromachined Sensors and Acoustic and Vibration Sensors," IEEE Trans. Electron. Devices, Vol. 40, No. 5, May 1993, pp.903-909.